Effect of morphology on molecular organic solar cells

Dissertation

zur Erlangung des
Doktorgrades der Naturwissenschaften
(Dr. rer. nat.)

eingereicht an der
Mathematisch-Naturwissenschaftlich-Technischen Fakultät
der Universität Augsburg

vorgelegt von

Stefan Grob

Augsburg, November 2015

Universität Augsburg
Mathematisch-Naturwissenschaftlich-
Technische Fakultät

1. Gutachter:	Prof. Dr. Wolfgang Brütting
2. Gutachter:	Prof. Dr. Achim Wixforth
Tag der mündlichen Prüfung:	27.01.2016

Contents

Chapter 1

Motivation

> *"We really only need one power plant to supply us. It needs to have good distribution over most of the populated areas and easily available to anyone. It should be a proven design with no maintenance required and last a very long time without any upgrades or modifications. There should be no waste to deal with and be inaccessible to terrorists for their use. Such a power plant already exists. It is 93,000,000 miles away but, oh, so easy to hook up to..."*
>
> Unknown[1]

The amount of fossil fuels on earth is limited and their combustion is one of the major sources for the emission of carbon-dioxide and other greenhouse gases with detrimental long-term consequences on the climate. For that reason, the demand for clean and renewable energy keeps growing.[2] Already in the year 2000, the German Federal Government has passed a law concerning renewable energies, which includes a steady increase of the fraction of renewable energy sources within the German power mix. At the beginning of this work in 2011, this fraction amounted to merely 17 %. Within only four years, this portion could be enhanced by a factor of almost 1.5 up to 25 % by now. According to the German Federal Government this amount will be further increased to at least 40 % in 2025 and even to 55 % in 2035.[3]

In general, renewable energies are (on a human timescale) inexhaustible or extremely fast regrowing energy resources such as sun, wind, biomass, geothermics or hydropower. Within the frame of the German Renewable Energies Act (EEG), the contribution of each of them to the German energy mix shall be enhanced. For solar energy, an annual increment of 2,500 megawatt is intended.[3] In this context, talking about harnessing solar energy by means of photovoltaics, usually means the application of conventional,

inorganic solar cells. Most of the solar cells, which are used nowadays, are composed of silicon (Si), possessing average efficiencies close to 20 % and typical lifetimes exceeding 20 years.[4] On a laboratory scale, however, much higher efficiencies can be reached using further materials like gallium, indium, phosphorus and arsenic. The current efficiency record for a concentrator multijunction device is 46 %.[5]

Despite these considerable development of inorganic photovoltaics, they also have some significant drawbacks. Their fabrication is very energy consuming and their rigid shape requires plane surfaces for mounting so that they cannot be installed directly on three-dimensionally shaped or even flexible substrates. This is where organic solar cells come into play. Although they will never reach the efficiency records of their inorganic counterparts, organic photovoltaics possesses a number of significant advantages of scientific, ecological and economical interest. Due to high absorption coefficients, organic photoactive layers can be fabricated very thin leading to potentially lower material costs and a reduced consumption of materials, which makes organic solar cells already interesting from an economic perspective. The characteristic low melting point of organic materials also allows less energy consuming fabrication processes. Due to low melting temperatures, high vapor pressures and their ability to be solubilized in numerous organic solvents, both solution and gas-phase methods are possible for the fabrication of organic thin films.[6] Such processing techniques usually allow for both high speed and low cost, e.g. by roll-to-roll production, where the materials are directly printed onto a foil substrate, leading to light-weight and large-area flexible solar panels. In combination with the (semi)transparency of organic solar cells, this offers entirely new possibilities in terms of solar cell architecture and application, e.g. for mobile devices, house facades or windows.

Moreover, less material input also leads to ecological advantages of organic solar cells compared to Si cells. Less environmental impact is also given as the usage or emission of hazardous materials, inevitable in manufacturing or disposal of conventional photovoltaics, can be avoided.[7] In general, organic semiconductors consist of ecologically harmless hydrocarbons. This leads to a further benefit as hydrocarbons offer innumerable possibilities for improvement by tailoring photoactive materials to adapt structural and photoelectric properties. Nevertheless, there are mainly two significant drawbacks, which still prevent a large scale market entry of organic solar cells. One reason is long-term stability. Organic solar cells are very sensitive to ambient conditions. The influence of e.g. water and oxygen has to be prevented to avoid rapid degradation.[8] For that reason, efficient sealing techniques are required, which do not counteract the benefits of organic solar cells. The second crucial disadvantage is the efficiency, which is steadily increasing but still too low compared to conventional devices (Fig. 1.1).

Therefore, a further improvement of organic solar cells concerning their power conversion efficiency is essential. For that reason, there is still a great need for research to gain a better understanding of the basic processes within organic photovoltaics to en-

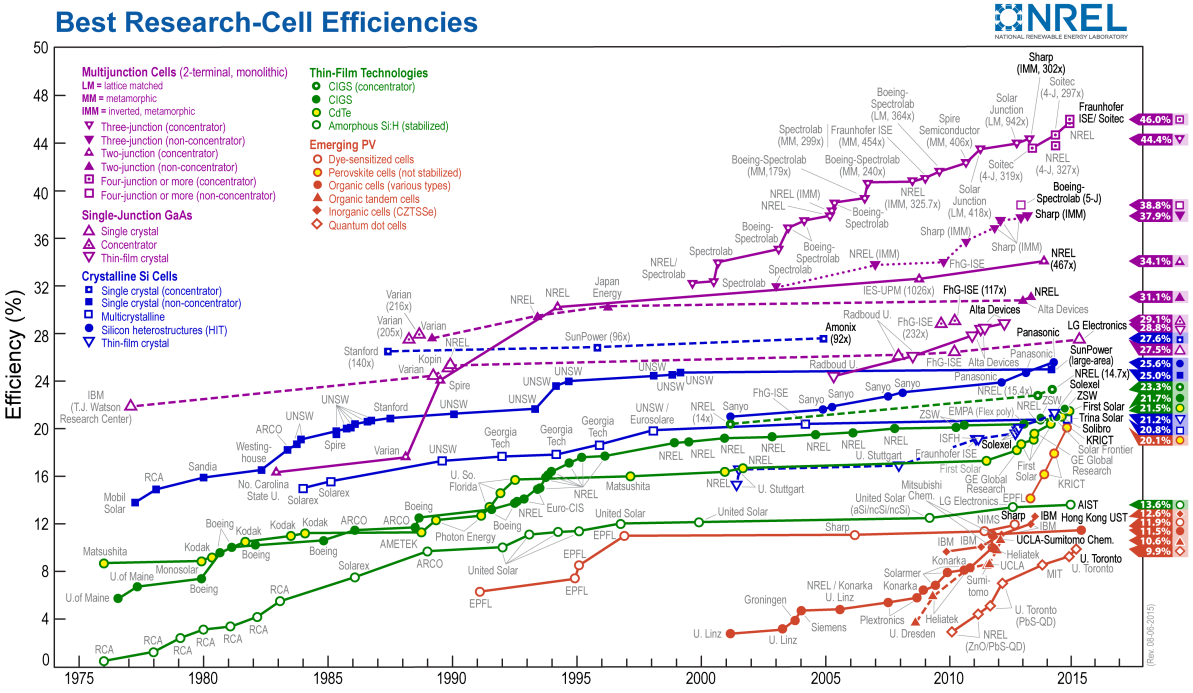

Figure 1.1: Efficiency development of all types of photovoltaic cells within the last 40 years. Nowadays, the best organic solar cells on a laboratory scale (red filled circles) reach efficiencies of up to 11.5 %.[9]

able their optimization. One crucial aspect is the morphology of the photoactive layers. This thesis provides a detailed look on the influence of changing morphologies on organic solar cell performance. Particular attention is paid on the comparison of crystalline and amorphous donor materials. These materials are chosen to be structurally similar so that upcoming differences can be almost completely attributed to morphological deviations. Moreover, a possibility to enhance the power conversion efficiency is presented by inserting an additional blocking layer beneath the donor. Again, there is a focus on the morphology. In particular, the question is answered whether and to what extent the morphology of the blocking layer influences the efficiency improvement. Typically, the morphology of organic thin films is already set after its preparation due to certain material properties. However, it is shown that a post-production process, annealing of the organic layers with solvent vapor, leads to a reorientation of the molecules and thus morphological changes. It is shown that such a treatment can improve several sub-processes within the overall charge generation process and thus also the efficiency of an organic solar cell. An alternative approach to improve organic photovoltaics is the application of tailor-made organic semiconductors. Therefore additionally, a detailed analysis of a new donor material is provided within the last section of this thesis.

Chapter 2

Principles of organic photovoltaics

Photovoltaics (PV) is defined as the generation of electricity by the direct conversion of sunlight within a device containing photoactive semiconductors. Organic photovoltaic cells (OPVC) utilize organic semiconductors (OSC) for that purpose. The particular features of OSCs are presented in the first section of this chapter. The following section describes the typical architecture and the basic physics of OPVC devices.

2.1 Organic semiconductors

Organic semiconductors are hydrocarbons with semiconductor properties. Semiconductors possess the ability to conduct electricity, in contrast to conductors like e.g. metals, however, this ability depends on some conditions. Only if sufficiently high voltage is applied or a certain radiation (infrared, visible, ultraviolet) impinges on the semiconductor's surface, electricity is conducted. Semiconductors can be either pure elements or compounds of two or even more different elements. In the field of conventional, inorganic semiconductors most common are silicon (Si) and germanium (Ge) or gallium arsenide (GaAs), respectively, all of them being typical representatives of inorganic solar cells.[10]

There are no elemental semiconductors in the field of organic semiconductors. Inherently, OSCs are composed of at least two different elements, mainly carbon (C) and hydrogen (H), with carbon always forming the backbone of the molecular structure. But also hetero-atoms like oxygen (O), nitrogen (N), fluorine (F), or sulfur (S) are common. These different elements can assemble to two different material classes of OSCs, with low weight molecular materials on the one hand, and polymers on the other hand, both being used within organic electronic devices. However, within this work the focus will be exclusively on the first of these two material classes.
The conductivity of OSCs is a consequence of a conjugated π-electron system, i.e. alter-

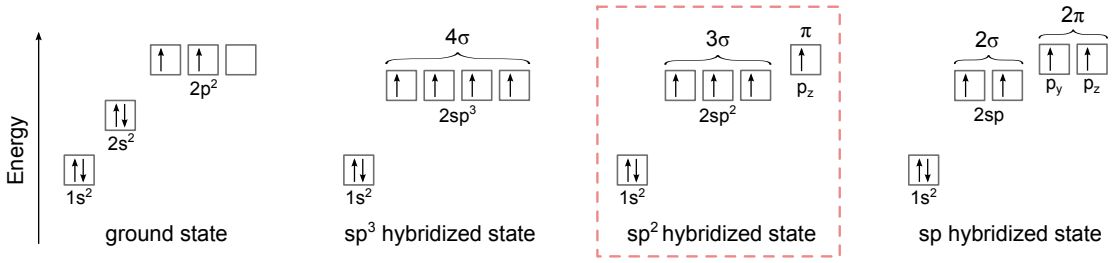

Figure 2.1: The four different electron configurations of carbon: Ground state, sp^3-, sp^2-, and sp-hybridization. The required conjugated π-electron system to achieve semiconductor properties is provided by sp^2-hybridization.

nating covalent single and multiple bonds (typically double bonds), which arises from a peculiarity of the electronic structure of carbon.[11] Generally, carbon possesses six electrons overall and four valence electrons with a configuration $1s^2\,2s^2\,2p_x^1\,2p_y^1$ in the ground state. However, carbon is able to undergo a hybridization of its atomic orbitals. This means that orbitals can be energetically lifted or lowered, while electrons are redistributed. Consequently, there are three different hybrid states, as a result of so-called sp-, sp^2-, and sp^3-hybridization (Fig. 2.1). Triple bonds are achieved for sp-hybridization and double bonds result from sp^2-hybridization whereas the sp^3-hybridization leads to four equal σ-bonds, i.e. single bonds to four other atoms. In turn, this means, that only sp- an sp^2-hybridized carbon can form the backbone of OSCs, as these states can provide the required conjugated π-electron system. However, molecules containing sp^2-hybridized carbon are by far more common.

In the case of an sp^2-hybridization, the 2s orbital combines with the $2p_x$ and the $2p_y$ orbital so that they level energetically, resulting in three equal sp^2 orbitals. These orbitals are aligned in plane, separated from each other by an angle of 120 °, leading to a trigonal planar structure. The remaining $2p_z$-orbital, however, remains unchanged and is aligned perpendicular to the other orbitals (Fig. 2.2 (a)). The four valence electrons of carbon are redistributed so that each orbital is occupied by one electron. The overlap of two sp^2-orbitals of two different C-atoms leads to a σ-bond between these atoms. In the molecular orbital (MO) theory, this means that the electron of one sp^2-orbital combines with the other in the binding σ-molecular orbital (Fig. 2.2 (b)). As a result of the strong overlap of the two sp^2-orbitals, the σ-bond is also strong. Hence, it requires comparatively high energies to lift one electron from the binding σ-MO to the antibinding σ^*-MO.

As already mentioned, the sp^2-hybridization of carbon provides double bonds. The second bond, the so-called π-bond, arises from the overlap of the parallel aligned $2p_z$-orbitals. As this overlap is weaker, also the π-bond is weaker than the σ-bond. In terms of the MO theory this means that the energetic difference between binding (π) and antibinding (π^*) molecular orbital is less. As indicated in Fig. 2.2 (b), the π-MO is the *highest occupied molecular orbital* (HOMO), while the π^*-MO is the *lowest unoccupied*

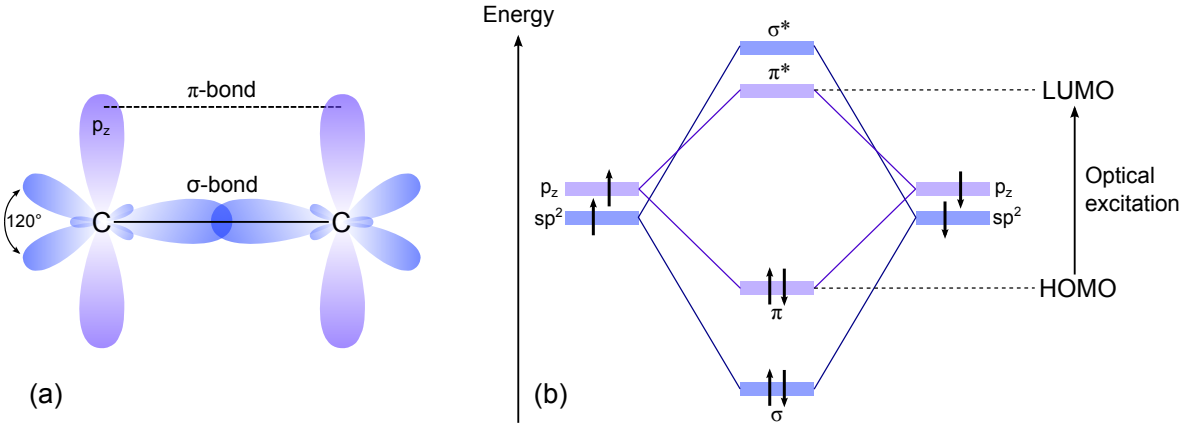

Figure 2.2: (a) sp^2-hybridization of carbon: The 2s orbital combines with $2p_x$ and $2p_y$ in a plane while the $2p_z$ orbital remains unchanged perpendicular to it. When connecting to another C-atom, one sp^2 hybrid orbital is responsible for the σ and the p_z orbital for the π-bonding. (b) Associated energy diagram of the molecular orbitals defining the HOMO-LUMO gap of an organic semiconductor with the levels of bonding π- and antibonding π^*-orbital, respectively.

molecular orbital (LUMO). Thus, the difference between these two orbitals is usually denoted as the HOMO-LUMO gap. The HOMO-LUMO or π-π^*-transition is the smallest and thus most probable transition in organic semiconductors. As a result, the HOMO-LUMO gap also determines the minimum energy of light, which can be absorbed and consequently also defines the optical gap[i]. Typical values of the HOMO-LUMO gap are between 1.5 and 3 eV, the exact value is determined by the extent of the conjugated π-electron system. Hence, optical excitation is possible in the range of visible light and near infra-red.[12] In conclusion, the π-bonds form the molecular backbone, while the π-electron system is responsible for most electronic and optical properties of the organic semiconductor.

In analogy to inorganic semiconductors the HOMO level can be described as the valence band and the LUMO level as the conduction band of the organic semiconductor.[13] However, the width of the energy bands in inorganic semiconductors is much larger ($\sim$ eV) compared to its organic counterparts ($\sim$ meV), which has great impact on charge transport. The charge carrier mobility μ in organic single crystals at room temperature is limited to a maximum of $\sim 20\,\mathrm{cm^2/Vs}$,[14,15] while real band transport in inorganic semiconductors enables mobilities, which are typically 100 - 10000 times higher.[16] In addition, organic semiconductors used in organic photovoltaics are usually no single crystals, in most cases they are not even polycrystalline but amorphous. As a result, in most organic semiconductors used for organic electronics incoherent hopping transport prevails with mobilities of merely $10^{-5} - 10^{-1}\,\mathrm{cm^2/Vs}$.[17]

[i]Keep in mind that for organic semiconductors, optical and transport gap are not completely identical. The large exciton binding energy leads to an optical band gap which is at a lower energy than the transport gap. A detailed comparison can be found elsewhere.[11]

Hopping transport is a consequence of the weak intermolecular *van der Waals forces* prevailing between two organic molecules within the solid, which leads to relatively small electronic coupling between molecular orbitals of adjacent lattice sites. As a result, charge carriers are strongly bound to the molecule they are located on and need a certain thermal energy to become mobile. Hence, the charge carrier mobility μ is determined by temperature. Moreover, also some other parameters can influence the mobility. So μ increases by an increasing applied electric field F and an increasing temperature T as well as by a decreasing activation energy ΔE. At high fields, these empirical correlations are typically expressed by

$$\mu \propto \exp\left(\gamma\sqrt{F}\right) \exp\left(-\frac{\Delta E}{k_\mathrm{B}T}\right) \tag{2.1}$$

with the field activation parameter γ.[18] Typical values for the activation energy ΔE are between 0.3 and 0.5 eV[12] At low fields, however, a non-Arrhenius temperature dependence was found using the disorder parameter σ.[19] Nevertheless, also within this model, increasing temperatures lead to an enhanced charge carrier mobility.

Due to the strong coupling of charge carriers to the molecule, also excitons are strongly bound to the molecule they are generated on. An exciton is a bound state consisting of an electron and a hole, which are connected via the attractive Coulomb force. Due to equal but opposite charges of electron and hole, an exciton is an electrically neutral quasiparticle. In organic semiconductors[ii], excitons can be generated by the injection of charge carriers or by the absorption of photons. While the first case is utilized to generate light through *organic light emitting diodes* (OLEDs), the second case is decisive for organic solar cells. The excitons generated in OPVCs are *Frenkel excitons*. This kind of excitons occurs within materials featuring a low relative dielectric constant (permittivity) ϵ_r. This is true for current organic semiconductors used for OPVCs having relative dielectric constants in the range of 2 - 4.[20] In contrast, inorganic semiconductors possess significantly larger values for ϵ_r usually between 12 and 16.[21] A high dielectric constant means that the screening of charges within the material is high, thus the Coulomb interaction between electron and hole of the exciton is weakened markedly. Therefore, a different type of exciton occurs in inorganic semiconductors, the *Wannier-Mott exciton* (Fig. 2.3 (a)). Its average radius is larger than the lattice spacing and the binding energy, i.e. the minimum energy required to dissociate an exciton into electron and hole is merely in the range of 5 - 15 meV,[22] and thus sufficiently below thermal energy at room temperature ($k_\mathrm{B}T \approx 25$ meV). As a result, excitons in conventional, inorganic photovoltaic cells are easily separated into free charge carriers without any further effort. Frenkel excitons (Fig. 2.3 (b)), however, are usually entirely located on one molecule and are strongly bound due to less screening of the Coulomb interaction between electron and hole.

[ii] Of course this is also valid for inorganic semiconductors, however, the focus in the following will be mainly on organic semiconductors and organic electronics.

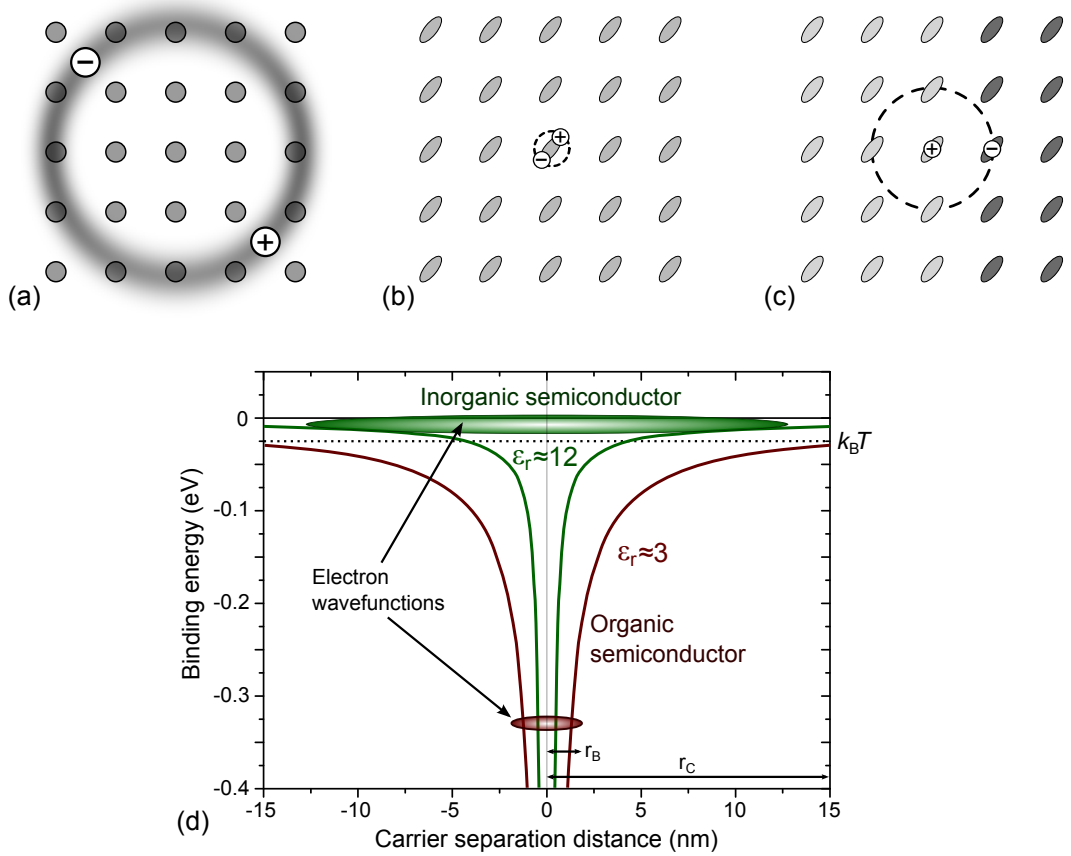

Figure 2.3: The three different types of excitons: (a) Delocalized and weakly bound Wannier-Mott excitons, possess an average radius which exceeds the lattice spacing. (b) On the contrary, in strongly bound Frenkel excitons, being present in organic semiconductors, the average radius is very small so that they are usually entirely located on one molecule. (c) The intermediate case, charge-transfer excitons occur between adjacent molecules. In organic semiconductors they are found at the donor-acceptor interface. (d) Illustration of the different binding energies of Wannier-Mott and Frenkel excitons and their consequences for inorganic and organic semiconductors, respectively.

Assuming $\epsilon_r = 3$ and an electron-hole distance $r = 1\,\mathrm{nm}$ (due to the small average radius of the Frenkel exciton), the exciton binding energy can be estimated via

$$E_\mathrm{B} = \frac{e^2}{4\pi\epsilon\epsilon_0 r} \tag{2.2}$$

to approximately 0.5 eV, with the vacuum permittivity ϵ_0. Consequently, thermal energy is not nearly sufficient to separate excitons in organic semiconductors. The difference between inorganic and organic semiconductors concerning exciton binding energy and required distance between electron and hole to overcome the Coulomb potential (the so-called Coulomb radius r_C) is illustrated in Fig. 2.3 (d).

The Coulomb radius of a an electron-hole pair at room temperature has to be at least

$$r_{\mathrm{C}} = \frac{e^2}{4\pi\epsilon\epsilon_0 kT} = 19\,\mathrm{nm} \tag{2.3}$$

to overcome the binding energy. As a result, a spontaneous dissociation of Frenkel excitons into free charge carriers is very unlikely. For most Frenkel excitons, in fact, electron and hole recombine within a few nanoseconds[23] and thus are lost for charge generation. Nevertheless, to achieve more efficient exciton dissociation, a heterojunction concept is typically used for OPVC, employing two different kinds of semiconductors. There, one OSC acts as electron donor and the other as electron acceptor, resulting in the so-called *donor-acceptor* (D/A) *concept*.[24]

Besides Wannier-Mott and Frenkel, there is one further kind of exciton, the *charge-transfer* (CT) *exciton*, which lies in between the first two concerning its spatial extent (Fig. 2.3 (c)). For CT excitons, electron and hole are located on adjacent but different molecules. For OPVC, this means that CT excitons occur at the D/A interface. Therefore, the relevance of CT excitons increases with an increasing D/A interface.

2.2 Organic solar cells

Organic solar cells (organic photovoltaic cells, OPVC) are electronic components, which directly convert sunlight (photons) into electrical power by using thin films of organic semiconductors as photoactive materials. The research on the photovoltaic effect in organic semiconductors started in the late 1950s by working on materials like anthracene and phthalocyanines.[25,26] However, as only *homojunction* devices were fabricated, containing only one sort of OSC, they all suffered from very poor efficiency. It took many years before the first OPVC exceeding 1 % efficiency has been presented by Tang in 1986.[24] This breakthrough was realized by the invention of *heterojunction* devices following the D/A-concept, which combines two organic semiconductors with different electrical properties. Tang used copper-phthalocyanine (CuPc) as donor material and a perylene derivative as the acceptor. Possible material combinations are generally determined by the respective HOMO and LUMO levels of donor and acceptor. The charge generation process within OPVCs will take place only for suitable energy levels.

2.2.1 Charge generation process

To enable charge carrier transfer between both OSCs, HOMO and LUMO level of the acceptor have to be lower than the corresponding energy levels of the donor. Moreover, exciton dissociation will take place only if the energy gained by the transfer of the charge carrier from donor to acceptor (or vice versa) compensates for the binding energy of the Frenkel exciton. For that reason, it is critical that the charge separated state, i.e. electron on LUMO of the acceptor and hole on HOMO of the donor, is the lowest excited

state compared to the HOMO-LUMO gaps of donor and acceptor, respectively.[27] If these conditions are fulfilled, an electron of an exciton generated by absorption in the donor can be transferred into the LUMO of the acceptor, while the hole remains on the HOMO of the donor. Otherwise, if the exciton is generated within the acceptor, the hole is transferred to the HOMO of the donor, and the electron remains on the LUMO of the acceptor.

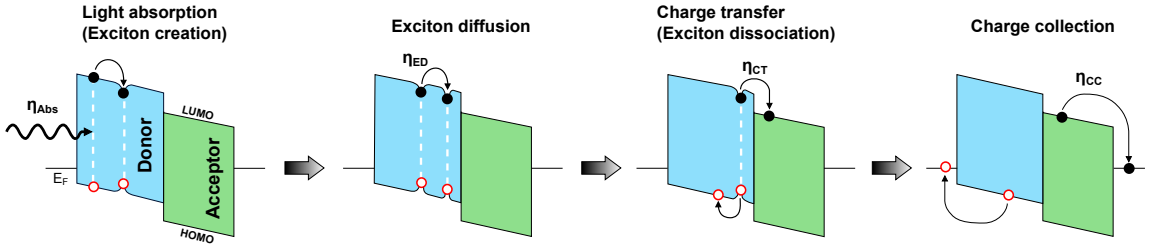

Figure 2.4: Idealized charge generation process within an organic D/A solar cell: Excitons are generated by the absorption of light and diffuse subsequently towards the D/A interface where they are dissociated. Resultant electrons and holes are then transported to and collected at the respective electrode.

However, this is only one sub-process. The complete charge generation process occuring in OPVCs can be divided into four sub-processes[28,29] as illustrated in Fig. 2.4. First of all, photons are absorbed, leading to the formation of Frenkel excitons. In the second step, these excitons can diffuse to the donor-acceptor interface. Exciton dissociation and the transfer of the separated charge carriers to donor and acceptor, respectively, represent the third sub-process. Consequently, all free electrons are then located on the acceptor, while all holes are located on the donor. Finally, the free charge carriers are transported to the electrodes, where they are collected and thus contribute to the photocurrent. This charge carrier transport is driven by the internal field, which is caused by the different work functions of anode and cathode material, respectively.

Each of these four sub-processes can be characterized by a separate efficiency, labeled as the absorption efficiency η_{Abs}, the exciton diffusion efficiency η_{ED}, the charge-transfer efficiency η_{CT}, and the charge collection efficiency η_{CC}. The product of these partial efficiencies finally results in the *external quantum efficiency* η_{EQE}:

$$\eta_{\mathrm{EQE}} = \eta_{\mathrm{Abs}} \cdot \eta_{\mathrm{ED}} \cdot \eta_{\mathrm{CT}} \cdot \eta_{\mathrm{CC}}. \tag{2.4}$$

The EQE is usually known as the ratio of the number of generated electrons to the number of impinging photons at a given wavelength. Hence, Eq. (2.4) can be used to describe the losses, which prevent an EQE of 100 %. The first loss channel for example are optical losses like reflection at the surface or transmission through the sample, which reduce η_{Abs}. Losses in reflection are caused by different refractive indices of different materials and thus are inevitable. Equally, transmission also cannot be completely prevented. It is determined by material specific properties and thus given by the choice of the OSCs

and the thicknesses of the organic films, which cannot be chosen randomly. Due to these inevitable losses, η_{Abs} is sometimes omitted, which then leads to the so-called *internal quantum efficiency* (η_{IQE}), describing the ratio of the number of generated electrons to the number of actually absorbed photons.

However, the other three terms are part of the calculations of both η_{EQE} and η_{IQE}, as they describe the conversion process of light into electricity. The first of them, the exciton diffusion efficiency η_{ED} represents the probability of an exciton to reach the D/A interface. Again, it is not possible to reach 100 %. The most important factor for that loss channel, is the poor exciton diffusion length (L_{D}) of most OSCs of typically only a few nanometers.[30,31] As a consequence, layer thicknesses of OSCs in OPVCs are usually chosen to be very thin ($10 < d < 50\,\mathrm{nm}$). However, L_{D} is a monotonic function of the extent of crystalline order,[32] which means that highly crystalline OSCs possess a significantly enhanced L_{D}. Nevertheless, even for a rather long diffusion length, some excitons will not reach the D/A interface. Due to their charge neutrality, excitons cannot be guided to the D/A interface by the intrinsic electrical field. As a result, some of them recombine within the bulk or are quenched at interfaces in the opposite direction (*surface recombination*). The recombination of excitons, which have not been dissociated yet, is also called *geminate recombination*, as electron and hole of one exciton recombine with each other.[33] This recombination happens partly radiatively by emitting photoluminescence and partly non-radiatively. Thus, η_{ED} is also limited by the random direction of exciton diffusion. However, there are two possibilities to optimize η_{ED}. For example, η_{ED} can be enhanced by increasing the D/A interface, as it enables more excitons to reach it and dissociate before recombining within the bulk. That point is explained in more detail in the following subsection concerning solar cell architecture. Moreover, the thickness of the acceptor layer can be chosen in such a way to exploit cavity effects. The number of photons absorbed in the photoactive layers does not follow a straight line but a wavy behavior, induced by the interference between the incident light and the light reflected from the back electrode.[34–36] In this way, more excitons can be generated near the D/A interface, reach it and thus contribute to the photocurrent.

The next factor determining η_{EQE} is the charge-transfer efficiency η_{CT}. In contrast to all other processes, hardly any losses are expected during charge transfer. The dissociation process at the D/A interface typically takes place over time scales of only a few hundred femtoseconds or even less.[37–39] Thus, it is much shorter than any other competing process and the charge-transfer efficiency typically approaches $\eta_{\mathrm{CT}} = 100\ \%$.[40,41]

The final factor is the charge collection efficiency η_{CC}. The main losses that occur here, are again due to transport and recombination issues. In contrast to exciton diffusion, the charge carrier transport is directed and driven by the internal field. However, as already mentioned, hopping transport impedes a high mobility of charge carriers. This in turn can enhance charge carrier recombination. During the charge collection process, mainly two types of recombination occur, *non-geminate (bimolecular) recom-*

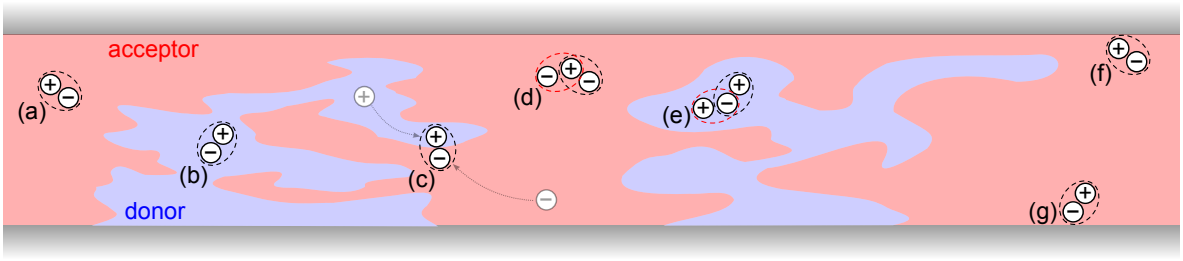

Figure 2.5: Recombination processes in organic solar cells: geminate recombination of an undissociated exciton within acceptor (a) or donor (b), non-geminate recombination at the D/A interface (c), exciton-polaron quenching (d, e), and surface recombination (f, g). Non-geminate recombination can also occur within the bulk due to the existence of traps, which is then called trap-assisted recombination.

bination and *exciton-charge annihilation (exciton-polaron quenching)*. Non-geminate recombination (also called Langevin-type recombination) is the recombination of electron and hole stemming from different, already dissociated excitons.[42] As non-geminate recombination mainly occurs at the D/A interface, it is more dominant in devices with large interfacial areas.[43] However, non-geminate recombination can also occur within the bulk, namely as trap-assisted recombination (Shockley-Read-Hall, SRH recombination) through a trap state originating from impurities or structural inhomogeneity.[44,45] Furthermore, exciton-polaron quenching occurs due to the coexistence of excitons and charges and thus also within the bulk. In spite of their short lifetimes, excitons are notably quenched by charges due to strong optical resonance for resonant energy transfer, which could be shown to be a general feature in organic semiconductors owing to the stabilization energies of excitons and polarons.[46]

2.2.2 Organic solar cell architectures

Due to the high absorption coefficients of OSCs ($> 10^5\,\mathrm{cm}^{-1}$)[iii], only 100 nm thickness for the photoactive layers is enough to absorb most of the impinging photons when a reflective back contact is used.[48] This high reflectivity of the back contact is typically ensured by aluminium or silver, selected as the cathode material. The anode material, however, has to be chosen transparent (or at least semi-transparent) to enable photons to penetrate the device. Indium tin oxide (ITO) is by far the most common anode material in OPVCs, as it combines excellent optical transparency ($> 90\,\%$) and low electrical resistivity ($\sim 10^{-4}\,\Omega$ cm).[49]

The probably most important difference of OPVCs compared to its inorganic counterparts, however, is the already described strong binding energy of Frenkel excitons. For that reason, OPVCs belong to the group of so-called excitonic solar cells.[50] To handle

[iii] To compare, the absorption coefficient of amorphous silicon, which is an indirect bandgap semiconductor, is only $10^3 \sim 10^4\,\mathrm{cm}^{-1}$ within the visible range of light.[47]

this obstacle, OPVCs nowadays contain (at least) two different OSCs, which serve as electron donor or electron acceptor, respectively. These OSCs are sandwiched between anode and cathode together with some additional materials, which form e.g. hole injection or exciton blocking layers. These additional materials, however, and their impact on the perfomance of an OPVC will be further described in chapter 3.

Within this subsection, the influence of the architecture on solar cell performance is described. For simplicity, only solar cell architectures with one electron donor and one electron acceptor material are considered. This is sufficient as still most of the fabricated OPVCs contain only two photoactive OSCs and the vast majority of relevant features can be explained on this basis. Talking about different solar cell architecture usually targets the D/A interface. For this thesis, different architectures have been fabricated as well, leading to (widely) varying OPVC efficiencies. A schematic drawing of the used devices containing different D/A interfaces is shown in Fig. 2.6.

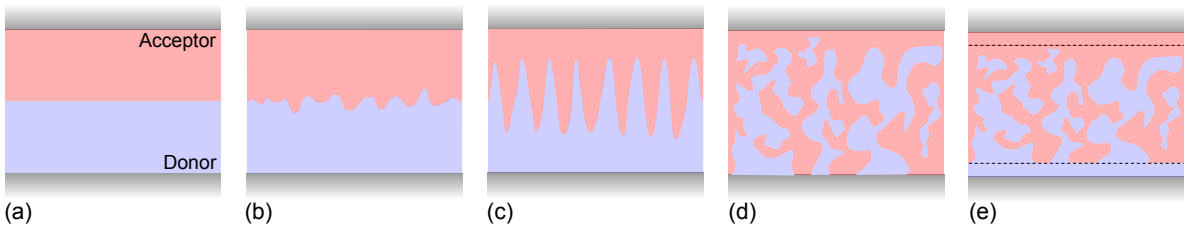

Figure 2.6: Architectures of the fabricated donor/acceptor heterojunction solar cells: The D/A interface is gradually increased from (a) the planar heterojunction, to (b) a PHJ with roughened interface, and (c) a PHJ with column-shaped donor, to finally (d) a bulk heterojunction fabricated by co-evaporation. The planar mixed heterojunction device (e) combines the benefits of PHJ and BHJ solar cells.

The simplest design for an OPVC is the *planar heterojunction* (PHJ). For its fabrication, electron donor and electron acceptor are evaporated subsequently without any further effort. The surface roughness of the primarily evaporated donor determines the interface roughness and thus the interface area. As most OSCs form amorphous films, which are innately very smooth, PHJ devices possess a comparatively small D/A interface. This interface, however, can be enlarged, e.g. by using highly crystalline donor materials, or by post-evaporation treatments like annealing (thermal annealing, solvent vapor annealing). Of course, the resulting effects on the D/A interface are rather small and not exactly reproducible. For that reason, techniques have been searched, which reproducibly provide a column-shaped donor and thus a greatly enhanced D/A interface. A possible preparation technique for this aim is *glancing angle deposition* (GLAD), which yields nano-columns of the donor by using shadowing effects during its evaporation process.[51] For polymer solar cells, another process has been invented, which also provides a column-shaped donor and thus a greatly enlarged D/A interface, the so-called nanoimprint technology.[52,53]

A drastic enlargement of the D/A interface and thus a strongly increased exciton dissociation has been achieved by the invention of the *bulk heterojunction* (BHJ) concept.[54,55] In this case, the interface is extended over the entire bulk. For evaporated small molecule OPVCs this architecture can be realized by a simultaneous evaporation of donor and acceptor material in the aim of obtaining an interpenetrating network of segregated donor and acceptor phases. Controlling the morphology of the BHJ in order to ensure maximum exciton dissociation at the D/A interface, in parallel to an efficient charge-carrier extraction, has been found to be the key for high performance.[56] However, the mixing of donor and acceptor is material specific and cannot be directly determined, but at least, it can be improved e.g. by substrate heating during co-evaporation or by varying the mixing ratio.[57] Such treatments increase the probability of continuous percolation paths of both materials towards its respective electrode and thus improve the charge transport. Nevertheless, these paths can also connect both electrodes with each other leading to shunts. To prevent this, an additional design was developed, which combines the advantages of the PHJ and the BHJ concept. There, a co-evaporated blend is sandwiched between neat layers of donor and acceptor, each connected to the associated electrode. This architecture is called *planar-mixed heterojunction* (PMHJ). Today, for evaporated small molecule OPVCs, this concept is by far more widespread than the BHJ concept. For solution processed polymeric solar cells, however, it is more difficult to realize and thus less common.

The individual factors determining EQE, $\eta_{\mathrm{Abs}}, \eta_{\mathrm{ED}}$, and η_{CC}, are influenced by the solar cell architecture in different ways. The absorption efficiency η_{Abs} for example is increased due to a roughened interface, which induces more scattering. As a result, the light path through donor and acceptor layers is extended and hence more photons can be absorbed. This effect increases steadily for the architectures shown in Fig. 2.6 from (a) to (d). Equally, also η_{ED} increases from PHJ to BHJ. The enlarged D/A interface offers the possibility to overcome the problem of a short exciton diffusion length, increases the probability of exciton dissociation and leads to reduced geminate recombination within the photoactive layers. For the charge collection efficiency η_{CC}, however, there is an opposing trend. While non-geminate recombination is a comparatively small problem for PHJ devices, this loss channel becomes increasingly important for an enlarged D/A interface. Moreover, BHJ devices often do not provide continuous percolation paths of donor and acceptor to anode anode cathode, respectively. Hence, charges are trapped and therefore cannot contribute to the photocurrent. Nevertheless, due to enhanced η_{Abs} and strongly increased η_{ED}, the BHJ (PMHJ) concept reveals greater potential than the PHJ approach, however, only if efficient charge-carrier extraction can be ensured by an appropriate morphology of the blend.

2.2.3 Parameters of organic solar cells

The most important parameter of an organic solar cell (or a photovoltaic device in general) is its *power conversion efficiency* (PCE, η_{PCE}), which describes the ratio between

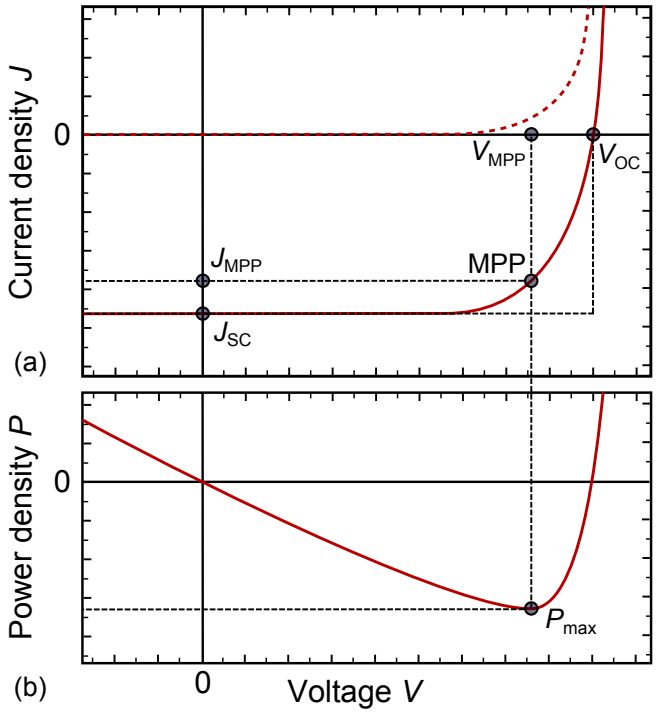

Figure 2.7: Current-voltage characteristics of an idealized solar cell in dark (dashed line) and under illumination (solid line) featuring no series resistance and infinite parallel resistance. The curve intersects the y-axis at J_{SC} and the x-axis at V_{OC}. The maximum output power density of the solar cell is set by J_{MPP} and V_{MPP}, which in turn determines the maximum power point (MPP). The ratio between the inner rectangle $J_{MPP} \cdot V_{MPP}$ and the outer rectangle $J_{SC} \cdot V_{OC}$ defines the fill factor.

electrical output and radiative input. The electrical output is generally determined by measuring the current-voltage (J-V) characteristics of an OPVC under illumination (Fig. 2.7 (a), red solid line). The resulting J-V-curve contains the three crucial parameters required to calculate the PCE of the device, the *short-circuit current density* (J_{SC}), the *open-circuit voltage* (V_{OC}), and the *fill factor* (FF). Then the PCE can be obtained by dividing the product of these three parameters by the incident light power density P_{in}:

$$\eta_{PCE} = \frac{J_{SC} \cdot V_{OC} \cdot FF}{P_{in}} \tag{2.5}$$

If no voltage is applied to an irradiated solar cell, the device is under short-circuit conditions and the flowing current is called short-circuit current (I_{SC}). Of course, its value depends among others on the irradiated area as more photons impinging on the solar cell result in more absorption and thus more current. Hence, I_{SC} is divided by the area of the device and J_{SC} is obtained, which provides comparability to other OPVCs of different dimensions. For a J-V-curve, J_{SC} represents the intersection of the curve with the y-axis within the negative current regime. The idealized case depicted in Fig. 2.7 shows a completely horizontal curve around J_{SC}. In fact, the maximum photocurrent j_{ph}, which is reached in reverse bias, is larger than J_{SC}. This means that some of

the generated charge carriers cannot be extracted but are lost due to recombination. In other words, the steepness of the *J*-*V*-curve at J_{SC} already gives a first measure of losses occurring within the device.

The intersection of the *J*-*V*-curve with the x-axis represents V_{OC}. At this point, no current flows anymore as the generated current due to illumination is completely compensated by the recombination current arising from charge carriers being injected from the electrodes. As a consequence, the section between J_{SC} and V_{OC} represents the by far most interesting part of the curve, as it marks the regime where the OPVC generates power. The maximum power is achieved at the maximum power point (MPP, Fig. 2.7), which is chosen to be the operating point of the OPVC. It can vary for one device due to the intensity of irradiation (changed current but almost constant voltage) or due to the temperature of the solar cell (increasing temperature reduces the voltage). At constant temperature of the device, the value of V_{OC} is determined by the choice of donor and acceptor material, or more specifically by the gap between HOMO of the donor and LUMO of the acceptor (E_{DA}[iv].). Due to its importance, this gap, which represents the CT state at the D/A interface, is also called photovoltaic gap[58] or effective gap.[59] It has already been shown that the value of V_{OC} is typically 0.5 - 0.6 V lower than E_{DA} for BHJ solar cells,[60] but also for molecular PHJ devices.[61] This drop of V_{OC} compared to E_{DA} can be explained by radiative and non-radiative recombination losses:

$$V_{OC}(T) = \frac{E_{DA}}{e} - \Delta V_{OC}^{rad}(T) - \Delta V_{OC}^{non}(T)\,, \tag{2.6}$$

taking into account the elementary charge e. While the radiative losses ΔV_{OC}^{rad} are thermodynamically unavoidable, it is worthwhile to minimize the non-radiative losses. If this is possible, and $\Delta V_{OC}^{non} = 0$, the thermodynamic efficiency limit of OPVC is reached. This efficiency limit can be seen in analogy to the Shockley-Queisser limit for inorganic solar cells.[62] However, for organic solar cells it is always a bit lower resulting from the presence of a CT state at the D/A interface.[63–65]

The third important parameter for the efficiency of an OPVC is the fill factor, which is given by the squareness of the *J*-*V*-curve. It can be calculated by the ratio of the rectangle $J_{MPP} \cdot V_{MPP}$ to the rectangle $J_{SC} \cdot V_{OC}$ (Fig. 2.7 (a)):

$$FF = \frac{J_{MPP} \cdot V_{MPP}}{J_{SC} \cdot V_{OC}} \tag{2.7}$$

High performance OPVCs yield FFs around 70 %, which is still significantly below the 85 % achieved for some inorganic III-V solar cells.[5] This difference mainly originates from the poor charge carrier mobility and the high free carrier recombination in organic semiconductors.[66] The resulting deviation of the *J*-*V*-curve of the ideal (rectangular)

[iv] In literature, this gap is often also called E_{CT} or E_{PVG}, however, within this work it will always be denoted as E_{DA}

behavior can be described by resistances (series and parallel). A more detailed consideration of the influence of resistances on the shape of the J-V-curve follows at the end of this subsection.

Another possibility which can contribute to a deeper understanding of the performance of an organic solar cell is measuring its *incident photon to current efficiency* (IPCE) via:

$$\eta_{\mathrm{IPCE}}(\lambda) = \frac{hc}{e\lambda} \cdot \frac{J_{\mathrm{SC}}(\lambda)}{P_{\mathrm{in}}(\lambda)} \tag{2.8}$$

with Planck's constant h, speed of light c, wavelength λ, and the spectral sensitivity $J_{\mathrm{SC}}(\lambda)/P_{\mathrm{in}}(\lambda)$ of the solar cell. IPCE is just another name for the already introduced EQE. The main advantage of such a measurement is the possibility to obtain a wavelength dependent response of the OPVC to irradiation. Thereby, one obtains insight concerning the light harvesting efficiency at different wavelength regions. Nevertheless, this method only provides a more detailed analysis of J_{SC}, while V_{OC} and FF are not concerned. As a result, IPCE cannot be used to make a statement concerning the overall performance of an OPVC.

The J-V-characteristics of an OPVC measured without illumination (Fig. 2.7 (a), dashed line) are very similar to the typical diode curve, which can be described by the Shockley equation:

$$j(V) = j_0 \left[\exp\left(\frac{eV}{nk_{\mathrm{B}}T} \right) - 1 \right] , \tag{2.9}$$

with the dark saturation current (recombination current) j_0, the diode ideality factor n, and the Boltzmann constant k_{B}. The ideality factor describes how exactly the J-V-characteristics follow the ideal diode equation. For an ideal diode without trapping of charge carriers and where recombination is absent or governed by bimolecular recombination, n is expected to be equal to unity.[67] However, the ideality factor of real OPVC devices typically varies between 1 and 2, depending on the prevailing recombination mechanism. In general, the more trap-assisted recombination occurs, the closer n comes to 2, with the exact value depending on the distribution of the traps.[68] It follows from all these correlations that n is also connected to the morphology of the photoactive layers. As disorder, transport issues and recombination are usually enhanced in BHJ devices, they typically possess a higher ideality factor than their planar counterparts.[69]

When the solar cell is illuminated, its J-V-curve is shifted downwards by the value of the photocurrent density j_{ph} and the Shockley equation has to be adapted to:

$$j(V) = j_0 \left[\exp\left(\frac{eV}{nk_{\mathrm{B}}T} \right) - 1 \right] - j_{\mathrm{ph}} \, . \tag{2.10}$$

Constructing an equivalent circuit for that behavior leads to a diode in parallel with an additional current source, representing the photocurrent due to illumination. Moreover, within a real device two unavoidable parasitic resistances has also to be considered. On

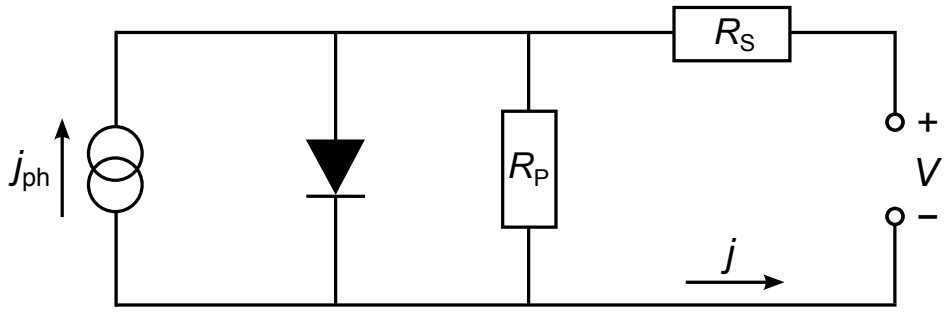

Figure 2.8: Equivalent circuit of a solar cell. Under illumination, a photocurrent j_{ph} is generated. The efficiency of a real solar cell is reduced by resistive effects dissipating power in series resistance R_S and parallel resistance R_P, respectively.

the one hand, there is the series resistance R_S, which adds up from all series resistance contributions in the device: from transport through the photoactive layers, from interface transfer and from transport through the contacts.[70] To achieve a high FF, R_S has to be as low as possible. On the other hand, there is also a parallel (shunt) resistance R_P, taking into account leakage currents due to pinholes[v] or leakage currents at the edge of the device.[71] For high FFs, R_P has to be large to prevent these leakage currents. The resulting equivalent circuit is shown in Fig. 2.8.

Including the series resistances $R_S A$ and the parallel resistance $R_P A$ as a function of the solar cell area A into Eq. (2.9), one obtains the adapted Shockley equation for real organic solar cell devices:

$$j(V) = j_0 \left[\exp\left(\frac{e(V - j(V)R_S A)}{n k_B T} \right) - 1 \right] + \frac{V - j(V)R_S A}{R_P A} - j_{ph} \,. \tag{2.11}$$

Like for J_{SC}, the values of the resistances correlate with the dimensions of the device. For that reason, R_S and R_P are typically given area-normalized, i.e. in dependence of A. The key impact of these parasitic resistances on solar cell performance is the reduction of the fill factor. The negative effects of an increasing series resistance and a decreasing shunt resistance are shown in detail in Fig. 2.9 (a) and (b), respectively.

Already for rather small values of R_S, the fill factor decreases, while J_{SC} and V_{OC} remain unchanged. That a changing R_S does not affect V_{OC} seems logical as there is no current flowing at V_{OC}, which could be influenced by a series resistance. The decrease of FF grows continuously with increasing values of R_S so that the J-V-curve changes its characteristic exponential growth into a completely linear behavior. As a consequence, for high series resistances, also J_{SC} is diminished. By comparing two similar devices with identical V_{OC} and (at least) similar J_{SC}, an increasing R_S can be easily detected by a decreasing slope in the forward bias regime above V_{OC}.

[v] Leakage paths, which are caused by one continuous material connecting both electrodes with each other, are usually denoted as pinholes.

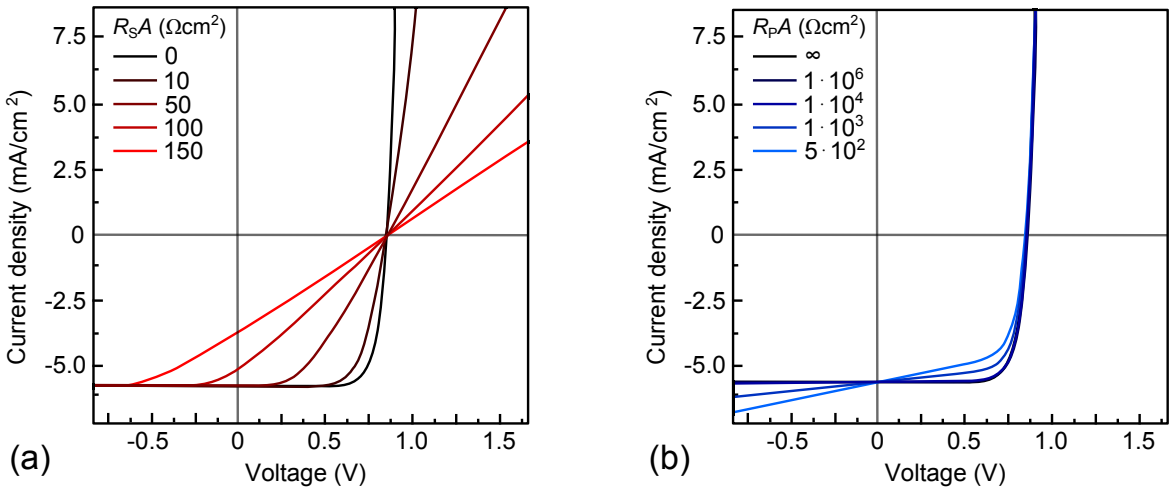

Figure 2.9: Influence of (a) series resistance and (b) parallel resistance on the shape of the j-V-characteristics of a solar cell. If R_S gets too big or R_P too small, both lead to a decreasing fill factor of the device. Illustration adapted from literature.[21]

On the contrary, a decreasing R_P, which is similarly adverse for a high fill factor, becomes apparent within the reverse bias regime, i.e. by an increasing slope of the J-V-curve around J_{SC}. J_{SC} itself, however, is not affected by a changing parallel resistance. In contrast, as a finite R_P leads to leakage currents or pinholes, which in turn promotes (surface) recombination, V_{OC} slightly decreases for decreasing values of R_P.

Nevertheless, for most devices, which typically posses a rather high parallel resistance, the influence of the parasitic resistances on V_{OC} is very small and thus can be neglected. Moreover, for high values of R_P (and not too high values of R_S), there is no difference between j_{ph} and J_{SC}. With this in mind, an expression for V_{OC} can be achieved by solving the Shockley equation under illumination (Eq. (2.9)) for the open-circuit voltage $\big(j(V_{OC}) = 0\big)$:

$$V_{OC} = n\frac{k_B T}{e} \ln\left(\frac{J_{SC}}{j_0} + 1\right), \tag{2.12}$$

which in turn illustrates the influence of temperature, dark saturation current, and ideality factor on V_{OC}.[72] To take into account the great influence of the photovoltaic gap E_{DA} on V_{OC}, the correlation

$$j_0 = j_{00} \cdot \exp\left(\frac{-E_{DA}}{k_B T}\right) \tag{2.13}$$

between the recombination current, the photovoltaic gap and the so-called coupling factor j_{00}, is inserted into Eq. (2.12). The coupling factor describes the electronic coupling strength between donor and acceptor and is therefore constant for a given material combination.[73] By assuming $J_{SC}/j_0 \gg 1$, which is reasonable for a decent

OPVC, this provides the common correlation:[74–76]

$$eV_{\mathrm{OC}} \approx nE_{\mathrm{DA}} - nk_{\mathrm{B}}T \cdot \ln\left(\frac{j_{00}}{J_{\mathrm{SC}}}\right) . \tag{2.14}$$

Thus, there is a linear decrease of V_{OC} with increasing temperature. As a consequence, E_{DA} can be obtained by a temperature dependent measurement of V_{OC} and linear extrapolation of the curve towards 0 K.

In conclusion, organic solar cells have particular characteristics owing to some immanent physical properties. Most decisive are the high exciton binding energy and the weak intermolecular van der Waals forces in organic semiconductors. To overcome the resulting obstacles, the progress of the D/A concept led to various D/A architectures with interacting advantages and drawbacks. This results from the close interconnection between molecular structure, morphology and device properties as indicated in Fig. 2.10. A better understanding of these interrelated properties and their influence on the performance of organic solar cells are the aim of this thesis.

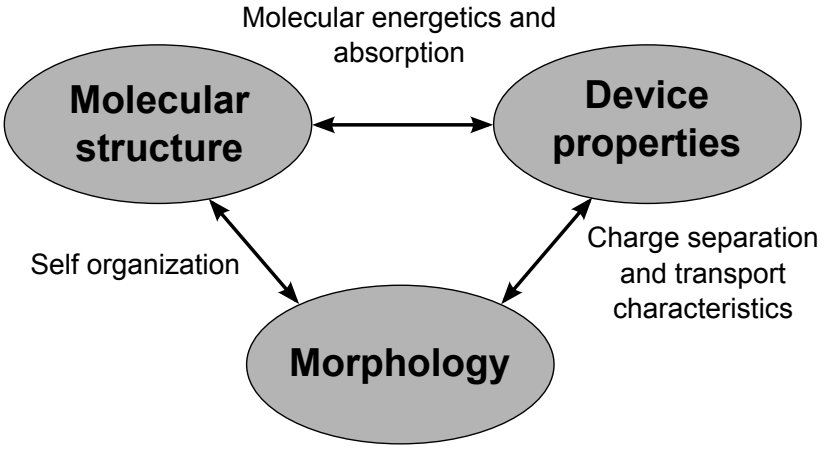

Figure 2.10: Interdependence between molecular structure, morphology and device properties. Sketch adapted from literature.[70]

Chapter 3

Materials

Following the well-established D/A concept, two different types of materials build up the photoactive layer of an organic photovoltaic cell. One of these materials acts as an electron donor and the other one as an electron acceptor. This requires the ability of donors to transport holes, and of acceptors to transport electrons. Beside this basic requirement, by looking for a well-working D/A combination, two crucial aspects have to be taken into account:

1. Matching energy levels: The LUMO of the acceptor has to be located energetically in the band gap of the donor and the HOMO of the acceptor has to be deeper than that of the donor (Fig. 3.1). Furthermore, as V_{OC} is in principle determined by the intermolecular energy gap, a rather big gap between the HOMO of the donor and the LUMO of the acceptor is of advantage (*cf.* subsection 2.2.3). The energy values of HOMO and LUMO shown in Fig. 3.1 are taken from literature. It has to be kept in mind that these values usually change material-specifically in the vicinity of other layers. To obtain the effective energy level alignment, a measurement of each individual device stack would be necessary.[87,88]

2. Complementary absorption: In the best case, donor and acceptor absorb at different wavelengths while covering the whole light spectrum collectively. The absorption characteristics of the materials used in this thesis are shown in Fig. 3.2.

Note that these are just the two most important factors. Of course there are several other material-depending aspects that can affect the solar cell performance, however, this goes beyond the scope of this thesis.

In this work 6T, DIP and DBP are used as donors. Moreover, the perylenes DIP and DBP can also be applied as acceptors as they transport both holes and electrons quite efficiently. More common acceptors, however, are the fullerenes C_{60}, C_{70} as well

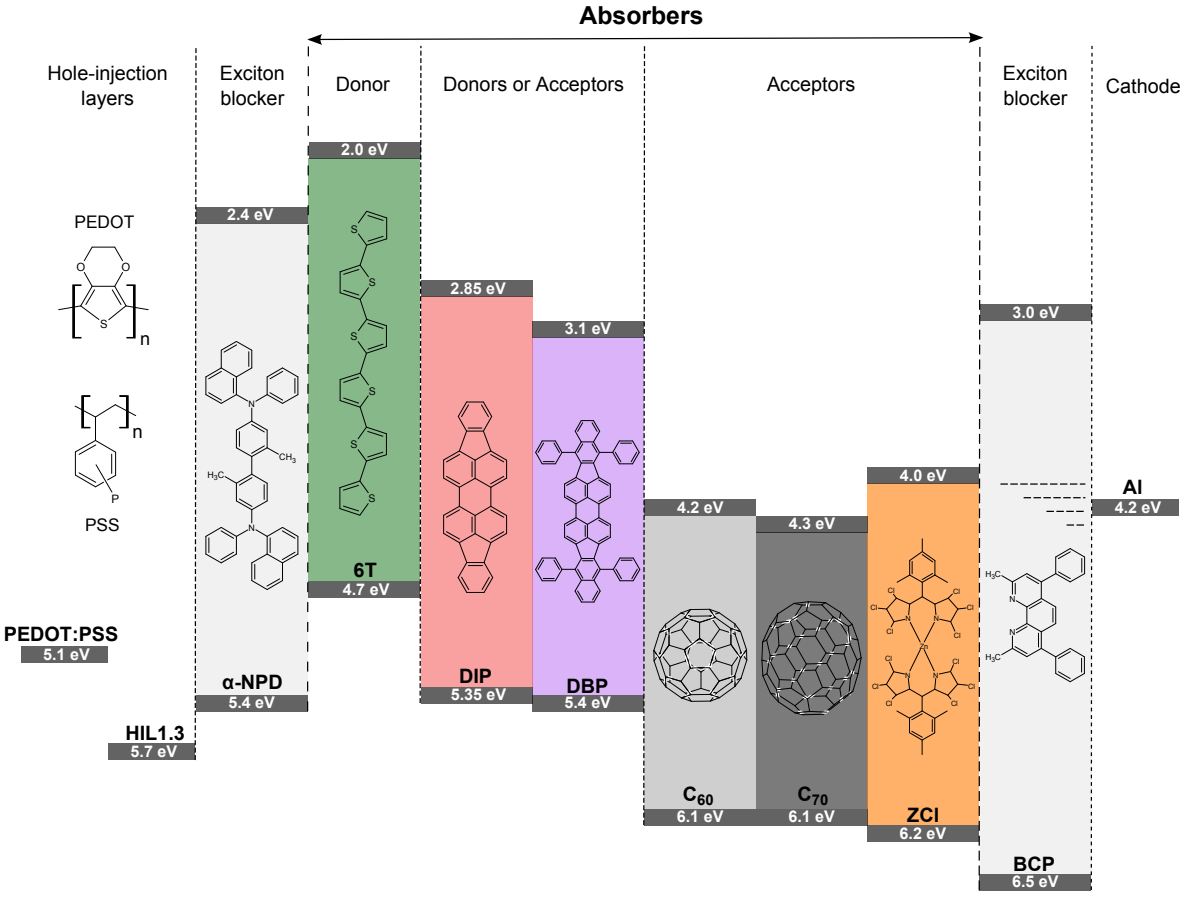

Figure 3.1: Molecular formulae and energy level of the used materials PEDOT:PSS (AI4083),[77] HIL1.3,[77] α-NPD,[78] 6T,[79] DIP,[58] DBP,[80] C_{60},[81] C_{70},[82] ZCl,[83] BCP[84] and Al.[85] 6T LUMO is estimated by adding the transport gap to the HOMO.[86] However, all values are only guidelines and may vary in actual devices. The materials are divided in several categories as they fulfill different tasks shown at the top. Of particular importance are the absorbers with 6T as donor, C_{60}, C_{70} and ZCl as acceptors, and DIP as well as DBP, which can serve both as donor and acceptor. Electron transport through exciton blocking BCP is enabled by defect states indicated by dashed lines.[84]

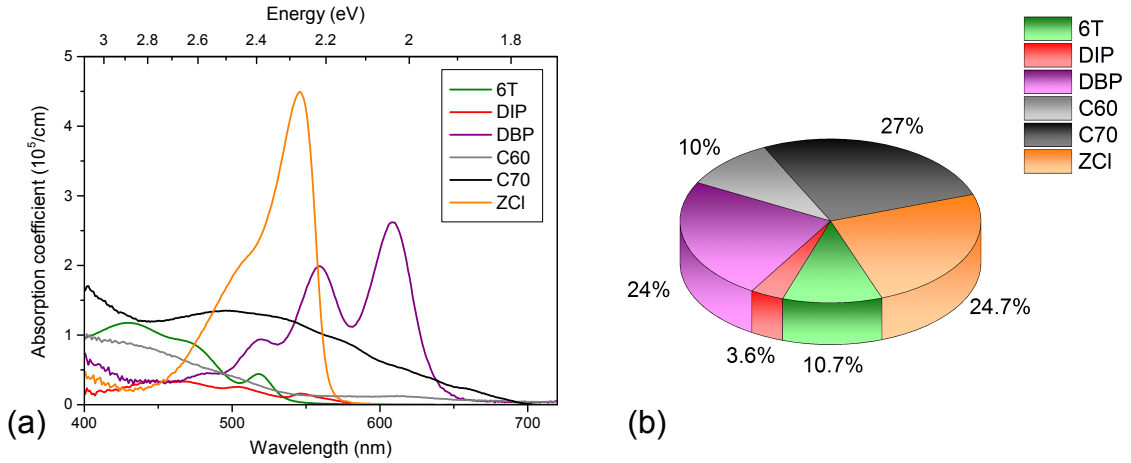

Figure 3.2: (a) Spectral dependence of the absorption ability of all absorbers used within this thesis. (b) For better comparability of the overall absorption strengths all curves are integrated between 400 nm $< \lambda <$ 700 nm. By summing up all resulting areas and dividing through the respective value, the absorption strengths can be compared. For example, ZCl and DBP, which show completely different characteristics, yield almost identical overall absorption strengths. However, broad spectra are generally more favorable than narrow absorption peaks.

as ZCl. Beside these absorbers, some other organic materials are applied in OPVC devices. While the polymers PEDOT:PSS and HIL1.3 build a hole injection layer, the small molecule materials α-NPD and BCP serve as exciton blockers at the anode or the cathode side, respectively. The features of all these materials are further explained in the following sections.

3.1 Photoactive organic semiconductors

Organic materials that are used either as donor or as acceptor in an OPVC are labeled as photoactive organic semiconductors. They are the by far most decisive materials in an OPVC because they are responsible for the harvesting of light. Also other important factors like transport processes or charge-transfer are determined by the choice of the active organic semiconductors. Their number and variety is huge as the combination of atoms to different molecules is almost unlimited. Thus, the used materials represent only a small part of organic molecules possibly used in OPVCs. The large structural possibilities are getting obvious by looking at the structural formulae of the used materials shown in Fig. 3.1. The molecular shapes vary from spherical (C_{60}, C_{70}), to flat and rod-like (6T, DIP), or flat with twisted side-groups (DBP) to molecules that are twisted as a whole (ZCl). Each different shape leads to an altered growth behavior and changes the morphology. Beyond, there is hardly any process in an OPVC which is not influenced somehow by the choice of donor and acceptor material. Hence, the used active organic semiconductors are described in detail in the following subsections.

3.1.1 α-sexithiophene

α-sexithiophene ($C_{24}H_{14}S_6$) has been used in the field of organic electronics since several years. Already in the late 1980s, 6T was used as organic semiconductor in field-effect transistors.[89] Some years later, in 1996, it was introduced for the first time in organic solar cells in combination with C_{60}.[90] 6T has a simple structure consisting of six thiophene rings lined up planarly resulting in a rod-shaped molecule of approximately 27 Å in length (Fig. 3.1).[91] Upon evaporation, 6T can orient on the substrate in two opposing ways, either upright-standing or flat-lying. Which of these orientations actually emerges can be influenced by altering substrate temperature, film thickness, the substrate itself or the deposition rate.[92–94] By changing orientation, OPVC relevant properties like optical (e.g. absorption) or transport (e.g. charge carrier mobility) properties are influenced.[95,96]
6T is used as donor material in OPVCs. A drawback of 6T is its high oxidation sensitivity. Due to its high-lying HOMO level, 6T is susceptible to oxidation by ambient air and thus it is less stable.[97,98] However, the high-lying HOMO offers the possibility to combine 6T with other materials, which are typically used as donors, like DIP and DBP (which are then used as acceptors), to achieve remarkably high V_{OC}s.[99] Moreover, 6T features a comparably high exciton diffusion length of 60 ± 5 nm.[100] 6T was purchased from Sigma-Aldrich (United States).

3.1.2 Diindenoperylene

Diindeno(1,2,3,-*cd*,1',2',3'-lm)perylene ($C_{32}H_{16}$) has already been patented in the year 1934[101] and was initially used as a red dye. It consists of a perylene core with one indeno-group attached on each side resulting in a planar, rod-shaped molecule with dimensions of approximately 18.4 Å × 7 Å.[102] Its planar shape enables DIP to grow highly crystalline leading to good charge carrier transport properties[103–105] and an exceptionally high exciton diffusion length of up to 100 nm[106] due to the direct correlation between crystalline order and exciton diffusion length.[32] This in turn, makes DIP a promising candidate for organic electronic devices. Indeed, investigations on organic field-effect transistors (OFETs) using DIP as molecular semiconductor yield exceptionally high charge carrier mobilities for both holes (0.05 cm^2/Vs) and electrons (0.14 cm^2/Vs).[107] This allows DIP to be used in OPVCs either as donor or as acceptor with high FFs to be expected. When used as a donor, DIP is typically connected with C_{60},[65,108–110] as this combination provides matching energy levels and thus promises high open-circuit voltages. As an acceptor, however, DIP can be utilized in combination with thiophene derivatives (6T, P3HT), yielding even higher V_{OC}s.[99] The big drawback of DIP as organic solar cell material, however, is its weak absorption resulting in low short circuit current densities. Generally, DIP shows two different orientations depending on the underlying substrate. If the interactions between substrate and DIP molecules are dominant, molecules are lying (λ-orientation),[111,112] while strong molecule-molecule interactions result in the nearly upright standing σ-orientation. For typical OPVC substrates like PEDOT:PSS (or its derivative HIL1.3, which is mainly used in this work), DIP molecules orient in

the σ-orientation, standing almost upright, tilted by an angle of $\phi \approx 17°$ with respect to the surface normal.[113] DIP was obtained from Stephan Hirschmann, University of Stuttgart (Germany).

3.1.3 Tetraphenyldibenzoperiflanthene

Tetraphenyldibenzoperiflanthene (DBP) was synthesized for the first time 1995 by Debad *et al.* by the oxidative coupling of (7,12-diphenyl)benzo[*k*]fluoranthene to dibenzo{[*f,f'*]-4,4',7,7'-tetraphenyl}diindeno[1,2,3-*cd*:1',2',3'-*lm*]perylene ($C_{64}H_{36}$).[114] In simplified terms, DBP consists of a DIP core with one additional benzene ring and two additional phenyl groups on each side. Due to this similarity, the energy levels of DIP and DBP are comparable, especially the HOMOs are almost identical (5.35 eV and 5.4 eV, Fig. 3.1). DBP as a polycyclic aromatic hydrocarbon (PAH) shows intense fluorescence emission. Therefore, it was first used in the field of organic electronics in a red organic light emitting diode (OLED) in 2006.[115] It took a further 3 years before DBP was first introduced in an OPVC as an electron donor in combination with C_{60}.[80] Since then, DBP developed to a highly promising small molecule organic solar cell material, which is used as donor in PHJ,[116–119] BHJ[120] and PMHJ devices,[121–123] usually in combination with a fullerene (C_{60} or C_{70}). Nevertheless, due to its energy level alignment and its ability to transport electrons and holes, it could potentially be used as acceptor material as well. One of its major advantages is the strong absorption. Mainly in the spectral range 500 nm $< \lambda <$ 650 nm, DBP reveals remarkable absorption with three local maxima at about 520 nm, 560 nm and 610 nm. Especially the last two are a characteristic feature of DBP (Fig. 3.2). The strong absorption originates from the almost horizontal alignment of the DBP molecules[118] and thus the transition dipole moment, which is - like for DIP - aligned along the long axis of the molecule. Compared to DIP, however, the absorption is red-shifted due to the additional benzene ring on each side leading to an enlarged π-electron system. Furthermore, the horizontal molecular orientation facilitates charge transport perpendicular to the substrate (and thus towards the electrodes) due to the overlap of molecular orbitals.[118] The rather flat-lying orientation of the DBP molecules is caused by the four rotatable phenyl groups, which hinder a well-ordered growth and thus lead to an amorphous character of thermally evaporated DBP layers. As a result, DBP films are very smooth and feature a short exciton diffusion length of merely 9 ± 3 nm[116] favoring thin DBP layers in PHJ devices. DBP was purchased from Lumtec (Taiwan).

3.1.4 C_{60} Fullerene

C_{60} is the most prominent representative of fullerenes, a modification of carbon, where the C-atoms are composed to spheres, ellipsoids, tubes or similar hollow shapes. It is a highly symmetric and extremely stable spheric molecule consisting of 60 carbon

atoms[i] forming 20 hexagons and 12 pentagons (Fig. 3.1). C_{60} is also called Buckminster fullerene or buckyball and has the shape of a soccer ball with a diameter of 7.1 Å. At room temperature, C_{60} molecules are centered on sites of a face-centered cubic (fcc) structure with a lattice constant of 14.2 Å.[124] For the first time, C_{60} was predicted in 1970,[125] however, it took a further 15 years before it was initially synthesized.[126] Due to its high electron affinity, its absorption ability, its ability to transport charge effectively and its HOMO/LUMO energies, C_{60} (or its derivatives) are the by far most common acceptor material in OPVCs.[127] Furthermore, the high electron affinity enables efficient photoinduced electron transfer and exciton dissociation[128] and also the exciton diffusion length of 30–35 nm is above average.[129] Hence, electron mobilities in OFETs of more than 3 cm^2/Vs are possible[130] and charge transfer happens ultrafast (sub-picosecond time scale).[131] C_{60} was obtained pre-purified from CreaPhys (Germany).

3.1.5 C_{70} Fullerene

Compared to C_{60}, the fullerene C_{70} has ten additional carbon atoms resulting in 25 hexagons and 12 pentagons. The five additional hexagons are inserted in the form of an equatorial belt (Fig. 3.1). They reduce the symmetry and lead to an ellipsoidal molecular structure (point group D_{5h}).[132] Nevertheless, the positive features of C_{60} are retained and also the energy levels are equivalent, making C_{70} a good electron acceptor in organic electronic devices, too. Moreover, absorption is even enhanced (Fig. 3.2). As a result, by replacing C_{60} through C_{70}, the photocurrent of an OPVC is increased, while fill factor and open-circuit voltage remain comparable.[133] C_{70} was purchased from Lumtec (Taiwan).

3.1.6 Zinc Chlorodipyrrin

A very new material in the field of organic electronics is bis(dodecachloro-5-mesityldipyrrinato)zinc (ZCl), which was first used in an OPVC in 2013.[83] Publications reveal its potential to be an alternative to fullerenes as acceptor material.[134,135] It shows strong absorption in the range of λ = 450 - 550 nm, reaching almost the same overall absorption strength as C_{70}, although it has a wider band gap leading to a blue-shifted and more narrow absorption range (Fig. 3.2). ZCl consists of two chlorinated mesityldipyrrinato anions coupled to the central zinc cation. For simplicity, in Fig. 3.1., ZCl is shown as a planar molecule. Actually, however, the two dipyrrin ligands are held nearly perpendicular to each other by the Zn center with a dihedral angle of 87.6 °, forming a quasi-spherical molecular shape, comparable to fullerenes.[83] A spherical shape and the consequential isotropy toward electron transfer is advantageous over planar molecular structures because it greatly increases the chance for a beneficial alignment with the donor π-system.[136] Moreover, in contrast to all other active semiconductor materials used within this work, ZCl possesses the ability to undergo a so-called symmetry-

[i] Actually, C_{60} consists of 60 carbon and 60 hydrogen atoms, resulting in the molecular formula $C_{60}H_{60}$.

breaking charge transfer (SBCT). SBCT can occur on molecules composed of two or more identical parts, which is given for ZCl by the two dipyrrin ligands. Thereby, an exciton, which is initially formed on one ligand dissociates and undergoes intramolecular charge transfer (ICT), leading to a state in which a hole and an electron are localized on the same molecule but on different ligands.[137] The presence of this ICT state within a device is expected to markedly affect charge transfer and separation at the D/A interface, resulting in an enhanced V_{OC}.[135] ZCl was synthesized in the group of Prof. Mark E. Thompson at the University of Southern California (USC, United States).

3.2 Hole injection and exciton blocking layers

Donor and acceptor are usually sandwiched between a hole-injection layer (HIL) on the anode and an exciton blocking layer on the cathode side. In some cases, an additional exciton blocking layer is inserted at the anode interface between HIL and donor (*cf.* section 5.2).

3.2.1 PEDOT:PSS

Poly(3,4-ethylenedioxythiophene):poly(styrenesulfonate) (PEDOT:PSS) is a conductive polymer composed of the two ionomers poly(3,4-ethylenedioxythiophene) (PEDOT, positively charged) and poly(styrenesulfonate) (PSS, negatively charged). For its use in organic electronic devices it is available as aqueous dispersion. As a result, it cannot be thermally evaporated but requires a wet-chemical process (usually spin coating) to be applied as thin layer in a device. PEDOT:PSS combines excellent conductivity (organic standard) with good chemical, thermal and UV stability as well as high transparency.[138,139] For that reasons, it is widely used in the integration of electronic devices such as OPVCs, actuators, capacitors, sensors and organic-light emitting diodes.[140] In OPVCs it has the additional benefit, that it flattens the rough ITO anode, which reduces the chance of micro-shorts during device operation and increases its work function ($\Phi_{ITO} \approx 4.4$ - 4.5 eV[141]) for a better hole-injection and extraction.[142] For "normal" PEDOT:PSS (Clevios AI4083) this means a work function of $\Phi \approx 4.9$ eV or even $\Phi \approx 5.2$ eV when it is heated in vacuum.[77] By adding isopropanol, one obtains another hole injection layer material called HIL1.3, with an even further increased work function of $\Phi \approx 5.7$ eV. Hence, HIL1.3 was used almost exclusively within this work as it requires no further heating process and assures unimpeded hole transfer between anode and donor. Both AI4083 and HIL1.3 were purchased from Heraeus Clevios (Germany).

3.2.2 α-NPD

N,N' - bis (naphthalen -1- yl) - N,N' - bis (phenyl) -2,2'- dimethylbenzidine (α-NPD) is commonly used as hole transport material in OLEDs.[143] However, within this work, it is applied in an OPVC as amorphous exciton blocking layer (EBL) between HIL and donor. Such a layer is not absolutely necessary for an OPVC, however, it can raise its efficiency

(*cf.* section 5.2). An exciton blocking material is selected based on the alignment of its energy levels related to HOMO and LUMO of the adjacent active semiconductor. In the case of α-NPD this is the donor material. To ensure hole transport and efficient exciton blocking simultaneously, the HOMO level must be smaller (or at least similar), while its energy gap has to be wider compared to the donor (Fig. 3.1). Furthermore, the EBL should not absorb by itself in the visible range, which is also given by α-NPD through its wide band gap. α-NPD avoids exciton quenching at the metal/donor interface with the result that more excitons have the possibility to reach the D/A interface and contribute to the generation of charge carriers. α-NPD was obtained from Lumtec (Taiwan).

3.2.3 Bathocuproine

2,9-dimethyl-4,7-diphenyl-1,10-phenantroline (bathocuproine, BCP, $C_{26}H_{20}N_2$) was first introduced in OLEDs,[144] however, it is now the most commonly used exciton blocking material in OPVCs at the cathode interface.[17,145,146] In contrast to the anode interface, it is mandatory to insert an EBL between acceptor and cathode as it prevents the penetration of subsequently evaporated metallic cathode material. Especially for polycrystalline films, metal atoms can achieve large penetration depths, which considerably increase the probability of OPVC failure due to short-circuiting.[147] Moreover, the eponymous purpose of blocking excitons is also fulfilled. Like α-NPD, BCP also allows charge carrier transport while blocking excitons at the same time. Efficient blocking is ensured by the large band gap of BCP (Fig. 3.1), which also prevents any parasitic absorption of the blocking material in the visible and near infra-red. Due to the blocking effect, exciton quenching at the cathode interface is strongly reduced, which in turn enhances J_{SC} and thus PCE. The transport of electrons through the EBL is enabled by defect states below the LUMO of BCP (dashed lines in Fig. 3.1), resulting from metal penetration of the cathode material into BCP. Hence, the optimal thickness of the EBL has to be found by a trade-off between exciton blocking, suppression of metal penetration into the acceptor, and electron transport.[148] Depending on the electrode material and preparation parameters, this thickness is between 5 and 15 nm.[149] BCP was purchased from Sigma-Aldrich (United States).

Chapter 4

Sample preparation and characterization

The following chapter concerning preparation and characterization of the devices is roughly divided into four sections: The first one describes two different techniques for organic thin film preparation, which were used within this work. The consequential fabrication of organic solar cells and organic field-effect transistors (OFETs) represents the second section. In the third part, solvent vapor annealing (SVA) is presented in detail, which is used to influence the organic film morphology. The fourth section, finally, comprises all experimental methods used for sample characterization.

4.1 Preparation methods

Organic photovoltaic devices are built up either by polymers or small molecule organic materials, requiring different techniques for thin film preparation. Small molecule thin films are usually prepared by thermal evaporation, however, this method is unsuitable for polymers as most of them would decompose due to the prevailing high temperatures.[150] Hence, polymer thin films are commonly prepared from solution, e.g. by spin-coating.

4.1.1 Spin coating

Spin coating is a standard preparation method for organic polymer thin films. To start, the substrate is laid on a chuck and adhered via vacuum. Then, the polymer solution is dribbled onto the substrate and the rotation is started. The solution spreads radially owing to the action of centrifugal force and covers the substrate's surface with a homogeneous film. By further rotation, the film becomes continuously thinner due to the radial flow of the solution and evaporation of the solvent until it reaches its final thickness. The film thickness h_f is determined by the initial solution viscosity η_0, its

density ρ, the spin speed ω and the initial solvent mass fraction in the solution x_1^0 via

$$h_f \propto \left(\frac{\eta_0}{\rho\omega}\right)^{1/2} (1 - x_1^0) \tag{4.1}$$

and can thus be controlled by choosing an appropriate rotation speed.[151] Moreover, also the acceleration up to the final spin speed is of importance. While slower acceleration supports complete wetting of the substrate even for highly viscous solutions, more uniform layers, however, are achieved using faster acceleration.[152] In sum, spin coating can be described as a combination of four consecutive steps, illustrated in Fig. 4.1. In this work, it was executed with a Delta 6 from Süss MicroTec.

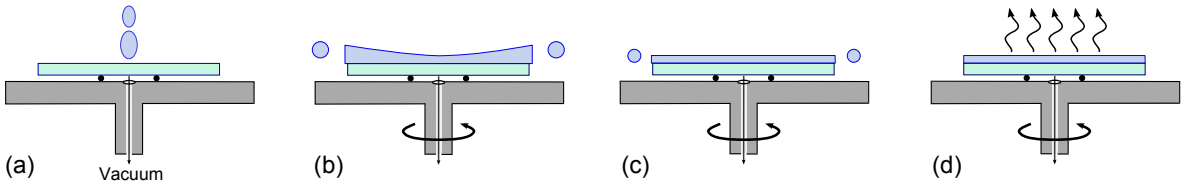

Figure 4.1: Spin coating process sketched in four steps starting with (a) dribbling of the polymer solution onto the substrate, followed by (b) the acceleration of the substrate holder to a given spin speed leading to (c) a thinning of the film. Evaporation of the solvent (d) finally results in a polymer film of desired thickness. During the whole process, the sample is adhered to the substrate holder by vacuum.

4.1.2 Vacuum thermal evaporation

Usually, small molecule organic semiconductors show no or only weak solubility in most solvents. As a result, wet-chemical deposition processes like spin-coating, dip-coating or spray-coating are inapplicable. Therefore, thermal evaporation in ultra-high vacuum (UHV, $p < 1 \times 10^{-6}$ mbar) is the most common thin film deposition technique for this material class.[153] The typical geometry of vacuum thermal evaporation (VTE) is "bottom up", which means that the substrate is placed above the evaporation source to avoid contamination by material previously deposited onto the vacuum chamber wall.[154] A big advantage of this method is the high precision of evaporated layer thicknesses controlled via quartz microbalances, exposed to the molecular vapor just below the sample holder. The layer thickness is then calculated by the change of their resonance frequency due to the additional mass evaporated on. Furthermore, VTE yields more flexibility in device design compared to wet-chemical processes, where interactions between different organic materials and solvents have to be taken into account. For VTE, several layers can be put together on top of each other. Moreover, different structures can be chosen by applying different shadow masks. Also mixed layers can be achieved easily via co-evaporation of two or even more materials. A further advantage is the possibility of heating the substrate during the evaporation process to influence the morphology of the deposited thin film. However, VTE is wasteful of material, depending on the distance between

effusion cell and sample and the time that it takes to achieve a stable evaporation rate. Typical rates range from 0.1 to 1 Å. As a result, VTE is a more time-consuming method than common wet-chemical processes.
Not only organic materials can be deposited by VTE, also metals, which are used as top-electrode materials, are applied in this way. For metals, higher evaporation rates up to several Å/s are possible.[155] An exemplary design of a VTE chamber and an explanation of its functional principle are given in Fig. 4.2.

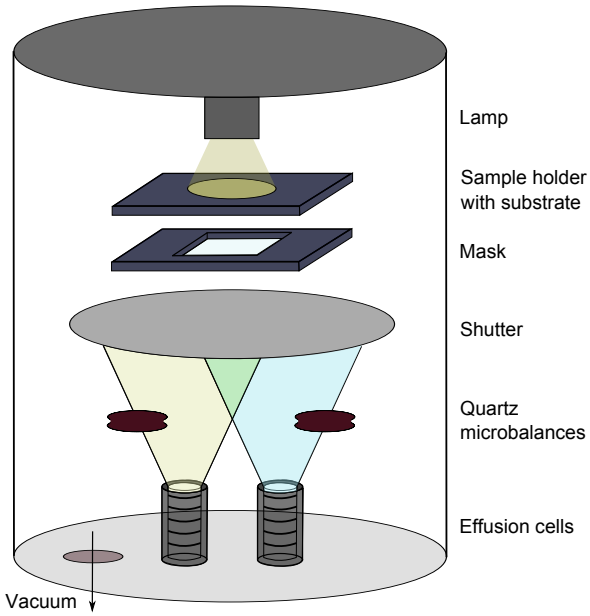

Figure 4.2: Thermal evaporation is executed in an evacuated chamber with $p < 1 \times 10^{-6}$ mbar. The highly purified organic powder, is placed in a crucible surrounded by a heating coil. Co-evaporation is possible due to four individual effusion cells containing different materials, however, only two are drawn for simplicity. The deposition rate is checked by quartz microbalances. Until reaching a stable evaporation rate, the sample can be shielded by a shutter. Evaporation occurs through a mask to achieve desired structures. During evaporation, the substrate can be heated from the back by a lamp. Heat transfer is guaranteed by graphite platelets.

4.2 Device fabrication

In the production of organic electronic devices absolute cleanliness is of major importance. For that reason, all production processes are carried out either in a clean room, under nitrogen atmosphere or at UHV with the previously described methods. How this leads to OPVC and OFET devices, respectively, is described in detail in the following two subsections.

4.2.1 Fabrication of solar cells

A patterned ITO layer on a $2 \times 2\,\mathrm{cm}^2$ glass slice is the substrate for all OPVC devices. The ITO layer is of $145 \pm 10\,\mathrm{nm}$ thickness, has a sheet resistance of $15\,\Omega/\square$ and serves as anode. ITO is the most common anode material for OPVC as it combines good electrical conductivity with a high optical transparency.[156] Transparency of one of the electrodes is essential so that the light to be converted can get into the device. The ITO layer is patterned in a way that on each substrate four diodes can be produced and contacted separately (Fig. 4.3). The substrates were purchased from Thin Film Devices (United States). In a first step, the substrates are cleaned in technical grade acetone, UV/IR grade acetone and UV/IR grade isopropanol for ten minutes each in an ultrasonic bath. Further cleaning is done by a subsequent UV/ozone treatment, which is performed for 15 minutes. Moreover, this treatment increases the substrate's surface energy leading to an improved wettability for aqueous dispersions. The aqueous HIL material is dribbled from a syringe and through a nylon filter onto the activated substrate. In the following step, the spin coater is accelerated with a ramp of nine seconds to a spin velocity of 5000 rpm, which is held for 30 further seconds. The samples are then placed onto a 125 °C hot plate for 30 minutes to remove remaining water. Spin coating and drying process finally lead to a HIL layer of 45 nm thickness. All these steps were performed in a clean room. The next layers (donor and acceptor) are thermally evaporated in UHV either consecutively or simultaneously for PHJ or PMHJ devices, respectively. Usually, an evaporation rate of $0.5\,\text{Å/s}$ is chosen. The thickness of the active organic layers depends on the respective exciton diffusion length of each material and is usually chosen between 20 and 50 nm.

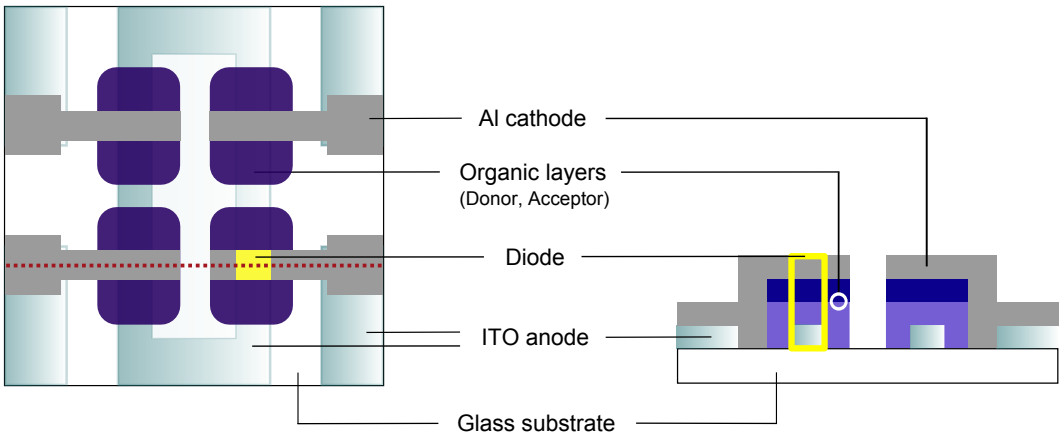

Figure 4.3: Schematic drawing of the typical sample geometry with a top view on the left and a cross section on the right side. The position of the cross section is shown by the red dotted line. The whole device contains four identical diodes (solar cells) with an active area of $2 \times 2\,\mathrm{mm}^2$, each consisting of ITO anode, organic layers and Al cathode. The organic layers include HIL, donor, acceptor and EBL, however, for simplicity, only donor and acceptor are indicated here.

EBL and cathode are thermally evaporated as well, however, in another vacuum chamber. Sample transfer between these two chambers is carried out with a vacuum transfer system to avoid contamination of the organic layers with ambient air[i]. Always, 5 nm of BCP (0.1 - 0.4 Å/s) as EBL and 100 nm of Al (1 - 2 Å/s) as cathode are evaporated through different shadow masks consecutively to complete the OPVC device. Finally, one obtains a sample with four identical diodes (solar cells), each with an active area of 0.04 cm^2.

4.2.2 Fabrication of field-effect transistors

For OFET devices, a strongly p-doped silicon (p^{++}-Si) wafer serve as substrate and gate electrode simultaneously. On top, they have a thermally grown silicon dioxide (SiO_2) layer of 300 nm thickness, which acts as gate dielectric. The wafer is broken into parts of 2 × 2 cm^2. Their cleaning is equal to that of the OPVC substrates. That means that they are also sonicated in technical grade acetone, UV/IR grade acetone and UV/IR grade isopropanol for ten minutes each. To remove remaining organic substances from the surface, they are subsequently exposed to a UV/ozone environment for 15 minutes. All materials are applied via thermal evaporation. Tetratetracontan (TTC, $C_{44}H_{90}$), an unbranched, long-chain hydrocarbon, with a layer thickness of 20 nm is used as passivation layer.[157–159] It is evaporated with a rate of 0.3 Å/s and subsequently annealed for two hours at 60 °C to smoothen its surface. In the next evaporation step, a 25 nm thick organic semiconductor layer[ii] is deposited through a shadow mask, yielding six transistors per substrate (Fig. 4.4). Finally, the contacts are evaporated. They consist either of aluminum (50 nm) to determine the electron mobility or of the organic metal Tetracyanoquinodimethane-tetrathiafulvalene (TTF-TCNQ, 125 nm) if the hole mobil-

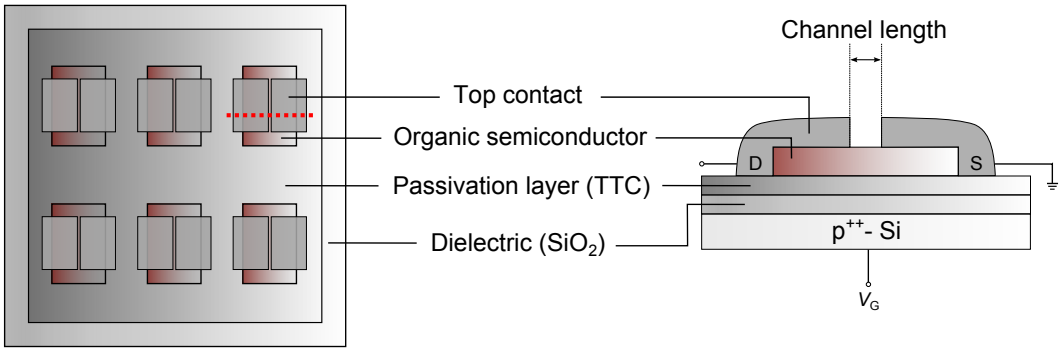

Figure 4.4: Schematic structure of a sample with six transistors. They all consist of p^{++}-Si/300 nm SiO_2/20 nm TTC/25 nm OSC/top contact. Beside different contact materials (Al, Au, TTF-TCNQ), the only difference between these transistors is the channel length. It varies from 50 to 150 nm in 20 nm steps.

[i] Especially oxygen and water are harmful to most organic semiconductor materials.

[ii] Usually, pure semiconductor layers are deposited. However, it is also possible to produce mixed layers by co-evaporation.

ity is investigated. For some transistors, also gold contacts (50 nm) are used to achieve ambipolar transistors. By evaporating the top contact metals through a mask, varying channel lengths of 50, 70, 90, 110, 130 and 150 µm are defined (Fig. 4.4). These channels create two seperated contact areas, one working as drain and the other as source of the transistor.
Within this work, OFETs are fabricated to determine the charge carrier mobility in active organic semiconductor materials used for OPVC devices.

4.3 Solvent vapor annealing (SVA)

A method to grow single crystals of anorganic semiconductors like silicon, germanium or gallium arsenide, the Czochralski process, is known for almost 100 years and well understood.[160] Single-crystalline silicon solar cells belong to the most efficient photovoltaic single-junction devices with a PCE more than twice as high as the PCE of its amorphous counterparts.[5] By contrast, controlling the morphology of organic materials for photovoltaic cells still remains a challenge. Commonly, deposition of organic materials yields amorphous or polycrystalline films. However, the relatively weak van der Waals bonds prevailing between organic molecules in comparison to the covalent bonds in anorganic semiconductors enable gentler methods to modify the morphology. This includes annealing techniques using either comparatively low temperatures or solvent processing methods, like solvent vapor annealing (SVA). As the name suggests, SVA means the treatment of functional layers with solvent vapor while avoiding direct contact between the liquid solvent and the organic film. It has already been shown that SVA is able to increase the crystalline order of organic molecules[161–163] and by that improve the PCE of both polymer-based[164] and small-molecule organic solar cells.[165] Moreover, SVA is a simple method, very easy to handle, and carried out with simple equipment at room temperature and atmospheric pressure. Exposure times vary from seconds[166] to several hours[167] as they depend strongly on the material, the desired degree of crystallization and the solvent. In general, the solvent has to offer a decent solubility of the treated material to enable free molecules to be transported with the solvent as well as a minimum affinity to the surface to allow high mobility during the reorganization process.[167] Moreover, solvents of high vapor pressures and medium donor solubilities are most suitable for SVA in the context of organic solar cell application.[166] This is given by chloroform (trichlormethane, $CHCl_3$), which has already been applied successfully for SVA on organic semiconductor films.[163,167,168] $CHCl_3$ is a liquid, colorless and hydrophobic solvent with a boiling point of 61.15 °C, a vapor pressure of 25.9 kPa at room temperature and thus was used for all SVA treatments within this work.

4.3.1 Physical background

To describe the physics behind SVA, the overall process can be divided in five steps. However, it has to be mentioned that the following steps do not strictly occur in sequence but take place more or less simultaneously:

Solvent vaporization and diffusion

Nevertheless, the whole process has to start with the vaporization of the solvent. As most solvents, e.g. the used chloroform, usually have low boiling temperatures, a significant vaporization in the annealing chamber starts instantaneously. As the sealed chamber is a closed system, the vaporization process of the liquid takes place until there is an equilibrium concentration of its vapor in the surrounding air.[169] To achieve equilibrium, the solvent vapor has to be transported from the region of high concentration at the surface of the liquid uniformly through the air. This happens by diffusion. Finally, a decent amount of solvent molecules reach the surface of the organic film.

Adsorption and absorption

The solvent molecules interact with the molecules of the film. Some of them are adsorbed and bind to the surface via van der Waals' interaction. As molecular semiconductor films often exhibit polymorphism and therefore one or more metastable structures,[170] the energetic requirements to change the topography are comparatively low. The contamination of the surface with solvent molecules is sufficient to imbalance the previously stable film. The net inward force given on each surface due to missing binding partners on one side is reduced by adhering solvent molecules, leading to a change in the balance of forces. This can already be the starting point for a reorganization process of the film. Of even more importance, however, are molecules being absorbed into the film. How efficient the solvent molecules are able to enter the film depends mainly on the packing, which is generally denser for crystalline than for amorphous materials. Thus, amorphous films yield more crevices for solvent molecules to penetrate into the film. After incorporation, the solvent molecules induce a swelling of the film,[171] shield the cohesive but rather weak van der Waals' forces between the organic molecules and can dissolve the film.

Figure 4.5: Vaporized solvent molecules are ad- and absorbed, induce a swelling of the organic film and initiate the reorganization process. Adapted from Yu.[169]

Delocalization and Reorganization

The delocalization process of the dissolved organic molecules within the organic film is dominated by diffusion. A mass transport of the molecules on the surface takes place over hundreds of microns[172] until the molecules reorganize themselves. The energetics

behind are very complex, however, one dominant factor is the minimization of surface energy. The desire to reduce the surface free energy is generally a defining factor in the morphology and composition of surfaces. It has already been shown, that the reorganization of different molecules leads to different aggregation structures like highly anisotropic elongated needles or isotropic rounded domes.[172] Besides the minimization of the surface energy, the interplay between molecule-molecule, molecule-surface and molecule-solvent interactions is of importance. Again, all these interactions are dominated by van der Waals' forces. As these forces are found between (induced) dipoles, it is obvious that composition and structure of the assembling molecules are of importance.

Dewetting

The breakup of thin films into structures with a lower surface energy is a commonly observed phenomenon in liquids, but dewetting also occurs for thin solid films.[173] It has also already been shown that dewetting is of particular importance for organic semiconductors[174,175] due to the weak van der Waals forces' already mentioned. Even for DIP, like it is also used in this work, dewetting could have already been observed, albeit without drop formation and initiated by temperature and not by solvent vapor treatment.[170] However, the formation of drops resulting from the competition between intermolecular forces and surface tension is the most common form of dewetting. In this case, dewetting leads to small droplets, which develop to larger drops by so called drop coarsening as described theoretically elsewhere[176] and shown exemplary in Fig. 4.6 (b) and (c). This

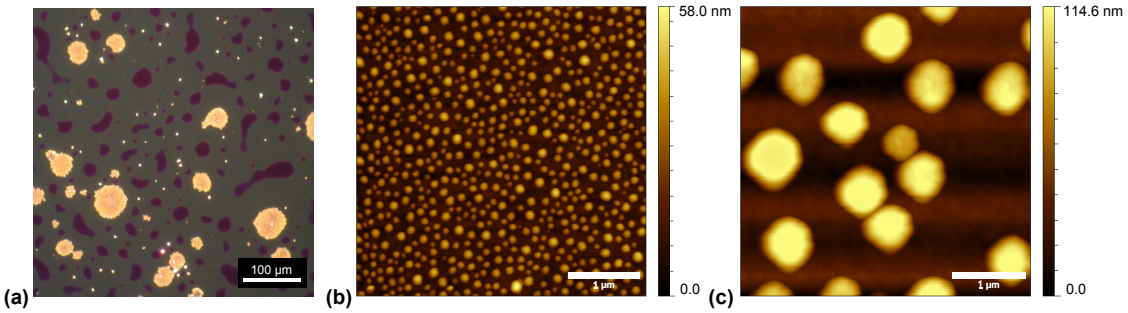

Figure 4.6: (a) Example of a dewetting DBP film after 13 minutes of SVA treatment studied by optical microscopy under 20-fold magnification. (b) Finely-spaced and (c) coarsely-spaced drops of DBP after SVA showing drop coarsening.

coarsening process can occur either through drop migration or Ostwald ripening. In the first case, drops migrate toward each other until they collide and merge, while in Ostwald ripening, pressure differences between adjacent drops drive flow through the ultra-thin film connecting adjacent drops.[169] In both cases, the driving force is again the minimization of surface energy as for bigger drops fewer atoms are at the unfavorable surface. However, dewetting of the organic thin film during SVA does not necessarily take place. Again, the SVA time is a crucial factor determining whether dewetting occurs or not. But also the treated material and the used solvent are of importance.

Crystallization

When an organic molecule diffuses to the vicinity of a nucleated region, it will bind to the nucleus and expel its no longer needed solvent molecules. In analogy to thermally-driven solidification, solvent concentration plays the role of thermal energy and solvent that is expelled during crystallization represents latent heat.[169,177] The driving force behind that process is the tendency of the mobile organic molecules to go into a more energetically favorable state. In general, the crystalline state is relatively more stable than the amorphous state even though the energy difference is small. However, the shape of some molecules, e.g. due to steric hindrance caused by side groups, may counteract the crystallization process. This is another reason why different molecules show different degrees of order after the same time of SVA. In general, however, there is a correlation between SVA time and the size of the emerging crystalline structures. For very long SVA times (up to 48h) it is even possible to form millimeter-scale crystalline organic needles with cross sections of less than a micron in size,[163] providing potentially convenient applications in nanowire-based optoelectronic devices as the charge carrier mobility is expected to be optimal along the 1D molecular packing. However, for PHJ OPVC a more homogeneous and more areal (2D) extent of the organic material is desired. For that reason, rather short SVA times[iii] are chosen within this work.

4.3.2 Practical implementation

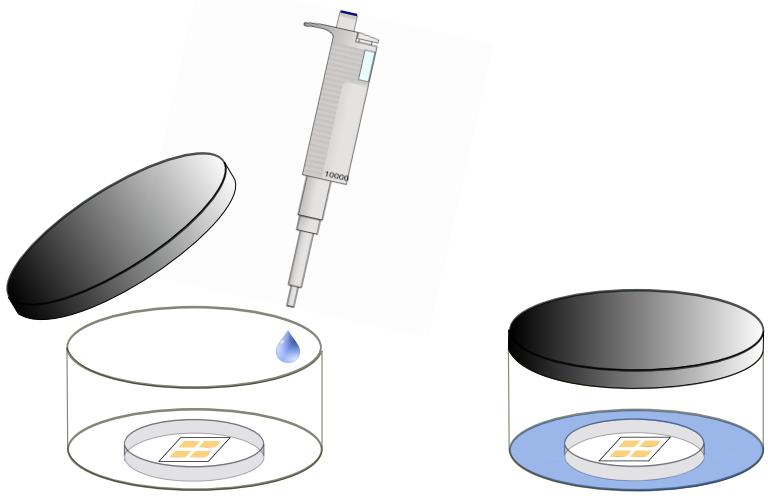

Figure 4.7: Practical implementation of the SVA process: The sample is lying face up in small Petri dish, which is placed in a sealable jar. The Petri dish is surrounded with the solvent, then the jar is closed and the time measured until the jar is reopened again and the sample is removed.

[iii] Typical annealing times in this work are in the range of 2 minutes to a maximum of 12 minutes.

For SVA the substrate along with the organic film is removed from the evaporation chamber and brought to the clean room. There it is laid face up in a small Petri dish, which is then placed in a sealable jar with 300 ml volume. After that, 1 ml of chloroform is injected by a pipette around the dish, so that there is no direct contact between solvent and sample. However, the solvent evaporates and the vapor can act on the organic material, as described in the previous sections. The time is measured while the jar is closed. Typical SVA times are 2, 4, 6, 8, 10 and 12 minutes for solar cells. After that treatment, these devices are reinstalled into the evaporation chamber. For simple films to be investigated via microscopy (optical microscopy or atomic force microscopy) or x-ray reflection, however, longer annealing times are additionally carried out.

4.4 Experimental methods

Already in the year 1267, the English theologian and natural philosopher Roger Bacon formulated: *Sine experientia nihil sufficienter sciri potest* - without experience nothing can be known sufficiently. In the following, all experimental methods used within this work will be introduced.

4.4.1 X-ray scattering

X-ray scattering (XRS) comprises several characterization techniques using X-ray radiation for the structural analysis of crystalline materials. In the present work, mainly X-ray reflectivity (XRR) was used, executed by a Seifert XRD 3003 PTS deploying the $K_{\alpha 1}$-line of Copper ($\lambda = 1.5406$ Å). In the generally used configuration, the Bragg-Brentano geometry, beam source and detector are on a fixed radius from the sample position. Then the beam source is fixed, while sample and detector are rotated by θ and 2θ, respectively (Fig. 4.8(a)). By varying the angle of incident X-rays θ and thus the detector position 2θ, this measuring process is also called θ-2θ-scan. This configuration provides out-of-plane information of the sample. The higher the integration time and the smaller the step width, the better are these information, however, measurements get very time-consuming. Integration times are chosen between three and ten seconds, while step widths of 0.01 - 0.02 ° are set.
Fig. 4.8 (b) shows an impinging X-ray beam reflected by two parallel lattice planes. For certain angles of incident θ the optical path difference is an integer multiple n of the wavelength λ. This leads to constructive interference of the reflected beams and a so-called Bragg peak emerges. This geometrical correlation is expressed by the Bragg condition

$$2d_{\perp} \cdot \sin\theta = n\,\lambda, \tag{4.2}$$

which correlates the peak position with the distance of the lattice planes $d_{\perp}$.
The scattering vector $\Delta\vec{k}$ can be defined by the wave vectors of the incoming and the reflected beam. In the case of constructive interference, it corresponds to the reciprocal lattice vector $\vec{q}$. Due to the Bragg-Brentano geometry, which can only detect lattice

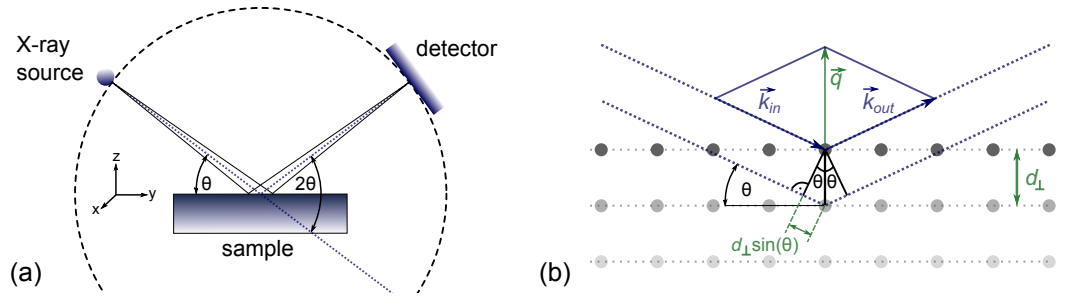

Figure 4.8: (a) Bragg-Brentano geometry of the XRR setup yielding a θ-2θ-scan by varying the angle of incidence θ. (b) Fulfilled Bragg condition due to constructive interference of reflected beams at parallel lattice planes with spacing $d_\perp$.

planes lying parallel to the surface, the condition for scattering $\Delta\vec{k} = \vec{q}$ can be considered to be one-dimensional.[178] With $k = 2\pi/\lambda$, this leads by geometrical considerations to

$$q_z = \frac{4\pi}{\lambda} \sin\theta. \tag{4.3}$$

By using Eq. (4.3), X-ray spectra of θ-2θ-scans can be plotted against the scattering vector q_z. This enables a direct comparison of measurement data taken by different X-ray scattering systems as q_z is independent of the used X-ray wavelength λ. By combining Eq. (4.2) and (4.3) one obtains a simplified expression for the out-of-plane lattice spacing

$$d_\perp = 2\pi/q_z. \tag{4.4}$$

Besides the possibility to determine the crystallinity of a sample by its characteristic lattice plane spacing, also the vertical crystallite size D can be estimated by a modified Scherrer equation

$$D = \frac{2\pi K}{\Delta q_z} \tag{4.5}$$

with Δq_z equal to the full width at half maximum (FWHM) of a Bragg peak and the Scherrer constant $K \approx 0.94$ for spherical domains. However, this value is just an empirically derived estimation.[179]

As XRR measurements only detect parallel oriented lattice planes, also an in-plane XRS technique is used - grazing incidence X-ray diffraction (GIXD[180]). In GIXD, x-rays impinge on the sample surface at a grazing angle below the angle of total external reflection. As a consequence, GIXD is very surface sensitive and provides information on lattice planes (almost) perpendicular to the surface of a sample. Moreover, due to the changed geometry, GIXD offers the possibility to determine horizontal crystallite sizes. GIXD has already been proven to be a well-suited characterization method for organic thin films.[181] It was performed on the X04SA beamline at the Swiss Light Source, Paul Scherrer Institut, Villigen, Switzerland (12 keV photon energy).[182]

4.4.2 X-ray absorption

The absorption of X-rays provides the possibility to determine the local geometric and electronic structure of matter at sub-molecular resolution. For varying purposes, different methods have been developed. However, within this work, only Near-Edge X-ray Absorption Fine Structure (NEXAFS) spectroscopy was applied, as it has already proven to be ideally suited to determine the molecular orientation of amorphous and crystalline organic semiconductor films.[183]

NEXAFS spectroscopy was introduced in the early 1980s.[184] It uses X-rays to excite core level electrons from the ground state to an unoccupied state, usually an unoccupied molecular orbital. These core level electrons mostly stem from the innermost shell, the K-shell, and thus are 1s electrons. The absorbed X-ray intensity is not measured directly, but by detecting the refilling of the (now empty) ground state with Auger and/or secondary electrons. There are three different measurement modes, however, throughout this work, the total electron yield mode was chosen, which determines the electron yield by measuring the sample current. The choice of the energy of X-rays used for the excitation of electrons determines the specific element being probed. Therefore, monochromatic X-radiation is used. Carbon for example, the most important element in organic chemistry, features a binding energy of 285 eV at the C1s-edge, however, NEXAFS is applicable to most elements in the periodic table. The broad range of X-ray energies is provided by synchrotron sources.[185]

In sp^2-hybridized atoms like carbon in an organic semiconductor material, π^* and σ^* are the lowest and the second lowest unoccupied molecular orbitals, respectively (*cf.* Fig. 2.2 (b)). Hence, the lowest electronic excitations and thus most common transitions are the $1s \rightarrow \pi^*$ and the $1s \rightarrow \sigma^*$ transition. For organic semiconductors with alternating carbon single (C−C) and double (C=C) bonds, there are two different σ^* transitions indicated in Fig. 4.9 for a 15 nm thick evaporated DIP film. However, while the σ^*_{C-C} transition is located at about 292.5 eV, the $\sigma^*_{C=C}$ transition peak at higher energies is not clearly identifiable. On the contrary, two separate peaks appear at lower energies. These peaks at ≈ 285 eV are π^* transitions. The split of the $1s \rightarrow \pi^*$ transition into two peaks has also been observed for the structurally similar molecule pentacene.[183]

A very interesting feature of NEXAFS is its ability to determine molecular orientations. A first model for this technique, which is based on the angular dependence of NEXAFS spectra, was developed in 1987.[186] It demands NEXAFS measurements under varying angles of incidence θ of the impinging X-ray photons. By measuring the absorption intensity I, the molecular orientation α with respect to the surface plane can be calculated via

$$I = A\left[\frac{P}{3}\left(1+\frac{1}{2}\left(3\cos^2\theta-1\right)\left(3\cos^2\alpha-1\right)\right)+\frac{1-P}{2}\sin^2\alpha\right], \tag{4.6}$$

with the normalization constant A and the polarization factor P which is also constant and depends on the beam line. The reason for different intensities at different angles θ is also visualized in Fig. 4.9 for the organic semiconductor DIP. DIP shows almost upright standing orientation (*cf.* subsection 3.1.2). The dipole moments for π^* and σ^* transitions are oriented perpendicular or parallel to the (upright standing) C-C chemical bonds,

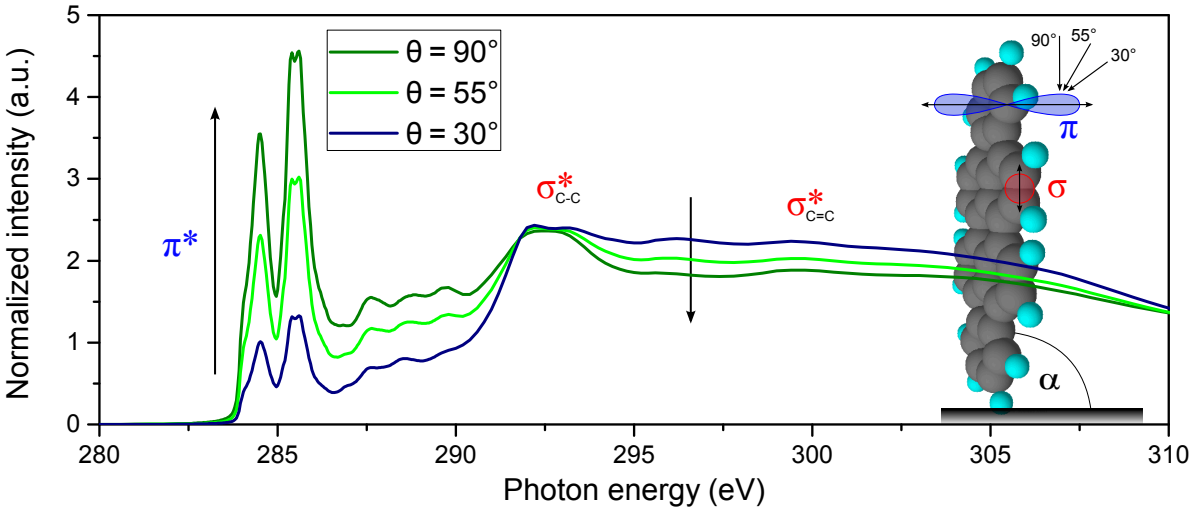

Figure 4.9: NEXAFS spectra of a 15 nm thick evaporated DIP film at 30 °, 55° and 90 ° angle of incidence θ of the impinging X-ray photons. The inset shows a DIP molecule with one of its π^* and σ^* orbitals each, as well as the orientation of the corresponding transition dipole moments. For reasons of clarity, the DIP molecule is drawn in a completely upright standing orientation. The data was recorded by Dr. Andreas Opitz (HU Berlin).

respectively, indicated by the double-headed arrows. This means that the π^* transition intensity is greatest at normal incidence (280 eV $< E <$ 292 eV), while glancing incidence leads to higher intensities for σ^* transitions (293 eV $< E <$ 310 eV). This is in analogy to optical absorption, which has already been introduced (subsection 3.1.2, Eq. (3.1)). Moreover, there is a point at about 292 eV, where no difference in absorption for different angles θ can be observed. It is called the isosbestic point[iv]. For all other wavelengths, there is a dependence of the absorption intensity on the angle of incident X-rays. This phenomenon is called dichroism and occurs not only for DIP, but for almost every molecule. Only for point symmetric molecules like the spherical C_{60} no dichroism can be observed.[187] NEXAFS spectroscopy measurements were performed at the beamline D1011 (Max-lab, Lund, Sweden) at 30 °, 40 °, 55 °, 70 °, and 90 ° angle of incidence of the impinging X-rays.

4.4.3 Optical absorption

For OPVCs or solar cells in general, optical absorption is one of the key parameters, as the amount of absorbed light directly determines the maximal producible electricity. The absorption coefficient α of organic thin films is measured via reflectometry. This method combines the measurement of transmission and reflection of incident white light in the spectral range $400 < \lambda < 900$ nm, where the solar spectrum has its highest intensity (visible and near infra-red).

[iv] In general, an isosbestic point describes a specific wavelength - and thus energy - where no change in absorption during a certain process or reaction occurs.

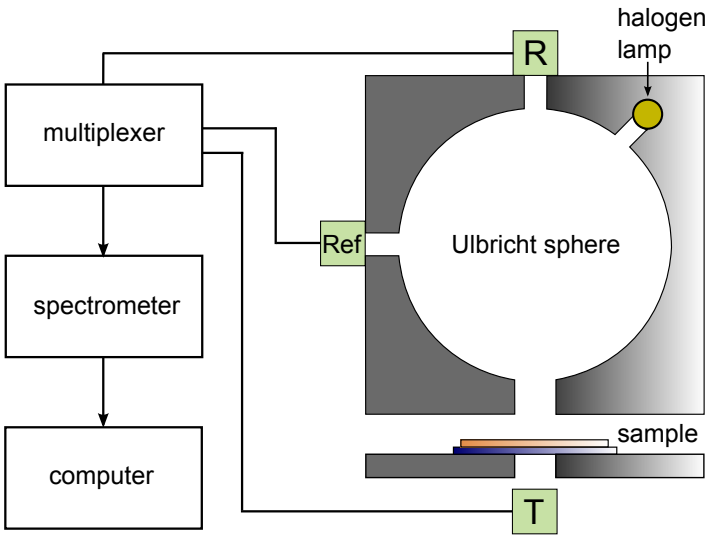

Figure 4.10: Schematic picture of the reflectometer used to determine the absorption coefficient of organic layers. The light from a halogen lamp impinges almost perpendicularly on the sample leading to transmission and reflection, detected by **T** and **R**, respectively. **Ref** is measured to compensate fluctuations of the lamp. Via fiber optic cables, the light is guided to a multiplexer and finally to the spectrometer.

Transmission ($T = I_\mathrm{T}/I_0$) is described by the Beer-Lambert law. It defines the attenuation of the intensity of an electro-magnetic wave by traveling through a sample of given thickness d:

$$\frac{I_\mathrm{T}(d)}{I_0} = \exp(-\alpha d) \tag{4.7}$$

with the initial intensity I_0 and the transmitted intensity I_T. To determine the reflection ($R = I_\mathrm{R}/I_0$) of the sample, it is assumed that the whole reflection occurs exclusively at the surface of the sample. As a result, I_0 is reduced by the intensity of the reflection I_R and Eq. (4.7) can be written as

$$\frac{I_\mathrm{T}(d)}{I_0 - I_\mathrm{R}} = \exp(-\alpha d) \tag{4.8}$$

By multiplying numerator and denominator on the left side of Eq. (4.8) with $1/I_0$, one obtains:

$$\frac{T}{1-R} = \exp(-\alpha d) \tag{4.9}$$

In a last step, the absorption of the substrate A_subs has to be taken into account via $A_\mathrm{subs} = 1 - T_\mathrm{subs} - R_\mathrm{subs}$ by separately measuring transmission (T_subs) and reflection (R_subs) of the substrate. Inclusion in Eq. (4.9) finally yields the expression for the absorption coefficient:

$$\alpha = \frac{1}{d} \ln\left(\frac{T}{(1-A_\mathrm{subs})(1-R)}\right) . \tag{4.10}$$

However, this calculation does not include strongly scattered light, which might occur at the sample's surface and thus does not enter the integrating sphere. In this case, some of the reflected light cannot be detected with the result that R is underestimated leading to a slight overestimation of α. However, this problem only occurs for films with very rough surfaces.
The measurement setup mainly consists of a halogen lamp, a spectrometer and an integrating sphere (Ulbricht sphere), which is connected to a multiplexer via fiber optic cables. A schematic drawing and the functional principle is shown in Fig. 4.10.

4.4.4 Atomic Force Microscopy

Atomic force microscopes (AFMs) belong to the group of scanning probe microscopes (SPMs), which gain information on the sample not by any optical or electro-optical tools, but by direct interaction of a probe with the sample. This probe is surface sensitive and images the sample's topography in molecular or even sub-molecular resolution.[188,189] The first AFM was designed 1985 by Binnig, Quate and Gerber.[190]

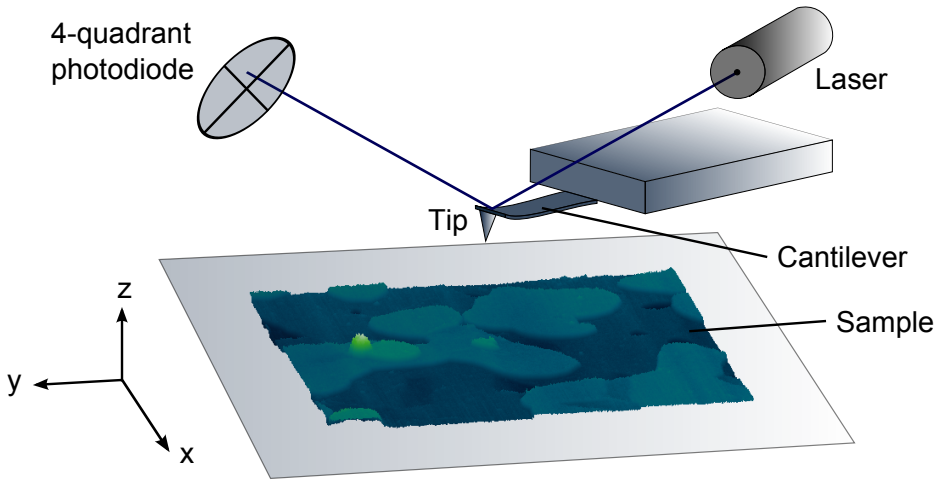

Figure 4.11: Functional principle of an atomic force microscope: A cantilever, which can be moved in all three dimensions by a piezo crystal, scans the surface of a sample. At its end, a tip is mounted, which is attracted or repulsed by the sample. These forces lead to a deflection of the cantilever and are detected by a laser and a 4-quadrant photodiode.

The functional principle of an AFM is shown in Fig. 4.11. A tip, which is mounted on the end of a cantilever is scanned over a small area of the sample. The scanning area for all AFM images recorded within this work was 4×4 µm^2. A piezo crystal ensures a very accurate positioning of the tip. There are three different operating modes, contact, non-contact and tapping mode, which vary in terms of contact between tip and sample. For soft materials like organic thin films, contact mode is not suitable as the permanent contact between tip and surface results in lateral forces, which might modify

morphological features of the sample. In tapping mode, which was used throughout this work, the cantilever oscillates with a frequency close to its resonance frequency, while being raster-scanned across the sample and only tapping on its surface. As there is no continuous contact, degradation of both tip and sample is minimized.[191] Attractive or repulsive forces between tip and sample surface change the oscillation frequency of the cantilever. This deflection is detected by a laser spot, focused on the back of the cantilever, from which it is reflected onto a 4-quadrant photodiode. As a result, the height profile can be visualized either as a false color plot or directly as a three-dimensional plot.
All AFM images were recorded under ambient conditions by a Thermo Microscopes Autoprobe CP-Research device.

4.4.5 Electrical characterization of organic solar cells

All previously described characterization methods have been performed on organic thin films. The electrical characterization, however, is executed on complete solar cell devices and provides a direct insight into the efficiency of an OPVC. The measurement of J-V-curves yields J_{SC}, V_{OC} and FF, i.e. all parameters determining the solar cell efficiency (*cf.* subsection 2.2.3).

The performance of OPVCs is commonly rated in terms of their efficiency with respect to standard reporting conditions defined by temperature, spectral irradiance, and total irradiance. Measurements are therefore performed at 25 °C cell temperature using the air mass (AM) 1.5 Global (G) reference spectrum with an integrated power of 100 mW/cm^2.[192] The AM1.5 G spectrum is defined by the American Society for Test-

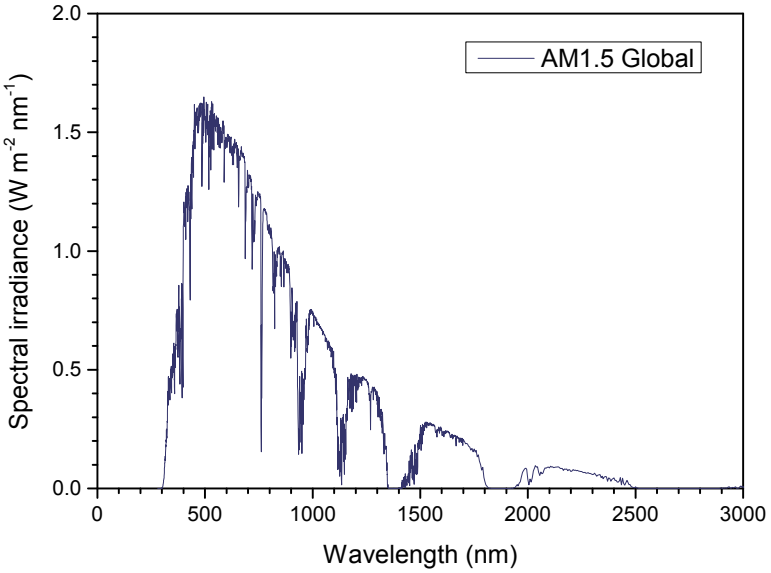

Figure 4.12: AM1.5 G spectrum with integrated power of 100 mW/cm^2. Data is taken from the American Society for Testing and Materials.[193]

ing and Materials (ASTM) in close collaboration with the photovoltaic industry and government research. It describes the average irradiance of the sun reaching the earth's surface under a solar zenith angle of 48.19 °. It takes into account one set of specified atmospheric conditions including the eponymous absolute AM of 1.5, which is a measure for the specific path length of sunlight travelling through the atmosphere. The corresponding spectrum is shown in Fig. 4.12.

All electrical characterization measurements are performed either in an inert atmosphere or in vacuum, respectively, to avoid degradation. The standard recording of the J-V-curves is carried out in a so-called solar simulator placed within a nitrogen filled glovebox. After mounting an OPVC into the solar simulator, voltage is applied and gradually increased, while current is measured with a Keithley 236 source measure unit (SMU). For each solar cell, this is always done twice, at first in the dark and then under illumination. To achieve the desired sun-like spectrum, a xenon arc lamp (LOT-Oriel 300 W) is linked with an AM1.5 G filter set. The typical illumination intensity of approximately 100 mW/cm^2 is approved by a calibrated 1×1 cm^2 silicon reference cell (RERA systems, PV Measurement Facility, Radboud University, Nijmegen). However, also several smaller intensities can be set using a filter wheel with neutral density filters attenuating the incident light (Fig. 4.13 (a)).

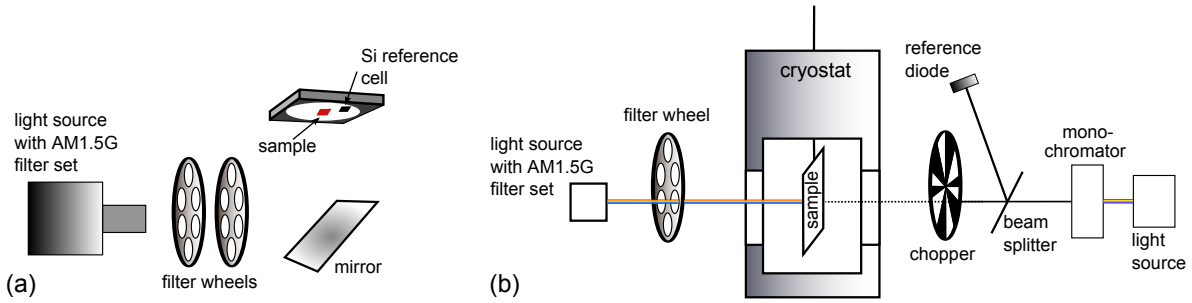

Figure 4.13: (a) Schematic illustration of the used solar simulator: The light of a xenon arc lamp linked with an AM1.5 G filter set passes two filter wheels, which can be used for light attenuation. By a mirror, the light is then deflected onto the sample and a Si reference photodiode to detect the exact light intensity. (b) Setup for measuring IPCE-curves (right part of the sketch) as well as temperature and intensity dependent J-V-characteristics (left part). Cryostat and filter wheels are used to adapt temperature and illumination intensity, respectively.

To perform temperature dependent J-V-curves, the sample is transferred without air exposure to a second setup attached to a nitrogen cryostat, which allows measurements at various lower temperatures down to about 100 K. For this setup, all measurements are recorded by a Keithley 237 SMU and illumination is provided by a halogen lamp (Xenon arc lamp, Osram XBO 150 W), while intensity dependent measurements are again possible by the use of a filter wheel (Fig. 4.13 (b, left part)).

With the same setup, also incident photon-to-current efficiency (IPCE) measurements can be carried out. IPCE describes the ratio of the number of generated charge carriers to the number of incident photons of a given wavelength λ. For that reason, the halogen lamp has to be linked with a monochromator (Omni-λ300, LOT-Oriel Instruments), while signal extraction is supported by a lock-in amplifier (SR830, Stanford Research Systems). Wavelengths in the range from 360 - 1100 nm can be applied in 1 nm steps. Calibration of the setup is done by use of Si reference diodes (OSRAM, BPW34B) with known IPCE. One such diode is measured from time to time instead of an OPVC. Another, identical diode is always measured simultaneously during the IPCE measurement of an OPVC, enabled by using a combination of beam splitter and optical fiber, which guides identical beams on sample and reference diode, respectively.[194] Due to the connection to the cryostat, also temperature dependent IPCE measurement can be performed (Fig. 4.13 (b, right part)).

4.4.6 Charge carrier mobility measurements

Charge carrier mobility in organic films is determined by electrical transport measurements of OFETs, executed within an evacuated cryostat ($p \approx 10^{-6}$ mbar). The contact between gate electrode and sample holder is ensured by using conductive silver lacquer, while source and drain are contacted separately by small needle probes. All measurements are performed under exclusion of light as incident light generates additional charge influencing the result.[195] Transfer characteristics are measured applying a constant drain voltage of $\pm$ 2 V, using a positive voltage for electron transport and a negative voltage for hole transport measurements. Meanwhile, the gate voltage is varied in 1 V steps from $\mp$ 10 V to $\pm$ 90 V for unipolar transistors and from - 90 V to + 90 V for ambipolar transistors. Finally, the charge carrier mobility μ can be calculated using the so-called Shockley method via:

$$\mu = \frac{L}{WC'V_{\mathrm{D}}} \cdot m_{\mathrm{S}} \tag{4.11}$$

with channel length L, channel width W, capacity C', drain voltage V_{D} and the slope of the transfer characteristics m_{S}. Measurements are performed using a Keithley 4200 semiconductor parameter analyzer.

Chapter 5

Results and Discussion

The main chapter of this thesis comprises the experimental data and their discussion. To investigate the effect of morphology on molecular organic solar cells, the focus will be on two structurally similar materials which show opposite morphology. The first section will give a detailed comparison of these two organic materials, crystalline DIP and amorphous DBP. The second section deals with the influence of morphology of exciton blocking layers on the efficiency of PHJ and PMHJ organic solar cells by comparing crystalline and amorphous EBLs. In the third section, the effect of SVA on organic solar cells is examined. SVA affects the morphology of organic thin films, however, big differences for SVA on crystalline DIP and amorphous DBP occur. In the fourth section, finally, ZCl is introduced as new acceptor material in OPVCs.

5.1 Characterization and comparison of crystalline DIP and amorphous DBP in terms of organic solar cells

DIP and DBP are well established materials in organic solar cells.[108–110,116–123] Both provide features, which are beneficial during the conversion process of light into free charge carriers. Although having similar molecular structures, their most striking advantages are completely different. The following chapter will concentrate on similarities and differences and thus will provide a detailed explanation for the varying solar cell performances of devices using either DIP or DBP as donor and acceptor material, respectively.

5.1.1 Molecular structure and thin film morphology

To determine the influence of morphology on solar cell performance, it is not useful to compare two completely different molecules as there are always various factors, which influence the complete charge generation process and thus the performance of the device. A good approach is to contrast similar molecules, which nevertheless yield different thin film morphologies. This is the case for the two perylene derivatives DIP and DBP. While DIP consists of a perylene core and two indeno-groups, DBP possesses one further benzene ring on each side, as well as four additional phenyl groups. The molecular architectures of DIP and DBP are shown in Fig. 5.1 (a), where the additional groups of DBP are marked in green. The structural similarities of both materials lead to a comparable energy level alignment. As a result, DIP and DBP can be used both as donor and acceptor material in OPVCs with the same partners. For example, when being used as acceptor, they can be combined with 6T. Otherwise, both can be employed as donors in connection with fullerenes like C_{60} or C_{70}. Due to the two additional benzene rings, DBP possesses a slightly enlarged π-electron system, which leads to a red-shift of absorption and thus to a little smaller energy gap. Therefore, the LUMO of DBP is lower than that of DIP. However, the HOMO level alignments of DIP and DBP are almost identical. This can be confirmed by ultraviolet photoelectron spectroscopy (UPS).

UPS typically uses monochromatic photons of the ultraviolet regime to excite electrons from the valence band into the vacuum.[196] For organic semiconductors, however, no valence band exists and the excited electrons stem from the frontier occupied molecular orbitals.[187] Of main interest is the binding energy of the excited electrons, which can be determined by measuring their kinetic energy. At the same time, the energy of the impinging photons and the work function of the detector must be known. Knowing the binding energy, in turn yields the HOMO level of the examined organic semiconductor with respect to the Fermi level.[197] UPS measurements and evaluation of the obtained data were carried out by Dr. Andreas Wilke (HU Berlin) at the synchrotron light source BESSY II using 35 eV ultraviolet photons.

These measurements reveal an identical HOMO-offset between DIP/C_{60} and DBP/C_{60} of 1.0 eV and thus also an identical photovoltaic gap E_{PVG} ($= E_{\mathrm{DA}}$) of 1.6 eV with an

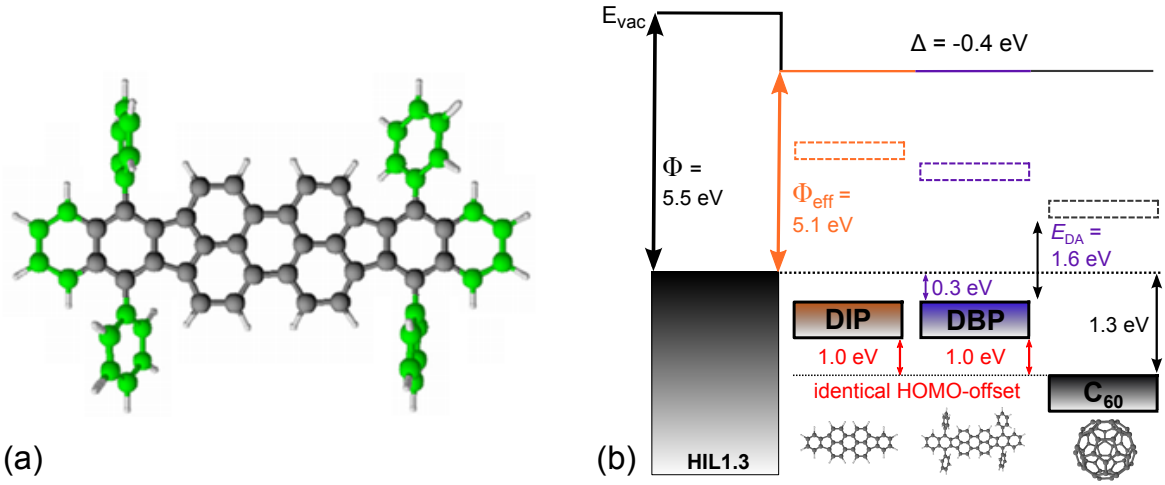

Figure 5.1: (a) Structural similarity of DBP and DIP: DBP consists of a DIP backbone (grey) with two further benzene rings and four additional, rotatable phenyl groups (green). (b) Consequences on energy level alignment: UPS measurements reveal an ionisation energy of DBP of 5.4 eV and thus an identical HOMO-offset between DIP/C_{60} and DBP/C_{60}. As a result, for both material combinations, the same V_{OC} is expected.

assumed transport gap of C_{60} of 2.6 eV[198,199] (Fig. 5.1 (b)). As it has already been explained in subsection 2.2.3, E_{DA} mainly determines V_{OC} of an OPVC. Therefore, V_{OC} is assumed to be identical or at least very similar for DIP/C_{60} and DBP/C_{60} devices.

Beside all these similarities, there are also major differences between DIP and DBP, which are mainly caused by the four additional, rotatable phenyl groups of DBP. As they are typically not oriented in-plane to the perylene core, these groups act as steric hindrance during thin film growth and thus lead to a completely changed growth behavior. This can be observed by XRD measurements. For a 50 nm thick DIP film, three peaks - (001), (002), and (004) - appear (Fig. 5.2 (a)). More sophisticated measurements of DIP on ITO even revealed Bragg reflections up to the seventh order,[104] which is indicative of a highly crystalline thin film. The different peaks are separated by q_z = 0.378 Å^{-1}. This result is in perfect agreement with former measurements.[21] With that, the out-of-plane lattice spacing $d_\perp$ can be calculated via Eq. (4.4), which yields $d_\perp$ = 16.6 Å. By knowing the molecular length of DIP of approximately 18.4 Å,[102] it can be concluded that the DIP molecules grow highly crystalline on the ITO substrate, standing almost upright, just tilted by an angle of $\approx 17\,°$. This upright standing phase is denoted as σ-phase.

Moreover, XRD data offers the possibility to estimate the minimal vertical crystallite size D of the measured film. For that, the FWHM of a Bragg peak has to be determined via a Gaussian fit. In Fig. 5.2 (b) this is done for the σ(001)-peak of the 50 nm thick DIP film. The fit yields a FWHM of 0.0116 Å^{-1}. By inserting this result into the modi-

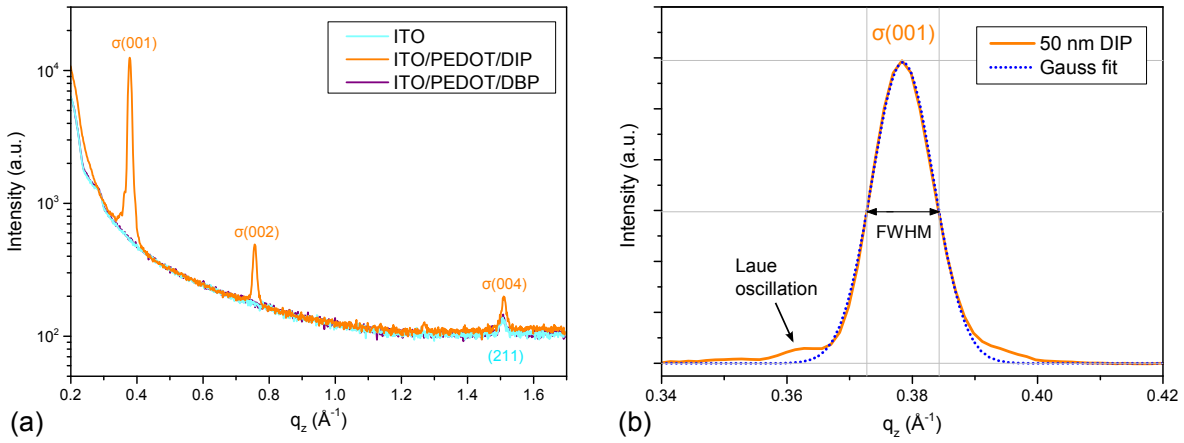

Figure 5.2: (a) XRD spectra of ITO, ITO/PEDOT/DIP and ITO/PEDOT/DBP: For highly crystalline DIP, three peaks - (001), (002), and (004) - of the upright standing σ-phase are visible. For DBP, however, no peaks appear, indicating the amorphous growth of DBP thin films. For all three samples the (211)-peak of the ITO substrate appears at $q_z \approx 1.51\,\text{Å}^{-1}$. (b) Enlarged presentation of the σ-DIP (001) peak: A Gaussian fit to this peak yields FWHM and thus the vertical extent of the DIP crystallites.

fied Scherrer equation (Eq. (4.5)), one obtains a vertical crystallite size of $D = 50.8\,\text{nm}$. This means, that layer thickness and vertical coherence length are identical and the DIP domains vertically extend across the entire layer. This means that the choice of the layer thickness already determines the vertical crystallite size, which is in perfect accordance with previous results.[108,110,200] The deviations between measured curve and fit on both sides of the peak are so-called Laue oscillations, which can indicate the number of layers contributing to the reflection. However, for this measurement, they are too weak to obtain further information.

The XRD data of a DBP thin film, however, reveal no Bragg reflections (Fig. 5.2 (a)). The only peak which occurs at $q_z \approx 1.51\,\text{Å}^{-1}$ can be attributed to the ITO substrate as this (211)-peak also appears for measurements on pure ITO. Missing Bragg peaks are a strong indication for an amorphous growth of DBP thin films. This assumption is supported by results of Zhou *et al.* using reflection high energy electron diffraction (RHEED), where also no signs of DBP crystallinity can be found for samples grown at room temperature. However, very weak patterns appear when DBP is grown at elevated temperatures and with small evaporation rates indicating at least weak crystallinity for certain evaporation conditions.[117]

The influence of these parameters can be confirmed by AFM measurements, which reveal the topography of the film. In general, the surface of an evaporated DBP film is very smooth. A typical measure of the surface roughness is the so-called root-mean-squared (RMS) roughness, which is the standard deviation of the average surface height. For a 20 nm thick DBP film grown at room temperature and with the typical evaporation

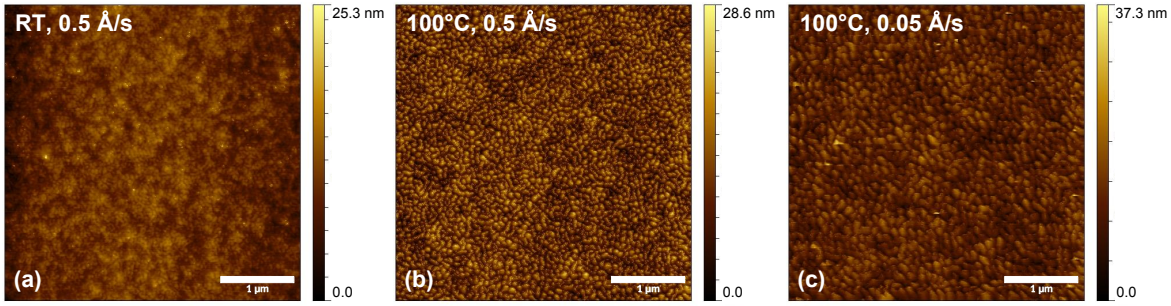

Figure 5.3: AFM images of different morphologies of a 20 nm thick DBP layer evaporated under varying conditions: sample (a) is evaporated at room temperature with a deposition rate of 0.5 Å/s. For sample (b) the substrate temperature during evaporation is increased to 100 °C. Additionally, for sample (c) the deposition rate is decreased to 0.05 Å/s.

rate of 0.5 Å/s the RMS roughness is merely 1.7 nm (Fig. 5.3 (a)). When the substrate temperature during evaporation of DBP is increased to 100 °C, however, the roughness increases to RMS = 3.9 nm. This is caused by various small, almost spherical structures appearing on the surface of the film (Fig. 5.3 (b)). Hence, the arrangement of DBP molecules during the evaporation process changes, indicating a slightly increased order. If the evaporation rate is additionally lowered to 0.05 Å/s, these structures seem to merge and thus grow. This might imply an even higher order of the film, although its roughness does not further increase and it is RMS = 3.4 nm, probably due to less grains (Fig. 5.3 (c)). Nevertheless, although a change in the short-range order of DBP for varying growth conditions can be confirmed, XRD measurements do not show any peaks for all of these films. As a result, with these methods DBP films cannot be grown crystalline but have always amorphous character.

The crystalline character of DIP, however, cannot only be observed by XRD, but is also visible on AFM images. For a 50 nm thick DIP layer grown on a heated substrate (100 °C), well-ordered, terrace-like structures appear, indicating the individual DIP monolayers stacked one upon the other (Fig. 5.4). It is striking that such terracing is significantly increased for thicker layers. This could be explained by the growth mode of DIP. It has already been proven that DIP shows the tendency to grow in Stranski-Krastanov mode on various substrates.[201,202] In this growth mode, initially complete closed films of one or more monolayers are formed. Beyond a critical thickness, however, the adsorbate begins to show island growth. This island growth finally is responsible for terracing. Otherwise, that means that thin layers of DIP, with dominant layer-by-layer growth are much smoother. Another factor, which influences the DIP layer structure is the substrate temperature during evaporation. It has already been shown that higher substrate temperatures lead to enhanced crystallinity associated with growing structures. While the surface of an unheated sample shows small round-shaped islands with about 80 nm in diameter, the big terraces of the heated sample indicate extended crystallites.[21]

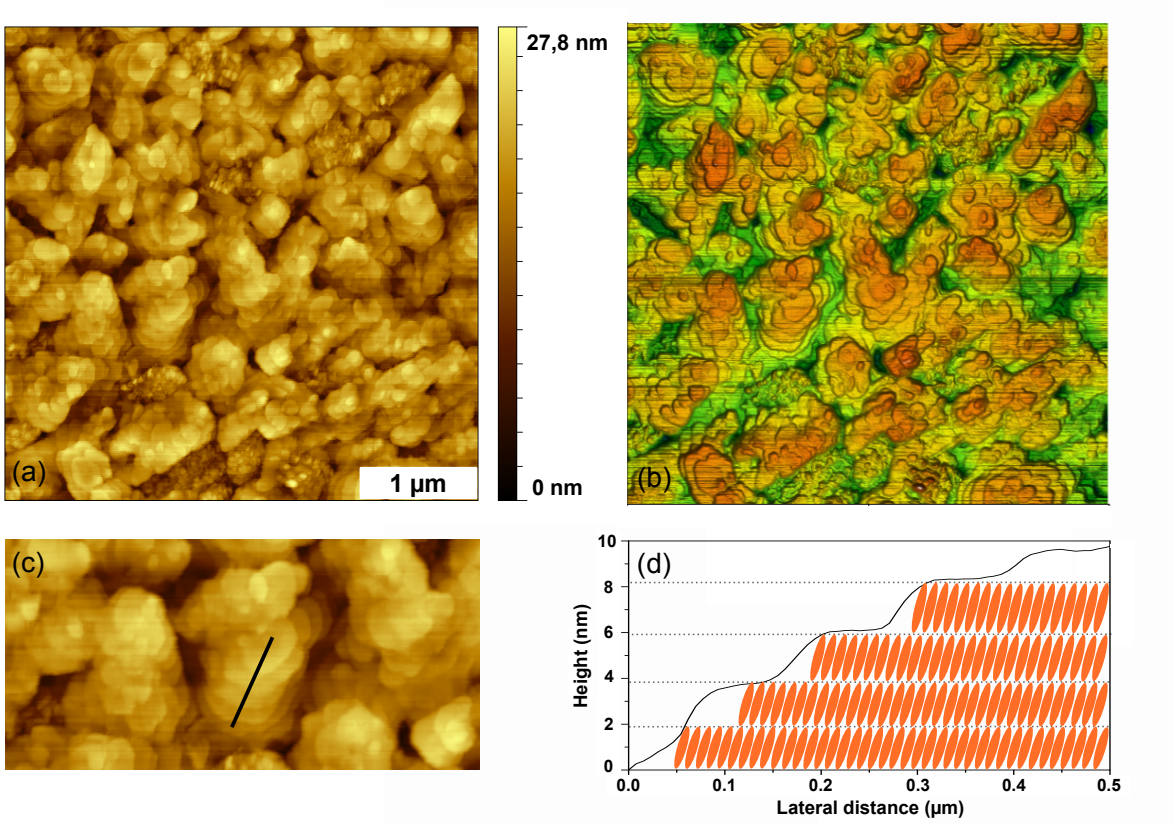

Figure 5.4: AFM image of a 50 nm thick DIP layer evaportated on ITO/PEDOT at 100 °C. For a better visualization of the evolving DIP terraces, different color mappings are chosen for the same sample sections in (a) and (b). Zooming in provides section (c), where a line profile is drawn. The resulting line profile is presented in (d) and shows the highly crystalline arrangement of the DIP monolayers stacked one upon the other indicated by the orange ellipses, which in turn represent the DIP molecules.

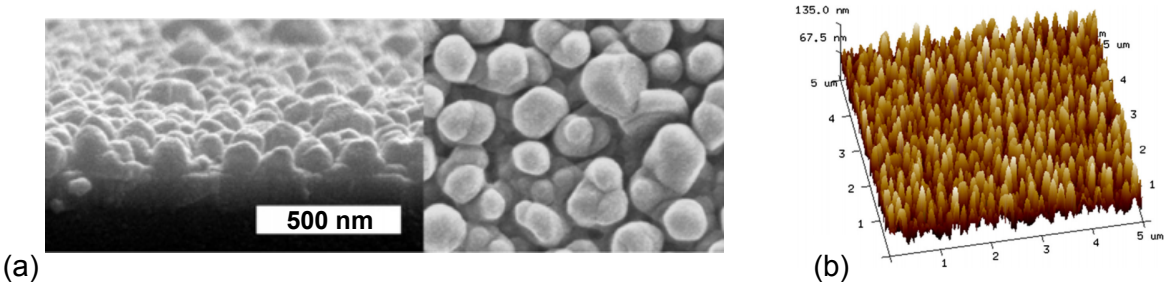

Figure 5.5: SEM ((a), cross section and top view) and AFM (b) micrographs of 100 nm DIP nanocolumns fabricated by GLAD. The images have been recorded within a collaboration by Yu *et al.* and have already been published.[203]

The roughness of a DIP film can be even further increased by using an alternative deposition method - glancing angle deposition (GLAD). For this technique, the sample holder has to be rotated during evaporation. Moreover, the molecular flux has to impinge upon the substrate under a certain angle. This leads to shadowing effects and limited adatom diffusion during the evaporation process. As a result, one obtains a film with a columnar microstructure.[51,204,205] Micrographs of such DIP nanocolumns are shown in Fig. 5.5. Compared to normal evaporation, the roughness of the DIP layer can be drastically increased by using GLAD. This in turn leads to an increased D/A interface by subsequent (normal) evaporation of the acceptor material, which is expected to be favorable for solar cell performance in terms of enhanced exciton dissociation. However, after evaporation of the acceptor material, stability issues of the nanocolumns could be observed, leading to accelerated degradation and problems with reproducibility.

As a short summary, it can be stated that when evaporated under normal conditions, DIP generally forms highly crystalline thin films with rough and structured surfaces, while DBP films are usually amorphous and smooth. A full analysis of thin film architecture, however, also requires knowledge about molecular orientations. A powerful tool to get insight into the orientation of molecules in solids is NEXAFS. For that purpose, NEXAFS spectra are recorded by Dr. Andreas Opitz (HU Berlin) for 15 nm thick films of DIP and DBP under varying angles of incidence of the impinging X-rays. The molecular orientation within the films can then be calculated via Eq. (4.6). The results are depicted within Fig. (5.6 (a)). For DIP, the expected tendency for almost upright standing molecules is clearly confirmed. Data evaluation yields a molecular orientation, i.e. an angle between substrate and the long axis of the DIP molecule of $\alpha \approx 80\,^\circ$. Vice versa, DBP molecules exhibit a rather horizontal orientation of their perylene cores with $\alpha \approx 40\,^\circ$. However, it has to be kept in mind, that in the amorphous DBP film, it is not expected that all molecules show the same orientation. Hence, this value of α merely represents the average orientation, while some of the DBP molecules lying more flat and others standing more upright. Nevertheless, this result of a preferred horizontal alignment is consistent with previous results obtained from variable angle spectroscopic ellipsometry (VASE) measurements.[118]

By summing up the results of UPS, XRD, AFM and NEXAFS measurements on DIP and DBP, a complete picture of molecular structure, energy level alignment and thin film morphology for both materials can be drawn. A schematic illustration is shown in Fig. 5.6 (b) and (c). It can be seen that despite their similarities concerning molecular structure and thus HOMO-LUMO alignment, DIP and DBP possess completely different thin film architectures. While DIP films are highly crystalline and the molecules within almost upright standing, DBP films are amorphous and consist of molecules with a preferred horizontal alignment. Thus, DIP and DBP are a perfect pair of molecules to examine the influence of morphology on the performance of organic solar cells.

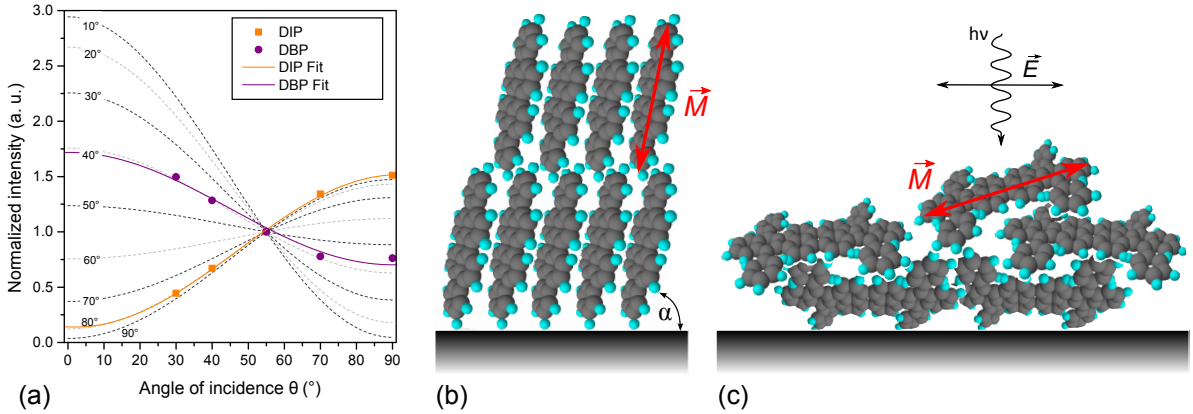

Figure 5.6: (a) NEXAFS measurements reveal almost upright standing DIP molecules and a preferred horizontal alignment of DBP molecules. In combination with XRD measurements this leads to the schematic illustration of structure and molecular orientation of (b) DIP and (c) DBP thin films. Moreover, the respective transition dipole moment $\vec{M}$ for DIP and DBP, as well as the light electric field $\vec{E}$ of an impinging photon are shown.

5.1.2 Absorption and transport

By comparing the performance of different solar cells, it is useful to consider the three most important parameters defining the efficiency of the device: V_{OC}, J_{SC} and FF. In the previous subsection, it could already be shown, that the photovoltaic gaps of DIP/C_{60} and DBP/C_{60} solar cells are identical. As a result, also V_{OC} is assumed to be the same for both devices. In the following, some features of DIP and DBP are compared, which indicate some qualitative expectations for J_{SC} and FF in DIP and DBP containing solar cells, respectively.

One of the most decisive features that determines J_{SC} is the absorptivity of the photoactive organic layers. Of course, there are also several other aspects, which influence J_{SC}. The best absorption is useless, when the generated excitons do not reach the D/A interface or are not dissociated effectively. Nevertheless, strong absorption is the basic requirement for high values of J_{SC}. A crucial property for strong or weak absorption is the molecular orientation, as absorption depends on the coupling between direct incident light and the transition dipole moment of the molecule ($\vec{M}$). For most molecules - and also for DIP and DBP - $\vec{M}$ is aligned along the long molecular axis. In general, light absorption (i.e. the transition probability A) is proportional to the scalar product of the incident light electric field $\vec{E}$ (which is perpendicular to the direction of light propagation) and the transition dipole moment of the molecule $\vec{M}$

$$A \sim |\vec{M} \cdot \vec{E}|^2 \ , \tag{5.1}$$

so that A is maximal when $\vec{M}$ and $\vec{E}$ are parallel and null when they are oriented perpendicular to each other.[206,207] This correlation is also shown in Fig. 5.6 for DIP

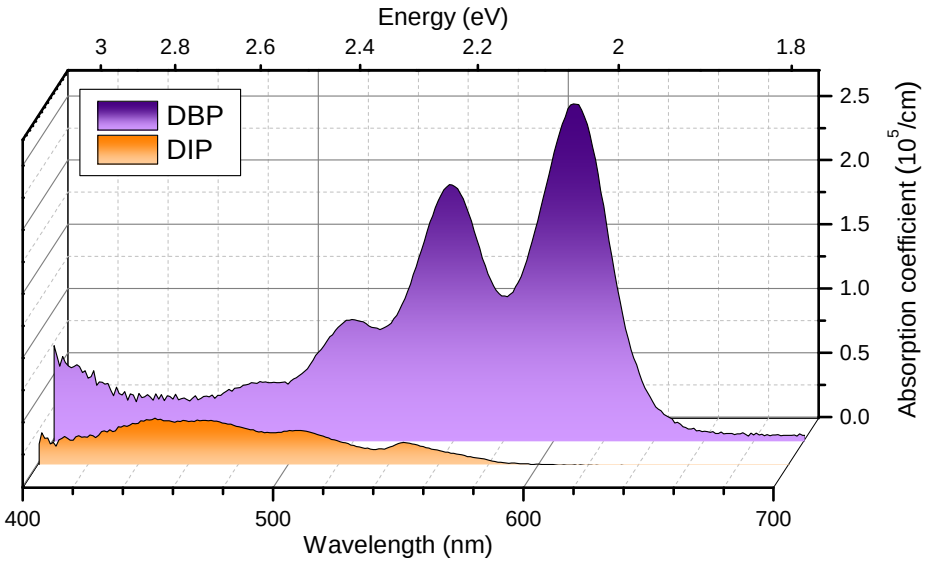

Figure 5.7: Absorption characteristics of DIP and DBP thin films. The absorption of DBP is more than 6 times stronger than that of DIP, resulting from different molecular orientations.

(b) and DBP (c). Due to the almost upright standing orientation of the DIP molecules, there can be only very weak coupling between the electric field of the impinging photons and the transition dipole moment of the molecules. As a result, only weak absorption is expected for DIP films. On the contrary, the rather horizontal alignment of the DBP molecules enables a much stronger coupling between $\vec{E}$ and $\vec{M}$, which in turn leads to stronger absorption and thus more generated excitons within the DBP film.

This behavior can be attested via reflectometry measurements. By measuring transmission and reflection of DIP and DBP films, their absorption coefficients α can be calculated via Eq. (4.10). The wavelength-dependent values of α for DIP and DBP are shown in Fig. 5.7. Integrating the areas below the respective curves yield an absorption of DBP which is more than six times stronger than that of DIP. Of course, due to different refractive indices, a direct comparison is not absolutely correct, however, variations of the refractive indices are negligible for strong absorption of thin films. A detailed comparison of refractive indices n and extinction coefficients k for DIP and DBP can be found elsewhere.[118,208] Beside the different molecular orientations, another factor contributes to the stronger absorption of DBP. Due to the enlarged π-electron system caused by the two additional benzene rings, DBP reveals a slightly smaller optical gap. As a result, the absorption of DBP already sets in at photon energies of about 1.9 eV. For DIP, however, the absorption edge is shifted to higher energies by approximately 0.2 eV. Finally, these results lead to the assumption, that DBP containing solar cells provide significantly higher values of J_{SC} than their DIP counterparts.

Another factor, which influences J_{SC} is the exciton diffusion length (L_D) within the organic film, as it determines whether an exciton can reach the D/A interface and thus contributes to the current. L_D represents the average distance an exciton can travel before it is lost by recombination and depends on the exciton diffusivity D and on its lifetime τ by $L_D = \sqrt{D\tau}$. The value of τ is strongly affected by the sort of excitons, which are generated. While the lifetime of singlet excitons is only in the order of ns, the lifetime of triplet excitons is extended by many orders of magnitude due to the forbidden decay of spin 1 triplet states to the spin 0 singlet ground state.[209] However, due to the structural similarities hardly any differences concerning singlet and triplet excitons and thus τ are expected for DIP and DBP. This means that variations of L_D can be completely explained by different exciton diffusivities. As an improved crystallinity is associated with enhanced diffusivity,[210] higher values of D and thus L_D are expected for DIP compared to DBP. This is true as DIP provides exceptionally long exciton diffusion lengths of up to 100 nm,[106] while typical values of L_D for DBP are only in the range of 10 nm.[116] As a result, the thickness of DBP layers is strongly limited to a maximum of 20 - 30 nm to avoid huge recombination losses within the film. DIP layers, however, can be chosen to be much thicker. The advantages of thicker layers are a more efficient absorption as well as greater architectural possibilities to adapt layer thicknesses more precisely.

While exciton diffusion mainly affects J_{SC}, the transport of free charge carriers is one of the major factors determining the fill factor of an OPVC. A measure of the transport ability is the charge carrier mobility μ within the organic films. A determination of μ can be done by use of OFETs. The preparation of OFETs and the data evaluation were accomplished in cooperation with Stefan Schmidt in the scope of his bachelor's thesis.[211] The OFET devices consist of p^{++}-Si/300 nm SiO_2/20 nm TTC/25 nm DIP or DBP/top contact. The choice of the top contact material depends on which charge carrier mobility should be measured. To determine the mobility of holes, a 125 nm thick layer of the charge transfer salt TTF-TCNQ is chosen, while 100 nm of Al serve as top contact for electron mobility measurements. Then, the electrical characterization is carried out under high vacuum conditions and the measured output characteristics are analyzed by the transfer length method. The best results for DIP and DBP transistors are summarized in Tab. 5.1. For comparison, additional values of charge carrier mobilities in DIP films are added from literature.[107]

Semiconductor	μ_{hole} (cm^2/Vs)	$\mu_{electron}$ (cm^2/Vs)
DIP (lit.[107])	$5 \cdot 10^{-2}$	$1 \cdot 10^{-1}$
DIP	$5 \cdot 10^{-3}$	$2 \cdot 10^{-2}$
DBP	$1 \cdot 10^{-3}$	$5 \cdot 10^{-4}$

Table 5.1: Charge carrier mobilities μ_{hole} and $\mu_{electron}$ in OFETs with DIP or DBP as semiconducting layer, respectively. For DIP, literature values and measured values are compared.

Both materials have a bipolar nature, i.e. they are able to transport both electrons and holes. Consequently, DIP as well as DBP can be used in OPVCs as donor as well as acceptor material. It is striking, however, that the mobility values taken from literature are about one order of magnitude higher than the measured ones, although the OFET architectures are more or less the same. Moreover, they have been fabricated and measured by the same equipment. Thus, the most probable explanation for that difference can be found in DIP quality. The purer the material, the more crystalline layers are expected to grow, which in turn enables higher values of μ. This assumption is supported by the fact that the exceptionally high FF of 74 % for an DIP/C_{60} OPVC, which has been reported by Wagner *et al.* in 2010,[108] could not be reproduced by our group in the last few years. The influence of DIP purity on the FF have already been published.[77] Nevertheless, the measured values show higher μ within DIP films compared to DBP layers, as it is expected due to morphological reasons. However, compared to other organic semiconductors also DBP shows decent charge carrier mobilities. For example, the values of μ within most polymer films are in the range of 10^{-6} - $10^{-3}\,\mathrm{cm^2/Vs}$.[15]

The measurement of μ by use of an OFET, however, is just an indirect hint for the FF in an OPVC as the obtained results cannot be directly translated from one device to the other. A better measure to estimate the FF of an OPVC is the series resistance R_S, because it is directly measured within the solar cell. In general, R_S is one of the most important factors limiting the FF of OPVCs.[212–214] To extract R_S, dark current characteristics can be analyzed. Although the physics behind it is not the same as in an inorganic p-n junction, it has been shown that the exponential part of the forward-bias characteristics can be described by a modified Shockley equation:[61,74]

$$j(V) = j_0 \left[\exp\left(\frac{q(V - j(V) R_\mathrm{S} A)}{n k_\mathrm{B} T} \right) - 1 \right] . \tag{5.2}$$

This equation is based on the Shockley equation for real organic solar cell devices (*cf.* Eq. (2.10)), neglecting the parallel resistance R_P. This approximation is reasonable for most solar cells as they possess very small leakage currents so that $R_\mathrm{P} \gg R_\mathrm{S}$.

For DBP/C_{60} as well as for DIP/C_{60} solar cells, temperature dependent $J-V$-characteristics are recorded[i] and R_S is extracted by fitting Eq. (5.2) to the obtained data for each temperature. The dark current characteristics and the fits are shown in Fig. 5.8 for the DBP/C_{60} (b) and the DIP/C_{60} (c) solar cell. By comparing both devices, it has to be mentioned that the photoactive layers in the DIP containing OPVC are - added together - twice as thick as the corresponding layers of the DBP device. The photoactive layer architectures are 20 nm DBP/45 nm C_{60} and 50 nm DIP/80 nm C_{60}, respectively. Nevertheless, the series resistance at room temperature is almost identical for both devices with $R_\mathrm{S} = 4.8\,\Omega\,\mathrm{cm^2}$ (Fig. 5.8 (a)). At this point, it has to be mentioned that the series resistance of the ITO substrate plays also a significant role for that value, so that the obtained results are only to some extent determined by the organic film. However, as all

[i] The data of the DIP/C_{60} solar cell were obtained from Ulrich Hörmann.

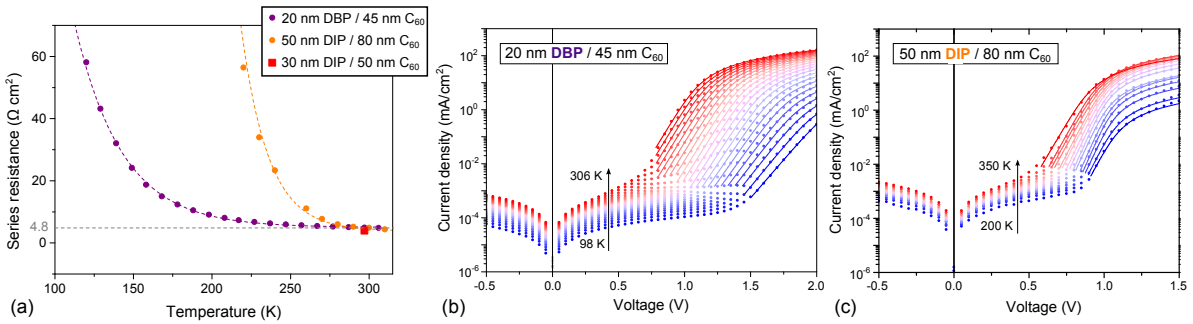

Figure 5.8: (a) Temperature dependent series resistance for DBP/C_{60} and DIP/C_{60} devices. At room temperature there is hardly any difference in R_S between the cells. The values of R_S are derived from Shockley-fits to the dark current curves of a DBP/C_{60} and a DIP/C_{60} solar cell, which are shown in (b) and (c), respectively.

compared devices use the same ITO substrate, different values of R_S can be traced back to different organic films. By comparing the curves in Fig. 5.8 (a), an influence of the layer thickness seems to occur for decreasing temperatures. Although both curves show an exponential increase of R_S with decreasing temperatures (indicated by the dashed lines following an exponential fit), the strong increase of R_S, sets in much earlier for the thicker DIP device. At room temperature, however, it seems like an increased layer thickness of DIP and C_{60} has no major impact on R_S. As a reference, an OPVC is fabricated with thinner photoactive layers (30 nm DIP/50 nm C_{60}), which possesses only a slightly lower series resistance (red square). On the contrary, once again it seems like the purity of the layers and thus the crystallinity is of much greater importance. Julia Kraus could show in her PhD thesis that the series resistance at room temperature of an OPVC with 50 nm DIP/80 nm C_{60} can be even lower with $R_S = 3.0\,\Omega\,cm^2$.[21] All in all, it can be stated that the series resistances in DBP and DIP containing solar cells are similar, which leads to the conclusion that also similar fill factors can be expected.

Now, the question arises why the values of R_S are that similar, although DIP provides (much) higher charge carrier mobilities in OFETs. This can be explained by the anisotropic transport within DIP. In a thin film of almost upright standing DIP molecules, there is a strong overlap of the delocalized π-electrons parallel to the substrate, while this overlap is markedly weaker in the perpendicular direction (*cf.* Fig. 5.6 (b)). This vertical direction, however, is crucial in OPVCs, as this is the direction from the D/A interface towards the electrodes, whereas OFETs measure the mobility in the horizontal direction parallel to the substrate. In a DBP film, however, due to its amorphous character, the transport anisotropy is expected to be weaker. As a result the obtained results of μ measured in an OFET are expected to be in better agreement with the actual mobilities in an OPVC. In contrast to DIP, the charge carrier mobilities are even expected to be a little bit higher within the solar cell as the preferred horizontal orientation of the DBP molecules denotes a stronger overlap of molecular orbitals in the vertical direction.[118]

Blend (mixing ratio)	μ_{hole} (cm^2/Vs)	μ_{electron} (cm^2/Vs)	$R_{\text{S}}A$ (@ RT) ($\Omega\,\text{cm}^2$)
DBP:C_{60} (1:2)	$2 \cdot 10^{-4}$	$2 \cdot 10^{-1}$	4.4
DBP:C_{60} (1:1)	$4 \cdot 10^{-4}$	$4 \cdot 10^{-2}$	2.4
DIP:C_{60} (1:2)	—	$3 \cdot 10^{-1}$	—
DIP:C_{60} (1:1)	—	$6 \cdot 10^{-2}$	1.9

Table 5.2: Charge carrier mobilities μ_{hole} and μ_{electron} from OFET measurements, comparing DBP:C_{60} and DIP:C_{60} blends. Two different mixing ratios (1:1 and 1:2) were investigated. Additionaly, the respective series resistances are given, obtained from Shockley-fits to the dark current characteristics of respective solar cells.

In a next step, charge carrier transport in co-evaporated organic films is investigated. Such films of mixed donor and acceptor materials are used as photoactive layer within BHJ and PMHJ organic solar cells. For DBP:C_{60} as well as for DIP:C_{60} films, two different mixing ratios are examined - 1:2 and 1:1. Electron and hole mobilities are again obtained by OFET measurements, the results are shown in Tab. 5.2. First of all, it is striking that only rather bad (DBP:C_{60}) or even no (DIP:C_{60}) hole mobilities can be measured. This is caused by the fullerene, which is known to be an (unipolar) n-type organic semiconductor. While showing good electron mobilities of up to $4.9\,\text{cm}^2/\text{Vs}$, no hole transport is usually detected in C_{60} films.[215,216] Consequently, hole transport within the investigated blends has to be ensured by continuous paths of DBP or DIP, respectively. For the DIP:C_{60} blend, it seems like no such paths exist within the OFET, though. The electron mobilities within all investigated films, however, are comparatively high. This can be explained by the decent electron mobilities within all of the blended materials. Moreover, it is conspicuous that 1:2-blends (with 66 % C_{60}) exhibit electron mobilities, which are about one order of magnitude higher than that of the 1:1-blends.

In addition, also the series resistances, which are again obtained by a Shockley fit to the dark current characteristics of corresponding OPVCs, are determined and shown in Tab. 5.2. The architecture of these devices is generally 5 nm donor/50 nm blend/10 nm acceptor. With this method, a better transport is indicated for the 1:1-blend compared to the 1:2-blend[ii] probably due to a better charge carrier balance. The temperature dependent development of the series resistance of the DBP:C_{60} (1:2) solar cell is given in Fig. 5.9. It is striking that, compared to the PHJ solar cells, the device yields lower series resistances for decreasing temperatures. This means that PMHJ devices exhibit less temperature dependency on charge carrier transport than PHJ devices, at least for this material combination. In general, the series resistances of the PMHJ devices are throughout smaller than that of their planar counterparts, which is surprising at first sight. However, also in literature, BHJ or PMHJ devices can be found with small values

[ii] At least for the DBP:C_{60} solar cell. A DIP:C_{60} (1:2) has not been fabricated during the work on this thesis, so that no value of R_{S} can be given.

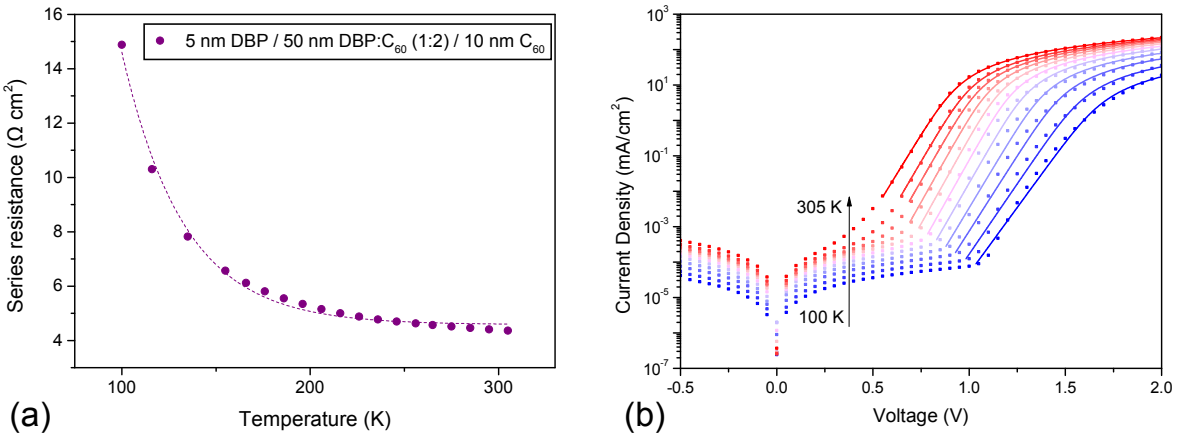

Figure 5.9: (a) Temperature dependent series resistance for a PMHJ DBP:C_{60} (1:2) device. (b) The values of R_S are derived from Shockley-fits to the dark current characteristics.

of R_S.[217,218] This can be realized, when there is an efficient phase separation between donor and acceptor and not a homogeneous mixture phase of the two materials. Conversely, this means that also DBP:C_{60} and DIP:C_{60} blends show good phase separation and are thus suitable material combinations for PMHJ solar cells[iii]. Nevertheless, PMHJ solar cells usually provide smaller fill factors than PHJ devices. This shows that also a comparison of R_S is just one indicator for the fill factor. Besides transport, there is a second crucial factor, which influences the FF. This factor is recombination, which is of greater importance for blended organic films. Due to the greatly enlarged D/A interface, non-geminate recombination is drastically enhanced within PMHJ devices,[43] which in turn reduces the fill factor of the solar cell. A measure for this correlation is the ideality factor n. A higher n indicates enhanced recombination and thus a lower FF. For the ideal case, it is assumed that $n = 1$ for planar and $n = 2$ for planar-mixed OPVCs.[69]

Finally, it can be stated that no big difference between DBP:C_{60} and DIP:C_{60} blends concerning charge carrier transport can be noticed. Both show comparably high charge carrier mobilities and low series resistances due to good phase separation when evaporated at elevated temperatures. As a consequence, it can be expected that both material combinations are well suited for PMHJ solar cells and provide similar fill factors.

5.1.3 Solar cell performance

Within this subsection, the previously made assumptions concerning J_{SC}, V_{OC} and FF of DIP and DBP solar cells are investigated via electrical characterization of the corresponding OPVCs. For that purpose, one decisive factor for J_{SC} has to be considered, namely the thickness of the photoactive layers. In general, the thicker the layer, the higher the absorption within. However, absorption and the resulting exciton generation

[iii] A prerequisite for such an efficient phase separation is substrate heating to 100 °C during co-evaporation, which was done throughout this work.

are only one factor determining J_{SC} as excitons, which do not reach the D/A interface for dissociation recombine and thus cannot contribute to J_{SC}. As a consequence, also the exciton diffusion length has to be considered. Moreover, there is a third contributing factor. As the organic layers are thin (due to limitations by L_D and hopping transport), a lot of light cannot be absorbed but transmits donor and acceptor. To a large extent, this portion is reflected at the Al back electrode. As a result, an optical interference effect (cavity effect) between incident and reflected light occurs due to a superposition of both beams.[219] With this in mind, the ideal active layer thicknesses can be simulated via the program SETFOS (Semiconducting Thin Film Optics Simulator). For such a simulation, one specific wavelength has to be chosen, which is usually the wavelength where the main absorber shows maximum absorption (e. g. DBP $\approx$ 610 nm). Then, thicknesses and complex refractive indices of each material within the device are inserted. On that basis, SETFOS calculates the intensity of the electric field at different positions within the OPVC. Now, the thickness of the acceptor can be adapted in such a way that the maximum of the electric field is located exactly at the D/A interface. By keeping in mind the exciton diffusion length as well, it could already be shown, that for C_{60} the optimal thickness is between 40 - 50 nm in combination with DIP.[220] Due to the similarities concerning their refractive indices, SETFOS yields almost identical results for OPVCs with DBP as donor material. As a result, in the following, the C_{60} acceptor layer is always chosen to be 45 nm thick. The thickness of the donor, however, does not influence the correlation between optical interference and position of the interface. The perfect thickness of the donor layer is thus mainly determined by the respective exciton diffusion length and by the transport abilities in general. As a result, donor layers of crystalline DIP can be chosen to be 50 nm, whereas layers of amorphous DBP have to be remarkably thinner. 20 nm layers have been proven to be ideal. These rather thin layers of DBP, however, are detrimental when being used as acceptor as they prevent a full exploitation of the cavity effect. Nevertheless, this is unavoidable as higher thicknesses would lead to a strong decrease in FF.

Based on these considerations, it follows that a comparison of DIP and DBP cells with identical layer thickness is not useful. Otherwise, the strong influence of the significantly different exciton diffusion lengths might obscure other decisive factors. For that reason, OPVCs with optimized active layer thicknesses for each material combination are investigated and compared with each other. At first, this is done for PHJ solar cells with C_{60} as acceptor. A comparison of the J-V-characteristics under illumination reveal that the assumptions made within the subsections 5.1.1 and 5.1.2 are accurate (Fig. 5.10). UPS measurements predicted identical values of V_{OC} for DIP and DBP in combination with C_{60}. This is true as both solar cells provide an open-circuit voltage of 0.91 V. Moreover, similar fill factors are assumed by measuring and comparing charge carrier mobilities and series resistances of DIP or DBP devices, respectively. Again, this can be confirmed as both solar cells yield a comparatively high FF of approximately 68 %. As already mentioned, for DIP in combination with C_{60} even higher fill factors of up to 74 % have already been demonstrated,[108] however, this requires very pure materials, as they were

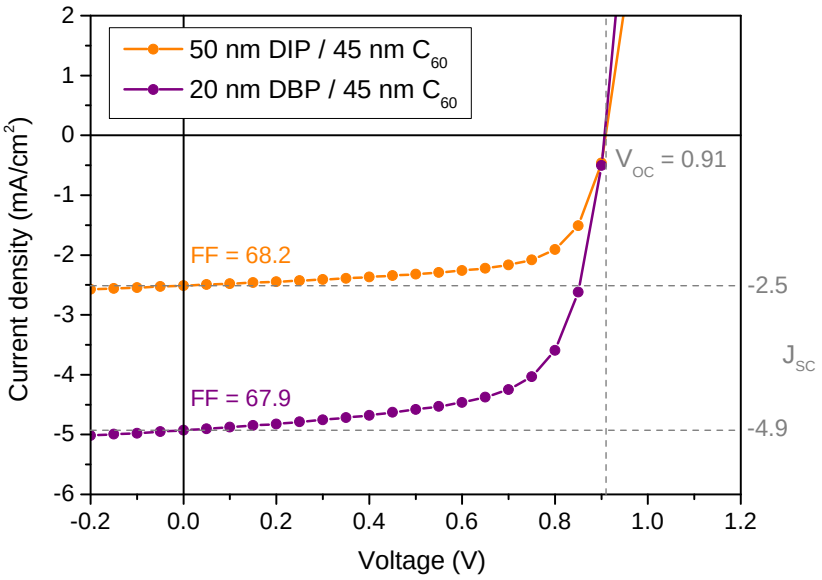

Figure 5.10: J-V-characteristics under illumination of PHJ solar cells with C_{60} as acceptor comparing the different donor materials DIP and DBP.

not available during the work on this thesis. Impurities within the DIP increase the probability of trap-assisted recombination, which leads to increasing ideality factors and thus decreasing fill factors.[21] Finally, reflectometry measurements revealed an absorption coefficient of DBP, which is more than six times larger than that of DIP, leading to the expectation of a significantly higher J_{SC} in DBP solar cells. J-V-measurements show that J_{SC} approximately doubles when DIP is replaced by DBP. That the enhancement of J_{SC} is not as great as the difference in absorption is due to several factors. First of all, light absorption is not equal to charge generation as generated excitons can recombine and thus do not contribute to the current. Moreover, the DIP layer is 50 nm thick and therefore 2.5 times thicker than the corresponding DBP layer. The compared absorption coefficients, however, are only representative for equal layer thicknesses. Another point is that the choice of the donor material also influences the absorption of the acceptor. It is likely that the C_{60} layer absorbs stronger in combination with DIP because DBP will absorb more of the light than DIP before it enters the C_{60} layer in an OPVC. This effect can be denoted as parasitic absorption. Summing up, due to equal or at least similar values of V_{OC} and FF, as well as a doubled J_{SC}, a replacement of DIP by DBP in a PHJ with C_{60} leads to almost a doubling of the power conversion efficiency from $\eta_{PCE} = 1.55\,\%$ to $\eta_{PCE} = 3.03\,\%$.

In a next step, a comparison of DIP and DBP with C_{60} as acceptor is done for PMHJ solar cells. Here, the exciton diffusion lengths are of less importance, as the PMHJ concept leads to a greatly enhanced D/A interface so that much more excitons are able to reach it. As a result, layer thicknesses can be chosen equal for DIP and DBP devices. However, another crucial parameter has to be considered, namely the phase separation

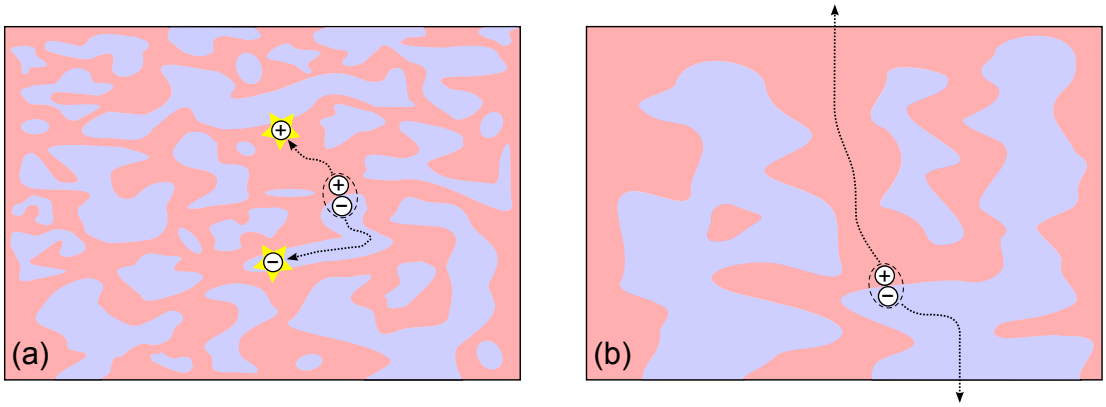

Figure 5.11: Idealized schematic illustration of the film morphology of co-evaporated donor-acceptor blends providing either bad (a) or good (b) phase separation.

within the blend. The decisive influence of well-separated donor and acceptor phases is visualized in Fig. 5.11. A more intimate mixing of the two materials leads to more recombination losses (indicated by the yellow stars in Fig. 5.11 (a)) and an aggravated charge carrier transport and thus entails reduced values of FF and J_{SC} compared to large-scale phase separation (Fig. 5.11 (b)) in corresponding OPVCs. Heating the substrate during co-evaporation is one possibility to improve the phase separation. This effect occurs equally for both material combinations, so that all blends are heated during evaporation. Another decisive factor is the choice of the mixing ratio. In the following, when mixing ratios are given, the first number always denotes DIP/DBP and the second number the fullerene. For DIP:C_{60} solar cells, it has already been shown, that an equal amount of donor and acceptor, i.e. a mixing ratio of 1:1, provides good results.[108] Furthermore, Theresa Linderl found out that for this blend a higher amount of DIP is more favorable than a higher amount of C_{60}, most likely because DIP is the more crystalline material within this blend. For DBP:C_{60} solar cells, however, it is the other way around. Here, C_{60} is the more crystalline material and so very poor performances are obtained for solar cells containing more DBP than C_{60} in the blend (Fig. 5.12 (a)). It shows up, that a mixing ratio of 1:2 provides a very good solar cell performance, which is in accordance with literature.[121] For this device, the expected differences compared to the PHJ can be observed (*cf.* Fig. 5.10): While J_{SC} is markedly enhanced, due to the drastically increased D/A interface, the FF and also V_{OC} are reduced. For the FF, this can be explained by enhanced recombination and additional transport problems. The enhanced recombination in PMHJ solar cells is also responsible for a slight decrease of V_{OC} (*cf.* Eq. (5.3)) from 0.91 V (PHJ) to 0.86 V (PMHJ, 1:1). However, for the 1:2 solar cell, V_{OC} is even further reduced to 0.81 V. This can probably be associated to shifting energy levels and a change of the effective work function of the anode. This assumption is supported by observations, which can be made when an additional blocking layer is inserted beneath the blend, leading again to a higher V_{OC} of 0.90 V (*cf.* subsection 5.2.3). Moreover, also literature indicates that correlation between V_{OC} and the buffer

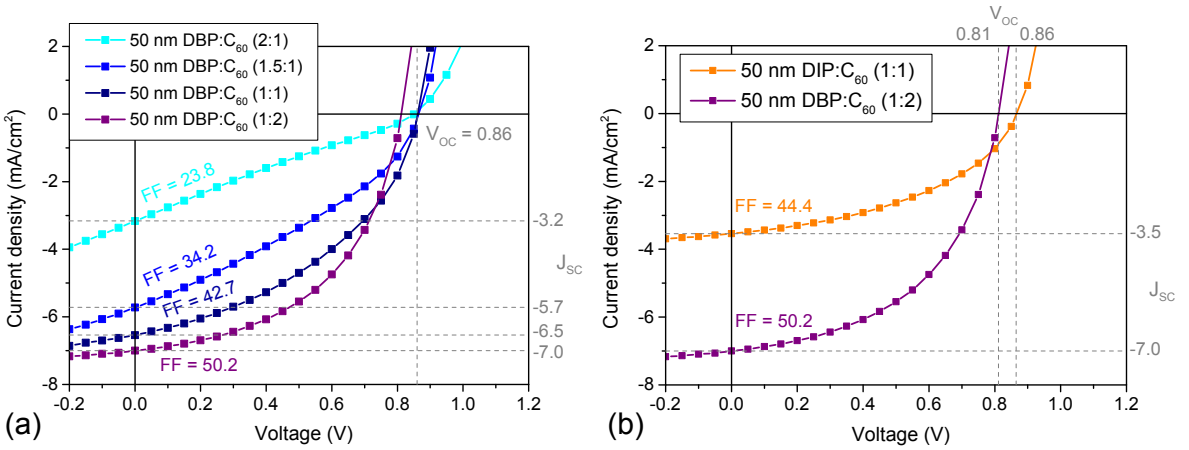

Figure 5.12: *J-V*-characteristics under illumination of PMHJ solar cells containing (a) different mixing ratios of the DBP:C_{60} blends and (b) either DIP:C_{60} or DBP:C_{60} blends. In general, all blends are sandwiched in between pure layers of 5 nm DBP and 10 nm C_{60}.

layer and thus the anode. When HIL1.3 is replaced by MoO_x, no losses in V_{OC} occur.[122] Nevertheless, by comparing DIP:C_{60} and DBP:C_{60} PMHJ solar cells, the same trends as for PHJ devices are obtained (Fig. 5.12 (b)), namely similar values for FF and V_{OC} but a doubling of the J_{SC} from 3.5 to 7.0 mA/cm^2. Consequently, also the efficiency more than doubles from $\eta_{PCE} = 1.34\,\%$ to $\eta_{PCE} = 2.85\,\%$. To sum up, the PMHJ devices confirm the expected trend but do not provide the desired efficiency enhancement compared to corresponding PHJ solar cells.

To exploit the benefits of the PMHJ architecture more efficiently, strong absorbing materials are necessary. Hence, an improvement can be expected by changing the acceptor from C_{60} to C_{70} as films of C_{70} provide an almost three times larger absorption coefficient than C_{60} films (*cf.* Fig. 3.2). Apart from that, both materials provide similar properties like energy level alignment and high electron mobilities. Thus, the expected improvement can be confirmed via *J-V*-characteristics shown in Fig. 5.13 (a). While there is again no big change visible for FF and V_{OC}, a drastic increase in J_{SC} occurs due to enhanced light absorption. This leads consequently to power conversion efficiencies of $\eta_{PCE} = 3.39\,\%$ for the DIP:C_{70} solar cell and $5.14\,\%$ for the DBP:C_{70} device. By comparing both OPVCs with each other, it is striking that the DBP containing solar cells once again yields less V_{OC}. Once more, this is attributed to shifting energy levels. To exclude recombination effects, the dark saturation currents j_0 of both OPVCs are compared, because j_0 is influenced by recombination and has direct influence on V_{OC} (*cf.* Eq. (2.12)). Its value can also be obtained by fitting the modified Shockley equation (Eq. (5.2)) to the dark current characteristics of the corresponding solar cell. For both OPVCs shown in Fig. 5.13 (a) the values of j_0 are in the same order of magnitude (10^{-9}), so that recombination seems not to be the reason for deviating V_{OC}s, but a changing effective work function of the anode. Unlike the previously shown OPVC comparisons, a doubling of J_{SC} and thus η_{PCE} does not occur for the C_{70} containing cells, however, the

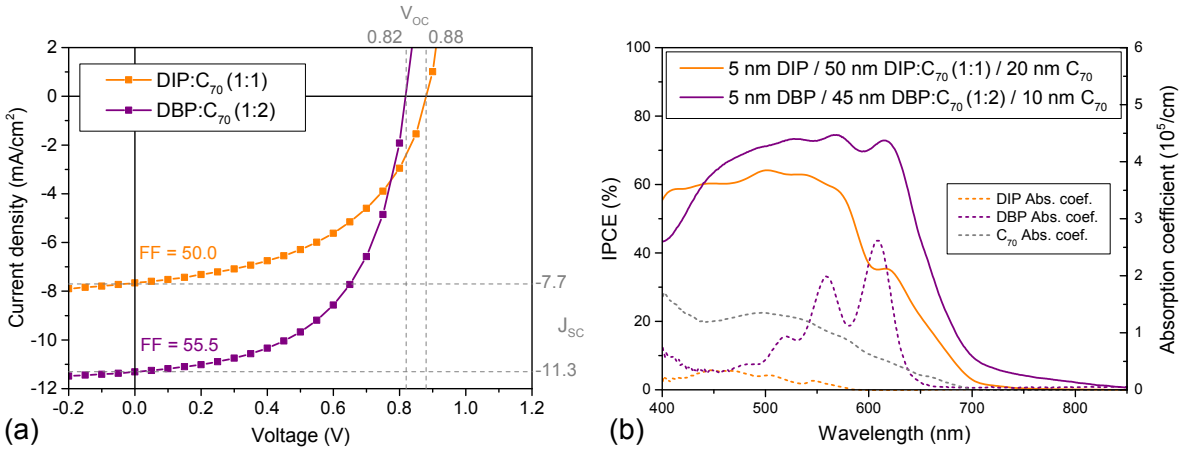

Figure 5.13: (a) J-V-characteristics under illumination of PMHJ solar cells with C_{70} as acceptor comparing the different donor materials DIP and DBP. (b) IPCE data of the respective OPVCs; additionally also the absorption characteristics of DIP, DBP and C_{70} films are given.

improvement still amounts to approximately 50 %. This deviation is ascribed to parasitic absorption between strongly absorbing DBP and C_{70}. The assumption is supported by IPCE measurements shown in Fig. 5.13 (b). The characteristic absorption peaks of DBP at $\lambda = 560\,\text{nm}$ and 610 nm are hardly visible anymore due to the comparatively strong absorption of C_{70} in the same region. The overlap of the absorption spectra of DBP and C_{70} is indicated by the dashed lines in Fig. 5.13 (b). Nevertheless, the IPCE spectrum reveals an impressively high conversion efficiency of almost 80 % over a very broad spectrum. This demonstrates the promising potential of this material combination.

Due to their ambipolar character and their suitable energy level alignment, both DIP and DBP can also be used as acceptor material. It has already been shown that such OPVCs can yield remarkably high V_{OC}s when connected to the donor 6T.[99,221] Once again, this can be confirmed via J-V-characteristics as both solar cells possess an V_{OC} of 1.22 V (Fig. 5.14). Also the other trends like a similar FF and an almost doubling of J_{SC} can be measured again. However, here the identical values of V_{OC} are surprising. As DIP and DBP are used as acceptor, their identical HOMO level alignment is not relevant anymore. The V_{OC} of the investigated solar cells is mainly determined by the HOMO level of 6T and the LUMO levels of DIP or DBP, respectively. However, the LUMO of DBP is reported to be $\approx 0.2\,\text{eV}$ lower than that of DIP (*cf.* Fig. 3.1). For that reason, a smaller V_{OC} would be expected for the DBP solar cell. A possible reason that this cannot be observed might be an energy level shift of DBP when evaporated on 6T. It is a well-known fact that the effective energy level alignment can vary when connected to other materials.[87,88] However, to verify this assumption, UPS measurements of DBP on 6T would be necessary. Another possible explanation might be given by different molecular coupling at the D/A interface due to different molecular structures. Such different structures can influence the electronic coupling between donor and acceptor

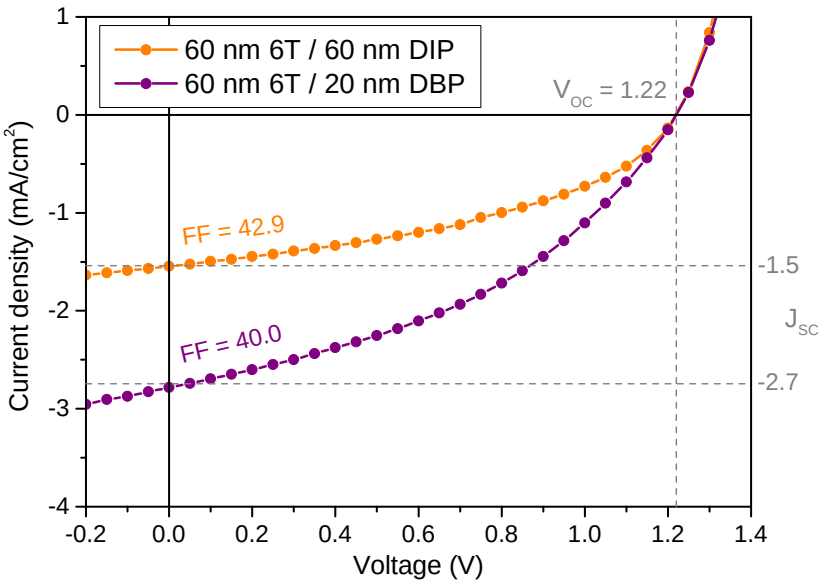

Figure 5.14: J-V-characteristics under illumination of PHJ solar cells with 6T as donor comparing DIP and DBP as different acceptor materials.

molecules, which in turn effects recombination and thus V_{OC}.[222] That this parameter actually plays a role will be shown in the following subsection 5.1.4.

In conclusion, a clear trend can be stated when comparing crystalline DIP and amorphous DBP concerning organic solar cell performance. This trend is visible for PHJ as well as for PMHJ devices and does also not depend on whether DIP/DBP are used as donor or as acceptor. For all investigated OPVCs, replacing DIP with DBP does not strongly influence FF and V_{OC}, but leads to a significant increase of J_{SC}. In most of the analyzed devices, J_{SC} can be even doubled. As a result, a corresponding increase of the power conversion efficiency is obtained as well.

5.1.4 Temperature and intensity dependent electrical characterization

Temperature and intensity dependent characterizations of organic solar cells provide a deeper insight into different processes occurring within the devices and can also be used to obtain some specific parameters of the investigated OPVCs. For example, a temperature dependent measurement of V_{OC} is a common method to determine the photovoltaic gap of a device.[59–61] This approach follows Eq. (2.14), which describes the correlation between V_{OC}, E_{PVG} and temperature. For that purpose, V_{OC} is measured at several temperatures. Then, an estimation of E_{PVG} is obtained by a linear extrapolation of the data towards 0 K. Moreover, Gruber *et al.* could show that the slope of this extrapolation is also a measure for the non-radiative recombination and/or the absorption strength of the CT state α_{CT} present within the solar cell.[65] Simulations showed that a decreasing

slope is indicative of either less non-radiative recombination or less CT absorption (or a combination of both). A decisive influence of α_{CT}, however, is expected only for very large values of α_{CT}, which are not assumed for the investigated material systems. Hence, in the following, a changed slope is ascribed to different recombination rates. In general, recombination is quantified by the recombination current j_0, which consists of thermodynamically unavoidable radiative recombination $j_{0,rad}$ and non-radiative recombination $j_{0,non}$:

$$j_0 = j_{0,rad} + j_{0,non} \ . \tag{5.3}$$

Comparing V_{OC} vs. temperature measurements of DIP and DBP containing solar cells yields, that the DBP cells always exhibit a smaller slope than the DIP devices (Fig. 5.15). This is the case for PHJ and PMHJ solar cells with C_{60} as acceptor as well as for PHJ devices with 6T as donor material. Most likely this can be attributed to different molecular electronic coupling at the D/A interface. Eq. (2.13) shows the direct dependency of the recombination current j_0 from the so-called coupling factor j_{00}. Hence, stronger coupling between donor and acceptor molecules leads to increased recombination. The main factor determining j_{00} is the mutual molecular orientation of donor and acceptor at the common interface. For example, parallel oriented molecules show stronger coupling than molecules which are perpendicular to each other.[223,224] However, this simplified approach is only reasonable for rod-shaped molecules like 6T and DIP. For DBP, there is another factor of even higher importance - steric hindrance. It has already been shown that steric hindrance of the involved molecules reduces electronic coupling between donor and acceptor and thus decreases recombination at the interface.[73,74,225] In the case of DBP, this steric hindrance arises from the four phenyl groups, which show a preferred orientation perpendicular to the perylene core and thus prevent an efficient

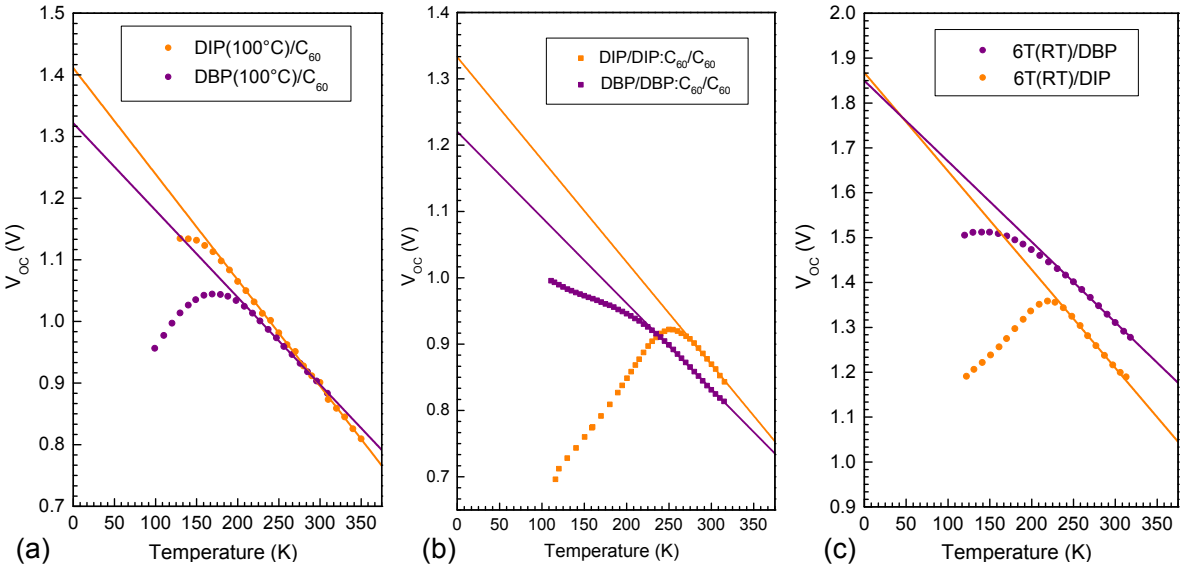

Figure 5.15: Comparison of DIP and DBP in corresponding OPVCs in terms of V_{OC} vs. temperature behavior: (a) PHJ with C_{60}, (b) PMHJ with C_{60}, and (c) PHJ with 6T.

intermolecular overlap at the D/A interface. As a consequence, less coupling leads to less recombination losses, which becomes visible by the smaller slopes of the DBP solar cells in Fig. 5.15.

In the following, temperature and intensity dependent electrical characterization measurements of DBP-C_{60} solar cells (both PHJ and PMHJ) are analyzed in detail. The approach is adopted from Ulrich Hörmann, who did the same for DIP devices in the scope of his PhD thesis.[187] That way, the obtained results of the DBP solar cells can be compared with the literature values of DIP. First of all, temperature dependent *J-V*-measurements are performed on an OPVC with a photoactive layer consisting of 20 nm DBP and 45 nm C_{60}. The results received under illumination are depicted in Fig. 5.16 (a). It is striking that the value of J_{SC} at room temperature is higher compared to previously shown results (*cf.* Fig. 5.10). This can be easily explained by different illumination intensities. While the *J-V*-curves in subsection 5.1.3 are measured with a solar simulator using a calibrated AM1.5 G spectrum, here an LED with higher illumination intensity ($\approx$ 1.9 suns) is applied leading to correspondingly larger currents. Moreover, for decreasing temperatures a growing s-shape behavior around V_{OC} can be observed. This is a common phenomenon and can usually be attributed to two factors.[77] On the one hand, there are growing injection barriers for charge carriers at the interface to cathode and anode, respectively. On the other hand, hopping transport in organic semiconductors is temperature dependent,[226] so that decreasing temperatures lead to a reduced charge carrier mobility (Eq. (2.1)). For the sake of completeness also the corresponding IPCE-curves as well as the absorption coefficients of DBP and C_{60} are shown in Fig. 5.16 (c). It can be seen that decreasing temperatures lead to similar losses within the DBP and the C_{60} dominated part of the spectrum.

Of more importance are the dark current characteristics depicted in Fig. 5.16 (b). As it has already been described in the previous subsections, the exponential part of the forward-bias characteristics can be fitted using the modified Shockley equation (Eq. (5.2)) to obtain the temperature dependence of the recombination current j_0 and the ideality factor n. The fits are described by the solid lines within that plot, while the measurement values are shown by colored dots, each color representing a measurement at one distinct temperature. The acquired values of j_0 and n are presented in Fig. 5.16 (d). In the following, values of n which are determined by means of *J-V*-measurements without illumination are labelled as dark ideality factors n_{dark}. At room temperature, a comparatively high value of $n_{dark} = 2.11$ is obtained, which is significantly larger than $n = 1$, assumed for an ideal PHJ organic solar cell showing only Langevin type direct recombination of free electrons and holes.[227] Moreover, the obtained results indicate that n_{dark} even increases for decreasing temperatures. However, it is a common assumption that such a temperature dependency of n does not really exist. This behaviour can rather be ascribed to a growing influence of R_P and thus is denoted as an artifact.[187] The roughly linear decrease of j_0 until T $\approx$ 200 K within this semilogarithmic plot, however,

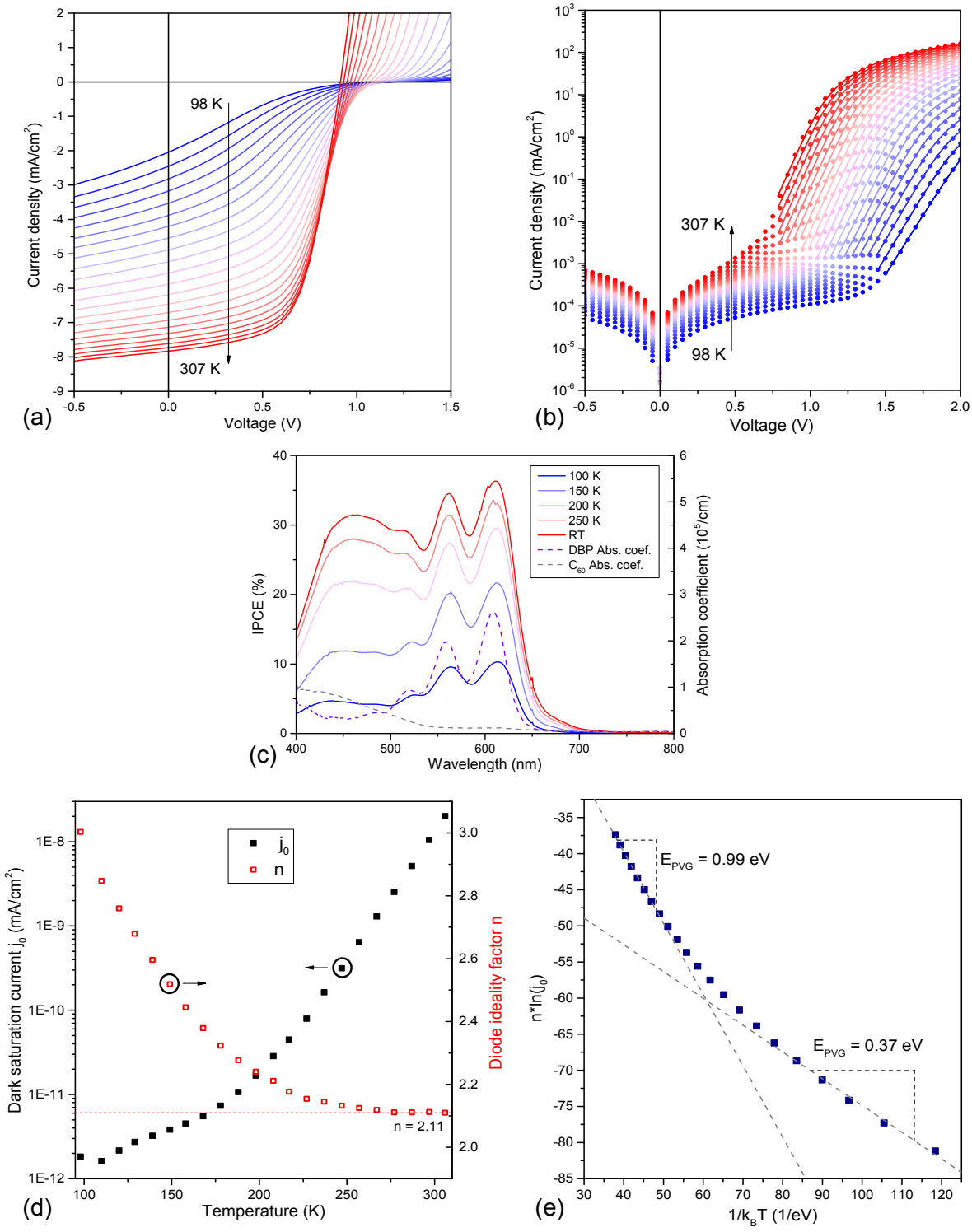

Figure 5.16: Temperature dependent J-V-characteristics under illumination (a) and in dark (b) of a solar cell with the architecture: ITO (140 nm)/HIL1.3 (45 nm)/DBP (20 nm)/C_{60} (45 nm)/BCP (5 nm)/Al (100 nm). The corresponding temperature dependent IPCE results are shown in (c). The values of j_0 and n derived from Shockley fits to the dark characteristics are plotted against temperature in (d). Finally, (e) shows the product $n \cdot \ln(j_0)$ versus $1/k_\mathrm{B}T$ to obtain a value for the photovoltaic gap E_PVG.

can be described by the relation

$$n \ln(j_0) \propto \frac{-E_{\mathrm{PVG}}}{k_{\mathrm{B}}T} \tag{5.4}$$

derived from Eq. (2.13) by adding the ideality factor n. This equation (5.4) can now also be used to obtain a value of E_{PVG} of the investigated solar cell by extracting the slope of $n \cdot \ln(j_0)$ plotted against $1/k_{\mathrm{B}}T$ (Fig. 5.16 (e)). With this method, two different values for E_{PVG} appear, one above and one below the so-called transition temperature.[187] However, both values are considerably lower compared to the first estimation, which was made by the V_{OC} vs. T measurement (*cf.* Fig. 5.15 (a)). Consequently, doubts arise concerning the correctness of the values of n and j_0 obtained by fits to the dark current characteristics. The problem concerning this type of data evaluation is the disturbing influence of parasitic resistances, especially for high currents and deep temperatures. Furthermore, the exponential current regime used for the Shockley fit is rather narrow and becomes even smaller for low temperatures. Therefore, a distinct separation of the series resistance R_{S} and the ideality factor n is almost impossible, which influences the fit and makes it prone to error.

For that reason, further measurements are performed under illumination of the OPVC. Here, V_{OC} and J_{SC} are measured for different temperatures and light intensities. In contrast to the recording of complete J-V-curves, this kind of measurement is faster and prevents unnecessary stress for the investigated solar cell, avoiding an undesirable degradation of the device during the experiment. Furthermore, measurements under short-circuit or open-circuit conditions have the additional benefit that negative impacts of both R_{S} and R_{P} are almost negligible (*cf.* Eq. (2.12)). Especially R_{S} is not able to affect V_{OC} since no current flows here. Moreover, only very small parallel resistances ($R_{\mathrm{P}} < 10^{-3}\,\Omega\,\mathrm{cm}^2$) have a slight negative impact on V_{OC}. For J_{SC} it is just the other way around. While R_{P} does not influence J_{SC}, only very high series resistances ($R_{\mathrm{S}} > 50\,\Omega\,\mathrm{cm}^2$) reduce its value (*cf.* Fig. 2.9). However, for this material combination such high series resistance can be excluded due to the first (rough) results obtained by dark-current characteristics, at least for temperatures above 150 K (Fig. 5.8 (a)). As well, no such small parallel resistances are expected, as high leakage currents would have a strong negative impact on FF, which cannot be observed.

The results of these measurement under illumination are depicted in Fig. 5.17. First of all, the received values of V_{OC} for different temperatures and light intensities are plotted in combination with linear extrapolations of the obtained data towards 0 K to estimate E_{PVG} (Fig. 5.17 (a)). However, these extrapolations do not provide one single value of the photovoltaic gap. Its value rather decreases monotonically with reduced illumination intensity. This is in contrast to results, which have been reported for DIP/C_{60} solar cells.[61] In general, there should be no connection between E_{PVG} and light intensity. However, such a deviant behavior has already been observed for other material combinations and is ascribed to structural disorder,[187] which is given in the present case by the amorphous character of DBP. Nevertheless, the linear extrapolations can easily

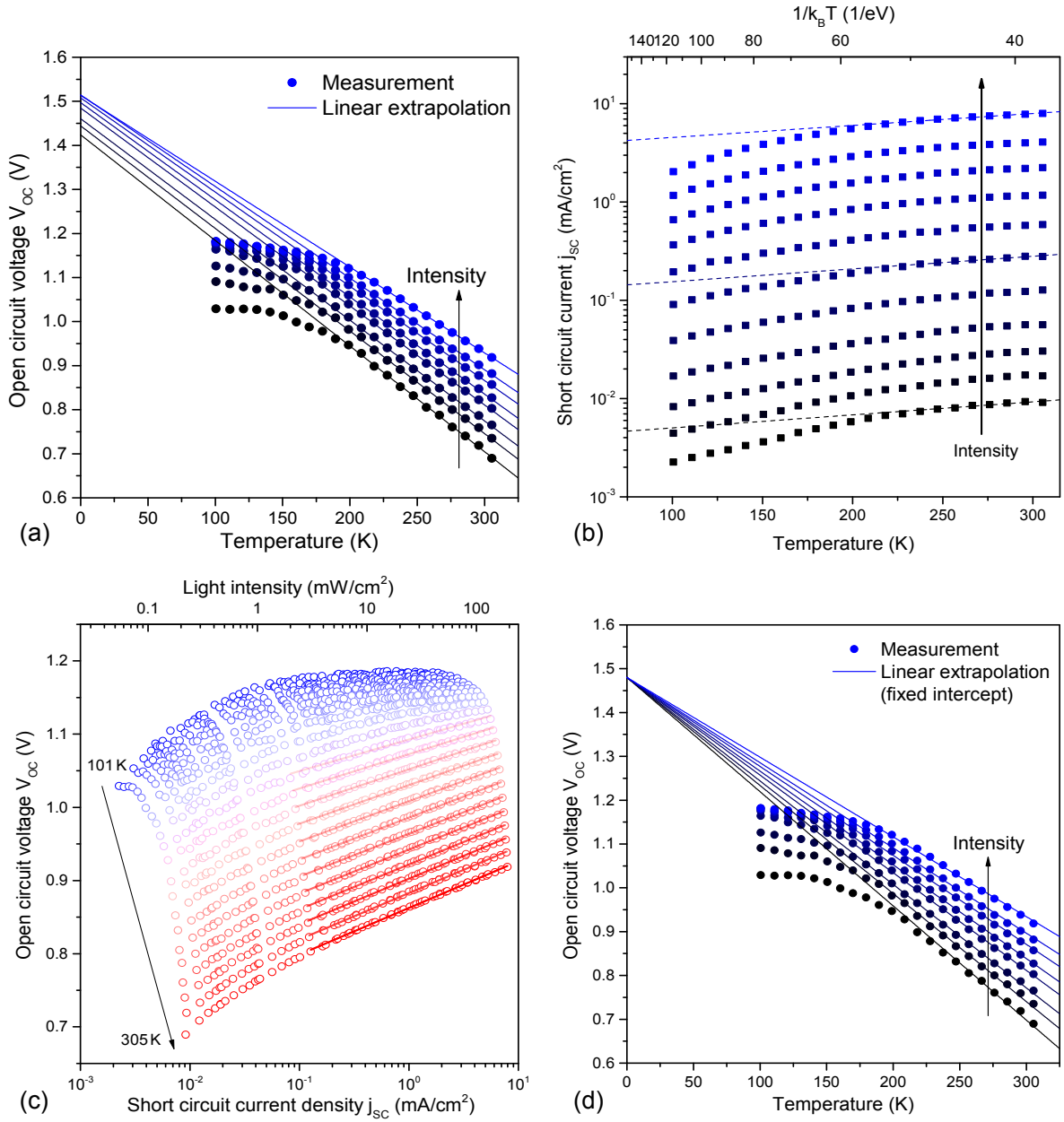

Figure 5.17: Temperature and intensity dependent measurements of V_{OC} and J_{SC} of a solar cell consisting of ITO (140 nm)/HIL1.3 (45 nm)/DBP (20 nm)/C_{60} (45 nm)/BCP (5 nm)/Al (100 nm). Different temperatures are enabled by a liquid nitrogen cryostat, while a white LED serves as light source and provides a total of 66 different light intensities between 1.9 and 2.3 $\times 10^{-3}$ suns. The results of V_{OC} vs. T and J_{SC} vs. T measurements for different illumination intensities are shown in (a) and (b), respectively. The summarized values of V_{OC} and J_{SC} at different temperatures are shown in (c). The solid lines are fits with Eq. (5.5) yielding n_{light} and j_0 shown in Fig. 5.18 (a). As shown in (d), the extrapolations of the temperature dependent V_{OC} values for different illumination intensities can be forced to end at one distinct photovoltaic gap energy, yielding good results except for the lowest illumination intensity. For reasons of clarity some measured data sets are omitted within (a), (b) and (d).

be forced to one single value of $E_{PVG} = 1.48\,eV$ at 0 K (Fig. 5.17 (d)). Moreover, also the values of J_{SC} at different light intensities can be plotted against temperature in a semilogarithmic presentation (Fig. 5.17 (b)). In the high temperature range above 200 K and for all illumination intensities, there is an almost linear decrease of J_{SC} (indicated by the dashed lines) with decreasing temperatures following a $\ln(J_{SC}) \propto -1/k_B T$ behavior. This can be most likely ascribed to a hampered hopping transport as the charge carrier mobility in organic semiconductors shows the same temperature dependence (Eq. (2.1)).

In the next step, the measured temperature and intensity dependent values of V_{OC} and J_{SC} are plotted against each other for different temperatures between 101 K and 305 K (Fig. 5.17 (c)). In this way, one obtains a pair of V_{OC} and J_{SC} for every measured temperature and intensity. The direct correlation between these two parameters can be described following Eq. (2.12) by:

$$V_{OC} = \frac{n k_B T}{e} \ln\left(\frac{J_{SC}}{j_0}\right) \tag{5.5}$$

This equation can now be used to fit the data in the linear regime at high illumination intensities. The fits are depicted in Fig. 5.17 (c) by the solid lines. However, below 200 K the fits do not converge, so that an evaluation is not possible in the low temperature range. For all other data sets one obtains the light ideality factor n_{light} and the recombination current j_0. In contrast to the dark current analysis, these fits are not influenced by the series resistance. For that reason, the results shown in Fig. 5.18 (a), are expected to be more precise. It is striking, that the values of n_{light} vary in a small range between 1.05 and 1.17 and thus are by far lower and show less temperature dependence than the comparable n_{dark} values, which were determined previously. This is in considerably better agreement with the common assumption of an PHJ ideality factor close to unity not showing any temperature dependence. Furthermore, also the values of the recombination current are significantly smaller than the values from the dark current characterization, although the curve characteristics are similar.

In Fig. 5.18 (b), a photovoltaic gap of 1.53 eV for the DBP/C_{60} PHJ solar cell is determined using Eq. (5.4) and the values of n_{light} and j_0. In contrast to Fig. 5.16 (e), derived from dark current analysis, the slope is completely linear over the whole temperature range, probably due to the fact that only temperatures above 200 K are considered. The value of 1.53 eV is in very good accordance to the previously found E_{PVG} determined by V_{OC} vs. T measurements, especially for high illumination intensities. For that reason, it can be stated that the values of n and j_0 obtained by measurements under open-circuit or short-circuit conditions are more reliable than comparable results from dark-current analysis. For DIP/C_{60} solar cells, a discrepancy between $n_{dark} = 1.56$ and $n_{light} = 1.26$ was found as well.[187] The generally higher value of n_{dark} is explained by trap states, which become deactivated under illumination. In dark current measurements these traps serve as recombination centres and thus enhance the ideality factor.[67,226] By comparing the DBP and the DIP device, it is striking that the difference of n_{dark} and n_{light} is clearly

more pronounced for the DBP solar cell. This is attributed to the amorphous character of DBP, which leads to a higher trap density compared to crystalline DIP.[228]

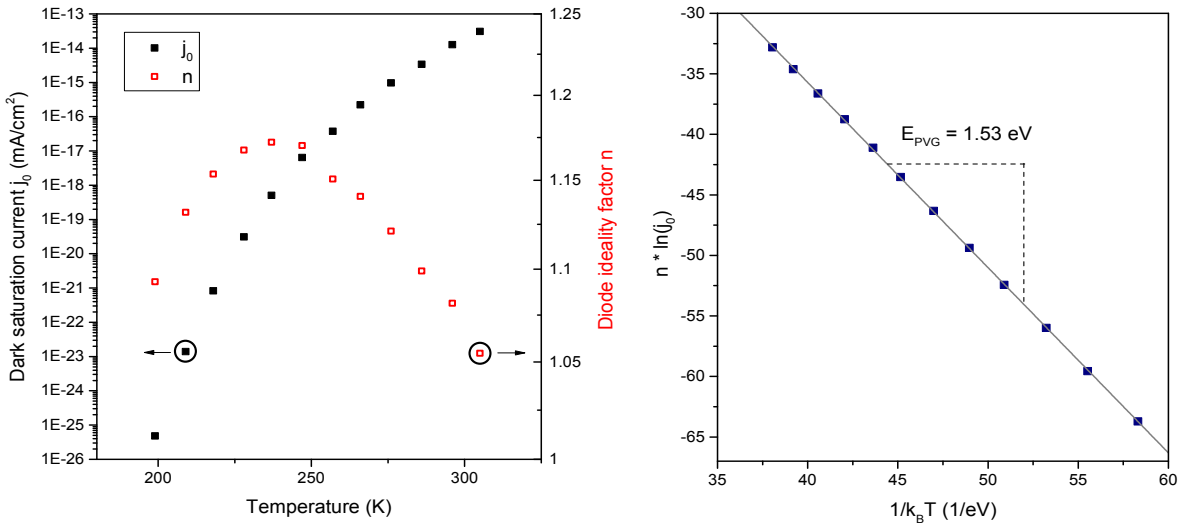

Figure 5.18: (a) Dark saturation current j_0 and diode ideality factor n_{light} plotted against temperature obtained by fits to the high intensity part of the V_{OC} vs. J_{SC} diagram shown in Fig. 5.17 (c). The slope of the $n \cdot \ln(j_0)$ vs. $1/k_{\text{B}}T$ diagram in (b) provides a photovoltaic gap of 1.53 eV for the DBP/C_{60} solar cell.

It has already been mentioned that organic solar cells have an ideality factor of $n = 1$ when Langevin type recombination is the dominant exciton recombination mechanism. Higher values of n, however, are related to additional trap assisted recombination (Shockley-Read-Hall (SRH) recombination[229,230]). Conversely, this means that the deviation of $n = 1$ can be taken as a measure of the trap assisted recombination rate. For such an interpretation the value of n_{light} has to be used, because n_{dark} is strongly influenced by trap states, which do not emerge under normal operation conditions ($T \approx$ RT and illumination intensity $I \approx 1\,\text{sun}$) and thus can be neglected.[67,226] However, also n_{light} contains some inaccuracies. It has been shown in literature, that the determined ideality factors have to be considered as average values over a broad voltage range.[231] For that reason, it is reasonable to determine n differentially. This is possible for both n_{dark} as well as for n_{light}. By means of the Shockley equation, the differential dark ideality factor can be calculated via:

$$n_{\text{dark,diff}} = \frac{e}{k_{\text{B}}T} \frac{\partial V}{\partial \ln(J)} \,. \tag{5.6}$$

The differential light ideality factor, however, can be obtained using Eq. (5.5):

$$n_{\text{light,diff}} = \frac{e}{k_{\text{B}}T} \frac{\partial V_{\text{OC}}}{\partial \ln(J_{\text{SC}})} \tag{5.7}$$

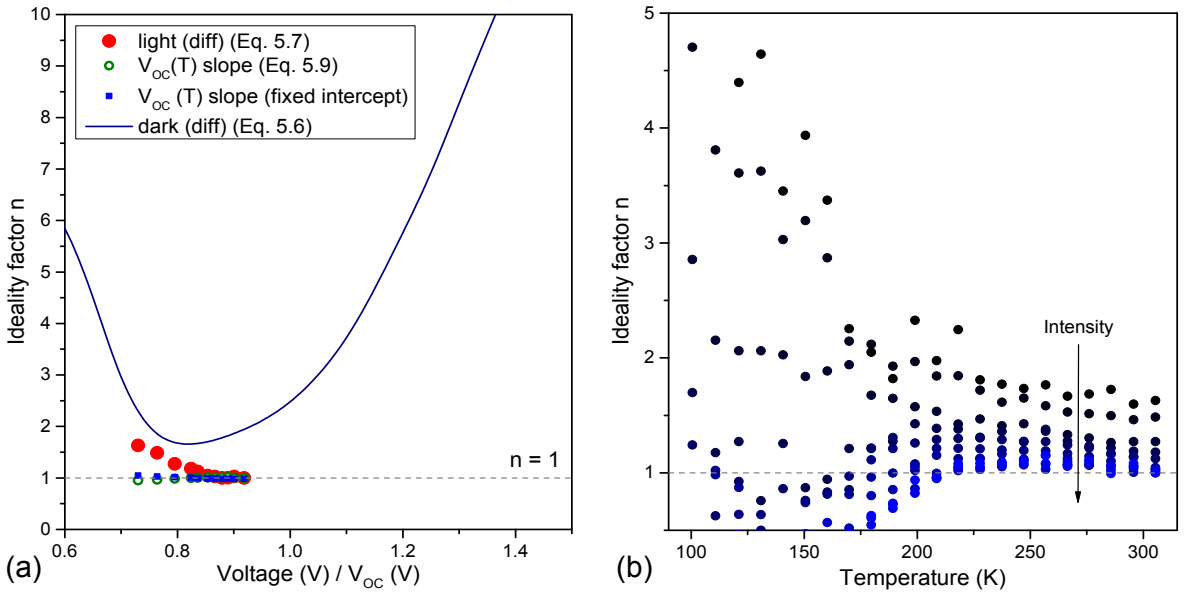

Figure 5.19: (a) Ideality factors determined in different ways are plotted against (open circuit) voltage. Except $n_{\mathrm{dark,diff}}$, all ideality factors almost perfectly approach unity around V_{OC}. (b) Increasing illumination intensities lead to a decreasing differential light ideality factor indicating efficient light induced detrapping under illumination.

These differentially determined ideality factors for the highest measured temperature are plotted against (open-circuit) voltage in Fig. 5.19 (a). Once again, the values of $n_{\mathrm{light,diff}}$ are significantly below that of $n_{\mathrm{dark,diff}}$. Around V_{OC}, where $n_{\mathrm{dark,diff}} = 1.68$ and the difference to $n_{\mathrm{light,diff}} = 1.0$ is smallest this is mainly due to light induced detrapping. For higher or lower voltages, however, the differences between $n_{\mathrm{light,diff}}$ and $n_{\mathrm{dark,diff}}$ are more pronounced. This can be attributed to the increasing impact of parasitic resistances for n_{dark} (R_{P} at low voltages, R_{S} at high voltages). Consequently, of all ideality factors shown in Fig. 5.19 (a), $n_{\mathrm{dark,diff}}$ contains the most inaccuracies and thus is the least appropriate parameter to draw conclusions on the recombination mechanisms in the solar cell. This can be done more reliable by $n_{\mathrm{light,diff}}$ which is unity around V_{OC}. Similar results are obtained for DIP/C_{60} solar cells exhibiting $n_{\mathrm{light,diff}} = 1.06$.[187] Consequently, this leads to the assumption that within DBP/C_{60} (and also DIP/C_{60}) PHJ solar cells under illumination, Langevin type recombination is the dominant loss channel, while almost no current is lost due to trap-assisted recombination. Indeed, it could be shown by dark current analysis, that DBP thin films contain many traps in consequence of structural disorder, however, the obtained results indicate that these traps are rather shallow. Such shallow traps feature trapping energies of the order of $k_{\mathrm{B}}T$, so that complete detrapping is possible either thermally or due to illumination (or by a combination of both).

To verify the accuracy of the $n_{\mathrm{light,diff}}$ values, another method is applied. For that purpose, the temperature dependent values of V_{OC} are once again taken into account

(Fig. 5.17 (a)). Using Eq. (2.14), the slope of the measured data can be determined by:

$$m = \frac{\mathrm{d}V_{\mathrm{OC}}}{\mathrm{d}T} = -\frac{nk_{\mathrm{B}}}{e} \ln\left(\frac{j_{00}}{J_{\mathrm{SC}}}\right) \ . \tag{5.8}$$

From that, another light ideality factor can be obtained via:

$$n = \frac{em}{k_{\mathrm{B}}(\ln J_{\mathrm{SC}} - \ln j_{00})} \ . \tag{5.9}$$

The values of n calculated via Eq. (5.9) are shown in Fig. 5.19 (a) as green open circles. Moreover, the same is done for the V_{OC} vs. T measurement with fixed intercept (Fig. 5.17 (d)). These values are depicted as blue squares in Fig. 5.19 (a). It is striking, that all values of n calculated via Eq. (5.9) come very close to unity over the whole voltage range. Consequently, there is hardly any difference between these two representations for this material combination. In addition, these values are also in very good agreement with the values of $n_{\mathrm{light,diff}}$ and thus confirm the validity of the previously obtained results.

Finally, the temperature and intensity dependent behavior of $n_{\mathrm{light,diff}}$ is depicted in Fig. 5.19 (b). It can be seen, that the ideality factor remains approximately constant for each measured intensity in the high temperature range above 200 K. For $T < 200\,\mathrm{K}$, however, strong deviations of this behavior can be observed, which do not allow any reasonable interpretation. This can be explained by the missing linear dependence between V_{OC} and J_{SC} for low temperatures as it has already been observed within Fig. 5.17 (c). Ideality factors with values smaller than unity can thus most likely be explained as an artifact. Another possible explanation might be an increase of so-called Auger recombination.[68] The fact that the ideality factor increases with decreasing illumination intensity supports the previously made conclusion of light induced detrapping within the device. While there is hardly any SRH recombination at normal operating conditions, the reduced light intensity leads to less efficient detrapping within the photoactive layers and thus an increasing ideality factor.

To summarize it can be stated, that the differentially determined light ideality factor $n_{\mathrm{light,diff}}$ is well suited to provide statements concerning the recombination mechanisms occurring in an organic solar cell. Dark ideality factors, however, are prone to error and thus less appropriate. With this in mind, it can be concluded that both DBP/C_{60} as well as DIP/C_{60} PHJ solar cells are dominated by Langevin type recombination, while almost no trap-assisted recombination occurs under normal operation conditions.

In a next step, the identical evaluation method is applied to DBP:C_{60} PMHJ solar cells. At first, J-V-characteristics under illumination and in dark as well as IPCE-curves are recorded. The corresponding data is depicted in Fig. 5.20 (a), (b) and (c), respectively. As expected, compared to the PHJ solar cell, higher values of J_{SC} and IPCE are obtained. Apart from that, no further remarkable differences occur. The previously found

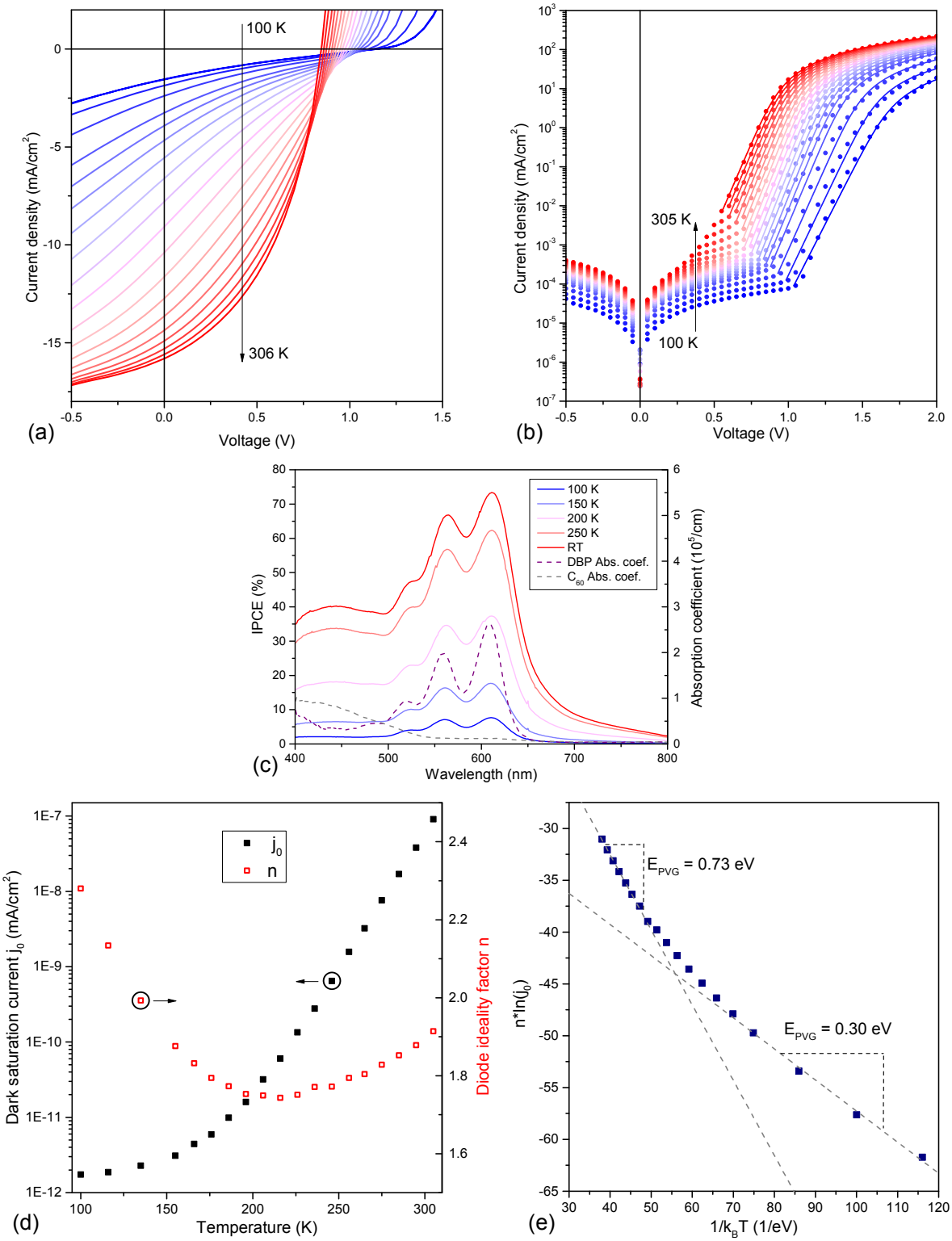

Figure 5.20: Temperature dependent J-V-characteristics under illumination (a) and in dark (b) of a solar cell with the architecture: ITO (140 nm)/HIL1.3 (45 nm)/DBP (5 nm)/DBP:C_{60} (50 nm, 1:2)/C_{60} (10 nm)/BCP (5 nm)/Al (100 nm). The corresponding temperature dependent IPCE results are shown in (c). The values of j_0 and n derived from Shockley fits to the dark characteristics are plotted against temperature in (d). Finally, (e) shows the product $n \cdot \ln(j_0)$ versus $1/k_\mathrm{B}T$ to obtain a value for the photovoltaic gap E_PVG.

weaknesses of the dark current analysis are checked once again. For that purpose, the exponential part of the dark *J*-*V*-curves is fitted by the modified Shockley equation to receive n_{dark} and j_0. The results are shown in Fig. 5.20 (d). n_{dark} exhibits a strong temperature dependence with a minimum of 1.75 around 200 K, which is lower than the comparable value of the PHJ solar cell. On the one hand, this is counter-intuitively as PMHJ devices are usually expected to show greater structural disorder and thus also more trap-assisted recombination. On the other hand, this reveals the same tendency like the previously shown result of R_{S}, which was also found to be smaller for the PMHJ than for the PHJ solar cell (subsection 5.1.2). Hence, this is another evidence of the effective phase separation within co-evaporated films of DBP and C_{60}. Apart from that, the values of the recombination current j_0 are very similar for PHJ and PMHJ solar cells. However, doubts concerning the accuracy of the obtained values of n_{dark} and j_0 arise once again by plotting $n \cdot \ln(j_0)$ against $1/k_{\mathrm{B}}T$ (Fig. 5.20 (e)), yielding two different photovoltaic gaps, which are obviously too small.

As a consequence, measurements under illumination are required once more to obtain reliable results regarding the prevalent recombination mechanism within the PMHJ solar cell. To start with, V_{OC} vs. T measurements are executed (Fig. 5.21 (a)). It is striking, that for that solar cell architecture hardly any deviations of $E_{\mathrm{PVG}} = 1.31\,\mathrm{eV}$ occur for different illumination intensities. Hence, almost identical results are received when the linear extrapolations are all forced to end at this single value (Fig. 5.21 (d)). As deviations of E_{PVG} for different intensities are usually ascribed to structural disorder,[187] this is a further hint of the well-ordered structure within this DBP:C_{60} (1:2) blend. Furthermore, this value is remarkably smaller than that of the DBP/C_{60} PHJ solar cell. This is another evidence of shifted energy levels for DBP:C_{60} (1:2) PMHJ devices as it has already been assumed within subsection 5.1.3 due to decreasing values of V_{OC}. A comparable behavior could not be observed for DIP PHJ and PMHJ solar cells.[187]

Surprisingly, no linear dependence between J_{SC} and temperature can be observed (Fig. 5.21 (b)), especially for high temperatures around $T = 300\,\mathrm{K}$. Such a behavior could not be found for any other investigated material combination, neither by U. Hörmann,[187] nor within this thesis (*cf.* also section 5.4). Thus, it can be assumed that the hopping transport in the DBP:C_{60} film presents the particular feature that it is not solely affected by temperature itself. Subsequently, to determine n_{light} and j_0, V_{OC} is again plotted versus J_{SC} and then fitted in the high intensity range with Eq. (5.5). The obtained data is shown in Fig. 5.22 (b). The ideality factor shows only weak temperature dependence and oscillates around 1.4. However, this behavior follows no particular trend and can be seen as evidence for the already mentioned consideration of average n values over a broad voltage range, requiring a differential determination of the ideality factor to obtain more reliable results.[231] Nevertheless, at least the determined combination of n and j_0 seems to be very accurate. By plotting $n \cdot \ln(j_0)$ against $1/k_{\mathrm{B}}T$ a photovoltaic gap of $E_{\mathrm{PVG}} = 1.32\,\mathrm{eV}$ can be identified (Fig. 5.22 (b)), which is in almost perfect accordance to the obtained result of the V_{OC} vs. T measurements (Fig. 5.21 (a)).

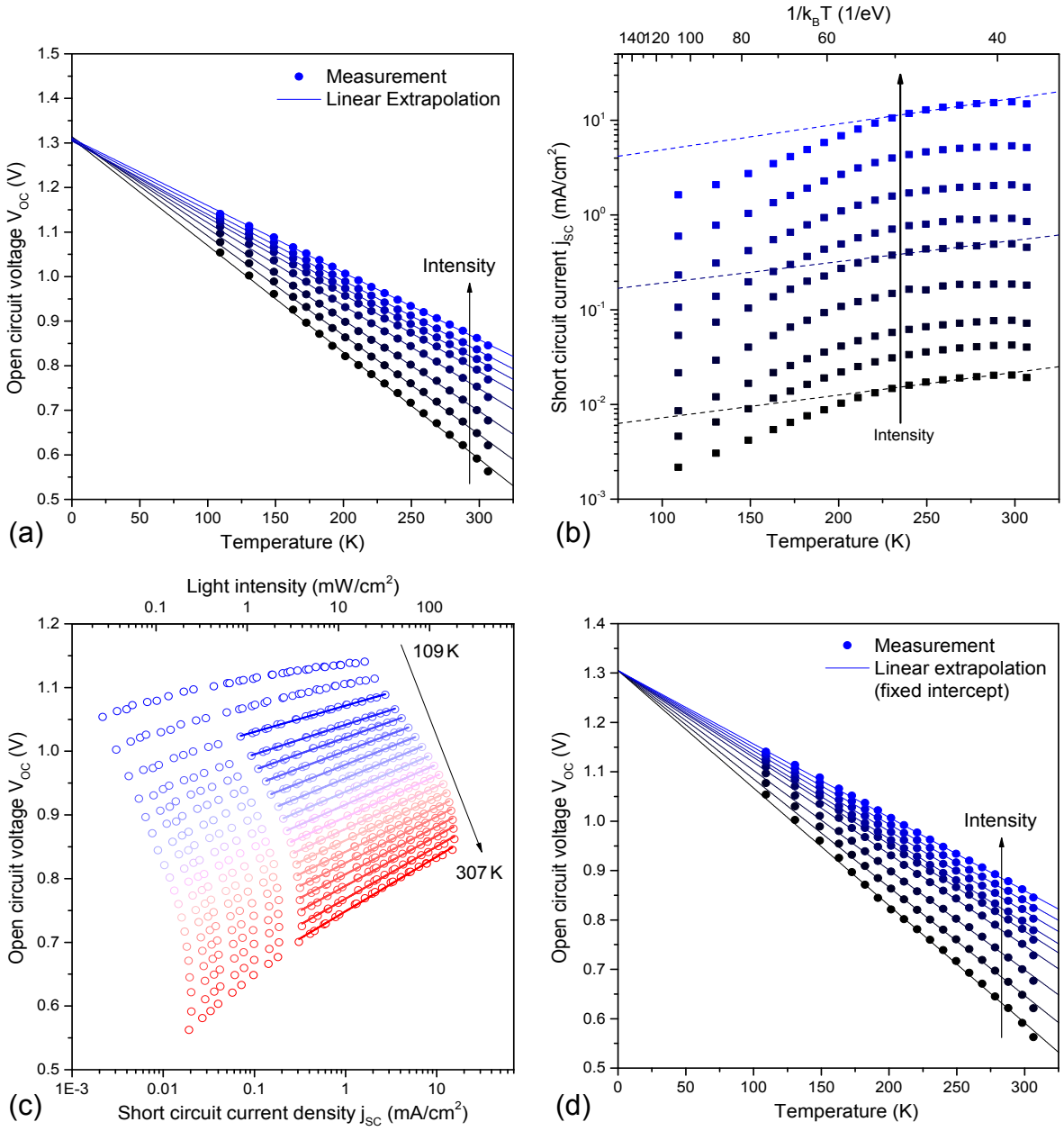

Figure 5.21: Temperature and intensity dependent measurements of V_{OC} and J_{SC} of a solar cell consisting of ITO (140 nm)/HIL1.3 (45 nm)/DBP (5 nm)/DBP:C_{60} (50 nm, 1:2)/C_{60} (10 nm)/BCP (5 nm)/Al (100 nm). Different temperatures are enabled by a liquid nitrogen cryostat, while a white LED serves as light source and provides a total of 33 different light intensities between 1.8 and 2.3 $\times 10^{-3}$ suns. The results of V_{OC} vs. T and J_{SC} vs. T measurements for different illumination intensities are shown in (a) and (b), respectively. The summarized values of V_{OC} and J_{SC} at different temperatures are shown in (c). The solid lines are fits with Eq. (5.5) yielding n_{light} and j_0 shown in Fig. 5.22 (a). As shown in (d), the extrapolations of the temperature dependent V_{OC} values for different illumination intensities can be easily forced to end at one distinct photovoltaic gap energy. For reasons of clarity some measured data sets are omitted within (a), (b) and (d).

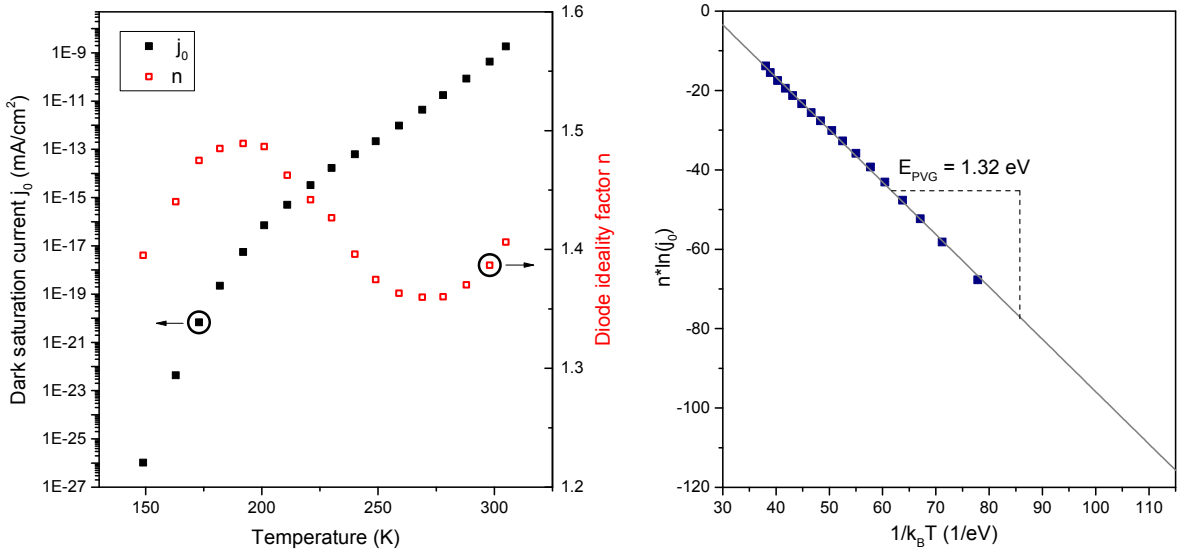

Figure 5.22: (a) Dark saturation current j_0 and diode ideality factor n_{light} plotted against temperature obtained by fits to the high intensity part of the V_{OC} vs. J_{SC} diagram shown in Fig. 5.21 (c). The slope of the $n \cdot \ln(j_0)$ vs. $1/k_{\mathrm{B}}T$ diagram in (b) provides a photovoltaic gap of 1.32 eV for the DBP/C_{60} solar cell.

Finally, n_{dark} and n_{light} are determined differentially and then compared to the results obtained from the slopes of the V_{OC} vs. T measurements with free and with fixed intercept (Fig. 5.23 (a)). As expected from Fig. 5.21 (a) and (d), there are almost no differences between the two ideality factors determined by the slopes of the V_{OC} vs. T measurements. Moreover, for the highest measured voltage around V_{OC} all light ideality factors are identical with $n = 1.16$. Compared to other PMHJ devices, this value of $n_{\mathrm{light}} = 1.16$ is very low. For example, for a DIP:C60 PMHJ cell a value of $n_{\mathrm{light}} = 1.62$ was found.[187] Only for smaller voltages, the differential light ideality factor approaches the differential dark ideality factor, which shows a minimal value of $n_{\mathrm{dark,diff}} = 1.87$. This comes close to the expected value of $n = 2$ for solar cells with fully trap-assisted recombination.[67] However, the light ideality factors indicate that there is indeed more pronounced SRH recombination within the PMHJ compared to the PHJ solar cell, nevertheless Langevin type recombination still seems to be the dominant loss channel. That is not usual for PMHJ solar cells and is another evidence for the comparatively high structural order within the blend. In a last step, n_{light} is plotted against temperature for different light intensities (Fig. 5.23 (b)). The data confirm that there is hardly no temperature dependence of the determined ideality factors for all investigated illumination intensities.

To conclude, the obtained values for PHJ and PMHJ DBP-C_{60} solar cells of E_{PVG}, j_0 and n are summarized in Tab. 5.3 and compared to the corresponding parameters of devices with DIP instead of DBP, taken from literature.[187] Most striking is the reduced E_{PVG} of the DBP:C_{60} solar cell, indicating shifting energy levels and explaining the re-

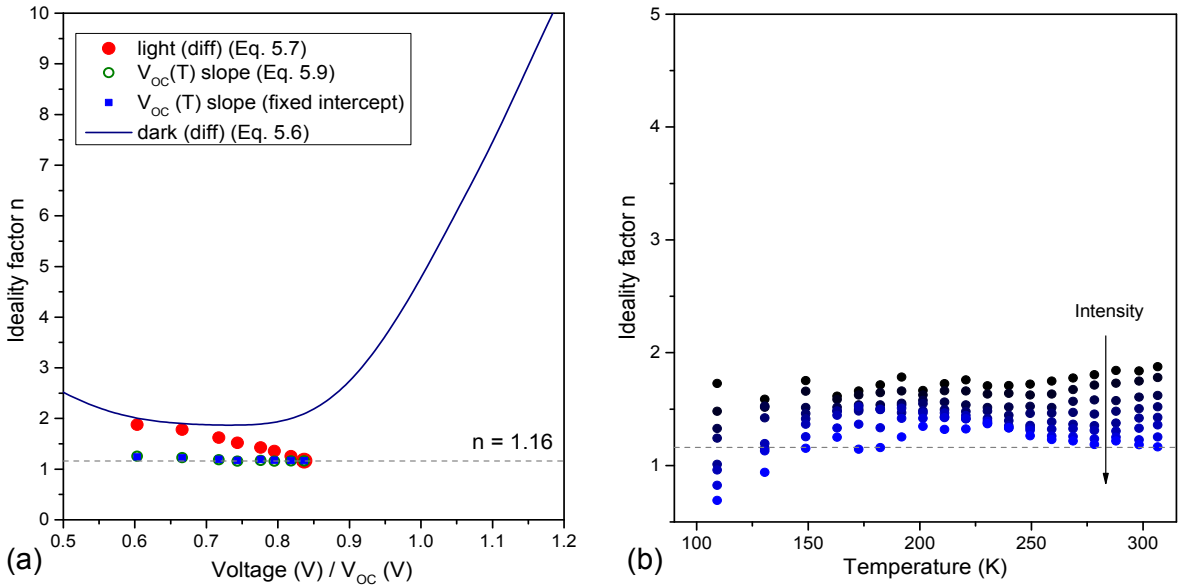

Figure 5.23: (a) Ideality factors determined in different ways are plotted against (open circuit) voltage. Except $n_{\mathrm{dark,diff}}$, all ideality factors almost perfectly approach unity around V_{OC}. (b) Increasing illumination intensities lead to a decreasing differential light ideality factor indicating light induced detrapping under illumination.

duced V_{OC} of that device, and the low ideality factors of both DBP solar cells. They can help to explain why DBP solar cells - despite their amorphous character - show good charge carrier transport and provide high fill factors.

Material system	Cell temperature (K)	E_{PVG} (eV)	j_0 (mA/cm^2)	n
DIP/C_{60}	296	1.43	2.1×10^{-12}	1.04
DBP/C_{60}	305	1.53	3.1×10^{-14}	1.00
DIP:C_{60} (1:1)	296	1.46	1.6×10^{-8}	1.62
DBP:C_{60} (1:2)	305	1.32	1.8×10^{-9}	1.16

Table 5.3: The values of E_{PVG} are taken from Fig. 5.18 (b) and 5.22 (b) ($1/k_{\mathrm{B}}T$ vs. $n \cdot \ln(j_0)$); j_0 values are taken from fits at J_{SC} vs. V_{OC} measurement (Fig. 5.17 (c) and 5.21 (c)); n is the differentially calculated light ideality factor at highest measured intensity. The values of the DIP solar cells are shown for comparison but were determined by U. Hörmann.[187]

5.2 Amorphous vs crystalline exciton blocking layers at the anode interface

Most of the results of this section have already been published.[232]
The use of exciton blocking layers (EBLs) in organic donor-acceptor solar cells is well established, however up to now, the focus has mainly been on the cathode side. There, such blocking layers are mandatory as they prevent the penetration of subsequently evaporated metallic cathode material into the active semiconductor layers. However, it has been shown that the application of materials like bathocuproine (BCP) or bathophenanthroline (BPhen[148,233,234]) also enhance the efficiency of organic solar cells by suppressing exciton-quenching at the metal-organic interface. At the opposite contact, it is also common to insert a buffer layer consisting of e.g. MoO_x or thiophene based polymers (e.g. PEDOT:PSS) between ITO anode and donor material. This is done because ITO, due to its insufficient work function, cannot act as the desired hole-selective contact leading to high leakage currents. But it is usually neglected that, like ITO itself, these buffer layers are also exciton quenchers due to their quasi-metallic nature. By inserting an EBL, however, the excitons are hindered to diffuse to and being quenched at the interface between buffer layer and donor. Consequently, non-radiative recombination is suppressed at this interface. As non-radiative recombination ($j_{non}(T)$) is connected to V_{OC} via[65]

$$V_{OC} = \frac{k_B \cdot T}{q} \cdot \ln\left(\frac{J_{SC}}{j_0(E_g, T) + j_{non}(T)} + 1\right), \tag{5.10}$$

less $j_{non}(T)$ will lead to an increase in V_{OC}. Radiative recombination (j_0), however, is not influenced by the insertion of an EBL. As a result, this effect is rather small. Of far greater significance is the influence of the EBL on J_{SC}. Excitons being blocked at the EBL have the possibility to diffuse back to the D/A interface. Moreover, blocking excitons at the donor/anode interface causes an exciton diffusion gradient away from the electrodes. By that, more excitons reach the D/A interface where they can be dissociated and by that contribute to the current.[194,235]

For PHJ organic solar cells, these positive effects have already been proven by inserting either crystalline[119] or amorphous blocking layers,[116] resulting in higher power conversion efficiencies by notably elevating the J_{SC}, while slightly increasing V_{OC} and leaving the value of FF almost unchanged. Moreover, it was suggested that the use of crystalline blockers as a nanostructured template could increase the area of the D/A interface, which would further enhance J_{SC}, indicating that crystalline blockers are more favorable.[119]

Within this section, the influence of EBL morphology is clarified by comparing blocking layers consisting of either crystalline DIP or amorphous α-NPD in planar as well as in planar-mixed heterojunction devices. The blocking materials are selected based on the alignment of their energy levels related to HOMO and LUMO of the donor material. To achieve hole transport and efficient exciton blocking simultaneously, the ionization

potential must be similar (but must not lie deeper than the HOMO of the donor), while its energy gap has to be wider compared to the donor. To emphasize the blocking effect highly absorbing DBP is chosen as donor material. As electron acceptor material, mainly the fullerene C_{60} is used. However, some selected cells are fabricated using the stronger absorbing fullerene C_{70} to achieve a maximum PCE of 5.8 % ± 0.2 % in single junction cells. Generally, the architecture of the PHJ solar cells is ITO (140 nm)/HIL1.3 (45 nm)/blocking layer (x nm)/DBP (15 nm)/fullerene (45 nm)/BCP (5 nm)/Al (100 nm), i.e. the only variables are the material and the thickness of the exciton blocking layer.

5.2.1 DIP as crystalline EBL in PHJ devices

DIP is chosen to form the crystalline blocking layer, exhibiting exceptionally high structural order in evaporated thin films.[104] To be used as EBL material at the anode interface, some prerequisites have to be fulfilled: suitable HOMO and LUMO levels, high hole mobility, and a small absorption coefficient. In combination with the donor DBP, DIP is the perfect fit. Due to their structural similarities, they have (almost) identical HOMO energy levels, preventing the occurrence of energy barriers which can hamper an efficient hole transport to the anode. Moreover, DIP provides good hole mobility due to its crystallinity[107] and absorption measurements reveal that DIP possesses a wider energy gap than DBP (*cf.* Fig. 3.1). This ensures exciton confinement in the DBP layer and thus provides efficient exciton blocking. The weak absorption of DIP, which is detrimental when being used as donor material, is also beneficial for an EBL. Otherwise parasitic absorption would create excitons within the EBL, which cannot reach the D/A interface and thus do not contribute to charge generation.

The impact of DIP absorption is excluded by varying the thickness of the blocking layer from 3 to 21 nm in 3 nm steps receiving almost identical values for J_{SC} (Fig. 5.24 (a)). This result leads to the assumption, that 3 nm of DIP already form a (nearly) closed layer, which is in accordance with investigations, revealing the tendency of DIP to grow in Stranski-Krastanov mode.[201,202] Compared to the reference without blocking layer, the gain in J_{SC} is between a minimum of 24 % (3 nm DIP) and a maximum of 30 % (6 nm DIP), staying almost constant for higher thicknesses of the DIP layer. Moreover, also the values for V_{OC} (continuously) and FF (at first) show a small increase (Fig. 5.24 (c)). As mentioned before, this slight but continuous gain in V_{OC} for thicker blocking layers is an additional effect of the reduced recombination.[65,236]

The fill factor increases from 69 % (0 nm) to a maximum of 72 % (6 nm). Due to (more or less) identical shapes of the *J*-*V*-curves of both samples in forward bias regime, an influence of R_S is not relevant here. The reason for the increase of the FF is assumed to stem from an increased parallel resistance. The *J*-*V*-characteristic of the sample with 6 nm DIP reveals a smaller slope near J_{SC} than the *J*-*V*-characteristic of the sample without EBL (Fig. 5.25 (a)). As shown in Fig. 2.9, a smaller slope indicates a higher

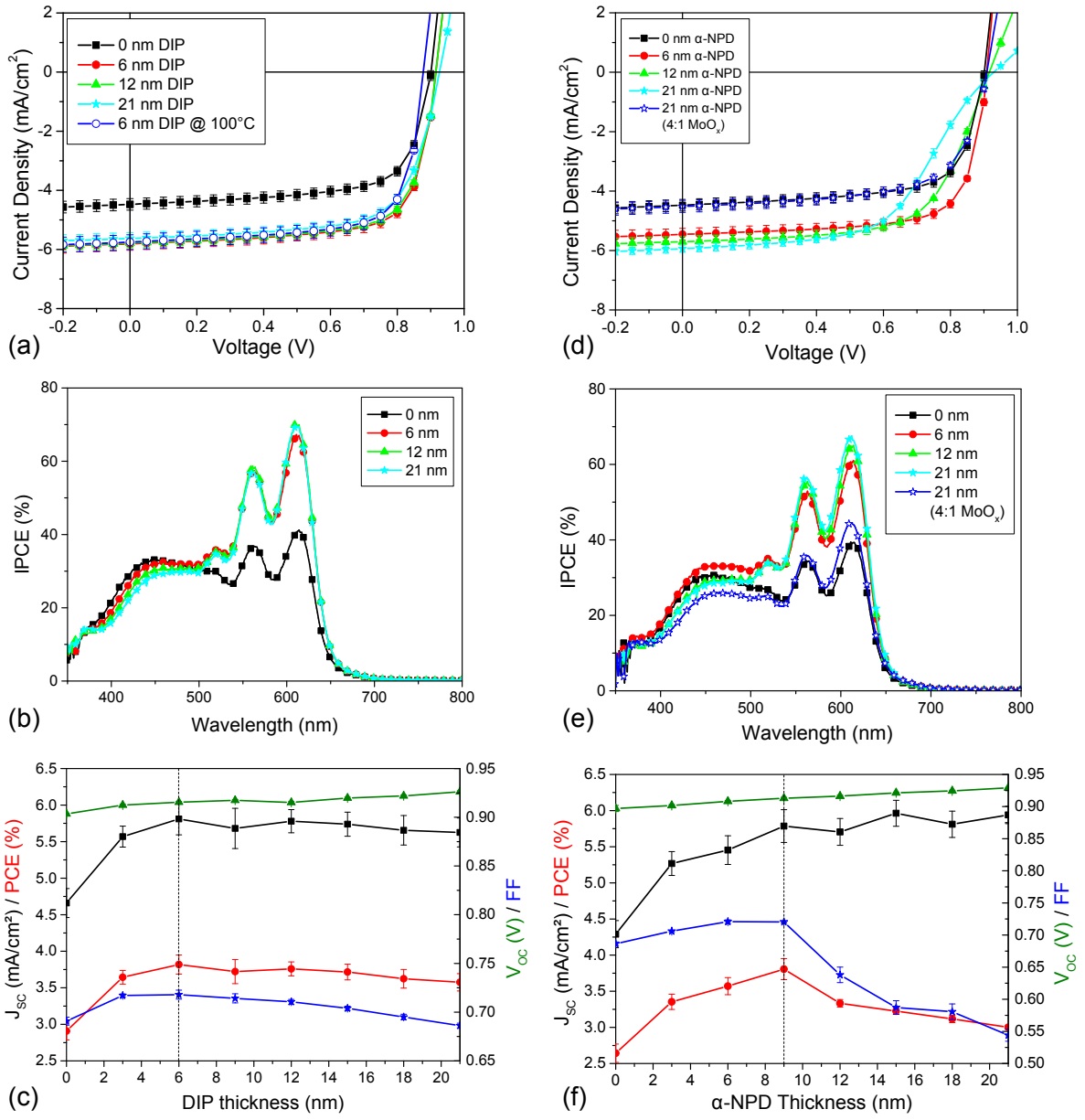

Figure 5.24: Comparison of crystalline EBL DIP and amorphous EBL α-NPD in terms of electrical characterization: (a, d) J-V-characteristics, (b, e) IPCE curves and (c, f) solar cell parameters vs. thickness of the exciton blocking layers. The architecture of the PHJ solar cells is ITO(140 nm)/HIL1.3(45 nm)/EBL(x nm)/DBP(15 nm)/C_{60}(45 nm)/BCP(5 nm)/Al(100 nm). For reasons of clarity, some curves were omitted in (a), (b), (d), and (e). Moreover, the J-V-characteristic of a sample with DIP evaporated at 100 °C is shown in (a). A sample possessing a 21 nm thick α-NPD layer highly doped with MoO_x (4:1) is fabricated as well. The associated J-V-characteristic is depicted in (d), the IPCE curve in (e).

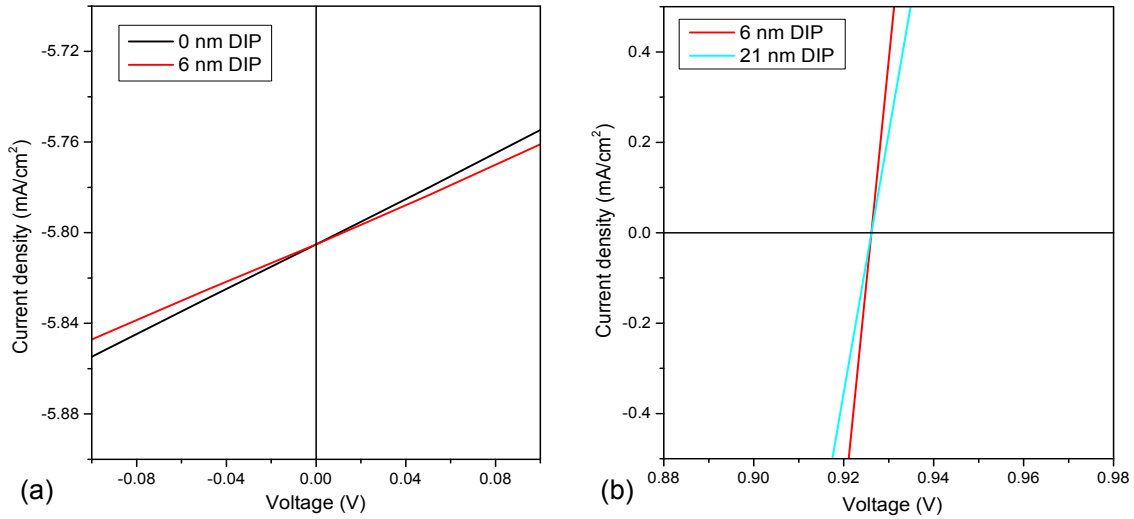

Figure 5.25: (a) The insertion of a 6 nm thick DIP EBL leads to a higher R_P indicated by the reduced slope of the J-V-characteristic near J_{SC} compared to a sample without EBL. (b) Further increase of the EBL thickness to 21 nm, however, leads to an increasing R_S. As a result, the highest FF is obtained by the sample with 6 nm DIP. For a better comparability, in both diagrams, curves are adapted to a common value of J_{SC} and V_{OC}, respectively.

R_P, and thus a higher fill factor of the corresponding OPVC. The most probable reason for an increased R_P is a reduced parasitic leakage current. Leakage currents in solar cells can be considered as undesirable currents that are injected from the electrodes prior to the turn on voltage.[237] It seems like an additional DIP layer between anode and donor layer is able to reduce that current. The subsequent decrease of the FF down to its initial value for a 21 nm thick EBL layer, however, is not caused by a further alteration of R_P, but by a growing R_S due to increasing transport issues, indicated by a smaller slope around V_{OC} (Fig. 5.25 (b)). Summing up the improvements in J_{SC}, V_{OC}, and FF, the PCE increases from 2.8 % for the reference up to 3.8 % for the best cell in this series containing a 6 nm DIP blocking layer. This is an improvement of more than 37 %.

The similarity of the J-V-characteristics of the solar cells with varying DIP thicknesses leads to the conclusion, that a possible template effect is not relevant. Due to pronounced island growth for higher DIP thicknesses, the RMS roughness for the DIP/DBP interface increases, however, this effect does not propagate to the DBP/fullerene interface, where it could lead to enhanced exciton dissociation and thus a higher J_{SC}. Even for DIP grown at elevated temperatures ($T_{substrate}$ = 100 °C), which leads to an enhanced lateral crystallinity of the DIP layer,[110] the subsequently evaporated DBP film, leads to a re-flattening of the sample surface and thus the D/A-interface. In general, AFM images do not reveal any signs of changed morphology or structure of a DBP layer grown on DIP, which is either evaporated at room temperature or at 100 °C (Fig. 5.26). However, investigations are only carried out for a 6 nm thick DIP layer. It is possible, that an enhanced DIP layer thickness, coming along inherently with a higher degree of

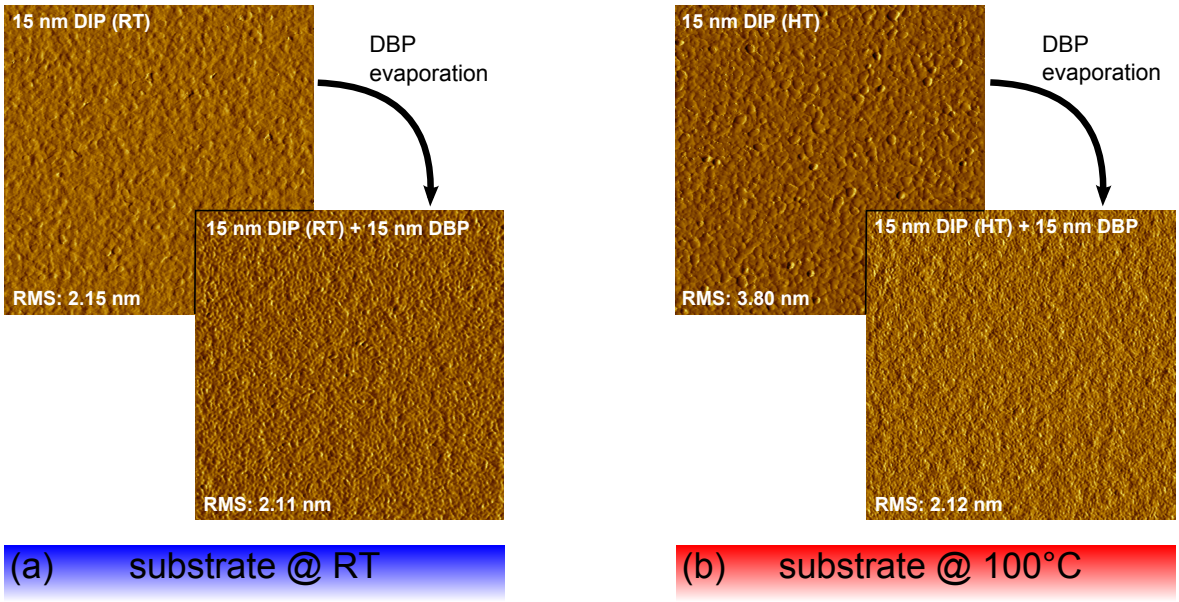

Figure 5.26: Investigation of a possible templating effect of a 6 nm thick DIP layer either evaporated on a substrate at room temperature ((a), RT) or at 100°C ((b), HT). The enhanced roughness of the DIP film evaportad at HT disappears by a subsequent evaporation of a 15 nm DBP layer. A templating effect cannot be observed. Data is presented in shaded mode for a better visualization of the surface structure.

crystallinity as well as an increased roughness, yields diverging results.
Consequently, also no changes in J_{SC} can be observed for an OPVC with a DIP layer evaporated at elevated substrate temperature (open symbols in Fig. 5.24 (a)). Therefore, the by far most dominant effect for the gain in J_{SC} is reduced exciton quenching at the HIL1.3/organic interface, which is also supported by IPCE measurements (Fig. 5.24(b)), revealing that the increment is mainly at wavelengths (λ) between 500 nm and 650 nm, where the maximum absorption of DBP occurs. In the main absorption region of C_{60} (400 nm $< \lambda <$ 500 nm), however, only small differences between the IPCE curves are visible. This is in accordance with the assumption that less excitons generated within the DBP layer are quenched at the HIL1.3 buffer layer, but instead dissociate at the DBP/C_{60} interface, generating free charge carriers.

5.2.2 α-NPD as amorphous EBL in PHJ devices

α-NPD also fulfills the requirements to form an efficient EBL in combination with DBP concerning energy level alignment and hole transporting ability,[238,239] while hardly absorbing itself in the visible range. In contrast to highly crystalline DIP, thermally evaporated α-NPD forms amorphous thin films.[240] The amorphous character usually comes along with a smooth surface.[241] This can be verified by AFM measurements (Fig. 5.27). As there is no template effect for DIP, a similar gain in J_{SC} for amorphous blockers is expected. This assumption is confirmed by electrical characterization. The

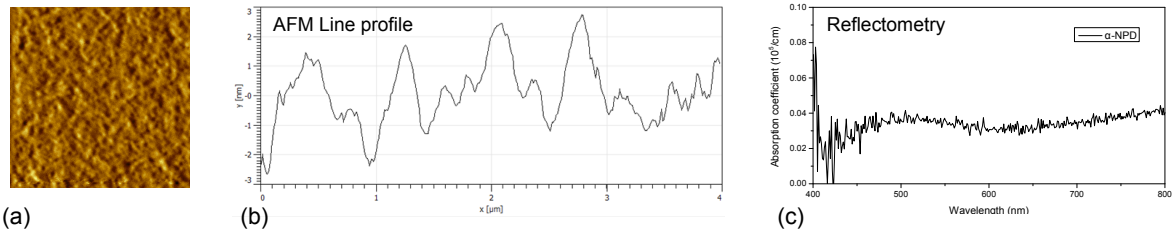

Figure 5.27: (a) AFM image reveals the smooth surface of a 9 nm thick, amorphous α-NPD layer with an RMS roughness of merely 1.16 nm. The corresponding line profile is shown in (b). The reflectometry measurement in (c) displays the extremely weak absorption of a 50 nm thick α-NPD layer in the visible range.

J-V-characteristics are shown in Fig. 5.24 (d)). For the best cell with a 9 nm thick α-NPD layer, J_{SC} increases by 29 %. Compared to the 30 % of the device exhibiting 6 nm DIP, one can state that there is no difference in J_{SC} between devices with crystalline or amorphous blocking layers within the range of error. Moreover, the same trends for V_{OC} and FF can be observed compared to devices with crystalline blocking layer (Fig. 5.24 (c)), so that there is again an increase in PCE of about 37 %. This leads to the conclusion that a possible template effect of crystalline blocking layers as proposed in literature[119] is not occurring or at least its impact is negligible. This result is illustrated by summing up the characteristic values of the best devices, containing either DIP (RT and HT) or α-NPD as EBL, in Tab. 5.4.

EBL	d_{EBL} (nm)	T_{subs} (°C)	J_{SC} (mA/cm^2)	V_{OC} (V)	FF (%)	PCE (%)
no	—	25	4.29	0.90	68.7	2.64
DIP	6	25	5.81	0.92	71.8	3.82
DIP	6	100	5.75	0.88	72.4	3.66
α-NPD	9	25	5.79	0.91	72.1	3.81

Table 5.4: Efficiency enhancement of an OPVC consisting of ITO/HIL1.3/15 nm DBP/45 nm C_{60}/5 nm BCP/100 nm Al by inserting an EBL between buffer layer and donor. There is no difference using either crystalline DIP (6 nm) or amorphous α-NPD (9 nm) as EBL. Heating the substrate during evaporation to increase DIP crystallinity does not show any further improvement.

Despite all these similarities, there is a big difference in the thickness dependence of device parameters between both blocking layers. While there is hardly any correlation between layer thickness and device performance for the DIP containing solar cells, this is not the case for the α-NPD devices. There are two different reasons for that deviating behavior. First, it is assumed that 3 and even 6 nm of α-NPD are not sufficient to form a closed layer, which leads to incomplete blocking and thus less gain in J_{SC} compared to architecturally identical DIP devices. Second, blocking layers exceeding 9 nm show

an increasing s-shape behavior. This feature is ascribed to a growing transport resistance,[77] an effect which is obviously much more pronounced for amorphous films as they generally feature lower charge carrier mobilities.[242]

To confirm, samples with 21 nm thick α-NPD layers highly doped with MoO_x (9:1 and 4:1) are prepared. As a result, the s-shape vanishes (open stars in Fig. 5.24 (d)). However, as MoO_x also acts as an exciton quencher,[243] J_{SC} decreases again with increasing percentage of MoO_x. The quenching effect is also revealed by the corresponding IPCE characteristics (open stars in Fig. 5.24 (e)), which show an increasing amount of generated charge carriers up to an α-NPD layer thickness of 9 nm followed by a saturation for thicker blocking layers.

In a last step, the electron acceptor C_{60} is replaced by the stronger absorbing C_{70} to increase J_{SC} and thus PCE. Due to the following results, it becomes obvious that the choice of the acceptor material is also of importance for the strength of the blocking effect at the anode interface, although no common interface between acceptor and blocking layer exists. This can be explained by looking at the IPCE characteristics of an appropriate device (Fig. 5.28 (a)). As C_{70} absorbs almost in the whole visible range, and thus, unlike C_{60} also in the same region as DBP does (Fig. 3.2 (a)), a redistribution in absorption occurs. That becomes apparent in the IPCE curves and results in less excitons being generated within the DBP, while parasitic absorption occurs within the acceptor. As a consequence, the gain in J_{SC} by introducing blocking layers beneath the donor is only half as big as in the case of C_{60} as acceptor (Fig. 5.28 (b)). Hence, as the small increase in V_{OC} and FF is retained for this material combination, an increase in PCE of 19 % occurs. This result shows that the success of introducing blocking layers at the anode interface depends strongly on the choice of materials. The more absorption occurs in the donor, the more gain in PCE can be achieved.

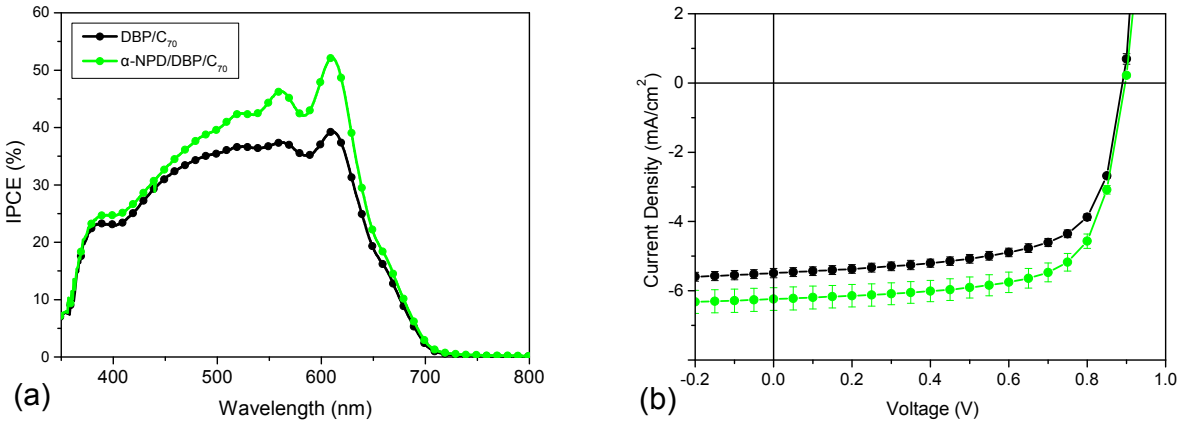

Figure 5.28: Change in (a) IPCE and (b) J-V-characteristics due to the insertion of a 6 nm thick α-NPD EBL in an OPVC with DBP/C_{70} as active organic semiconductors. Compared to devices containing C_{60}, the exciton blocking effect is weakened due to enhanced parasitic absorption of C_{70}.

5.2.3 Exciton blocking layers in PMHJ devices

Mixing donor and acceptor molecules to enhance their interface resulting in more efficient exciton dissociation is a well-established concept.[54,55] In this subsection, PMHJ devices are prepared, a combination of strictly planar and bulk heterojunction devices, combining the benefits of both concepts.[244] This means that a mixed layer of DBP and C_{60} is sandwiched between a DBP layer on the anode and a C_{60} layer on the cathode side. Further devices skipping the pure DBP layer on the anode side were fabricated. The volume ratio DBP:fullerene in the bulk was chosen 1:2, as this composition has proven to provide high PCEs for this material combination.[121]

In contrast to the PHJ devices, there are significant differences in J-V-characteristics comparing crystalline DIP and amorphous α-NPD as EBL (Fig. 5.29 (a)). As the main difference concerns V_{OC}, however, this is not related to the morphology of the blocking layers but can be associated to shifting energy levels and a change of the effective work function of the anode. Compared to PHJ devices, already the V_{OC} of the reference PMHJ cell drops from 0.90 V to 0.84 V. That is a typical behavior of mixed devices, as the enlarged interfacial area enhances recombination, which in turn reduces V_{OC}.[96,245] However, V_{OC} is further reduced to 0.79 V introducing a DIP layer and even to 0.76 V by additionally skipping the pure DBP layer. The opposite effect is observed inserting α-NPD. In these cells V_{OC} increases again to the value of the PHJ cell and even a little bit more when the neat DBP layer is omitted.

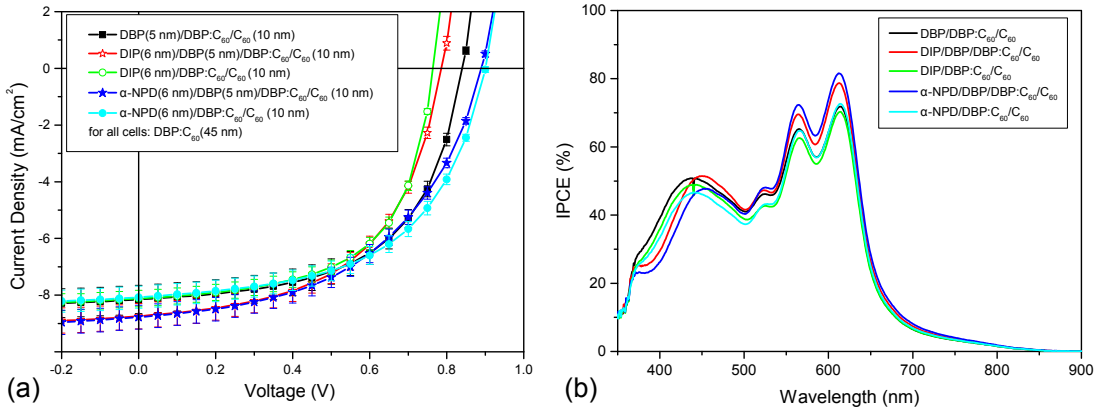

Figure 5.29: (a) J-V-characteristics and (b) IPCE curves of the fabricated PMHJ devices consisting a mixed layer of DBP and C_{60}. While V_{OC} is reduced by the insertion of DIP, it can be enhanced by using α-NPD as EBL.

For J_{SC} there is again an increase upon introduction of the blocker layer, however it is smaller compared to that in PHJ devices. This is explained by the more efficient exciton dissociation already given by the device architecture, leading to less excitons reaching the blocking layer interface. Despite that gain in J_{SC} there is hardly any rise in PCE as the cells showing a higher current either lack in V_{OC} (DIP, red open stars) or in FF (α-NPD, blue filled stars). The cells without the pure DBP layers show the same J_{SC}

as the reference. This is due to the fact that blocking excitons with DIP or α-NPD compensates additional absorption of the thin DBP layer. Thus, the best cell in this series is the α-NPD/DBP:C_{60}/C_{60} device, showing a small increase in PCE from 3.9 % of the cell without blocking layer to 4.0 %, mainly due to the gain in V_{OC}. While the gain in PCE for PHJ devices is decreased using C_{70} instead of C_{60}, it is just vice versa for PMHJ solar cells (Fig. 5.30). However, this is not explained by blocking reasons and therefore a higher gain in J_{SC}. On the contrary, compared to the reference without blocker even a small decrease in J_{SC} is observed. Though, this deficit is easily compensated by an increase of the fill factor from 55.5 % to 58.9 %. Due to the gain in V_{OC} an increase in PCE of 12 % is reached leading to an overall efficiency of 5.8 % ± 0.2 %.

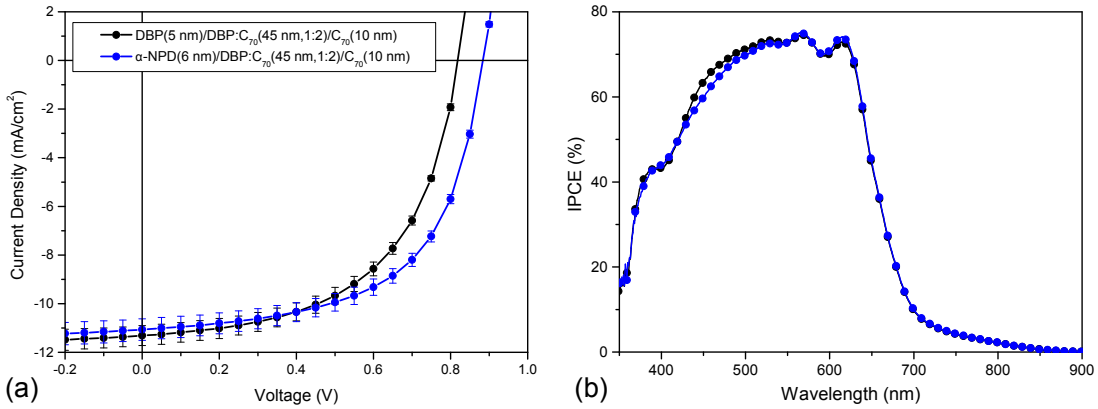

Figure 5.30: (a) J-V-characteristics and (b) IPCE curves of the fabricated PMHJ devices consisting a mixed layer of DBP and C_{70}. Using α-NPD as EBL, V_{OC} increases and an PCE of 5.8 % ± 0.2 % is achieved.

In conclusion, for small molecule OPVCs it could be shown that - depending on the choice of the buffer layer and the D/A combination - also for PMHJ solar cells a remarkable efficiency enhancement is possible, introducing suitable blocking layers at the anode interface. The most important results concerning the effect of EBLs on PMHJ solar cells are summarized in Tab. 5.5.

EBL	acceptor	J_{SC} (mA/cm²)	V_{OC} (V)	FF (%)	PCE (%)
no	C_{60}	8.15	0.84	57.1	3.91
DIP	C_{60}	8.12	0.76	59.8	3.71
α-NPD	C_{60}	8.07	0.90	55.5	4.03
no	C_{70}	11.3	0.82	55.5	5.14
α-NPD	C_{70}	11.1	0.88	58.9	**5.76**

Table 5.5: Solar cell parameters obtained by electrical characterization of PMHJ devices consisting of ITO/HIL1.3/DBP (or EBL)/DBP:Acceptor (1:2)/BCP/Al. When an EBL is inserted, it replaces the neat DBP layer beneath the mixed layer.

5.3 Solvent vapor annealing on perylene-based organic solar cells

Most of the results of this section have already been published.[246]
The first subsection 5.3.1 depicts the influence of SVA on the photovoltaic performance in general, and on the different processes occurring during charge generation in particular. SVA was performed on morphologically different organic thin films, namely on amorphous DBP and crystalline DIP. The influence of the SVA induced morphological changes of these thin films on solar cell performance is further investigated in OPVCs. The device architecture of the studied photovoltaic cells within this section has been 140 nm ITO/45 nm HIL1.3/30 nm donor/45 nm acceptor (C_{60} or C_{70})/5 nm BCP/100 nm Al. As donor either DBP (subsection 5.3.2) or DIP (subsection 5.3.3) is used. For these samples, SVA was performed after evaporation of the donor material. Furthermore, solar cells were fabricated consisting of two donor layers with 15 nm DIP and 15 nm DBP, which were evaporated consecutively. In this case, DBP is the primary absorber while DIP acts as an exciton blocking layer. For these solar cells only the DIP layer is treated by use of SVA (subsection 5.3.4). The results of this section have already been published in Ref. 246.

5.3.1 General impact of SVA on the performance of OPVCs

SVA on organic semiconductor films is usually carried out to enhance the crystalline order. However, this change in the morphological long-range order implies several other modifications on a smaller scale, which can alter the photovoltaic performance. By dividing the process of charge generation into four sub-processes (photon absorption, exciton diffusion, exciton dissociation, charge carrier transport, Eq. 2.4), it can be shown how SVA acts on the charge generation process in various ways.

An increased crystallinity is able to affect the efficiency of the first sub-process as η_{Abs} is, on the one hand, determined by the organic layer thickness. A thicker layer means enhanced absorption and it has already been shown that enhanced crystallinity allows the use of thicker active layers without negatively impacting the fill factor.[247] Furthermore, if SVA is able to change the molecular orientation, it could influence the second important factor determining η_{Abs}, the absorption strength of the utilized materials. The alignment of the transition dipole moment (which is defined by the molecular orientation) with respect to the incident light determines how efficient photons can be absorbed by the molecule. SVA may provide a potential route to alter the orientation of molecules within the film, modifying their coupling with incident light and resulting in a change in η_{Abs}.

Moreover, all transport processes are expected to improve within the treated layer with increasing crystallinity. The efficiency of the diffusion of excitons η_{ED},[32] as well as the transport of free charge carriers η_{CC}[248] should increase. This implies that if the donor

is annealed, the mobility of the holes rises, while a treatment of the acceptor should improve the electron transport[iv]. A measure for good transport is a low series resistance R_S. Again, the series resistance can be derived from a fit with the modified Shockley equation (Eq. 5.2) to the corresponding part of dark current data, as well as j_0 and n. The influence of the series resistance on solar cell performance is visible in the fill factor (FF), as a high R_S reduces FF.[71,214]

But not only the FF can be positively influenced, an improvement of η_{ED} might also contribute to an increase of J_{SC} as the second sub-process, the diffusion of excitons, also implies that excitons are able to diffuse to the D/A interface and do not recombine within the bulk. This is far from self-evident, considering that typical exciton diffusion lengths for organic materials are only a few nanometers.[31,32] An alternative to an increase of the exciton diffusion length is to increase the surface area of the D/A interface e.g. by co-evaporation. However, this results in a completely different concept, the bulk heterojunction (BHJ).[54,55] Nevertheless, the interface area can also be increased in planar heterojunction (PHJ) devices, albeit on a smaller scale, by enlarging the roughness of the donor layer. As roughness is usually connected to crystallinity, SVA also affects this parameter. Finally, the increase in the number of dissociated excitons leads to an increase in free charge carriers and thus a higher J_{SC}.

The only process not influenced by SVA is the charge-transfer process, occurring at the D/A interface. As this dissociation process typically takes place over time scales of a few hundred femtoseconds or less,[37–39] it is much shorter than any other competing process. Thus, as long as the nature of the D/A interface is not fundamentally changed, the charge-transfer efficiency already approaches $\eta_{CT} = 100\ \%$.[40,41]

5.3.2 SVA on amorphous donor DBP

In the treatment of organic layers with solvent vapor it is important to consider some correlations. First, the most suitable solvent has to be found for the material to be treated. For that reason, the solubility of DBP was evaluated in chlorobenzene, orthodichlorobenzene, chloroform, dichloromethane, toluene, xylene and tetrahydrofuran. Optical microscopy images show that chloroform yields the best results, as the DBP precipitates, which appear for all solvents, are surrounded by a purple-colored area as it is typical for (evaporated) DBP films.[249] However, DBP does not show particularly good solubility in any of these solvents. It is also observed that DBP, which was dissolved in chloroform, crystallizes after solvent evaporation. That can be studied filtering the DBP-chloroform solution through a 0.2 µm polytetrafluoroethylene (PTFE) filter to remove larger, undissolved components. During the vaporization process of the solvent, small, about 10 – 50 µm long, needle-shaped DBP-crystals grow out of the solution (Fig. 5.31 (a)). Therefore, in the following all SVA treatments are carried out with chloro-

[iv] Experiments have shown that an exclusive SVA treatment of the acceptor is hardly possible. SVA after evaporation of the acceptor always acts on both donor and acceptor.

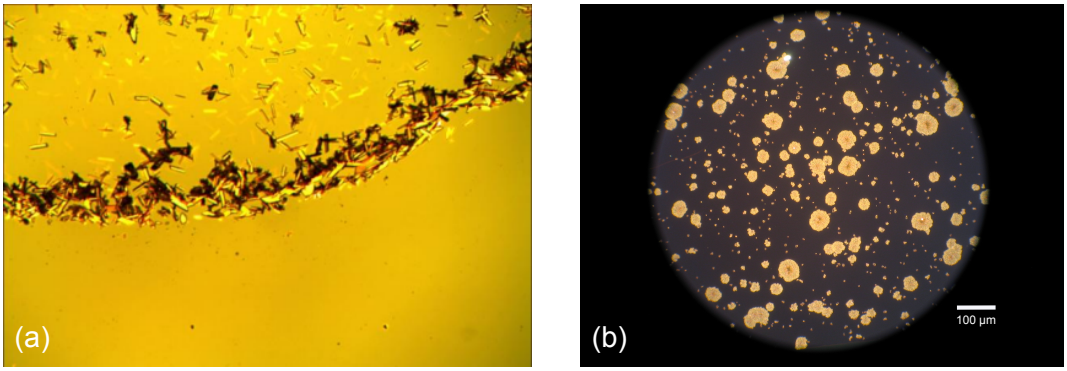

Figure 5.31: (a) Needle-shaped DBP crystals under 200-fold magnification grown from a filtered solution of DBP in chlorofrom. (b) Round crystallites formed in a 50 nm thick DBP-layer by annealing for 10 minutes in chloroform vapor. The images are recorded by Andreas Mittelberger and Florian Graßl, respectively, in the scope of their bachelor's theses.[249,250]

form. Beside the choice of a suitable solvent, it is important to find out an appropriate duration of the SVA treatment. This also depends largely on the treated material as well as on the layer thickness.

First of all, annealed DBP thin films are studied by optical microscopy. Inspection of an image taken from a sample annealed for 10 minutes under 20-fold magnification reveals that indeed round DBP crystallites are formed with diameters of approximately 50 µm (Fig. 5.31 (b)). To investigate the crystallinity of the annealed layer, X-ray diffraction (XRD) measurements are performed. Initially, out-of-plane X-ray reflection (XRR) was measured, but just like the pristine layers no reflections, indicating a well-ordered crystalline structure, can be observed (Fig. 5.32 (a)). Therefore, in-plane (grazing incident X-ray diffraction) measurements are recorded, but also in this configuration no peaks indicating DBP crystallinity are observable (Fig. 5.32 (b)). For that reason, it is assumed that the lattice planes are not oriented parallel to the substrate surface, necessary for detection. Also other groups have already reported on more crystalline DBP, achieved through different techniques. Growing on a crystalline template[119] or on a heated substrate[117] as well as applying organic vapor phase deposition (OPVD) using a hot inert carrier gas[247] were reported to result in DBP layers of higher order. However, also in these cases the crystallinity could neither be visualized by means of XRD,[119] nor via reflection high energy electron diffraction[117] (RHEED) nor by selected area electron diffraction[247] (SAED).

Next, the surface properties of 15 nm films of DBP annealed for various durations are investigated via AFM. There is no difference for layers growing either on ITO/HIL1.3 or on glass. Thus, it is assumed that the reorganization of the molecules does not depend on the substrate. The layers are treated by SVA for 4, 8 and 12 minutes, respectively, and then compared with each other as well as with an untreated sample. The resulting AFM images are shown in Fig. 5.33. As reported previously,[117,118] the pristine DBP layer has

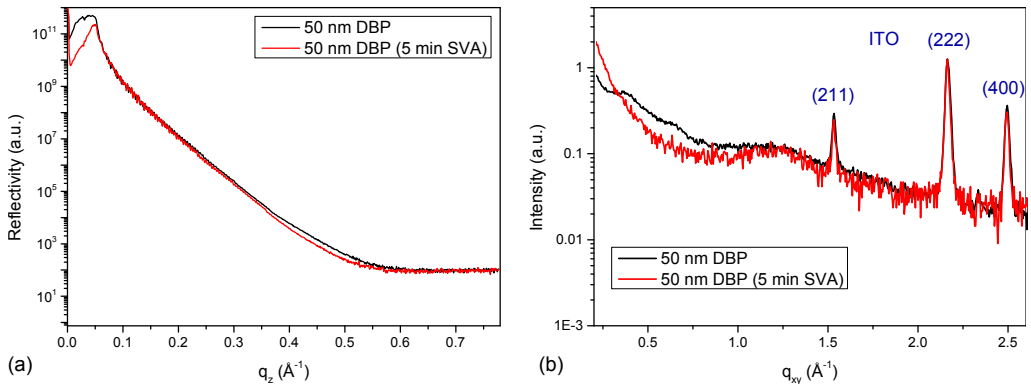

Figure 5.32: Out-of-plane ((a), XRR) and in-plane ((b), GIXD) X-ray diffraction measurements of pristine and annealed (5 minutes) DBP layers. The architecture of the samples is always ITO/HIL1.3/DBP (50 nm). Peaks indicating DBP crystallinity cannot be observed for annealed layers for both configurations. The peaks visible in (b) can be clearly attributed to the ITO substrate. Measurements were performed by Christopher Lorch (Universität Tübingen).

an extremely smooth surface with an RMS roughness of merely RMS = 0.63 nm. This leads to an almost completely flat line profile (Fig. 5.33 (b)). However, this changes completely by solvent vapor treatment. Employing chloroform, SVA causes a strong aggregation of the DBP molecules. After 4 minutes of SVA treatment, the RMS roughness increases more than thirtyfold to 21.65 nm. Longer exposure times enhance this effect. For example, after 12 minutes of SVA the RMS roughness amounts to 39.8 nm with DBP islands up to 130 nm height and diameters of approximately 500 nm. A comparison of the images taken for different annealing times show that there is no big difference between the samples annealed for 8 and 12 minutes, respectively, while the 4 minute sample (Fig. 5.33 (c)) represents a transition state between not (Fig. 5.33 (a)) and longer annealed DBP films (Fig. 5.33 (d) and (e)).

The aggregation of molecules leads to a strong inhomogeneity within the DBP film, which is detrimental to the charge transport properties required for devices like photovoltaic cells.[251] In addition to the negative effect on charge transport, the absorption also drops drastically. The change can already be seen with the naked eye, as the annealed layers become much more translucent, i.e. they absorb less. To quantify this observation, optical absorption measurements were performed. Here, further samples with additional annealing times are analyzed, namely 0, 2, 4, 6, 8, 10 and 12 minutes. It can be seen that there is an unambiguous correlation between the annealing time and the reduction of the absorption coefficient α (Fig. 5.34). There is hardly any change for the first two minutes of annealing followed by a slight decrease after four minutes. A more drastic drop occurs after six minutes. At longer times of SVA no further change is visible. This correlates quite well with images taken by AFM, which also reveal negligible differences for eight and twelve minutes and an intermediate topography after four minutes (Fig. 5.33). Thus, the drop of absorption is attributed to a dewetting process of DBP, leading to a decreased two-dimensional coverage of the substrate. Nevertheless,

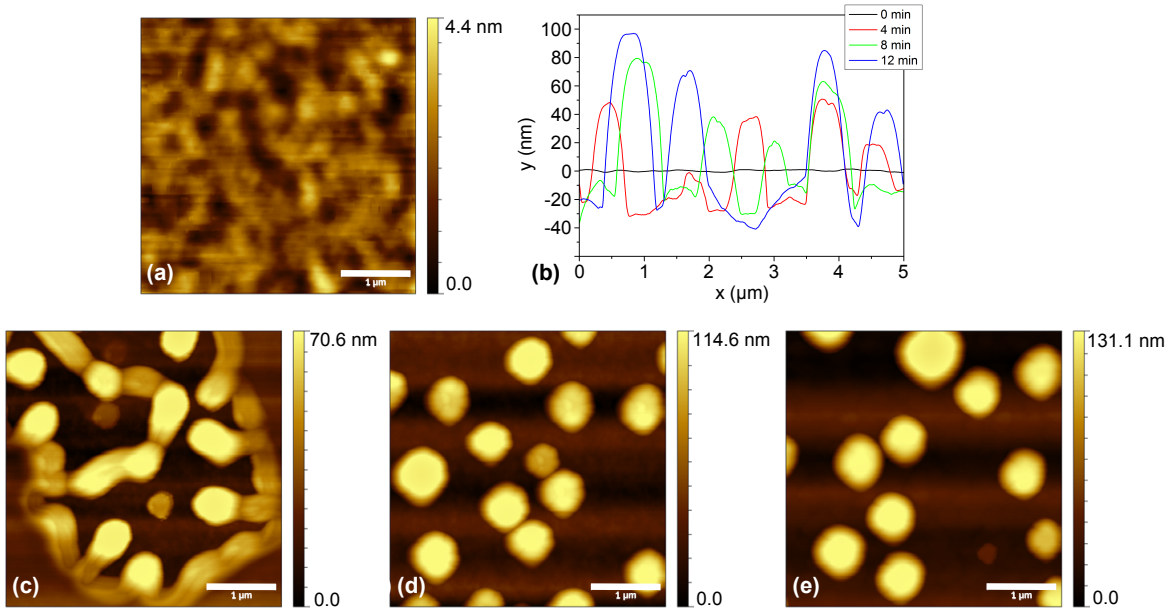

Figure 5.33: AFM images of a 15 nm DBP layer treated by SVA for (a) 0 minutes, (c) 4 minutes, (d) 8 minutes and (e) 12 minutes. Moreover, the line profiles for each sample are shown (b).

it seems like longer annealing times lead to an increasing absorption for wavelengths greater than about 630 nm. However, this can be attributed to scattering, resulting from the increasing roughness of the surface of the annealed DBP films. As scattering is neither detected in transmission nor in reflection, it is included in the calculated absorption $A = 1 - R - T$ and leads to that artifact.

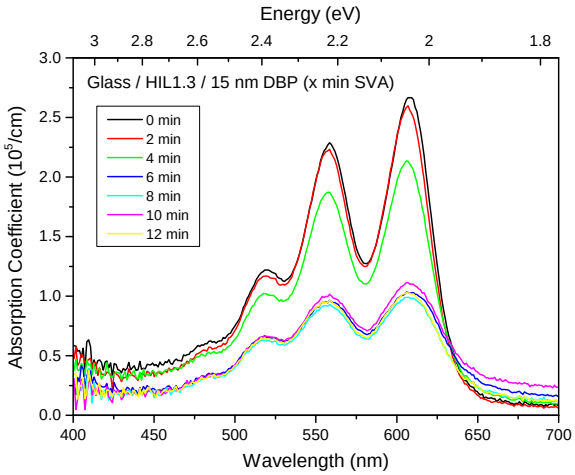

Figure 5.34: Correlation between SVA time and absorption drop of an annealed 15 nm DBP layer. Long annealing times ($t > 4$ min) lead to a strong decrease of the absorption coefficient.

However, dewetting is not the only process which contributes to the absorption drop. NEXAFS measurements reveal an additional change in molecular orientation. Measurements on pristine films yield a higher intensity of the 40° as compared to the 90° spectrum in the low energy region ($\approx$ 284.6 eV, *cf.* Fig. 5.35 (a)) which is related to the transition from the C1s core level to the LUMO level. This reveals a more flat lying perylene core. After 4 minutes of SVA, however, no angular dependence appears any more. This is indicative of a reorientation process which has started, leading to an intermediate configuration (Fig. 5.35 (b)). This is in perfect agreement to the results obtained by AFM and optical absorption measurements. Further annealing yields a reversed angular dependence indicating a change of molecular orientation due to solvent vapor annealing (Fig. 5.35 (c)). These results indicate a more upright oriented perylene core leading to an unfavorable orientation of the transition dipole moment – which is aligned along the long axis of the molecule – and thus less absorption. For this reason, the strong drop in optical absorption for SVA times exceeding 4 minutes can also be explained by an adverse change in molecular orientation. Nevertheless, the NEXAFS results also show that SVA indeed provides a potential route to alter the orientation of molecules within organic thin films. Although SVA reduces the optical absorption of DBP, it is likely that the absorption of other organic thin films (with initially rather upright standing orientation) can be enhanced by means of SVA.

The change in orientation of the DBP molecules can be made more visible through another illustration. For that purpose, it must be kept in mind, that the DBP molecule possesses two different π-systems. While the π-systems of the four phenyl rings can be taken as one, a clear distinction has to be made to the π-system of the perylene core. Each π-system possesses its own energy gap. In general, the energetic distance between HOMO and LUMO is defined by the spatial extent of the respective π-system. The larger the π-system, the smaller the $\pi - \pi^*$ distance and thus the energy gap. As a result, radiation of longer wavelengths (i.e. less energy) is sufficient for a $\pi - \pi^*$-transition to occur. In the case of DBP, the perylene core features a larger π-system then the phenyl rings. Hence, in the NEXAFS spectra, the first peak in the energy range from 283.8 eV to 284.8 eV can be referred to the perylene core, while the second peak between 284.9 eV and 285.5 eV represents the phenyl rings. By extracting the intensities of the respective energy ranges for varying angles θ, the change in orientation of perylene core and phenyl rings becomes apparent in Fig. 5.35 (d) and (e), respectively. The dashed lines within these figures are guides to the eye and represent some molecular orientations α calculated via Eq. (4.6). The change in orientation of the perylene core is clearly visible. While the molecules within the untreated film are oriented by an angle of $\alpha \approx 40\,^\circ$, they tilt up through 6 min of SVA to an angle of $\alpha \approx 60\,^\circ$ with respect to the substrate surface.

The molecular orientation of the sample annealed for 4 minutes is very close to the so-called magic angle of 54.7 °. For this angle, the term $(3\cos^2\alpha - 1)$ within Eq. (4.6) becomes zero so that there is no correlation between absorption and the angle of in-

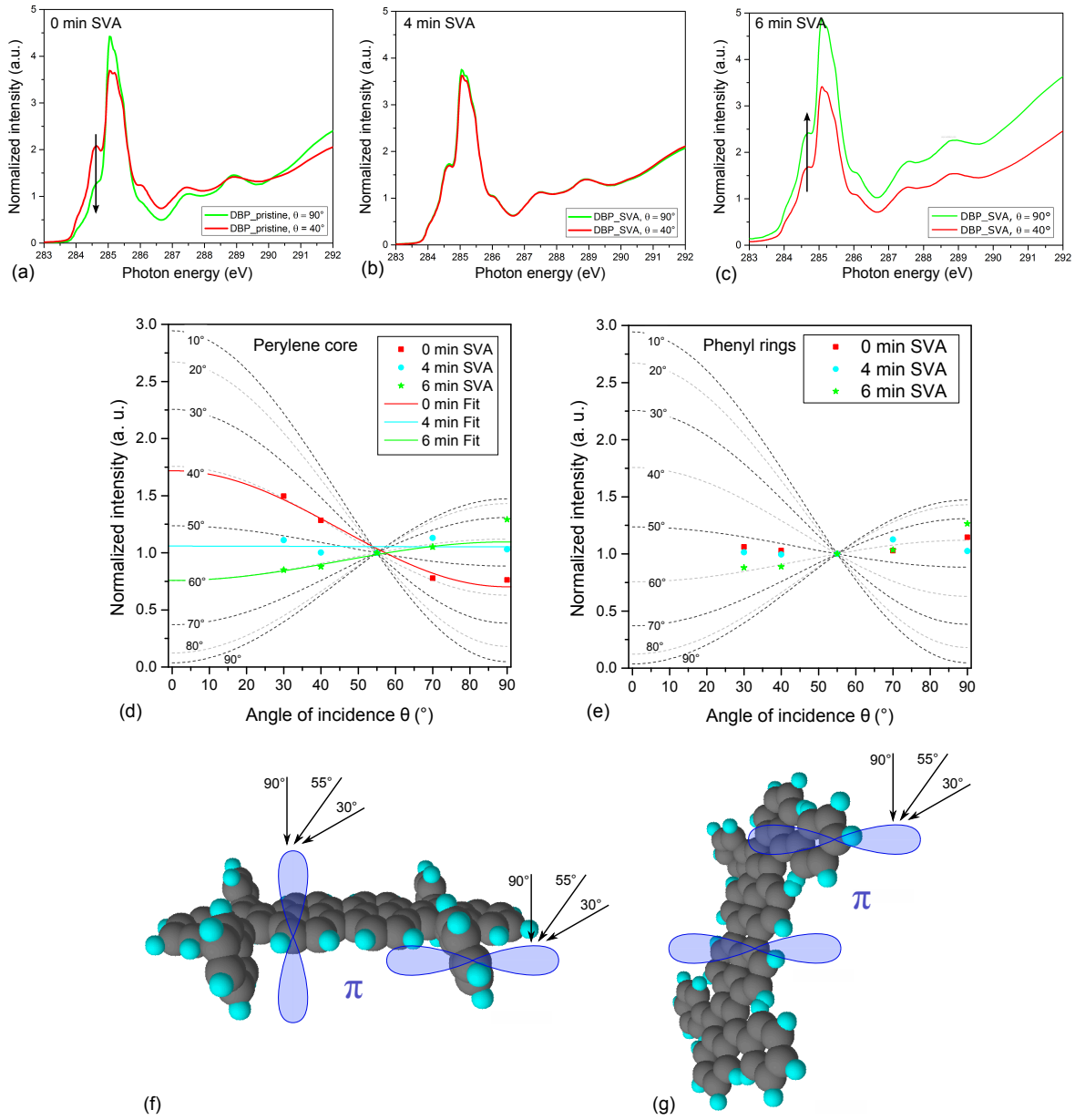

Figure 5.35: C1s NEXAFS spectra of a 15 nm DBP film annealed for 0 (a), 4 (b) and 6 minutes (c) at 40 ° and 90 ° angle of incidence (θ) of the X-ray photons. The black arrow in (a) and (c) at about 284.6 eV indicates a distinct change in dichroism, arising from a change in molecular orientation from rather horizontal to more upright standing alignment. Additional data for $\theta = 30\,°, 55\,°, 70\,°$ confirm this trend, but are omitted for clarity.
The complete data set, however, is used to extract the angular dependence of the NEXAFS intensity for the perylene core (d) and the phenyl rings (e). An energy range from 283.8 eV to 284.8 eV for the core and an energy range from 284.9 eV to 285.5 eV for the rings is taken into account.
(f) NEXAFS measurements reveal a rather lying perylene core and upright standing phenyl rings for an untreated DBP film. (g) After 6 minutes of SVA, however, both core and rings show a rather upright standing orientation. For reasons of clarity, the molecular orientations are drawn in an exaggerated way, the actual orientations are less explicit. The NEXAFS data was recorded by Dr. Andreas Opitz (HU Berlin).

cident X-rays anymore, leading to an isotropic absorption. There are three different possibilities yielding a molecular angle of $\alpha = 54.7\,°$.[187] The most obvious is that the molecules are actually oriented at an angle of 54.7 ° to the substrate. For the perylene core, this is indeed possible as that angle lies between the orientations of rather lying and rather standing molecules. The second possibility is an isotropic orientation of the molecules. This is also a realistic scenario for the transition state after 4 minutes of SVA. Finally, also molecules showing an intrinsic isotropy (like spherical C_{60}) reveal an angle of 54.7 °, however, this possibility can be excluded for the perylene core of DBP.

Furthermore, it seems to be the case that also the orientation of the phenyl rings changes similar to the perylene core. However, the trend towards a more upright standing orientation is attenuated (Fig. 5.35 (e)). Nevertheless, this supports an additional result comparing the untreated sample and the DBP film solvent annealed for 6 minutes. Fig. 5.35 (a) reveals a horizontally oriented perylene core and upright standing phenyl rings. This becomes obvious by the change of the dominant absorption intensity for $\theta = 40\,°$ and $\theta = 90\,°$ in the different energy ranges for perylene core and phenyl rings, respectively. Fig. 5.35 (c), however, indicates a more upright orientation of both core and rings as the absorption intensity for perpendicular impinging X-rays is higher in both energy ranges. As the out-of-plane orientation of the phenyl rings with respect to the perylene core for DBP molecules in pristine films is the main reason for its amorphous growth, a more parallel alignment of core and rings facilitates a more crystalline growth of DBP thin films. The change in orientation of perylene core and phenyl rings due to SVA is illustrated in Fig. 5.35 (f) and (g). Summing up, it is assumed that a combination of dewetting and molecular reorientation is responsible for the strong decrease of absorption of solvent vapor annealed DBP films.

Due to all these SVA induced alterations, OPVCs containing annealed DBP as a donor layer are expected to be less efficient. Evaluating the performance of corresponding solar cells confirms these problems. For elevated SVA times ($t \geq 6\,\text{min}$) all relevant values diminish. The decreased absorption leads to a smaller J_{SC}, the fill factor declines due to poor transport and a low parallel resistance and the open-circuit voltage (V_{OC}) is reduced by enhanced recombination as the strong DBP aggregation leads to the appearance of pinholes limiting V_{OC}.[252] The origin of the loss in J_{SC} can clearly be seen in the IPCE curves (Fig. 5.36 (b)). The main contribution of DBP ($500\,\text{nm} < \lambda < 650\,\text{nm}$) nearly vanishes completely for 8 and 12 minutes. However, for 4 minutes SVA, the decrease in DBP absorbance is small and is compensated by an enhanced response from the fullerene layer ($400\,\text{nm} < \lambda < 500\,\text{nm}$), resulting in a slight increase in J_{SC}. This increase is likely due to the enlarged area of the D/A interface caused by the surface roughening observed by AFM. In addition, the series resistance decreases slightly and the FF increases, resulting in a 10 % increase in PCE from 2.3 % to 2.5 % for the device without SVA and the device treated with 4 minutes SVA, respectively (Fig. 5.36 (c)).

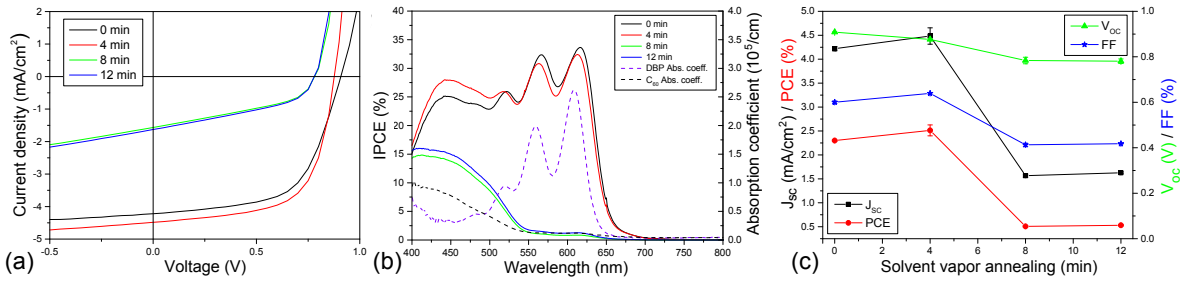

Figure 5.36: (a) J-V-characteristics, (b) IPCE curves with absorption spectra of DBP and C_{60} and (c) solar cell parameters vs. annealing time. The architecture of the solar cells is ITO(140 nm)/HIL1.3(45 nm)/DBP(30 nm)/C_{60}(45 nm)/BCP(5 nm)/Al(100 nm). The times listed in (a) and (b) represent the time of SVA treatment, which is always done after evaporation of the donor DBP.

Based on these results, the positive effects anticipated for SVA – the increase of η_{ED} and η_{CC} – do indeed occur, however the duration of SVA must be precisely controlled in order to avoid significant aggregation of molecules within the film which deleteriously affects absorption and charge transport. A possible strategy to circumvent this problem would be to increase the DBP-layer thickness, as the enhanced crystallinity should allow a thicker film without negatively impacting R_S or FF.[247] However, by changing the layer thickness, also the SVA time has to be adjusted. The result that 4 minutes of SVA are the best choice is only valid for a DBP film thickness of 15 nm.

Moreover, SVA was also tested for co-evaporated DBP:C_{60}-layers in cooperation with Florian Graßl in the scope of his bachelor's thesis.[250] The idea to use SVA on mixed layers has already been realized successfully for P3HT:PCBM polymer blends yielding a more favorable morphology.[253,254] However, AFM image reveal that already 5 minutes of SVA lead to a strong roughening of the mixed layer. Thus, similar problems like for the PHJ devices are expected. Nevertheless, OPV devices are fabricated to examine the influence of SVA on the performance of DBP:C_{60} BHJ solar cell. The thickness of the mixed layer is chosen to be 50 nm, while the mixing ratio is 1:2. Four identical samples are prepared. While one sample serves as a reference, the other three are solvent vapor annealed for 5, 10, and 15 minutes, respectively. As all the annealed samples show a strong decrease in J_{SC}, V_{OC}, and FF, no further samples have been fabricated. It is assumed that the strong aggregation of DBP which was found for PHJ solar cells is equally detrimental for BHJ as well as PMHJ devices.

5.3.3 SVA on crystalline donor DIP

In addition to DBP, the effect of SVA is also tested on DIP. Evaporated at reduced temperatures (200 K), DIP also grows amorphous on ITO.[200] However, it has already been shown that the substrate temperature plays a significant role for crystallization.[104,108,255] Already at room temperature, DIP is known to grow crystalline in Stranski-Krastanov

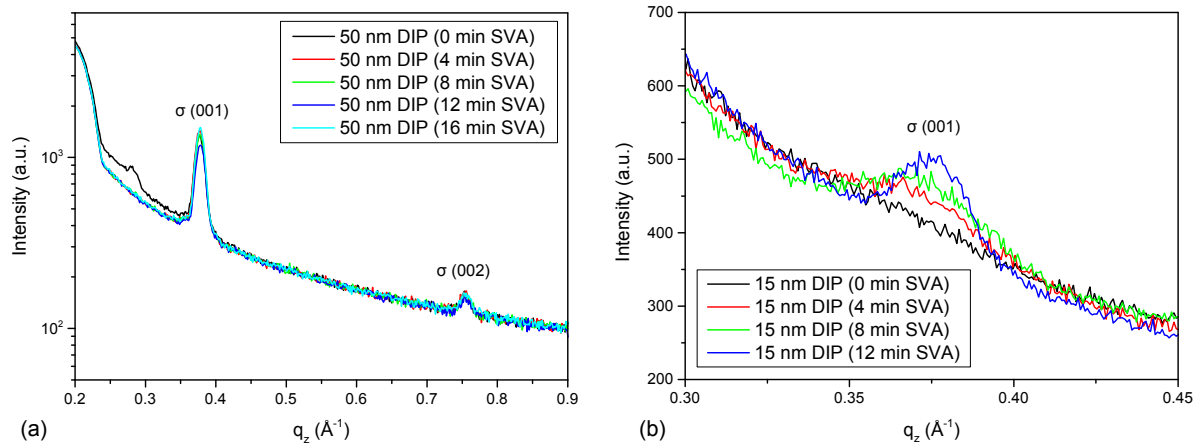

Figure 5.37: (a) Out-of-plane XRD measurements of samples consisting of ITO/HIL1.3/DIP (50 nm) either pristine or annealed for 4, 8, 12 and 16 minutes. For all samples the same peaks, $\sigma(001)$ and $\sigma(002)$, appear. They do not show any broadening due to SVA. (b) XRD measurements of samples with a reduced DIP layer thickness of 15 nm, however, reveal a growing $\sigma(001)$-peak due to SVA, indicating an increased crystallinity.

mode on various substrates.[201,202] This means that a possible roughening effect caused by SVA is expected to be more pronounced on rather thin DIP layers, which are smoother than thicker ones due to its growth mechanism. Similar to DBP, XRR measurements do not reveal any change in the out-of-plane crystallinity due to SVA on 50 nm thick DIP layers evaporated at room temperature. For the pristine as well as the SVA-treated sample, both the $\sigma(001)$ and the $\sigma(002)$-peak appear at $q_z = 0.38\,\text{Å}^{-1}$ and $q_z = 0.75\,\text{Å}^{-1}$ respectively. Moreover, neither broadening of these peaks, which indicates a change in the vertical extent of the crystalline domains, nor the presence of additional peaks are detected (Fig. 5.37 (a)). Full width at half maximum (FWHM) of each peak is determined and crystallite sizes are calculated via the modified Scherrer equation (Eq. (4.5)). The results are nearly identical, yielding vertical coherence lengths close to the layer thickness of 50 nm. Thus, SVA cannot increase the vertical extent of 50 nm thick DIP layers as already the choice of the layer thickness defines the vertical crystallite size (*cf.* subsection 5.1.1). However, the lateral grain size is expected to grow. This would be in accordance to results of DIP layers evaporated at elevated temperature,[110] which can be described as thermal annealing. However, to determine the increase of the lateral domain size via XRR, in-plane measurement on solvent vapor annealed DIP samples would have been necessary.

An effect of SVA on the crystallinity of DIP becomes apparent, however, by reducing the DIP thickness to 15 nm (Fig. 5.37 (b)). It is known that the thickness also influences the structure of DIP films.[113] Evaporated at room temperature, for such a low layer thickness the $\sigma(001)$-peak does not appear for pristine films. However, increasing the SVA time leads to a growth of the $\sigma(001)$-peak, which implies a more pronounced crystallinity of the film. This result is supported by the evaluation of 15 nm thick DIP layers

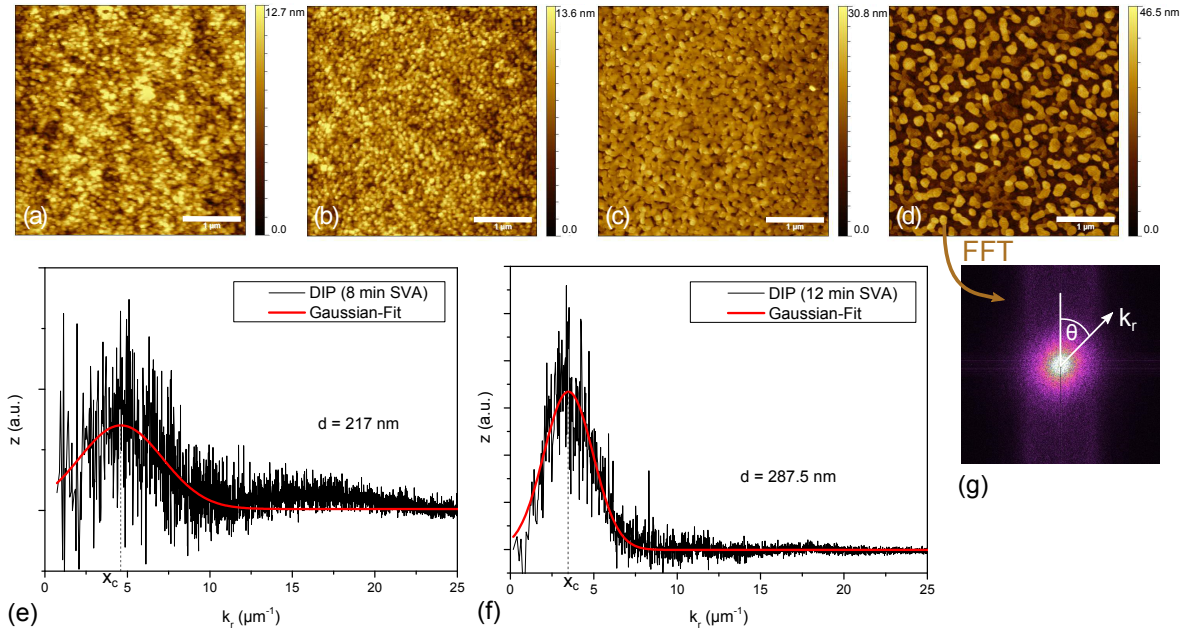

Figure 5.38: AFM images of a 15 nm DIP layer treated by SVA for (a) 0 minutes, (b) 4 minutes, (c) 8 minutes and (d) 12 minutes. By applying FFT (g) the average lateral domain distance can be obtained for the 8 minute (e) and the 12 minute (f) sample. It grows with increasing SVA time from 217 nm to 287.5 nm.

via AFM. A distinct change of topography is visible by comparing the AFM images of DIP layers which are either untreated or treated by SVA for four, eight, and twelve minutes, respectively (Fig. 5.38 (a-d)). The smooth surface of the pristine layer roughens continuously with increasing SVA time. The RMS roughness rises from 1.99 nm (0 min) to 2.14 nm (4 min) and 3.75 nm (8 min) up to 9.18 nm (12 min). Island-like structures appear on the surface with increasing diameters up to approximately 250 nm for the 12 minute sample. Thus, the increased surface roughness will provide an increased D/A interface area upon evaporation of the acceptor. At the same time, AFM images indicate that the long-range order within the DIP donor increases and this should also lead to a similar increase of structural order in the subsequently evaporated C_{60} acceptor layer.[256] This change of morphology, which has already been indicated by XRD on the 15 nm thick DIP film, is proven by means of AFM using a fast Fourier transform (FFT, Fig. 5.38 (g)). That mathematical operation converts the AFM image from the spatial domain into the frequency/wavelength domain. By that, repeating patterns coming along with crystallinity can be identified and distance distributions are provided. To interpret the results, data is averaged over the whole angle range of θ and fitted by Gaussian distributions.[110] Such a fit yields some parameters including FWHM, the area of the peak, and the position of the peak center x_c. For the desired purpose, however, only x_c is needed. By simply dividing $1/x_c$, the average lateral domain distances can be obtained. The results show, that indeed the lateral grain size grows by a factor of 1.3 from 217 nm (8 min SVA) to 287.5 nm (12 min SVA) with increasing SVA time (Fig.

5.38 (e, f). Due to the very weak crystallinity, it was not possible to detect the domain distances for the pristine and the 4 minute sample, though.

Increasing the grain size is a promising approach to increase the charge-carrier mobility within an organic semiconductor, as intermolecular charge hopping across grain boundaries, or through disordered domains, is not as efficient as within ordered domains.[257,258] To verify, OFETs are fabricated consisting of p^{++}-Si/300 nm SiO_2/20 nm TTC/25 nm DIP (x min SVA)/top contact. The top contact material is either 100 nm Al to measure electron transport or 125 nm TTF-TCNQ to investigate hole transport. SVA was performed on the DIP layer for 10 minutes and compared to a reference OFET without SVA. The expected increase of charge carrier mobility is detected for electrons. By using the Shockley method (Eq. (4.11)), one obtains $\mu_e = 6.8 \times 10^{-2}\,\mathrm{cm^2/Vs}$ for the reference and $\mu_e = 1.6 \times 10^{-1}\,\mathrm{cm^2/Vs}$ for the annealed sample. Consequently, the electron mobility in DIP has more than doubled, which is another strong indicator for the enhanced crystallinity of DIP by means of SVA. However, DIP is used in OPVCs as donor material at the anode side. Therefore it mainly transports holes. Unfortunately, hole mobility measurements on solvent vapor annealed OFETs failed due to the used top contact material. TTF-TCNQ consists of two molecules (TTF and TCNQ), which form an ion pair. Microscopy images reveal, however, that the solvent treatment seems to decompose that complex into its two separate components. Changing the contact material to nickel does also not enable any mobility measurements due to missing adhesion between nickel and DIP.

A prerequisite for good transport is a continuous organic layer. In contrast to DBP, this is given for the DIP molecules, which do not aggregate strongly in the process of SVA. As a result, a drastic decrease in absorption as was observed for the SVA treated DBP layer does not occur. In fact, absorption measurements even show a growing absorption coefficient, however it is just a minor effect (Fig. 5.39 (d)). As this effect appears over the whole measured spectral range, it is assumed to be a measurement artifact due to increased scattering caused by the enhanced surface roughness. This assumption is further supported as the main increase occurs for the 12 minutes sample. As shown before by AFM measurements, this is also the sample, which shows the most significant rise in surface RMS roughness.

NEXAFS measurements were performed to clearly identify the origin of the rising absorption coefficient. Comparing pristine and annealed DIP layers, NEXAFS measurements show no change in angular dependence, meaning that there is also no change in molecular orientation and thus absorption strength. The corresponding data is shown in Fig. 5.39 (a, b). The results for the pristine DIP film are in very good agreement to data found in literature.[96,259] The extracted intensities of the energy range between 284.5 eV and 286.5 eV confirm the tendency of standing molecules in both pristine and SVA treated DIP films (Fig. 5.39 (c)). A desired change to a more flat-lying orientation due to SVA does not occur.

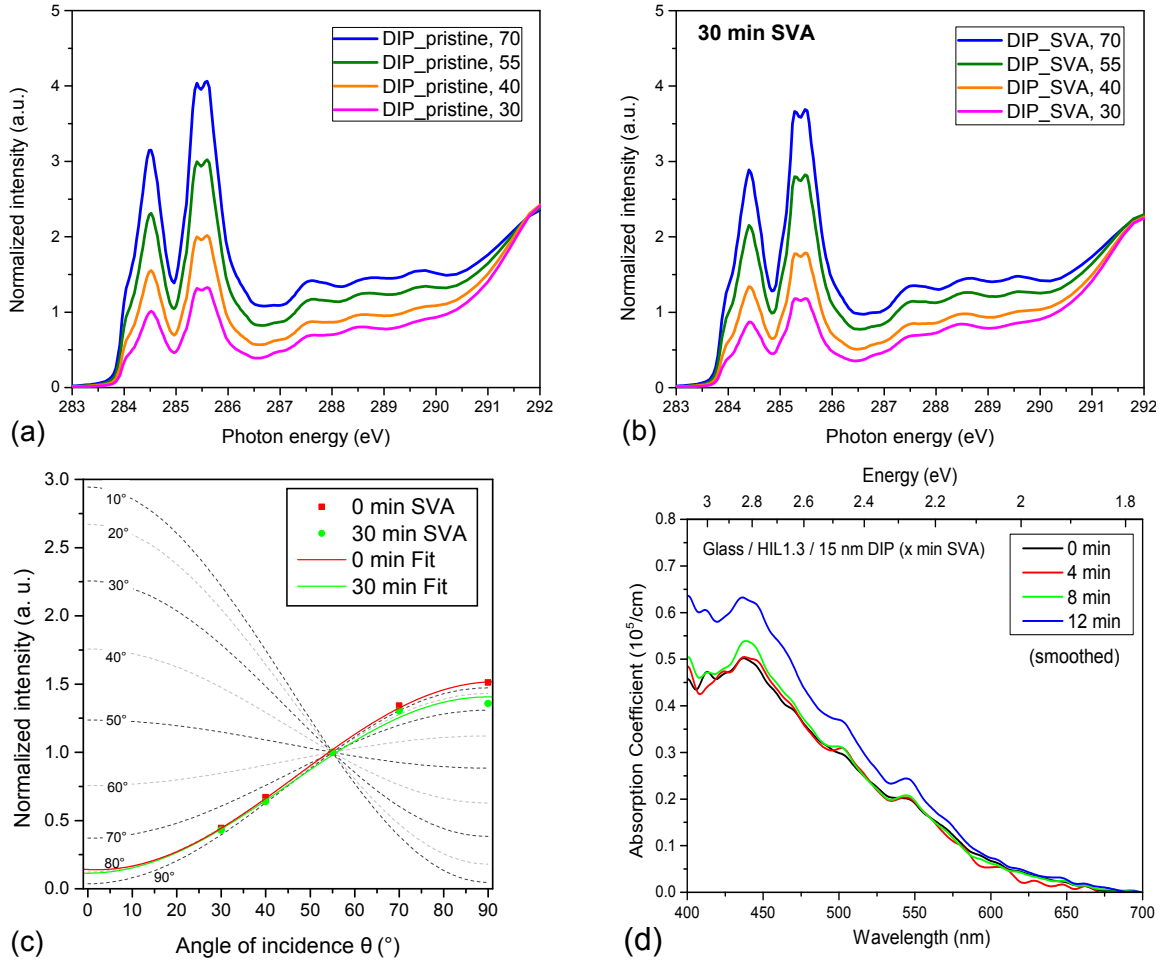

Figure 5.39: C1s NEXAFS spectra of a 15 nm DIP film annealed for 0 (a) and 30 minutes (b) at 30°, 40°, 55°, and 70° angle of incidence of the X-ray photons. No change in dichroism is visible, indicating that there is no change in molecular orientation. This is confirmed by the extracted angular dependence of the NEXAFS intensity in the energy range from 284.5 eV to 286.5 eV (c). Therefore, the increase in the absorption coefficient due to SVA (d) originates from enhanced scattering at the roughened DIP surface. The NEXAFS data was again recorded by Dr. Andreas Opitz (HU Berlin).

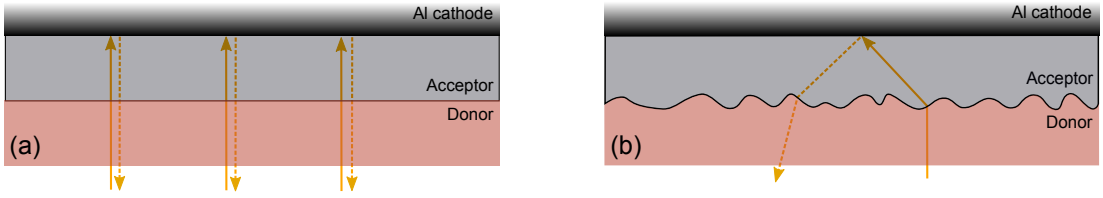

Figure 5.40: Sketch of light beams impinging on the donor and being reflected at the Al cathode. Due to a roughened interface, the light path through mainly the acceptor but also through the donor is enhanced in (b) compared to the smooth interface in (a). For that reason, more excitons are generated in OPVCs with a rough D/A interface.

It is assumed that such an alteration is more likely for initially amorphous layers. However, this confirms the interpretation that more scattering occurs at the roughened DIP surface, which results in an extended light path. In turn, this leads to more excitons generated within the organic layers, mainly in the acceptor layer (Fig. 5.40). As a result, the corresponding solar cells show a small but continuous increase in J_{SC}. Based on the AFM images, absorption, and NEXAFS measurements, it can be assumed that both the enlarged interface as well as the extended light path due to enhanced scattering are responsible for this gain. Moreover, the FF increases by almost 10 % while V_{OC} remains unaffected. The gain in FF comes along with a decrease in R_S, which drops continuously with increasing SVA time (Fig. 5.41 (d)). As a consequence, the efficiency of DIP-based solar cells is improved through SVA by 16.8 % (Fig. 5.41 (a, b)). These results are comparable with improvements achieved using glancing angle deposition.[203] However, SVA is the more viable method as it is very easy to handle and does not require any sophisticated equipment.

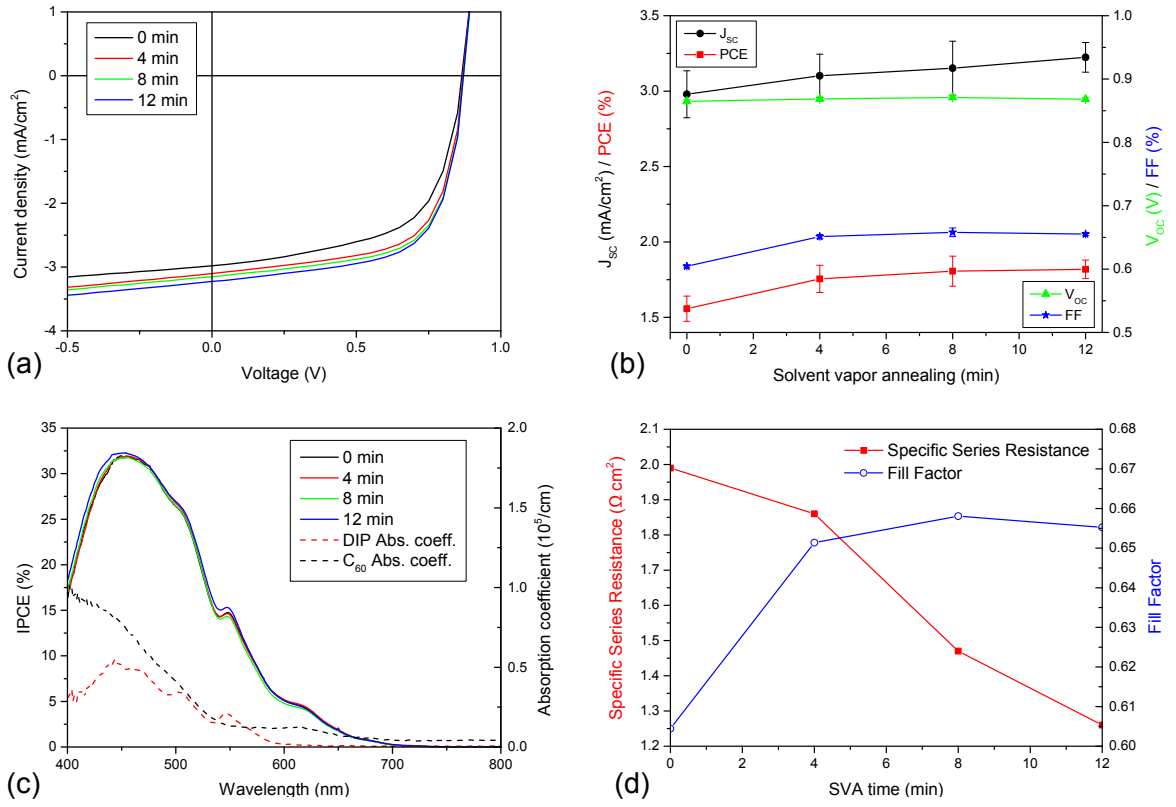

Figure 5.41: (a) J-V-characteristics, (b) solar cell parameters vs. annealing time, (c) IPCE curves with absorption spectra of DIP and C_{60}, and (d) development of R_S and FF vs. SVA time. The architecture of the solar cells is ITO(140 nm)/HIL1.3(45 nm)/DIP(30 nm)/C_{60}(45 nm)/BCP(5 nm)/Al(100 nm). The times listed in (a) and (c) represent the time of SVA treatment, which is always done after evaporation of the donor DIP.

Summing up, it can be shown that also already crystalline layers can be affected positively using SVA. Again the efficiencies η_{ED} and η_{CC} are raised, apparent from the gain in J_{SC} and FF, respectively. Moreover, negative effects like a strong aggregation or an unfavorable reorientation of the molecules accompanied with a decreasing η_{Abs}, which were observed for amorphous DBP, do not occur. However, as DIP inherently yields poor absorption, even for the SVA-treated case, the PCE is low. In this work it was increased from 1.55 % (no treatment) to 1.8 % applying 12 minutes SVA.

5.3.4 SVA on exciton blocking layer DIP

In a last step, solar cells are fabricated consisting of two donor layers, combining a 15 nm thick DIP layer with a 15 nm DBP layer, which are evaporated consecutively. Thus, in sum, there is again an overall donor thickness of 30 nm. In this case, DBP is the primary absorber while DIP acts as an exciton blocking layer (*cf.* section 5.2.1). For these solar cells only the DIP layer is treated by use of SVA. The idea is to combine the positive effects observed for solvent vapor annealed DIP with the exciton blocking concept[119,232] and strongly absorbing active organic semiconductors. For that reason, C_{70} replaces C_{60} as acceptor material to achieve more efficient absorption.

Again, it is not useful to perform the SVA after evaporation of DBP, because the strong aggregation of the molecules also occurs on a DIP substrate accompanied with the drop in absorption for longer SVA times. Absorption measurements even show that in this case the aggregation process of DBP already starts for shorter SVA times compared to HIL1.3/DBP (SVA) without DIP blocking layer. As a result, four minutes of SVA are already too long (Fig. 5.42 (a)). This can be explained by the different substrates. The surface of DIP is rougher than that of HIL1.3. Consequently, also the DBP layer evaporated on top is expected to be rougher. In this case it is easier for the $CHCl_3$ molecules to penetrate in and act on the DBP layer. As a result, the whole reorganization process and thus also the aggregation of the DBP molecules is accelerated. Therefore, the decrease of J_{SC} and FF sets in for shorter SVA times, too.

However, by treating only the exciton blocking layer DIP with solvent vapor these parameters can be enhanced. The gain in J_{SC} indicates that the SVA-induced increase in surface roughness of the DIP layer propagates to the DBP/C_{70} interface, where excitons dissociate and by that determine J_{SC}. This is confirmed by AFM images of samples consisting of glass/45 nm HIL1.3/15 nm DIP/15 nm DBP. The annealing was performed on DIP for 4, 8 and 12 minutes. The RMS roughness of the surface of the subsequently evaporated DBP layer increases from 0.69 nm to 1.44 nm and 3.14 nm up to 4.24 nm (Fig. 5.42 (b-d)). This means that the evaporation of the DBP layer smoothens the roughened DIP layer, however, as desired, the D/A interface is enlarged compared to a pristine DBP film. Moreover, scattering that occurs at the rough DIP surface should enhance the path of light through the DBP layer and by that also the absorption. Whether the enhanced crystallinity of the DIP layer also leads to a higher order in the amorphous

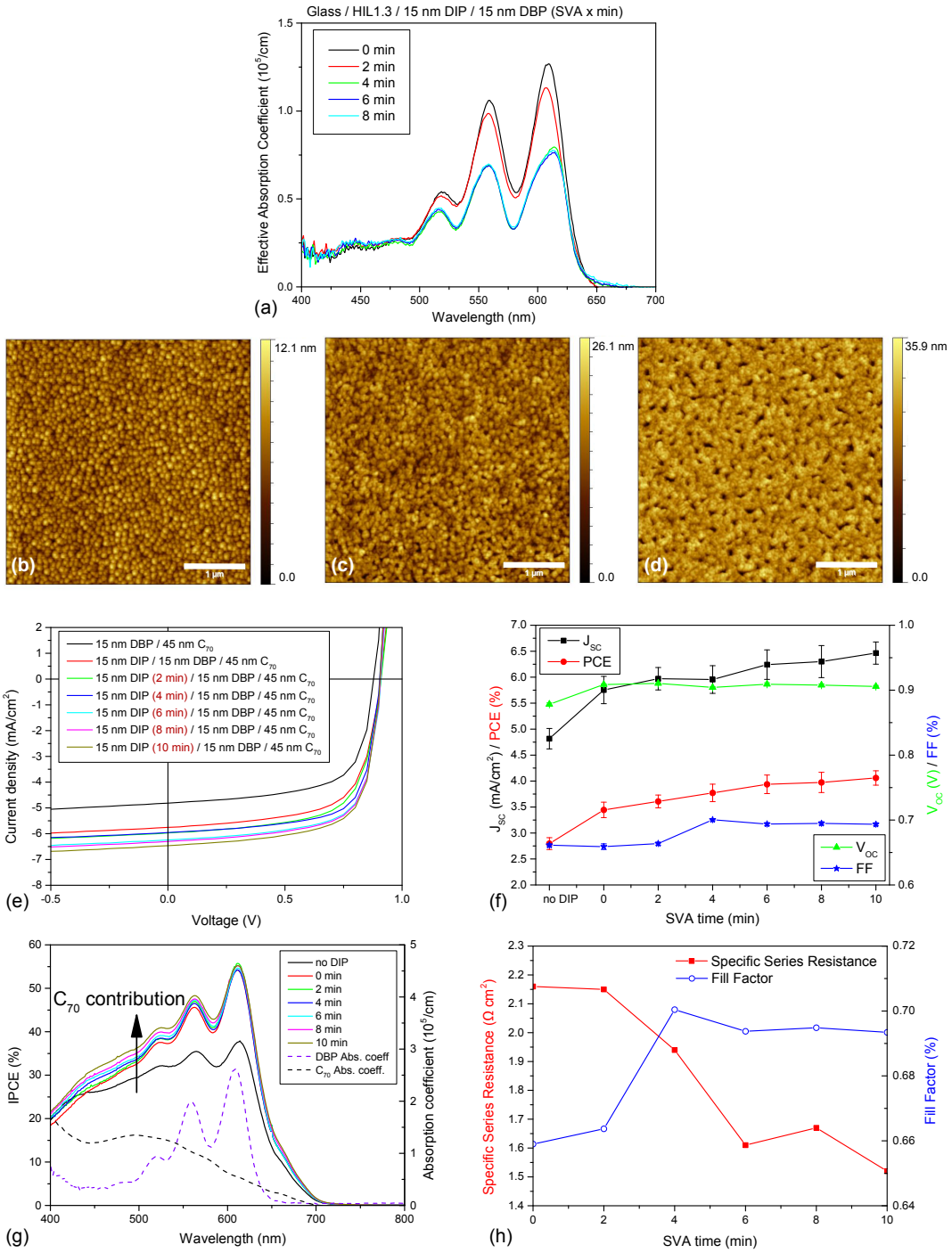

Figure 5.42: (a) Correlation between SVA time and absorption drop of a DIP/DBP (SVA) sample. Note that the spectra are the sum of 15 nm of DIP and 15 nm of DBP, however, the absorption coefficient is calculated with the overall thickness of 30 nm.
AFM reveals increasing roughness of a 15 nm DBP layer evaporated on a 15 nm DIP layer, solvent vapor annealed for 4 (b), 8 (c), and 12 (d) minutes.
(e) J-V-characteristics, (f) solar cell parameters vs. annealing time, (g) IPCE curves with absorption spectra of DBP and C_{70} and (h) development of R_S and FF vs. SVA time.

DBP layer cannot be clearly confirmed. However, it is suggested that this is the case, as again the FF of the corresponding photovoltaic cells increases while the values of their series resistance decline (Fig. 5.42 (h)). This correlation is not linear, which shows that R_S is just one factor contributing to FF.[71] The expected gain in J_{SC} appears (Fig. 5.42 (e, f)) and the PCE can be increased by 20 % from 3.4 % to 4.1 %. Compared to the reference without EBL with an initial PCE of 2.8 % it can be stated that by combining the exciton blocking concept with SVA an improvement of almost 50 % can be achieved. The results are summarized in Tab. 5.6.

EBL	SVA (min)	J_{SC} (mA/cm^2)	V_{OC} (V)	FF (%)	R_S (Ωcm^2)	PCE (%)
no	no	4.82	0.88	66.1	1.63	2.80
DIP	no	5.75	0.91	65.9	2.16	3.44
DIP	2	5.97	0.91	66.4	2.15	3.61
DIP	4	5.96	0.90	70.0	1.94	3.77
DIP	6	6.24	0.91	69.4	1.61	3.94
DIP	8	6.30	0.91	69.5	1.67	3.97
DIP	10	6.46	0.91	69.3	1.52	4.06

Table 5.6: Efficiency enhancement of an OPVC consisting of ITO/HIL1.3/(15 nm DIP (y min SVA))/15 nm DBP/45 nm C_{70}/5 nm BCP/100 nm Al. Efficiency is enhanced by SVA of the exciton blocking DIP layer.

IPCE-curves (Fig. 5.42 (g)) show that the gain in J_{SC} caused by the insertion of the additional exciton blocking layer is mainly due to a greater contribution of excitons generated within the DBP layer. However, the SVA on DIP leads mainly to more contribution of the fullerene C_{70}. A similar result was obtained for SVA on DBP (*cf.* Fig. 5.36 (b)) where C_{60} was used as acceptor material. Thus, this trend is not influenced by changing the acceptor from C_{60} to C_{70}. It is assumed that this behavior originates from two other factors. First, as already mentioned, the light path, which is enhanced mainly within the acceptor. Second, the longer exciton diffusion lengths in fullerenes compared to that in DBP. This multiplies the effect of the enhanced light path, as not only more excitons are generated, additionally more excitons can reach the D/A interface, where they are dissociated.

By changing the hole-injection layer from HIL1.3 to molybdenum oxide (MoO_x) another interesting feature of SVA occurs; it can reduce the energetic barrier between the Fermi level E_F of the ITO anode and the HOMO level of the donor (or exciton blocking) layer DIP. It has already been shown, that such energetic barriers cause the appearance of s-shapes in j-V curves of OPVCs.[77,260] Such an s-shape behavior also occurs for solar cells with the architecture: ITO/10 nm MoO_x/15 nm DIP/15 nm DBP/40 nm C_{60}/10 nm BCP/100 nm Al. However, by applying SVA onto DIP, this s-shape is reduced continu-

ously with increasing SVA time (Fig. 5.43 (a)). It is assumed that a changing ionization potential of DIP is connected to that effect. More precisely, the HOMO energy level of DIP on MoO_x seems to be slightly lifted by means of SVA. UPS measurements would be necessary to validate this assumption, however, have not been performed within the scope of this thesis. As the ionization potential of DIP depends on the molecular orientation,[261,262] SVA possibly changes the orientation of DIP molecules on MoO_x. Another interesting aspect, is the vanishing s-shape for samples of the same architecture, which are solvent vapor annealed after the evaporation of DBP (Fig. 5.43 (b)). This proves that SVA not only acts on the top layer which is in direct contact, it has the potential to influence subjacent layers as well, depending on the layer thicknesses.

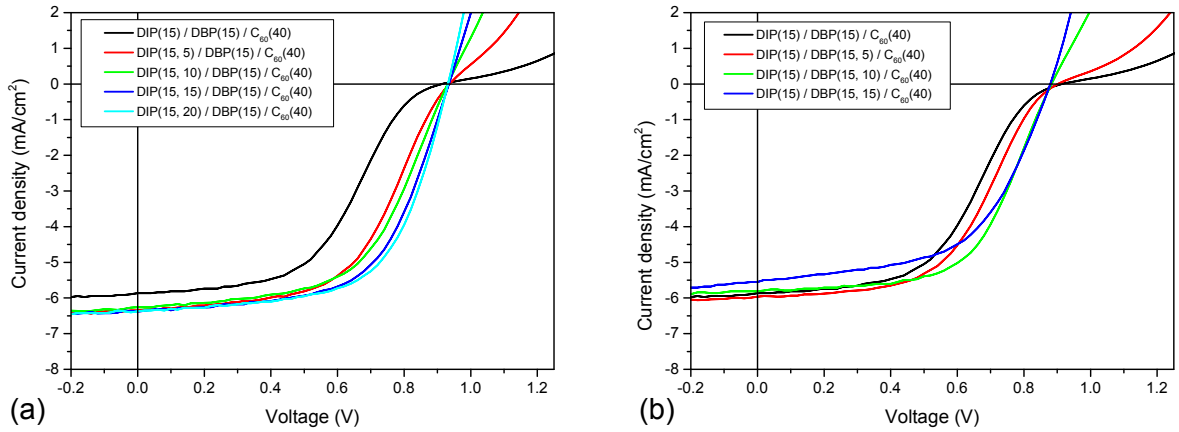

Figure 5.43: J-V-curves of solar cells consisting of ITO/10 nm MoO_x/15 nm DIP/15 nm DBP/40 nm C_{60}/10 nm BCP/100 nm Al. Due to SVA, the s-shape vanishes in both cases, (a) when applied after evaporation of DIP, and (b) when acting on subsequently evaporated DBP. The numbers in brackets represent the layer thickness and the SVA duration, respectively.

In conclusion, the influence of solvent vapor annealing on the morphology of perylene-based OPVCs could be shown. Depending on the initial state, SVA induces major or minor alterations. While initially amorphous DBP layers reorganize completely, the changes in already crystalline DIP films are less pronounced. Nevertheless, for both material systems several processes contributing to the conversion of light to electrical power can be improved. In fact, SVA contributes to a majority of the sub-processes involved in various ways. For instance, the absorption efficiency η_{Abs} is influenced by an aggregation and/or by reorientation of the molecules. The reorganization process also leads to a higher structural order within the organic film. This enhanced crystallinity, resulting in a decreasing series resistance, has a positive impact on transport processes so that the efficiencies of exciton diffusion η_{ED} and charge collection η_{CC} go up, resulting in a higher FF. Moreover, η_{ED} is increased by a roughening of the D/A interface, as this enlargement enables more excitons to reach the interface before recombining within the bulk. In this way, a higher J_{SC} can be achieved. However, it could be shown that the SVA-induced changes on organic solar cells are not necessarily positive and depend on

some crucial correlations, which are different for each organic material. Thus, SVA has the potential to improve organic solar cells of various compositions, nevertheless for each material a suitable solvent, the best layer thickness and a convenient SVA time has to be found.

5.4 Introduction of ZCl as acceptor material in organic photovoltaic cells

ZCl is a very new material, which was first synthesized in 2013, so that only few publications exist concerning the application of ZCl in organic solar cells.[83,134,135] It is not viable commercially but is exclusively synthesized by the Department of Chemistry of the University of Southern California, Los Angeles in the group of Prof. Mark Thompson. Due to its energy level alignment, ZCl is suitable for the application as acceptor material in OPVCs. Today, the vast majority of acceptor materials are fullerenes as they possess some unique advantageous features. However, their energy level alignment limits E_{DA}, so that the maximal achievable V_{OC} of fullerene-based OPVCs in combination with common donors does usually not exceed 0.9 V. ZCl offers the possibility to enhance V_{OC} on the one hand by a higher-lying LUMO (Fig. 3.1). On the other hand, it is reported to belong to a group of molecules, which are able to undergo a so-called symmetry-breaking charge transfer (SBCT). This process might offer a potential route to minimize the driving force necessary to form the CT state, which in turn would reduce recombination losses and thus enhance V_{OC}.[135] However, due to the novelty of ZCl, many uncertainties and open questions still exist.

Within a collaboration between USC and Augsburg University, ZCl could also be investigated as new acceptor material in organic solar cells within our group. First results were obtained in cooperation with Philippe Linsmayer in the scope of his bachelor's thesis.[263] It shows up that ZCl features very strong absorption between $450\,\mathrm{nm} < \lambda < 570\,\mathrm{nm}$. Its absorption coefficient α within this spectral range considerably exceeds the values of α of all other materials, which were considered within this thesis (Fig. 3.2 (a)). However, the main absorption occurs in a rather narrow regime, so that the overall absorption over the whole visible spectrum is (only) similar to that of e.g. DBP (Fig. 3.2 (b)). Moreover, XRD measurements do not reveal any diffraction peaks, which would indicate crystallinity of the ZCl thin film. This is in accordance with literature, which describes ZCl films as amorphous.[83]

Due to its energy level alignment, a combination of ZCl with DBP as donor material seems to be promising. The E_{DA} of this conjunction predicts a large V_{OC} and the high absorption coefficients of both materials a large J_{SC}. However, there are also some significant drawbacks. Both materials are amorphous and possess a short exciton diffusion length. For that reason, the photoactive layers have to be chosen rather thin. The J-V-characteristics of a solar cell with 20 nm DBP/20 nm ZCl reveal that an OPVC with this material combination actually possesses a remarkably large V_{OC} of 1.32 V, however, underperforms regarding J_{SC} (Fig. 5.44 (a)). The comparatively small J_{SC} of $2.1\,\mathrm{mA/cm^2}$ can be explained by some interacting factors. Intrinsicly, the thin layers cannot provide complete absorption of the impinging light. Moreover, the small layer thicknesses do not allow the exploitation of cavity effects arising from reflected light at the back electrode (*cf.* subsection 5.1.3). Nevertheless, a simple increase of the layer thicknesses cannot

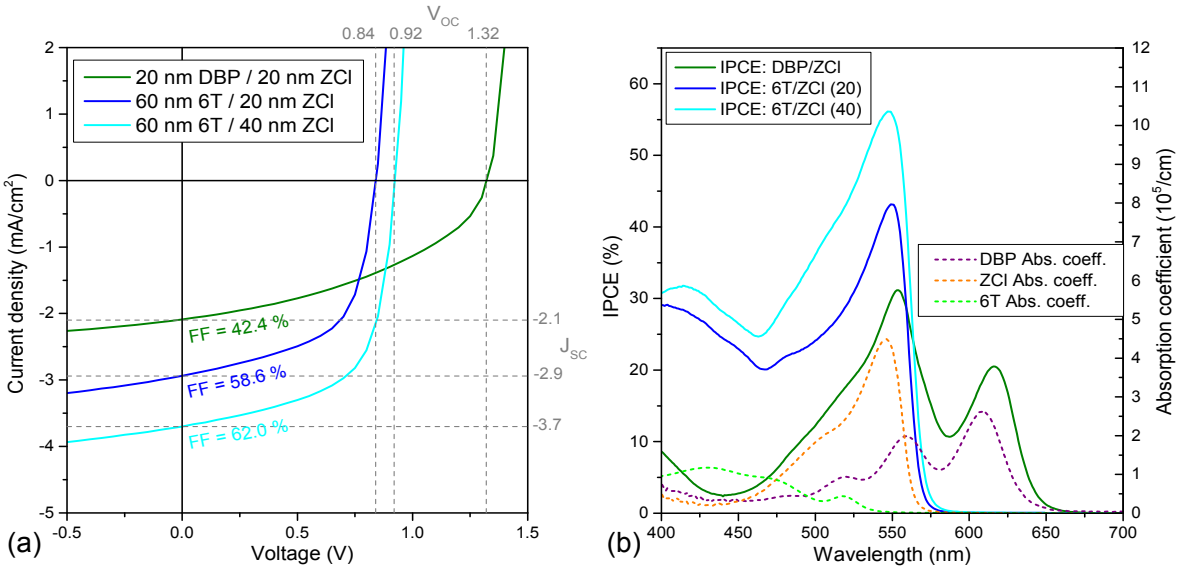

Figure 5.44: Comparison of OPVCs containing ZCl as acceptor with two different donors, DBP and 6T. The layer thickness of ZCl in combination with 6T is chosen to be either 20 nm or 40 nm. The corresponding J-V-characteristics are shown in (a), while the results of the IPCE measurements are depicted in (b).

solve this problem, as this would indeed enhance absorption, however, most of the generated excitons would not reach the D/A interface and thus would not contribute to the current. Another problem concerning the J_{SC} of this material combination is parasitic absorption, which occurs because both materials show strong absorption at similar wavelengths while almost no absorption happens at smaller wavelengths below $\lambda < 500\,\text{nm}$. This is confirmed by the IPCE measurements depicted in Fig. 5.44 (b). Furthermore, the amorphous character of both material also leads to a rather low fill factor for that OPVC of merely 42.4 %.

Higher J_{SC} and FF can be obtained by replacing DBP with 6T (Fig. 5.44 (a)). At first, solar cells are produced with a photoactive layer of 60 nm 6T and 20 nm ZCl. Although 6T shows significantly weaker absorption compared to DBP, this OPVC provides a higher J_{SC} of $2.9\,\text{mA/cm}^2$, which can be explained by a more complementary absorption and the increased donor thickness. A thicker donor layer is enabled by the higher structural order within 6T, coming along with a comparably large exciton diffusion length of approximately 60 nm.[100] The enhanced crystallinity is also responsible for the improved FF of 58.6 %. However, V_{OC} drops to 0.84 V. A further improvement of all relevant parameters can be obtained by doubling the ZCl layer thickness to 40 nm. The reason for the improved $V_{OC} = 0.92\,\text{V}$ can most likely be ascribed to incomplete covering of the rough 6T film by the thin 20 nm ZCl layer leading to pinholes and thus enhanced recombination reducing V_{OC}.[252] The extrem roughness of the 6T film can be confirmed via AFM images.[263] The improvement of J_{SC} to $3.7\,\text{mA/cm}^2$ and FF to 62 %

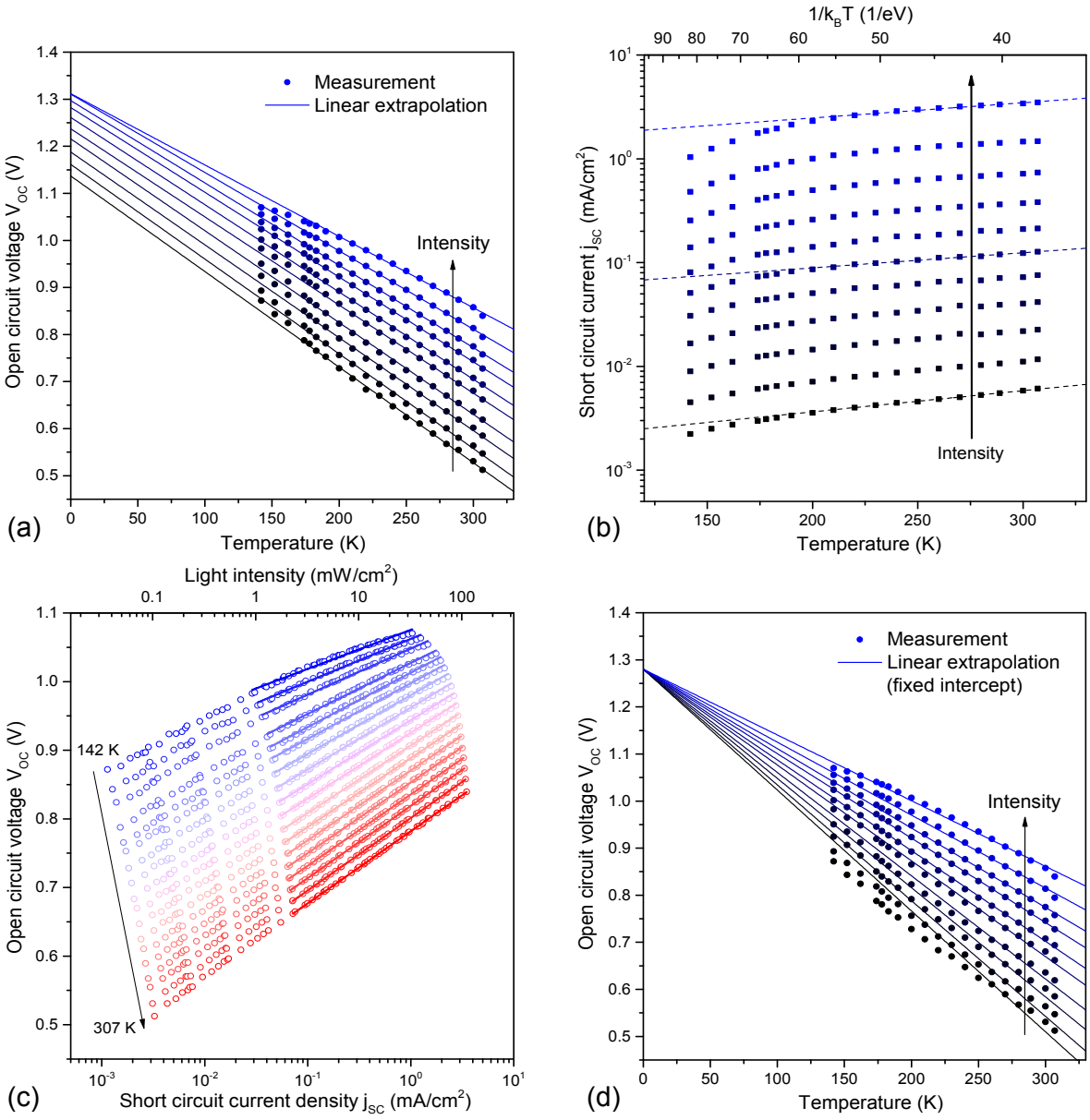

Figure 5.45: Temperature and intensity dependent measurements of V_{OC} and J_{SC} of a solar cell consisting of ITO (140 nm)/HIL1.3 (45 nm)/6T (60 nm)/ZCl (20 nm)/BCP (5 nm)/Al (100 nm). Different temperatures are enabled by a liquid nitrogen cryostat, while a white LED serves as light source and provides a total of 66 different light intensities between 1.2 and 1.1 $\times 10^{-3}$ suns. The results of V_{OC} vs. T and J_{SC} vs. T measurements for different illumination intensities are shown in (a) and (b), respectively. The summarized values of V_{OC} and J_{SC} at different temperatures are shown in (c). The solid lines are fits with Eq. (5.5) yielding n_{light} and j_0 shown in Fig. 5.46 (a). As shown in (d), the extrapolations of the temperature dependent V_{OC} values for different illumination intensities can be forced to end at one distinct photovoltaic gap energy, however, yielding good results only for high illumination intensities. For reasons of clarity some measured data sets are omitted within (a), (b) and (d).

is probably explained by the cavity effect. Due to the thicker acceptor, much more excitons are generated in close proximity to the D/A interface, so that less excitons are lost due to recombination within the bulk. As a consequence, the contributions of both 6T as well as ZCl to J_{SC} are enhanced as it is verified by IPCE measurements (Fig. 5.44 (b)). In addition, the rough 6T surface causes a large D/A interface advantageous to η_{ED} and is thus another reason for the improved values of J_{SC} and FF.

In the following, temperature and intensity dependent electrical characterization of the ZCl containing solar cells is carried out and presented in Fig. 5.45. Data measurement was performed in collaboration with Mark Gruber and Andrew Bartynski. As dark current characteristics revealed error-prone results (*cf.* subsection 5.1.4), the focus will be exclusively on measurements under open-circuit and short-circuit conditions. The first solar cell to be considered is the one with the 20 nm ZCl acceptor layer evaporated on 60 nm 6T. At first, V_{OC} vs. T measurements are performed for different illumination intensities (Fig. 5.45 (a)). Linear extrapolations of the obtained data yields, except for the highest intensities, a monotonic decrease of E_{PVG} with decreasing intensities, so that its value deviates by almost 0.2 eV. As a consequence, the method to force all extrapolations to one single value fails for low intensities (Fig. 5.45 (d)). The J_{SC} vs. T dependence in Fig. 5.45 (b), however, depicts the expected $\ln(J_{SC}) \propto -1/k_BT$ behavior in the high temperature range above 200 K. Subsequently, the received data of V_{OC} is plotted against J_{SC} for all measured temperatures in Fig. 5.45 (c) and fitted in the high intensity regime with Eq. (5.5). These fits yield the temperature dependent values of the light ideality factor and the recombination current shown in Fig. 5.46 (a). At room temperature the

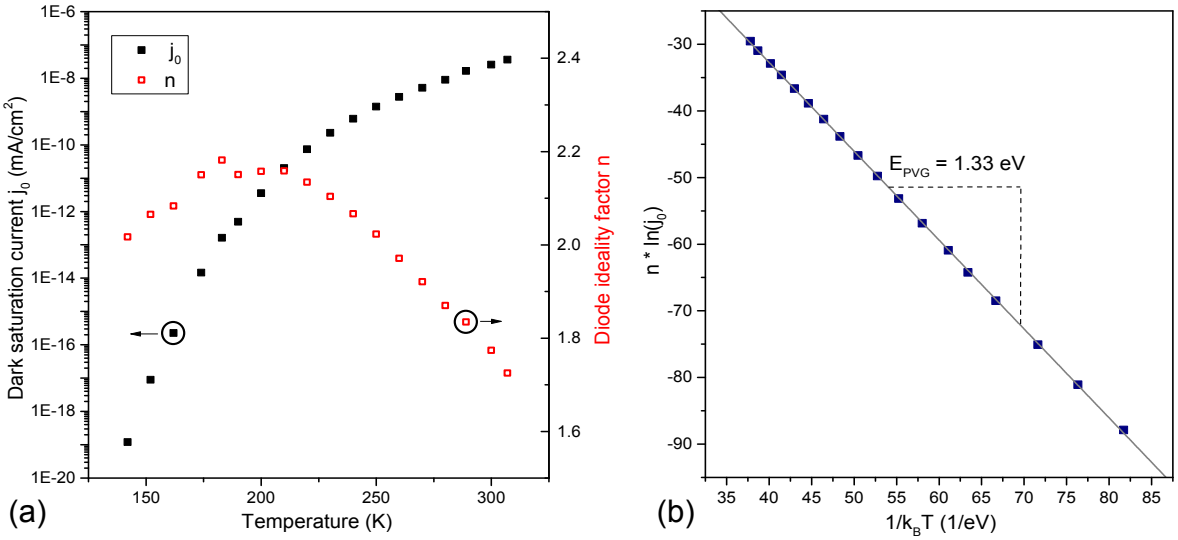

Figure 5.46: (a) Dark saturation current j_0 and diode ideality factor n_{light} plotted against temperature obtained by fits to the high intensity part of the V_{OC} vs. J_{SC} diagram shown in Fig. 5.45 (c). The slope of the $n \cdot \ln(j_0)$ vs. $1/k_BT$ diagram in (b) provides a photovoltaic gap of 1.33 eV for the 6T/ZCl (20 nm) solar cell.

comparatively high value of $n_{\text{light}} \approx 1.8$ confirms the rather high recombination losses, which are expected due to the incomplete covering of the rough 6T donor layer by 20 nm of ZCl. The behavior of j_0 for high temperatures above 200 K nicely follows Eq. (5.4), before showing a steeper decrease for lower temperatures. The photovoltaic gap of this solar cell can then be estimated by combining the obtained values of n_{light} and j_0 (Fig. 5.46 (b)). The result of $E_{\text{PVG}} = 1.33$ eV is in good accordance with the estimated value following from the extrapolation of V_{OC} vs. T data for the highest illumination intensity.

Finally, $n_{\text{light,diff}}$ is determined following Eq. (5.7) and is depicted together with the light ideality factors obtained from the slopes of the V_{OC} vs. T measurements (Fig. 5.45 (a), (d)) in Fig. 5.47 (a). The results confirm an ideality factor of $n = 1.8$, which can be found over a broad voltage range. Only the value of the ideality factor calculated by Eq. (5.9) from the V_{OC}(T) slope without fixed intercept decreases continuously for decreasing voltages due to deviating values of E_{PVG} at 0 K (*cf.* Fig. 5.45 (a)). Interestingly, $n_{\text{light,diff}}$ shows almost no intensity dependence at high temperatures (Fig. 5.47 (b)). From this it follows that within this OPVC hardly any light induced detrapping occurs. A possible explanation for this behavior is the presence of deep traps with energies exceeding the additional energy input due to illumination. Moreover, it is conceivable that the enhanced recombination due to pinholes, which does not occur for all other investigated solar cells, comes into play here.

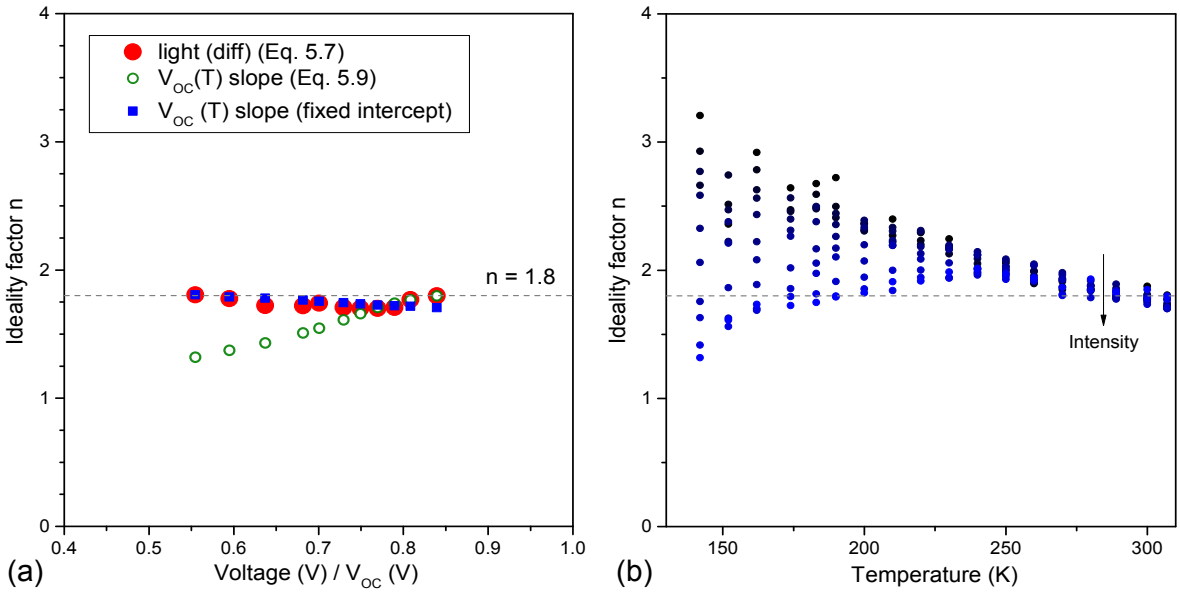

Figure 5.47: (a) Ideality factors determined in different ways are plotted against (open circuit) voltage. Around V_{OC} the values obtained by all methods approach $n = 1.8$. (b) Hardly no detrapping is visible due to increasing illumination intensities, so that the differential light ideality factors shows almost no intensity dependence, at least for high temperatures around RT.

This would mean that trap-assisted recombination is not the main recombination loss channel here and plays a comparatively smaller role than indicated by the high value of $n = 1.8$. This in turn could explain why an altered illumination intensity does not affect the ideality factor.

To circumvent the problem of incomplete 6T covering and thus enhanced recombination losses, the ZCl layer thickness is doubled to 40 nm. By looking at the corresponding V_{OC} vs. T data of this OPVC, it is striking that the estimated E_{PVG} raises by approximately 0.15 eV to 1.48 eV for maximal illumination intensity (Fig. 5.48 (a)). This increase is clearly confirmed by the slope of the $n \cdot \ln(j_0)$ vs. $1/k_BT$ plot (Fig. 5.49 (b)). As donor and acceptor material are identical of the compared solar cells, this increase can clearly be attributed to reduced recombination due to less (or even no) pinholes. Nevertheless, extrapolations of different intensity data do again not end up at one single value of E_{PVG}, so that the fixed intercept method does also not work properly here (Fig. 5.48 (d)). As expected, the temperature dependent behavior of J_{SC} is more or less identical comparing the solar cells with 20 nm and 40 nm ZCl (Fig. 5.45 (b) and Fig. 5.48 (b), respectively). The values of j_0 and n_{light} are then again obtained by fits to the V_{OC} vs. J_{SC} data (Fig. 5.45 (c)). The reduced recombination becomes apparent by a comparison of the fit results. The recombination current j_0 of the OPVC with 40 nm ZCl (Fig. 5.49 (a)) decreases roughly by two orders of magnitude, compared to the thinner device, while also the ideality factor drops to approximately $n_{light} = 1.55$ at room temperature.

This ideality factor further decreases down to $n = 1.44$ when it is determined differentially or by the slopes of the V_{OC} vs. T data (Fig. 5.50 (a)) and is thus significantly smaller than $n = 1.8$, which was found previously for the OPVC with only 20 nm ZCl. However, compared to DBP/C_{60} solar, which were investigated in subsection 5.1.4, this value is still comparably high and indicates that trap-assisted recombination plays a significant role for that material combination. Illumination induced detrapping can be observed when plotting the intensity dependent light ideality factor against temperature (Fig. 5.50 (b)). Such detrapping, which could not be found for the solar cell containing only 20 nm ZCl, indicates that the previously formulated deep trap theory is improbable for this material combination. All observed peculiarities could rather be traced back to the incomplete covering of the rough 6T film with the acceptor layer.

As a consequence of all these results, it can be stated, that the applied method of temperature and intensity dependent electrical characterization is better suited to solar cells with perfectly matched layer thicknesses, which are not affected by any additional loss channels. Only this way, correct and comparable values of E_{PVG}, n and j_0 can be obtained for a given donor-acceptor combination.

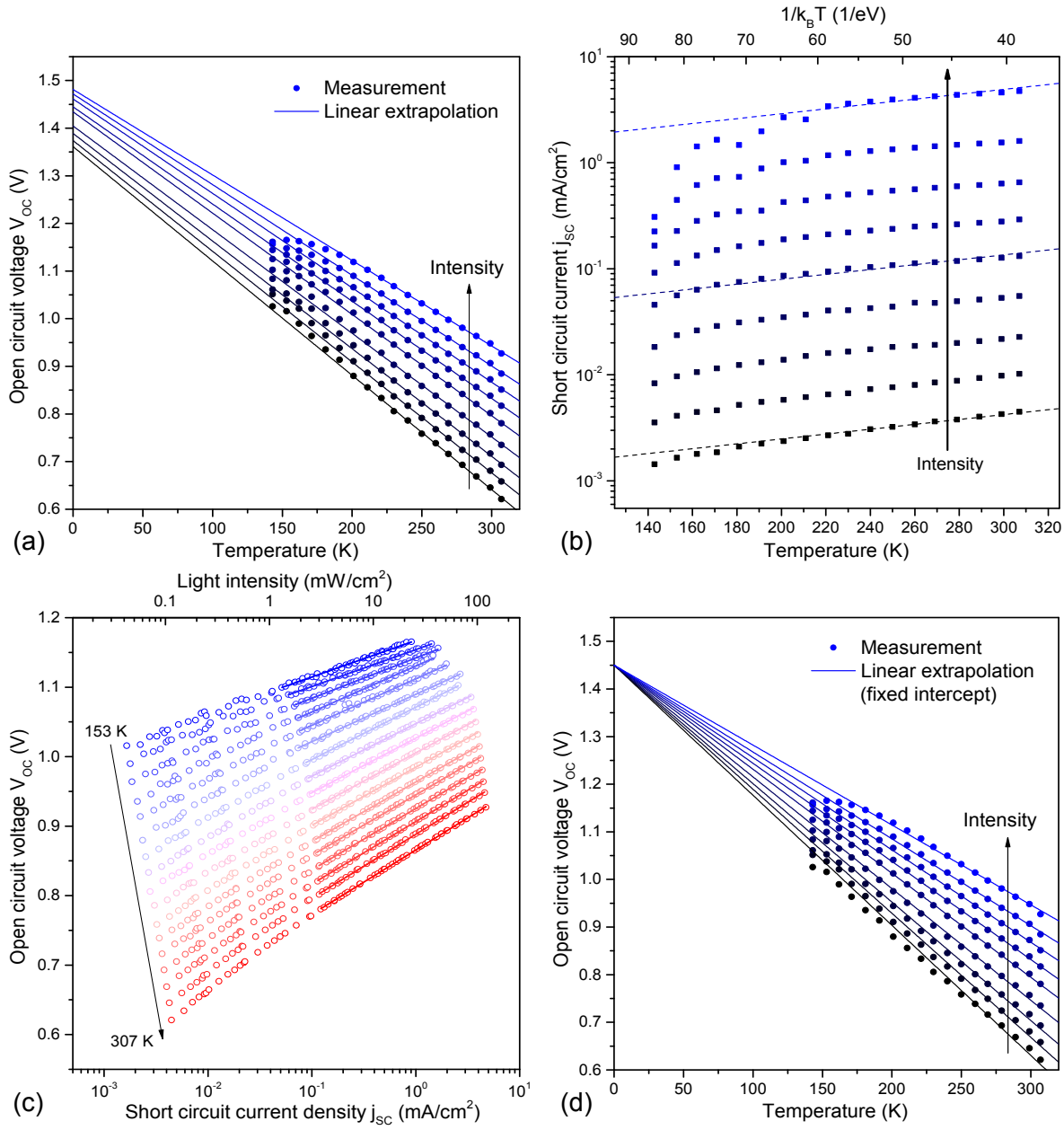

Figure 5.48: Temperature and intensity dependent measurements of V_{OC} and J_{SC} of a solar cell consisting of ITO (140 nm)/HIL1.3 (45 nm)/6T (60 nm)/ZCl (40 nm)/BCP (5 nm)/Al (100 nm). Different temperatures are enabled by a liquid nitrogen cryostat, while a white LED serves as light source and provides a total of 66 different light intensities between 1.2 and 1.2 $\times 10^{-3}$ suns. The results of V_{OC} vs. T and J_{SC} vs. T measurements for different illumination intensities are shown in (a) and (b), respectively. The summarized values of V_{OC} and J_{SC} at different temperatures are shown in (c). The solid lines are fits with Eq. (5.5) yielding n_{light} and j_0 shown in Fig. 5.49 (a). As shown in (d), the extrapolations of the temperature dependent V_{OC} values for different illumination intensities can be forced to end at one distinct photovoltaic gap energy, however, again yielding good results only for high illumination intensities. For reasons of clarity some measured data sets are omitted within (a), (b) and (d).

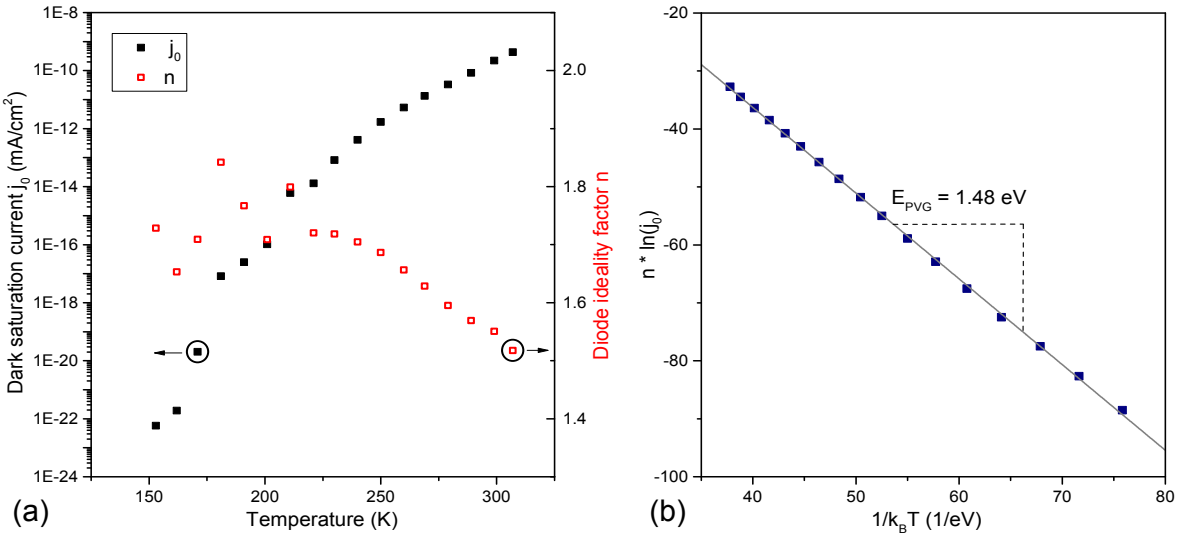

Figure 5.49: (a) Dark saturation current j_0 and diode ideality factor n_{light} plotted against temperature obtained by fits to the high intensity part of the V_{OC} vs. J_{SC} diagram shown in Fig. 5.48 (c). The slope of the $n \cdot \ln(j_0)$ vs. $1/k_{\text{B}}T$ diagram in (b) provides a photovoltaic gap of 1.48 eV for the 6T/ZCl (40 nm) solar cell.

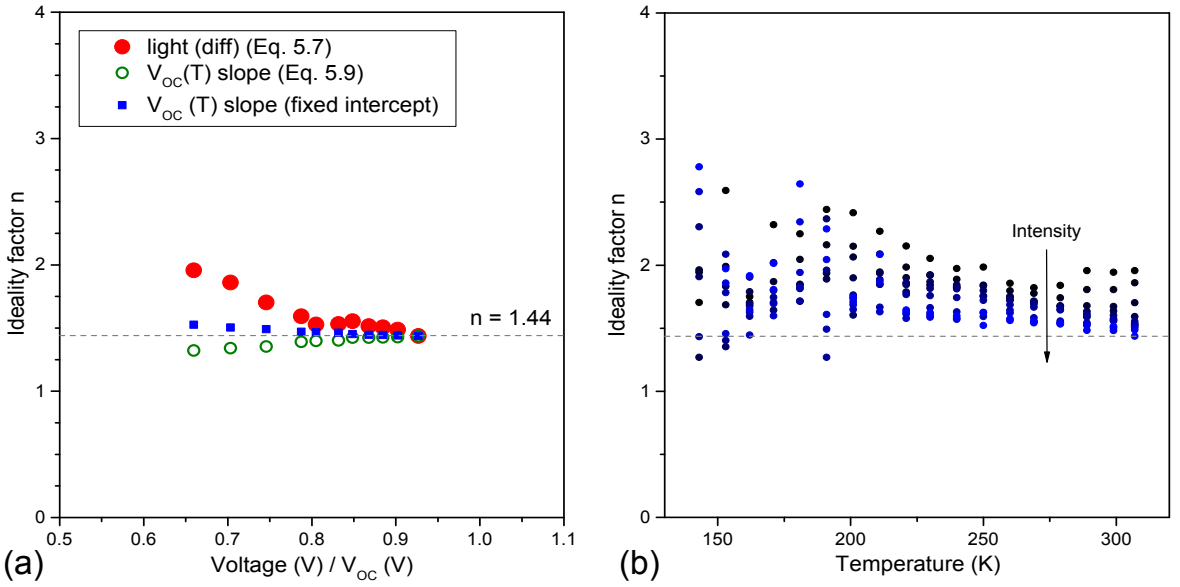

Figure 5.50: (a) Ideality factors determined in different ways are plotted against (open circuit) voltage. Around V_{OC} the values obtained by all methods approach $n = 1.44$. (b) Increasing illumination intensities lead to a decreasing differential light ideality factor indicating light induced detrapping under illumination.

In a final step, the temperature and intensity analysis is performed on a solar cell with 20 nm DBP / 20 nm ZCl. Although the photoactive layer is even thinner than that of the 60 nm 6T/20 nm ZCl solar cell, similar problems due to pinholes are not expected here because of the smooth DBP surface. Once again, the analysis starts with the evaluation of the V_{OC} vs. T measurement. Here, the linear extrapolations do not show a similar behavior with a intensity dependent monotonic decrease of E_{PVG} as previously observed for the 6T/ZCl solar cells. The obtained values of the photovoltaic gap rather fluctuate around 1.85 eV (Fig. 5.51 (a)). For that reason, all extrapolations can be easily forced to end up at this value (Fig. 5.51 (d)). Again, the accuracy of that value can be verified successfully by the slope of the $n \cdot \ln(j_0)$ vs. $1/k_BT$ plot (Fig. 5.52 (b)). Moreover, also for this material combination, J_{SC} decreases linearly with temperature in a semilogarithmic presentation for temperatures above 200 K (Fig. 5.51 (b)).

Subsequently, light ideality factor and recombination current are determined by fits to the V_{OC} vs. J_{SC} representation in the high intensity regime (Fig. 5.51 (c)). The obtained data is depicted in Fig. 5.52 (a). The obtained results reveal hardly no temperature dependence of n_{light} and a value of approximately 1.3 at room temperature. This value more or less coincides with the diffentially determined light ideality factor of 1.28 (Fig. 5.53 (a)). In comparison to DBP/C_{60} solar cells with $n = 1$, this reveals an increased trap-assisted recombination. As the donor layer is identical for the compared devices, this increase can be completely attributed to ZCl or to altered conditions at the interface. As a result, ZCl films seem to contain more traps than fullerene films. This counteracts possible gains in V_{OC} by exploiting SBCT when C_{60} is replaced by ZCl. Very strong detrapping is again found by plotting the light ideality factor for different illumination intensities (Fig. 5.53 (b)). However, this is attributed to DBP as a similar behavior could be observed previously for the DBP/C_{60} devices, but not for 6T/ZCl solar cells. In conclusion, the obtained results of E_{PVG}, j_0 and $n_{light,diff}$ of all investigated ZCl containing solar cells are summarized in Tab. 5.7.

Material system	Cell temperature (K)	E_{PVG} (eV)	j_0 (mA/cm^2)	n
DBP/ZCl	310	1.85	7.3×10^{-17}	1.28
6T/ZCl (20 nm)	307	1.33	3.6×10^{-8}	1.80
6T/ZCl (40 nm)	307	1.48	4.3×10^{-10}	1.44

Table 5.7: Summary of the most interesting parameters of the ZCl containing solar cells obtained by the temperature and intensity dependent analysis: The values of E_{PVG} are taken from Fig. 5.46 (b), 5.49 (b) and 5.52 (b), respectively ($1/k_BT$ vs. $n \cdot \ln(j_0)$). The values of j_0, however, are extracted from fits to the J_{SC} vs. V_{OC} plots (Fig. 5.45 (c), 5.48 (c) and 5.51 (c)). n is the differentially determined light ideality factor at highest measured intensity.

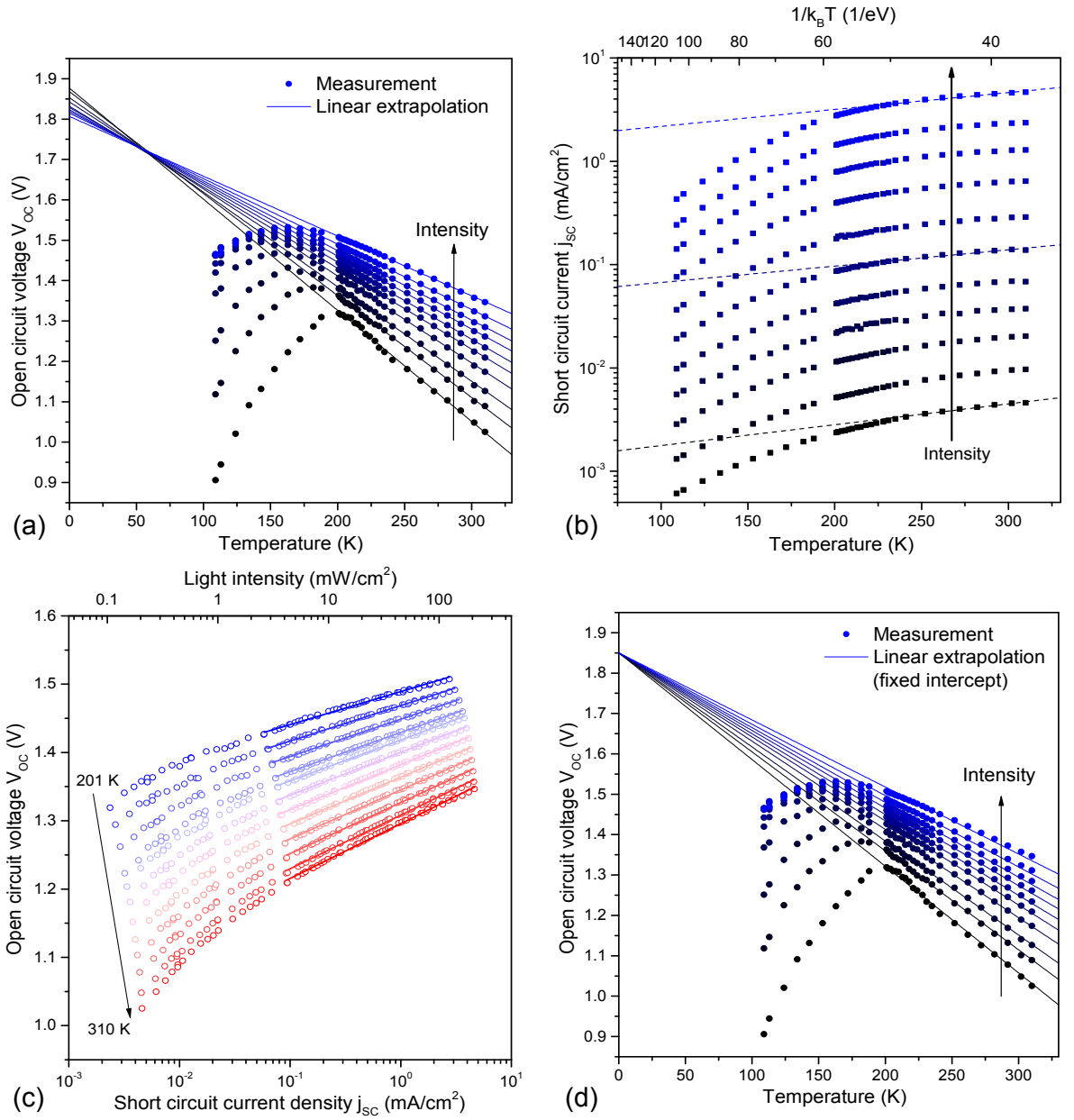

Figure 5.51: Temperature and intensity dependent measurements of V_{OC} and J_{SC} of a solar cell consisting of ITO (140 nm)/HIL1.3 (45 nm)/DBP (20 nm)/ZCl (20 nm)/BCP (5 nm)/Al (100 nm). Different temperatures are enabled by a liquid nitrogen cryostat, while a white LED serves as light source and provides a total of 66 different light intensities between 2.2 and 2.2 $\times 10^{-3}$ suns. The results of V_{OC} vs. T and J_{SC} vs. T measurements for different illumination intensities are shown in (a) and (b), respectively. The summarized values of V_{OC} and J_{SC} at different temperatures are shown in (c). The solid lines are fits with Eq. (5.5) yielding n_{light} and j_0 shown in Fig. 5.52 (a). As shown in (d), the extrapolations of the temperature dependent V_{OC} values for different illumination intensities can be forced to end at one distinct photovoltaic gap energy, yielding good results over the whole investigated intensity range. For reasons of clarity some measured data sets are omitted within (a), (b) and (d).

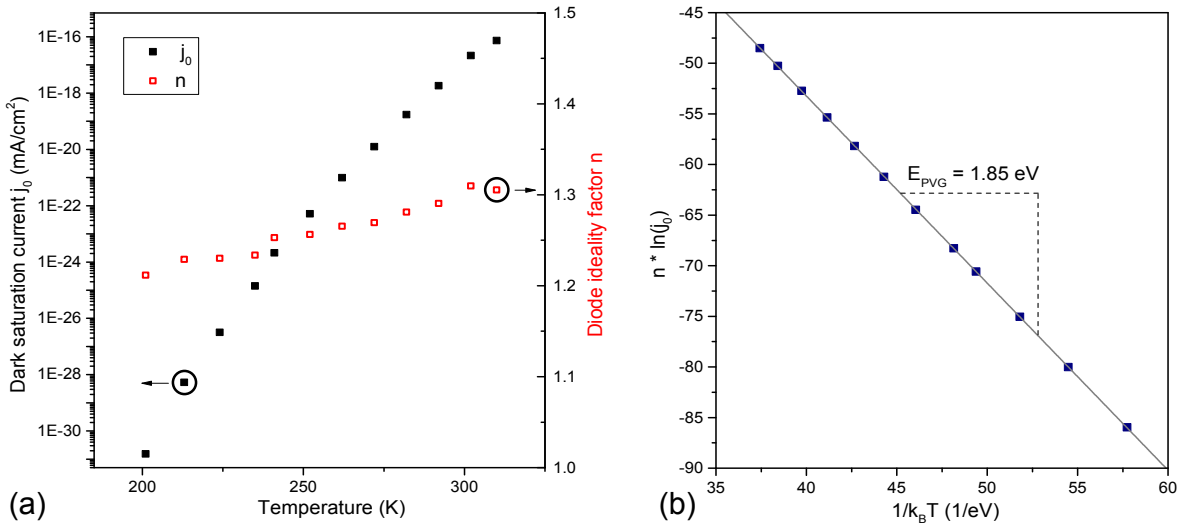

Figure 5.52: (a) Dark saturation current j_0 and diode ideality factor n_{light} plotted against temperature obtained by fits to the high intensity part of the V_{OC} vs. J_{SC} diagram shown in Fig. 5.51 (c). The slope of the $n \cdot \ln(j_0)$ vs. $1/k_{\text{B}}T$ diagram in (b) provides a photovoltaic gap of 1.85 eV for the DBP/ZCl solar cell.

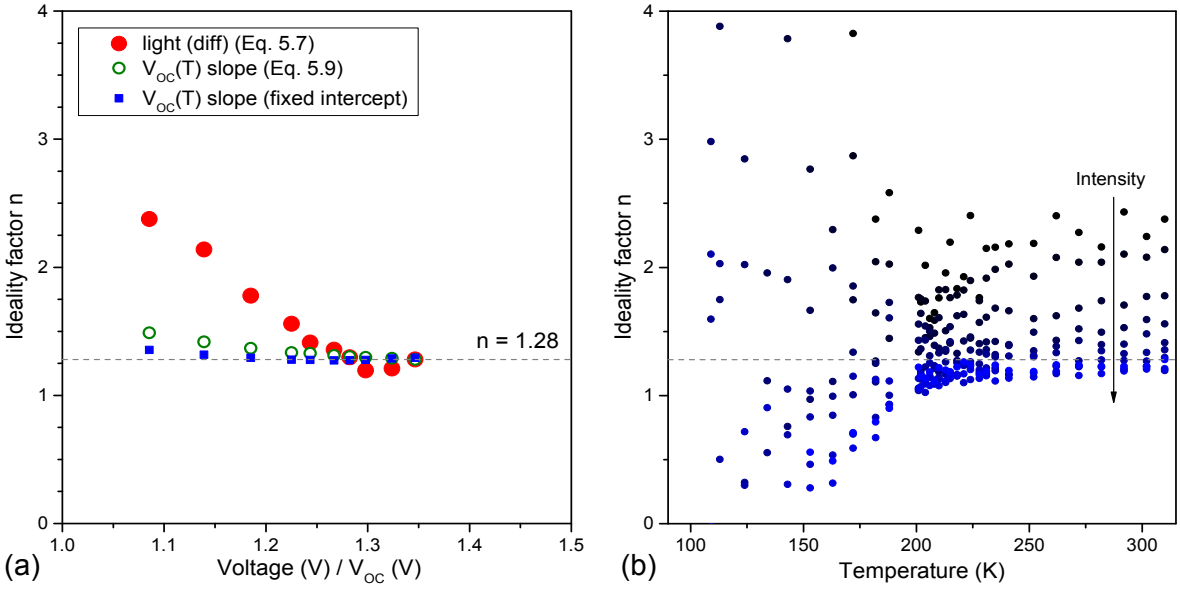

Figure 5.53: (a) Ideality factors determined in different ways are plotted against (open circuit) voltage. Around V_{OC} the values obtained by all methods approach $n = 1.28$. (b) Increasing illumination intensities lead to a strongly decreasing differential light ideality factor indicating efficient light induced detrapping under illumination.

Chapter 6

Conclusion and outlook

Within the scope of this thesis, the influence of thin film morphology on the efficiency of small-molecule organic solar cells was investigated. Numerous variables can affect solar cell performance, so that it is useful to address the influence of morphology by a comparison of similar molecules. This is the case for DIP and DBP which exhibit similar molecular structures and thus comparable energy level alignment, which was confirmed via UPS. However, it could be shown by XRD that DIP thin films grow highly crystalline, while DBP thin films possess an amorphous character. In turn, this means that both molecules differ concerning their molecular arrangement. This different arrangement includes not only structural order but also molecular orientation. The orientation was examined via NEXAFS and revealed almost upright standing DIP molecules and a preferential horizontal alignment of the DBP molecules.

This difference in molecular orientation drastically impacts the ability of the organic films to absorb the impinging light. In general, absorption depends on the coupling between incident light and the transition dipole moment of the molecule, which is, for both DIP and DBP, aligned along the long axis of the molecule. As a consequence, a horizontal orientation of the molecules leads to a more efficient coupling and thus absorption. This can be verified by reflectometry measurements, revealing an absorption coefficient of DBP films, which is more than six times higher than that of its crystalline counterpart. Nevertheless, the crystallinity of DIP films includes also some advantages. For example, it enables a by far longer exciton diffusion length and is also advantageous concerning charge carrier mobility. However, it could be shown by measurements on OFETs that also within amorphous DBP films surprisingly good charge carrier mobilities are achieved. It must be taken into account, however, that this measurement technique only determines mobilities parallel to the substrate and not towards the electrodes. As transport in DBP and especially in DIP is expected to be anisotropic, other methods or devices like CELIV (charge extraction by linearly increasing voltage[264]) or

metal-insulator-semiconductor (MIS) diodes[265] have to be utilized, though. Nevertheless, the good transport abilities of both DIP and DBP could also be confirmed by low series resistances within PHJ and PMHJ solar cells determined via dark current analysis.

On the basis of absorption, transport and energy level alignment, differences and similarities regarding OPVC performances of DIP and DBP solar cells can be explained plausibly. It could be shown, that replacing DIP by DBP provides a doubling of J_{SC} in PHJ and PMHJ solar cells when used as donor with C_{60} as well as in PHJ with 6T when applied as acceptor due to the improved absorption. To fully exploit the benefits of DBP, however, for PHJ devices, layer thicknesses have to be adjusted, while for PMHJ solar cells the right mixing ratio between donor and acceptor has to be found. This is necessary to achieve an effective phase separation between donor and acceptor. For DBP:C_{60}, a mixing ration of 1:2 was determined to be very well suited. Besides, similar values of V_{OC} and FF are measured for DIP and DBP solar cells, which is explained by similar energy level alignments and transport properties, respectively. Consequently, the doubled J_{SC} results in an approximate doubling of PCE.

J-V-characteristics indeed determine the efficiency of an OPVC, however, they provide only a very limited insight into the inherent processes, which are responsible for solar cell performance. This requires a deeper analysis, accessible via temperature and intensity dependent measurements. In this way, general statements can be made concerning the photovoltaic gap, while recombination losses can be quantified by identifying the recombination current j_0 and the diode ideality factor n. There are two different approaches for their determination. On the one hand, the dark current characteristics can be fitted by a modified Shockley equation. However, the obtained values are error-prone. Due to the absence of illumination, trap states occur, which do not appear under normal working conditions. For that reason, the value of n_{dark} was always found to be higher than that of n_{light}. Especially for amorphous DBP, which innately possesses more trap states than crystalline DIP, this plays a significant role. Additionally, parasitic resistances affect the determined values, especially R_S, which is calculated within the same fit like j_0 and n. On the other hand, both values can also be determined under open-circuit and short-circuit conditions. This method has the benefit that disturbing influences of parasitic resistances can be minimized. Moreover, due to sample illumination, efficient detrapping occurs. With this method, it could be shown that DBP/C_{60} solar cells possess an ideality factor of unity and thus do not (or only minimal) suffer from trap-assisted recombination. Even for PMHJ devices, the ideality factor is comparatively very low with $n = 1.16$, indicating the good phase separation within these solar cells. In comparison to DIP, less recombination losses can be assumed in DBP solar cells due to a reduced value of the recombination current. For PHJ devices with DBP, j_0 is about two orders of magnitude smaller compared to DIP devices, for PMHJ devices at least one order of magnitude. Nevertheless, the obtained picture is still not complete. An even more detailed characterization is possible by a combined analysis of electroluminescence data and CT determination via high-sensitive IPCE. Actually, these

measurements have already been performed on the same devices to ensure comparability of the different results, however, their evaluation will follow by Theresa Linderl.

In a next step, it could be shown how strongly the efficiency of organic solar cells can be enhanced by inserting an exciton blocking layer at the anode interface. Moreover, it is determined whether the morphology of this layer influences its effect. In general, the use of an EBL enables more excitons to reach the D/A interface and thus significantly increases J_{SC}. DIP was chosen to form the crystalline EBL, while DBP was used as donor and C_{60} as the acceptor. For that material combination, J_{SC} could be improved by 30 %. Moreover, a slight increase of V_{OC} due to reduced recombination and also a slight gain in FF, resulting from a higher R_P, could be observed. Summing up, the power conversion efficiency can be lifted by more than 37 % up to 3.8 %. With amorphous α-NPD as EBL, almost identical improvements regarding J_{SC}, V_{OC} and FF could be achieved, at least when the thickness of the EBL is chosen properly. Thus, it could be shown unambiguously that the morphology of the EBL has no impact on the performance of the OPVC. Furthermore, it could be shown for the first time that EBLs are also able to improve the efficiency of PMHJ devices. This, however, has other reasons than before. Due to the already greatly enlarged D/A interface of PMHJ solar cells, an improvement of J_{SC} is not achieved, however, V_{OC} and FF increase. The improved V_{OC}, which is more pronounced compared to PHJ devices, can be explained by shifting energy levels and a change of the effective work function of the anode. The increase of FF can again be attributed to a larger R_P and thus reduced leakage currents. This way, a PCE of 5.8 % could be achieved for a PMHJ solar cell using C_{70} as strongly absorbing acceptor material.

Usually, the structure of an organic semiconductor film and hence its morphology and the molecular orientation are already defined after the manufacturing process. However, it could be shown that these properties can be altered by a post-productional method called solvent vapor annealing. SVA was first applied to amorphous DBP to achieve more crystallinity coming along with an improved charge carrier transport and an extended exciton diffusion length. It could be revealed via optical microscopy that DBP actually forms crystallites when treated with chloroform. As a result, the efficiency of SVA treated DBP solar cells could be increased by almost 10 % because J_{SC} and the FF can be improved. This is explained by an enlarged D/A interface and higher structural order, respectively. However, this positive effect is restricted and only occurs for short annealing times of maximal 4 minutes. Longer treatments cause a strong aggregation of the molecules, leading to a pronounced inhomogeneity of the film detrimental for absorption and charge transport. Furthermore, longer annealing times cause a molecular reorientation, which could be proven via NEXAFS. The initially preferred horizontal orientation vanishes and a rather upright standing arrangement was found. Hence, the drop of absorption can be explained by a combination of dewetting and molecular reorientation leading to a decreasing J_{SC}. As also V_{OC} and FF diminish due to enhanced recombination and complicated transport, respectively, an extensive SVA

treatment causes a significant deterioration of DBP solar cell efficiency. Nevertheless, the possible improvement of solar cell performance could be confirmed for short SVA times. Moreover, the NEXAFS results demonstrate that SVA provides a potential route to alter the orientation of molecules, a fact that could prospectively exploited for organic films possessing a less favorable molecular orientation.

Subsequently, SVA was applied to already crystalline DIP films. Nevertheless, the treatment induces a further improvement concerning structural order, which could be reaveled via AFM. Furthermore, a fast Fourier transform of the obtained images proves the enhanced average lateral domain distance of the DIP crystallites. Besides, the roughness of the film increases due to SVA and thus the D/A interface leading to an increased J_{SC}. NEXAFS measurements demonstrate that a reorientation process, as it was observed for DBP, does not occur, so that the gain in J_{SC} can be ascribed exclusively to the enlarged interface. The enhanced crystallinity also leads to an increased FF, so that the PCE of DIP solar cells can be improved by almost 17 % using SVA.

By combining the positive results of SVA on DIP and DIP as exciton blocking layer, it is demonstrated that the efficiency of an OPVC can be improved by almost 50 %. By that, PCEs of more than 4 % can be achieved for PHJ organic solar cells. Besides, another feature of SVA could be observed. By using MoO_x as hole injection layer, the *J-V*-characteristics revealed an s-shape behavior, which disappears applying SVA. This indicates that SVA is able to reduce the energetic barrier between the Fermi level of the ITO anode and the HOMO of the donor. To visualize this effect, UPS measurements would be necessary to show that the HOMO of the donor is actually slightly elevated by means of SVA. In general, it can be stated that SVA offers many possibilities. It provides the ability to influence morphology, affect molecular orientation and change the energy level alignment of the treated organic semiconductor film. As a consequence, J_{SC}, V_{OC} and FF of OPVCs of various material combinations can potentially be increased. However, a reduction of all these factors is possible as well. Therefore, to fully exploit the benefits of SVA, material, layer thickness, solvent and SVA time have to be adjusted exactly and individually for each treated film. In conclusion, SVA still offers many possibilities for future improvements of organic solar cell efficiencies. For example, SVA could also be used for PMHJ devices. Here, it might be used to improve the phase separation of donor-acceptor blends, which inherently exhibit a homogeneous mixture phase of the two materials.

Finally, ZCl is introduced as new acceptor material in OPVCs. It possesses interesting properties like high absorption and the (probable) ability to undergo SBCT. However, ZCl forms amorphous films and thus provides only short exciton diffusion lenghts, limiting its layer thickness. In combination with DBP, very high V_{OC} values of more than 1.3 V are possible, compared to DBP/C_{60}, however, J_{SC} and FF are significantly reduced. This is mainly attributed by the layer thickness restrictions caused by the amorphous character of both materials, which leads to incomplete absorption and non-utilization

of the cavity effect. Temperature and intensity dependent measurements revealed enhanced trap-assisted recombination losses compared to DBP/C_{60} devices, leading to a light ideality factor of $n = 1.28$. As both considered solar cells have the same donor, the increased trap density can be ascribed to ZCl compared to C_{60}. Moreover, solar cells were fabricated using 60 nm of 6T as donor material. At first, a ZCl layer thickness of merely 20 nm was chosen, however, it became obvious that this thickness is not sufficient to fully cover the rough 6T surface. As a result, temperature and intensity dependent measurements are not useful for these solar cells, because the obtained results are obscured by this issue. For that reason, 40 nm of ZCl were evaporated on 6T leading to a solar cell with a PCE exceeding 2 %. A higher efficiency is, among others, hampered by comparatively strong trap-assisted recombination leading to $n = 1.44$. Nevertheless, ZCl is an interesting material, which adds new possibilities for future solar cells, especially when fullerens cannot or should not be used. However, for that purpose and to fully exploit its potential, a deeper understanding of this new material and the occurring processes within need to be gained.

Bibliography

[1] http://www.allnaturalenergy.com.au/quotable-quotes; visited on 9/23/2015.

[2] Y. Yang and F. Wudl. Organic electronics: From materials to devices. *Advanced Materials*, 21(14-15):1401–1403, 2009.

[3] http://www.bundesregierung.de/Content/DE/StatischeSeiten/Breg/Energiekonzept/0-Buehne/maßnahmen-im-ueberblick.html; downloaded on 9/23/2015.

[4] A. Skoczek, T. Sample, and E. D. Dunlop. The results of performance measurements of field-aged crystalline silicon photovoltaic modules. *Progress in Photovoltaics: Research and Applications*, 17(4):227–240, 2009.

[5] M. A. Green, K. Emery, Y. Hishikawa, W. Warta, and E. D. Dunlop. Solar cell efficiency tables (version 45). *Progress in Photovoltaics: Research and Applications*, 23(1):1–9, 2015.

[6] H. Jiang and C. Kloc. Single-crystal growth of organic semiconductors. *MRS Bulletin*, 38(1):28–33, 2013.

[7] S. Lizin, S. Van Passel, E. De Schepper, W. Maes, L. Lutsen, J. Manca, and D. Vanderzande. Life cycle analyses of organic photovoltaics: A review. *Energy & Environmental Science*, 6:3136–3149, 2013.

[8] M. Grätzel. Recent advances in sensitized mesoscopic solar cells. *Accounts of Chemical Research*, 42(11):1788–1798, 2009.

[9] National Center for Photovoltaics. Research cell efficiency records. http://www.nrel.gov/ncpv/ downloaded on 9/23/2015.

[10] B. G. Yacobi. *Semiconductor Materials: An Introduction to Basic Principles*. Springer Science & Business Media, 2003.

[11] A. Köhler and H. Bässler. *Electronic Processes in Organic Semiconductors: An Introduction*. Wiley-VCH Verlag GmbH & Co. KGaA, 2015.

[12] W. Brütting and W. Rieß. Grundlagen der organischen Halbleiter. *Physik Journal*, 7(5):33–38, 2008.

[13] J.-L. Brédas, J. P. Calbert, D. A. da Silva Filho, and J. Cornil. Organic semiconductors: A theoretical characterization of the basic parameters governing charge transport. *Proceedings of the National Academy of Sciences*, 99(9):5804–5809, 2002.

[14] V. Podzorov, E. Menard, A. Borissov, V. Kiryukhin, J. A. Rogers, and M. E. Gershenson. Intrinsic charge transport on the surface of organic semiconductors. *Physical Review Letters*, 93:086602, 2004.

[15] V. Coropceanu, J. Cornil, D. A. da Silva Filho, Y. Olivier, R. Silbey, and J.-L. Brédas. Charge transport in organic semiconductors. *Chemical Reviews*, 107(4):926–952, 2007.

[16] M. Schwörer and H. C. Wolf. *Organische Molekulare Festkörper*. Wiley-VCH Verlag GmbH & Co. KGaA, 2005.

[17] B. P. Rand, J. Genoe, P. Heremans, and J. Poortmans. Solar cells utilizing small molecular weight organic semiconductors. *Progress in Photovoltaics: Research and Applications*, 15(8):659–676, 2007.

[18] W. D. Gill. Drift mobilities in amorphous charge-transfer complexes of trinitrofluorenone and poly-n-vinylcarbazole. *Journal of Applied Physics*, 43(12):5033–5040, 1972.

[19] H. Bässler. Charge transport in disordered organic photoconductors - A Monte Carlo simulation study. *physica status solidi (b)*, 175(1):15–56, 1993.

[20] S. Torabi, F. Jahani, I. Van Severen, C. Kanimozhi, S. Patil, R. W. A. Havenith, R. C. Chiechi, L. Lutsen, D. J. M. Vanderzande, T. J. Cleij, J. C. Hummelen, and L. J. A. Koster. Strategy for enhancing the dielectric constant of organic semiconductors without sacrificing charge carrier mobility and solubility. *Advanced Functional Materials*, 25(1):150–157, 2015.

[21] J. K. Kraus. *Physics of molecular donor-acceptor solar cells - Correlation between interface morphology, energetics and device performance*. PhD thesis, Universität Augsburg, 2013.

[22] S.-S. Sun and L. R. Dalton. *Introduction to Organic Electronic and Optoelectronic Materials and Devices*. Taylor & Francis, 2008.

[23] A. Y. Kobitski, R. Scholz, D. R. T. Zahn, and H. P. Wagner. Time-resolved photoluminescence study of excitons in α-PTCDA as a function of temperature. *Physical Review B*, 68:155201, 2003.

[24] C. W. Tang. Two-layer organic photovoltaic cell. *Applied Physics Letters*, 48(2):183–185, 1986.

[25] H. Kallmann and M. Pope. Photovoltaic effect in organic crystals. *The Journal of Chemical Physics*, 30(2):585–586, 1959.

[26] H. Spanggaard and F. C. Krebs. A brief history of the development of organic and polymeric photovoltaics. *Solar Energy Materials and Solar Cells*, 83(2-3):125–146, 2004.

[27] J.-L. Brédas, D. Beljonne, V. Coropceanu, and J. Cornil. Charge-transfer and energy-transfer processes in π-conjugated oligomers and polymers: A molecular picture. *Chemical Reviews*, 104(11):4971–5004, 2004.

[28] P. W. M. Blom, V. D. Mihailetchi, L. J. A. Koster, and D. E. Markov. Device physics of polymer:fullerene bulk heterojunction solar cells. *Advanced Materials*, 19(12):1551–1566, 2007.

[29] P. Heremans, D. Cheyns, and B. P. Rand. Strategies for increasing the efficiency of heterojunction organic solar cells: Material selection and device architecture. *Accounts of Chemical Research*, 42(11):1740–1747, 2009.

[30] J. Nelson. Organic photovoltaic films. *Current Opinion in Solid State and Materials Science*, 6(1):87–95, 2002.

[31] S. Banerjee, A. P. Parhi, S. S. K. Iyer, and S. Kumar. Method of determining the exciton diffusion length using optical interference effect in schottky diode. *Applied Physics Letters*, 94(22):223303, 2009.

[32] R. R. Lunt, J. B. Benziger, and S. R. Forrest. Relationship between crystalline order and exciton diffusion length in molecular organic semiconductors. *Advanced Materials*, 22(11):1233–1236, 2010.

[33] R. A. Street, S. Cowan, and A. J. Heeger. Experimental test for geminate recombination applied to organic solar cells. *Physical Review B*, 82:121301, 2010.

[34] H. Hoppe, N. Arnold, N. S. Sariciftci, and D. Meissner. Modeling the optical absorption within conjugated polymer/fullerene-based bulk-heterojunction organic solar cells. *Solar Energy Materials and Solar Cells*, 80(1):105–113, 2003.

[35] T. Ameri, G. Dennler, C. Waldauf, P. Denk, K. Forberich, M. C. Scharber, C. J. Brabec, and K. Hingerl. Realization, characterization, and optical modeling of inverted bulk-heterojunction organic solar cells. *Journal of Applied Physics*, 103(8):084506, 2008.

[36] A. Armin, M. Velusamy, P. Wolfer, Y. Zhang, P. L. Burn, P. Meredith, and A. Pivrikas. Quantum efficiency of organic solar cells: Electro-optical cavity considerations. *ACS Photonics*, 1(3):173–181, 2014.

[37] C. J. Brabec, G. Zerza, G. Cerullo, S. De Silvestri, S. Luzzati, J. C. Hummelen, and S. Sariciftci. Tracing photoinduced electron transfer process in conjugated polymer/fullerene bulk heterojunctions in real time. *Chemical Physics Letters*, 340(3-4):232–236, 2001.

[38] P. A. van Hal, R. A. J. Janssen, G. Lanzani, G. Cerullo, M. Zavelani-Rossi, and S. De Silvestri. Full temporal resolution of the two-step photoinduced energy-electron transfer in a fullerene-oligothiophene-fullerene triad using sub-10 fs pump-probe spectroscopy. *Chemical Physics Letters*, 345(1-2):33 – 38, 2001.

[39] G. Zerza, C. J. Brabec, G. Cerullo, S. De Silvestri, and N. S. Sariciftci. Ultrafast charge transfer in conjugated polymer-fullerene composites. *Synthetic Metals*, 119(1-3):637–638, 2001.

[40] C. J. Brabec, N. S. Sariciftci, and J. C. Hummelen. Plastic solar cells. *Advanced Functional Materials*, 11(1):15–26, 2001.

[41] P. Peumans, A. Yakimov, and S. R. Forrest. Small molecular weight organic thin-film photodetectors and solar cells. *Journal of Applied Physics*, 93(7):3693–3723, 2003.

[42] D. Credgington, F. C. Jamieson, B. Walker, T.-Q. Nguyen, and J. R. Durrant. Quantification of geminate and non-geminate recombination losses within a solution-processed small-molecule bulk heterojunction solar cell. *Advanced Materials*, 24(16):2135–2141, 2012.

[43] S. Shoaee, S. Mehraeen, J. G. Labram, J.-L. Brédas, D. D. C. Bradley, V. Coropceanu, T. D. Anthopoulos, and J. R. Durrant. Correlating non-geminate recombination with film structure: A comparison of polythiophene:fullerene bilayer and blend films. *The Journal of Physical Chemistry Letters*, 5(21):3669–3676, 2014.

[44] L. G. Kaake, P. F. Barbara, and X.-Y. Zhu. Intrinsic charge trapping in organic and polymeric semiconductors: A physical chemistry perspective. *The Journal of Physical Chemistry Letters*, 1(3):628–635, 2010.

[45] M. Kuik, L. J. A. Koster, G. A. H. Wetzelaer, and P. W. M. Blom. Trap-assisted recombination in disordered organic semiconductors. *Physical Review Letters*, 107:256805, 2011.

[46] J. M. Hodgkiss, S. Albert-Seifried, A. Rao, A. J. Barker, A. R. Campbell, R. A. Marsh, and R. H. Friend. Exciton-charge annihilation in organic semiconductor films. *Advanced Functional Materials*, 22(8):1567–1577, 2012.

[47] Y. Hishikawa, N. Nakamura, S. Tsuda, S. Nakano, Y. Kishi, and Y. Kuwano. Interference-free determination of the optical absorption coefficient and the optical

gap of amorphous silicon thin films. *Japanese Journal of Applied Physics*, 30:1008–1014, 1991.

[48] S. Günes, H. Neugebauer, and N. S. Sariciftci. Conjugated polymer-based organic solar cells. *Chemical Reviews*, 107(4):1324–1338, 2007.

[49] S. Park and M.-K. Seo. *Interface Science and Composites*. Academic Press, 2011.

[50] B. A. Gregg. Excitonic solar cells. *The Journal of Physical Chemistry B*, 107(20):4688–4698, 2003.

[51] K. Robbie and M. J. Brett. Sculptured thin films and glancing angle deposition: Growth mechanics and applications. *Journal of Vacuum Science & Technology A*, 15(3):1460–1465, 1997.

[52] L. J. Guo. Recent progress in nanoimprint technology and its applications. *Journal of Physics D: Applied Physics*, 37(11):123–141, 2004.

[53] Y. Yang, K. Mielczarek, M. Aryal, A. Zakhidov, and W. Hu. Nanoimprinted polymer solar cell. *ACS Nano*, 6(4):2877–2892, 2012.

[54] J. J. M. Halls, C. A. Walsh, N. Greenham, E. A. Marseglia, R. Friend, S. C. Moratti, and A. Holmes. Efficient photodiodes from interpenetrating polymer networks. *Nature*, 376(6540):498–500, 1995.

[55] G. Yu, J. Gao, J. C. Hummelen, F. Wudl, and A. J. Heeger. Polymer photovoltaic cells: Enhanced efficiencies via a network of internal donor-acceptor heterojunctions. *Science*, 270(5243):1789–1791, 1995.

[56] G. Dennler, M. C. Scharber, and C. J. Brabec. Polymer-fullerene bulk-heterojunction solar cells. *Advanced Materials*, 21(13):1323–1338, 2009.

[57] C. Schünemann, D. Wynands, L. Wilde, M. P. Hein, S. Pfützner, C. Elschner, K.-J. Eichhorn, K. Leo, and M. Riede. Phase separation analysis of bulk heterojunctions in small-molecule organic solar cells using zinc-phthalocyanine and C_{60}. *Physical Review B*, 85:245314, 2012.

[58] A. Wilke, J. Endres, U. Hörmann, J. Niederhausen, R. Schlesinger, J. Frisch, P. Amsalem, J. Wagner, M. Gruber, A. Opitz, A. Vollmer, W. Brütting, A. Kahn, and N. Koch. Correlation between interface energetics and open circuit voltage in organic photovoltaic cells. *Applied Physics Letters*, 101:233301, 2012.

[59] J. Widmer, M. Tietze, K. Leo, and M. Riede. Open-circuit voltage and effective gap of organic solar cells. *Advanced Functional Materials*, 23(46):5814–5821, 2013.

[60] K. Vandewal, K. Tvingstedt, A. Gadisa, O. Inganäs, and J. V. Manca. Relating the open-circuit voltage to interface molecular properties of donor:acceptor bulk heterojunction solar cells. *Physical Review B*, 81:125204, 2010.

[61] U. Hörmann, J. Kraus, M. Gruber, C. Schuhmair, T. Linderl, S. Grob, S. Kapfinger, K. Klein, M. Stutzmann, H. J. Krenner, and W. Brütting. Quantification of energy losses in organic solar cells from temperature-dependent device characteristics. *Physical Review B*, 88:235307, 2013.

[62] W. Shockley and H. J. Queisser. Detailed balance limit of efficiency of p-n junction solar cells. *Journal of Applied Physics*, 32(3):510–519, 1961.

[63] N. C. Giebink, G. P. Wiederrecht, M. R. Wasielewski, and S. R. Forrest. Thermodynamic efficiency limit of excitonic solar cells. *Physical Review B*, 83:195326, 2011.

[64] L. J. A. Koster, S. E. Shaheen, and J. C. Hummelen. Pathways to a new efficiency regime for organic solar cells. *Advanced Energy Materials*, 2(10):1246–1253, 2012.

[65] M. Gruber, J. Wagner, K. Klein, U. Hörmann, A. Opitz, M. Stutzmann, and W. Brütting. Thermodynamic efficiency limit of molecular donor-acceptor solar cells and its application to diindenoperylene/C_{60}-based planar heterojunction devices. *Advanced Energy Materials*, 2(9):1100–1108, 2012.

[66] B. Ray and M. A. Alam. Achieving fill factor above 80 % in organic solar cells by charged interface. *IEEE Journal of Photovoltaics*, 3(1):310–317, 2013.

[67] G. A. H. Wetzelaer, M. Kuik, M. Lenes, and P. W. M. Blom. Origin of the dark-current ideality factor in polymer:fullerene bulk heterojunction solar cells. *Applied Physics Letters*, 99(15):153506, 2011.

[68] T. Kirchartz, B. E. Pieters, J. Kirkpatrick, U. Rau, and J. Nelson. Recombination via tail states in polythiophene:fullerene solar cells. *Physical Review B*, 83:115209, 2011.

[69] C. N. Hoth, R. Steim, P. Schilinsky, S. A. Choulis, S. F. Tedde, O. Hayden, and C. J. Brabec. Topographical and morphological aspects of spray coated organic photovoltaics. *Organic Electronics*, 10(4):587–593, 2009.

[70] H. Hoppe and N. S. Sariciftci. Organic solar cells: An overview. *Journal of Materials Research*, 19:1924–1945, 2004.

[71] B. Qi and J. Wang. Fill factor in organic solar cells. *Physical Chemistry Chemical Physics*, 15:8972–8982, 2013.

[72] W. J. Potscavage Jr., A. Sharma, and B. Kippelen. Critical interfaces in organic solar cells and their influence on the open-circuit voltage. *Accounts of Chemical Research*, 42(11):1758–1767, 2009.

[73] K. R. Graham, P. Erwin, D. Nordlund, K. Vandewal, R. Li, G. O. Ngongang Ndjawa, E. T. Hoke, A. Salleo, M. E. Thompson, M. D. McGehee, and A. Amassian.

Re-evaluating the role of sterics and electronic coupling in determining the open-circuit voltage of organic solar cells. *Advanced Materials*, 25(42):6076–6082, 2013.

[74] M. D. Perez, C. Borek, S. R. Forrest, and M. E. Thompson. Molecular and morphological influences on the open circuit voltages of organic photovoltaic devices. *Journal of the American Chemical Society*, 131(26):9281–9286, 2009.

[75] D. M. Stevens, J. C. Speros, M. A. Hillmyer, and C. D. Frisbie. Relationship between diode saturation current and open circuit voltage in poly(3-alkylthiophene) solar cells as a function of device architecture, processing conditions, and alkyl side chain length. *The Journal of Physical Chemistry C*, 115(42):20806–20816, 2011.

[76] S. Yamamoto, A. Orimo, H. Ohkita, H. Benten, and S. Ito. Molecular understanding of the open-circuit voltage of polymer:fullerene solar cells. *Advanced Energy Materials*, 2(2):229–237, 2012.

[77] J. Wagner, M. Gruber, A. Wilke, Y. Tanaka, K. Topczak, A. Steindamm, U. Hörmann, A. Opitz, Y. Nakayama, H. Ishii, J. Pflaum, N. Koch, and W. Brütting. Identification of different origins for s-shaped current voltage characteristics in planar heterojunction organic solar cells. *Journal of Applied Physics*, 111:054509, 2012.

[78] D.-H. Lee, Y.-P. Liu, K.-H. Lee, H. Chae, and S. M. Cho. Effect of hole transporting materials in phosphorescent white polymer light-emitting diodes. *Organic Electronics*, 11:427–433, 2010.

[79] O. Pellegrino, M. Rei Vilar, G. Horowitz, F. Kouki, F. Garnier, J. D. Lopes da Silva, and A. M. Botelho do Rego. Characterization of oligothiophene films by high resolution electron energy loss spectroscopy. *Thin Solid Films*, 327–329:252–255, 1998.

[80] D. Fujishima, H. Kanno, T. Kinoshita, E. Maruyama, M. Tanaka, M. Shirakawa, and K. Shibata. Organic thin-film solar cell employing a novel electron-donor material. *Solar Energy Materials and Solar Cells*, 93:1029–1032, 2009.

[81] G. Chen, D. Yokoyama, H. Sasabe, Z. Hong, Y. Yang, and J. Kido. Optical and electrical properties of a squaraine dye in photovoltaic cells. *Applied Physics Letters*, 101(8):083904, 2012.

[82] T. Zhuang, X.-F. Wang, T. Sano, Z. Hong, G. Li, Y. Yang, and J. Kido. Fullerene C_{60} as a p-type donor in organic photovoltaic cells. *Applied Physics Letters*, 105(9):093301, 2014.

[83] C. Trinh, K. O. Kirlikovali, A. N. Bartynski, C. J. Tassone, M. F. Toney, G. F. Burkhard, M. D. McGehee, P. I. Djurovich, and M. E. Thompson. Efficient energy sensitization of C_{60} and application to organic photovoltaics. *Journal of the American Chemical Society*, 135(32):11920–11928, 2013.

[84] B. P. Rand, J. Li, J. Xue, R. J. Holmes, M. E. Thompson, and S. R. Forrest. Organic double-heterostructure photovoltaic cells employing thick tris(acetylacetonato)-ruthenium(III) exciton-blocking layers. *Advanced Materials*, 17(22):2714–2718, 2005.

[85] R. M. Eastment and C. H. B. Mee. Work function measurements on (100), (110) and (111) surfaces of aluminium. *Journal of Physics F: Metal Physics*, 3(9):1738, 1973.

[86] P. I. Djurovich, E. I. Mayo, S. R. Forrest, and M. E. Thompson. Measurement of the lowest unoccupied molecular orbital energies of molecular organic semiconductors. *Organic Electronics*, 10(3):515–520, 2009.

[87] H. Ishii, K. Sugiyama, E. Ito, and K. Seki. Energy level alignment and interfacial electronic structures at organic/metal and organic/organic interfaces. *Advanced Materials*, 11(8):605–625, 1999.

[88] A. Opitz, J. Frisch, R. Schlesinger, A. Wilke, and N. Koch. Energy level alignment at interfaces in organic photovoltaic devices. *Journal of Electron Spectroscopy and Related Phenomena*, 190:12–24, 2013.

[89] G. Horowitz, D. Fichou, X. Peng, Z. Xu, and F. Garnier. A field-effect transistor based on conjugated alpha-sexithienyl. *Solid State Communications*, 72(4):381–384, 1989.

[90] S. C. Veenstra, G. G. Malliaras, H. J. Brouwer, F. J. Esselink, V. V. Krasnikov, P. F. van Hutten, J. Wildeman, H. T. Jonkman, G. A. Sawatzky, and G. Hadzioannou. Preparation of photovoltaic cells from sexithiophene-C_{60} blends. *SPIE Proceedings*, 2852, 1996.

[91] M. Kiel, K. Duncker, C. Hagendorf, and W. Widdra. Molecular structure and chiral separation in α-sexithiophene ultrathin films on Au(111): Low-energy electron diffraction and scanning tunneling microscopy. *Physical Review B*, 75(19):195439, 2007.

[92] B. Servet, S. Ries, M. Trotel, P. Alnot, G. Horowitz, and F. Garnier. X-ray determination of the crystal structure and orientation of vacuum evaporated sexithiophene films. *Advanced Materials*, 5(6):461–464, 1993.

[93] C. Aruta, P. D'Angelo, M. Barra, G. Ausanio, and A. Cassinese. Improved structural ordering in sexithiophene thick films grown on single crystal oxide substrates. *Applied Physics A*, 97(2):387–394, 2009.

[94] A. Moser, I. Salzmann, M. Oehzelt, A. Neuhold, H.-G. Flesch, J. Ivanco, S. Pop, T. Toader, D. R.T. Zahn, D.-M. Smilgies, and R. Resel. A disordered layered phase in thin films of sexithiophene. *Chemical Physics Letters*, 574:51–55, 2013.

[95] R. N. Marks, M. Muccini, E. Lunedi, R. H. Michel, M. Murgia, R. Zamboni, C. Taliani, G. Horowitz, F. Garnier, M. Hopmeier, M. Oestreich, and R. F. Mahrt. Disorder influenced optical properties of α-sexithiophene single crystals and thin evaporated films. *Chemical Physics*, 227(1–2):49–56, 1998.

[96] U. Hörmann, C. Lorch, A. Hinderhofer, A. Gerlach, M. Gruber, J. Kraus, B. Sykora, S. Grob, T. Linderl, A. Wilke, A. Opitz, R. Hansson, A. S. Anselmo, Y. Ozawa, Y. Nakayama, H. Ishii, N. Koch, E. Moons, F. Schreiber, and W. Brütting. V_{oc} from a morphology point of view: the influence of molecular orientation on the open circuit voltage of organic planar heterojunction solar cells. *The Journal of Physical Chemistry C*, 118(46):26462–26470, 2014.

[97] K. Takimiya, T. Yamamoto, H. Ebata, and T. Izawa. Design strategy for air-stable organic semiconductors applicable to high-performance field-effect transistors. *Science and Technology of Advanced Materials*, 8(4):273, 2007.

[98] M. Reig, J. Puigdollers, and D. Velasco. Molecular order of air-stable p-type organic thin-film transistors by tuning the extension of the π-conjugated core: the cases of indolo[3,2-b]carbazole and triindole semiconductors. *Journal of Materials Chemistry C*, 3:506–513, 2015.

[99] U. Hörmann, J. Wagner, M. Gruber, A. Opitz, and W. Brütting. Approaching the ultimate open circuit voltage in thiophene based single junction solar cells by applying diindenoperylene as acceptor. *Physica Status Solidi RRL*, 5(7):241–243, 2011.

[100] A. Mani, J. Schoonman, and A. Goossens. Photoluminescence study of sexithiophene thin films. *The Journal of Physical Chemistry B*, 109(11):4829–4836, 2005.

[101] J. von Braun and G. Manz. Verfahren zur Herstellung von Kondensationsprodukten des Fluoranthens. *Deutsches Reichspatentamt Berlin*, 595024, 1934.

[102] M. Münch. *Strukturelle Beeinflussung der elektrischen Transporteigenschaften dünner organischer Schichten.* PhD thesis, Universität Stuttgart, 2001.

[103] N. Karl. Charge-carrier mobility in organic crystals. In *Organic Electronic Materials*, pages 283–326. Springer Berlin Heidelberg, 2001.

[104] A. C. Dürr, F. Schreiber, M. Münch, N. Karl, B. Krause, V. Kruppa, and H. Dosch. High structural order in thin films of the organic semiconductor diindenoperylene. *Applied Physics Letters*, 81(12):2276–2278, 2002.

[105] A. C. Dürr. *Growth and Structure of DIP Thin-Films and Au Contacts on DIP Thin-Films.* PhD thesis, Universität Stuttgart, 2002.

[106] D. Kurrle and J. Pflaum. Exciton diffusion length in the organic semiconductor diindenoperylene. *Applied Physics Letters*, 92(13):133306, 2008.

[107] M. Horlet, M. Kraus, W. Brütting, and A. Opitz. Diindenoperylene as ambipolar semiconductor: Influence of electrode materials and mobility asymmetry in organic field-effect transistors. *Applied Physics Letters*, 98(23):233304, 2011.

[108] J. Wagner, M. Gruber, A. Hinderhofer, A. Wilke, B. Bröker, J. Frisch, P. Amsalem, A. Vollmer, A. Opitz, N. Koch, F. Schreiber, and W. Brütting. High fill factor and open circuit voltage in organic photovoltaic cells with diindenoperylene as donor material. *Advanced Functional Materials*, 20(24):4295–4303, 2010.

[109] A. Opitz, J. Wagner, W. Brütting, I. Salzmann, N. Koch, J. Manara, J. Pflaum, A. Hinderhofer, and F. Schreiber. Charge separation at molecular donor-acceptor interfaces: Correlation between morphology and solar cell performance. *IEEE Journal of Selected Topics in Quantum Electronics*, 16(6):1707–1717, 2010.

[110] M. Gruber, M. Rawolle, J. Wagner, D. Magerl, U. Hörmann, J. Perlich, S. V. Roth, A. Opitz, F. Schreiber, P. Müller-Buschbaum, and W. Brütting. Correlating structure and morphology to device performance of molecular organic donor-acceptor photovoltaic cells based on diindenoperylene (DIP) and C_{60}. *Advanced Energy Materials*, 3(8):1075–1083, 2013.

[111] A. C. Dürr, N. Koch, M. Kelsch, A. Rühm, J. Ghijsen, R. L. Johnson, J.-J. Pireaux, J. Schwartz, F. Schreiber, H. Dosch, and A. Kahn. Interplay between morphology, structure, and electronic properties at diindenoperylene-gold interfaces. *Physical Review B*, 68:115428, 2003.

[112] S. Kowarik, A. Gerlach, S. Sellner, L. Cavalcanti, O. Konovalov, and F. Schreiber. Real-time X-ray diffraction measurements of structural dynamics and polymorphism in diindenoperylene growth. *Applied Physics A*, 95(1):233–239, 2009.

[113] A. C. Dürr, F. Schreiber, K. A. Ritley, V. Kruppa, J. Krug, H. Dosch, and B. Struth. Rapid roughening in thin film growth of an organic semiconductor (diindenoperylene). *Physical Review Letters*, 90:016104, 2003.

[114] J. D. Debad, J. C. Morris, V. Lynch, P. Magnus, and A. J. Bard. Dibenzotetraphenylperiflanthene: Synthesis, photophysical properties, and electrogenerated chemiluminescence. *Journal of the American Chemical Society*, 118(10):2374–2379, 1996.

[115] K. Okumoto, H. Kanno, Y. Hamada, H. Takahashi, and K. Shibata. High efficiency red organic light-emitting devices using tetraphenyldibenzoperiflanthene-doped rubrene as an emitting layer. *Applied Physics Letters*, 89(1):013502, 2006.

[116] M. Hirade and C. Adachi. Small molecular organic photovoltaic cells with exciton blocking layer at anode interface for improved device performance. *Applied Physics Letters*, 99(15):153302, 2011.

[117] Y. Zhou, T. Taima, Y. Shibata, T. Miyadera, T. Yamanari, and Y. Yoshida. Controlled growth of dibenzotetraphenylperiflanthene thin films by varying substrate temperature for photovoltaic applications. *Solar Energy Materials and Solar Cells*, 95(10):2861 – 2866, 2011.

[118] D. Yokoyama, Z. Q. Wang, Y.-J. Pu, K. Kobayashi, J. Kido, and Z. Hong. High-efficiency simple planar heterojunction organic thin-film photovoltaics with horizontally oriented amorphous donors. *Solar Energy Materials and Solar Cells*, 98:472–475, 2012.

[119] Y. Zhou, T. Taima, T. Kuwabara, and K. Takahashi. Efficient small-molecule photovoltaic cells using a crystalline diindenoperylene film as a nanostructured template. *Advanced Materials*, 25(42):6069–6075, 2013.

[120] Y.-Q. Zheng, W. J. Potscavage, T. Komino, M. Hirade, J. Adachi, and C. Adachi. Highly efficient bulk heterojunction photovoltaic cells based on C_{70} and tetraphenyldibenzoperiflanthene. *Applied Physics Letters*, 102(14):143304, 2013.

[121] Z. Wang, D. Yokoyama, X.-F. Wang, Z. Hong, Y. Yang, and J. Kido. Highly efficient organic p-i-n photovoltaic cells based on tetraphenyldibenzoperiflanthene and fullerene C_{70}. *Energy & Environmental Science*, 6:249–255, 2013.

[122] X. Xiao, J. D. Zimmerman, B. E. Lassiter, K. J. Bergemann, and S. R. Forrest. A hybrid planar-mixed tetraphenyldibenzoperiflanthene/C_{70} photovoltaic cell. *Applied Physics Letters*, 102(7):073302, 2013.

[123] X. Xiao, K. J. Bergemann, J. D. Zimmerman, K. Lee, and S. R. Forrest. Small-molecule planar-mixed heterojunction photovoltaic cells with fullerene-based electron filtering buffers. *Advanced Energy Materials*, 4(7):1301557, 2014.

[124] P. A. Heiney, J. E. Fischer, A. R. McGhie, W. J. Romanow, A. M. Denenstein, J. P. McCauley Jr., A. B. Smith, and D. E. Cox. Orientational ordering transition in solid C_{60}. *Physical Review Letters*, 66:2911–2914, 1991.

[125] E. Osawa. Superaromaticity. *Kagaku*, 25:854–863, 1970.

[126] H. W. Kroto, J. R. Heath, S. C. O'Brien, R. F. Curl, and R. E. Smalley. C_{60}: Buckminsterfullerene. *Nature*, 318(6042):162–163, 1985.

[127] B. C. Thompson and J. M. J. Fréchet. Polymer-fullerene composite solar cells. *Angewandte Chemie International Edition*, 47(1):58–77, 2008.

[128] Y. Matsuo. Development of fullerene derivatives with high LUMO level through changes in π-conjugated system shape. *Pure and Applied Chemistry*, 84(4):945–952, 2012.

[129] D. Qin, P. Gu, R. S. Dhar, S. G. Razavipour, and D. Ban. Measuring the exciton diffusion length of C_{60} in organic planar heterojunction solar cells. *physica status solidi (a)*, 208(8):1967–1971, 2011.

[130] G. Schwabegger, M. Ullah, M. Irimia-Vladu, M. Baumgartner, Y. Kanbur, R. Ahmed, P. Stadler, S. Bauer, N. S. Sariciftci, and H. Sitter. High mobility, low voltage operating C_{60} based n-type organic field effect transistors. *Synthetic Metals*, 161(19–20):2058–2062, 2011.

[131] B. Kraabel, D. McBranch, N. S. Sariciftci, D. Moses, and A. J. Heeger. Ultrafast spectroscopic studies of photoinduced electron transfer from semiconducting polymers to C_{60}. *Physical Review B*, 50:18543–18552, 1994.

[132] K. Hedberg, L. Hedberg, M. Bühl, D. S. Bethune, C. A. Brown, and R. D. Johnson. Molecular structure of free molecules of the fullerene C_{70} from gas-phase electron diffraction. *Journal of the American Chemical Society*, 119(23):5314–5320, 1997.

[133] S. Pfuetzner, J. Meiss, A. Petrich, M. Riede, and K. Leo. Improved bulk heterojunction organic solar cells employing C_{70} fullerenes. *Applied Physics Letters*, 94(22):223307, 2009.

[134] C. Trinh, K. Kirlikovali, S. Das, M. E. Ener, H. B. Gray, P. Djurovich, S. E. Bradforth, and M. E. Thompson. Symmetry-breaking charge transfer of visible light absorbing systems: Zinc dipyrrins. *The Journal of Physical Chemistry C*, 118(38):21834–21845, 2014.

[135] A. N. Bartynski, M. Gruber, S. Das, S. Rangan, S. Mollinger, C. Trinh, S. E. Bradforth, K. Vandewal, A. Salleo, R. A. Bartynski, W. Brütting, and M. E. Thompson. Symmetry-breaking charge transfer in a zinc chlorodipyrrin acceptor for high open circuit voltage organic photovoltaics. *Journal of the American Chemical Society*, 137(16):5397–5405, 2015.

[136] Y. Lin, Y. Li, and X. Zhan. Small molecule semiconductors for high-efficiency organic photovoltaics. *Chemical Society Reviews*, 41:4245–4272, 2012.

[137] Z. R. Grabowski, K. Rotkiewicz, and W. Rettig. Structural changes accompanying intramolecular electron transfer: Focus on twisted intramolecular charge-transfer states and structures. *Chemical Reviews*, 103(10):3899–4032, 2003.

[138] F. Jonas and J. T. Morrison. 3,4-polyethylenedioxythiophene (PEDT): Conductive coatings technical applications and properties. *Synthetic Metals*, 85(1–3):1397–1398, 1997.

[139] J. Huang, P. F. Miller, J. S. Wilson, A. J. de Mello, J. C. de Mello, and D. D. C. Bradley. Investigation of the effects of doping and post-deposition treatments on the conductivity, morphology, and work function of poly(3,4-ethylenedioxythiophene)/poly(styrene sulfonate) films. *Advanced Functional Materials*, 15(2):290–296, 2005.

[140] Y. Wang. Research progress on a novel conductive polymer–poly(3,4-ethylenedioxythiophene) (PEDOT). *Journal of Physics: Conference Series*, 152(1):012023, 2009.

[141] Y. Park, V. Choong, Y. Gao, B. R. Hsieh, and C. W. Tang. Work function of indium tin oxide transparent conductor measured by photoelectron spectroscopy. *Applied Physics Letters*, 68(19):2699–2701, 1996.

[142] C. Winder and N. S. Sariciftci. Low bandgap polymers for photon harvesting in bulk heterojunction solar cells. *Journal of Materials Chemistry*, 14:1077–1086, 2004.

[143] Y. Sun, N. C. Giebink, H. Kanno, B. Ma, M. E. Thompson, and S. R. Forrest. Management of singlet and triplet excitons for efficient white organic light-emitting devices. *Nature*, 440(7086):908–912, April 2006.

[144] D. F. O'Brien, M. A. Baldo, M. E. Thompson, and S. R. Forrest. Improved energy transfer in electrophosphorescent devices. *Applied Physics Letters*, 74(3):442–444, 1999.

[145] P. Peumans, V. Bulovic, and S. R. Forrest. Efficient photon harvesting at high optical intensities in ultrathin organic double-heterostructure photovoltaic diodes. *Applied Physics Letters*, 76(19):2650–2652, 2000.

[146] H. Gommans, B. Verreet, B. P. Rand, R. Muller, J. Poortmans, P. Heremans, and J. Genoe. On the role of bathocuproine in organic photovoltaic cells. *Advanced Functional Materials*, 18(22):3686–3691, 2008.

[147] M. Scharnberg, J. Hu, J. Kanzow, K. Rätzke, R. Adelung, F. Faupel, C. Pannemann, U. Hilleringmann, S. Meyer, and J. Pflaum. Radiotracer measurements as a sensitive tool for the detection of metal penetration in molecular-based organic electronics. *Applied Physics Letters*, 86(2):024104, 2005.

[148] A. Steindamm, M. Brendel, A. K. Topczak, and J. Pflaum. Thickness dependent effects of an intermediate molecular blocking layer on the optoelectronic characteristics of organic bilayer photovoltaic cells. *Applied Physics Letters*, 101(14):143302, 2012.

[149] P. Peumans and S. R. Forrest. Very-high-efficiency double-heterostructure copper phthalocyanine/C_{60} photovoltaic cells. *Applied Physics Letters*, 79(1):126–128, 2001.

[150] X. Mo, T. Mizokuro, H. Mochizuki, N. Tanigaki, and T. Hiraga. Preparation of smooth polymer thin film using spray method under vacuum. *Japanese Journal of Applied Physics*, 43(1):307, 2004.

[151] D. B. Hall, P. Underhill, and J. M. Torkelson. Spin coating of thin and ultrathin polymer films. *Polymer Engineering & Science*, 38(12):2039–2045, 1998.

[152] W. W. Flack, D. S. Soong, A. T. Bell, and D. W. Hess. A mathematical model for spin coating of polymer resists. *Journal of Applied Physics*, 56(4):1199–1206, 1984.

[153] S. R. Forrest. Ultrathin organic films grown by organic molecular beam deposition and related techniques. *Chemical Reviews*, 97(6):1793–1896, 1997.

[154] S. R. Forrest. The path to ubiquitous and low-cost organic electronic appliances on plastic. *Nature*, 428(6986):911–918, 2004.

[155] M. Zhang, H. Wang, H. Tian, Y. Geng, and C. W. Tang. Bulk heterojunction photovoltaic cells with low donor concentration. *Advanced Materials*, 23(42):4960–4964, 2011.

[156] H. Kim, C. M. Gilmore, A. Piqué, J. S. Horwitz, H. Mattoussi, H. Murata, Z. H. Kafafi, and D. B. Chrisey. Electrical, optical, and structural properties of indium–tin–oxide thin films for organic light-emitting devices. *Journal of Applied Physics*, 86(11):6451–6461, 1999.

[157] M. Kraus, S. Richler, A. Opitz, W. Brütting, S. Haas, T. Hasegawa, A. Hinderhofer, and F. Schreiber. High-mobility copper-phthalocyanine field-effect transistors with tetratetracontane passivation layer and organic metal contacts. *Journal of Applied Physics*, 107(9):094503, 2010.

[158] M. Kraus, S. Haug, W. Brütting, and A. Opitz. Achievement of balanced electron and hole mobility in copper-phthalocyanine field-effect transistors by using a crystalline aliphatic passivation layer. *Organic Electronics*, 12(5):731–735, 2011.

[159] A. Opitz, M. Horlet, M. Kiwull, J. Wagner, M. Kraus, and W. Brütting. Bipolar charge transport in organic field-effect transistors: Enabling high mobilities and transport of photo-generated charge carriers by a molecular passivation layer. *Organic Electronics*, 13(9):1614–1622, 2012.

[160] J. Evers, P. Klüfers, R. Staudigl, and P. Stallhofer. Czochralski's creative mistake: A milestone on the way to the gigabit era. *Angewandte Chemie International Edition*, 42(46):5684–5698, 2003.

[161] M. Brinkmann, J. C. Wittmann, C. Chaumont, and J. J. André. Effects of solvent on the morphology and crystalline structure of lithium phthalocyanine thin films and powders. *Thin Solid Films*, 292:192–203, 1997.

[162] F. Toffolo, M. Brinkmann, O. Greco, F. Biscarini, C. Taliani, H. L. Gomes, I. Aiello, and M. Ghedini. Influence of the metal center on the morphology of coordination compounds thin films. *Synthetic Metals*, 101:140 – 141, 1999.

[163] D. J. Mascaro, M. E. Thompson, H. I. Smith, and V. Bulović. Forming oriented organic crystals from amorphous thin films on patterned substrates via solvent-vapor annealing. *Organic Electronics*, 6:211–220, 2005.

[164] S. Miller, G. Fanchini, Y.-Y. Lin, C. Li, C.-W. Chen, W.-F. Su, and M. Chhowalla. Investigation of nanoscale morphological changes in organic photovoltaics during solvent vapor annealing. *Journal of Materials Chemistry*, 18:306–312, 2008.

[165] J. D. Zimmerman, X. Xiao, C. K. Renshaw, S. Wang, V. V. Diev, M. E. Thompson, and S. R. Forrest. Independent control of bulk and interfacial morphologies of small molecular weight organic heterojunction solar cells. *Nano Letters*, 12(8):4366–4371, 2012.

[166] K. Sun, Z. Xiao, E. Hanssen, M. F. G. Klein, H. H. Dam, M. Pfaff, D. Gerthsen, W. W. H. Wong, and D. J. Jones. The role of solvent vapor annealing in highly efficient air-processed small molecule solar cells. *Journal of Materials Chemistry A*, 2:9048–9054, 2014.

[167] A. Datar, R. Oitker, and L. Zang. Surface-assisted one-dimensional self-assembly of a perylene based semiconductor molecule. *Chemical Communications*, 15:1649–1651, 2006.

[168] G. De Luca, E. Treossi, A. Liscio, J. M. Mativetsky, L. M. Scolaro, V. Palermo, and P. Samori. Solvent vapour annealing of organic thin films: controlling the self-assembly of functional systems across multiple length scales. *Journal of Materials Chemistry*, 20:2493–2498, 2010.

[169] T. S. Yu. *Solidification in a thin liquid film: Growing Alq_3 needles via methanol-vapor annealing.* PhD thesis, Massachusetts Institute of Technology, 2011.

[170] S. Kowarik, A. Gerlach, S. Sellner, L. Cavalcanti, and F. Schreiber. Dewetting of an organic semiconductor thin film observed in real-time. *Advanced Engineering Materials*, 11(4):291–294, 2009.

[171] S. Hüttner, M. Sommer, A. Chiche, G. Krausch, U. Steiner, and M. Thelakkat. Controlled solvent vapour annealing for polymer electronics. *Soft Matter*, 5:4206–4211, 2009.

[172] G. De Luca, A. Liscio, F. Nolde, L. M. Scolaro, V. Palermo, K. Mullen, and P. Samori. Self-assembly of discotic molecules into mesoscopic crystals by solvent-vapour annealing. *Soft Matter*, 4:2064–2070, 2008.

[173] P.-G. de Gennes, F. Brochard-Wyart, and D. Quere. *Capillarity and Wetting Phenomena: Drops, Bubbles, Pearls, Waves.* Springer Science & Business Media, 2004.

[174] G. Beernink, T. Strunskus, G. Witte, and C. Wöll. Importance of dewetting in organic molecular-beam deposition: Pentacene on gold. *Applied Physics Letters*, 85(3):398–400, 2004.

[175] S. Chattopadhyay and J. C. Meredith. Combinatorial screening of organic electronic materials: thin film stability. *Measurement Science and Technology*, 16(1):128, 2005.

[176] K. B. Glasner and T. P. Witelski. Coarsening dynamics of dewetting films. *Physical Review E*, 67:016302, 2003.

[177] J. S. Langer. Instabilities and pattern formation in crystal growth. *Reviews of Modern Physics*, 52:1–28, 1980.

[178] A. Steeger. Einfluss der Struktur auf exczitonische Transportprozesse in organischen Dünnschichten. Master's thesis, Julius-Maximilians-Universität Würzburg, 2013.

[179] J. I. Langford and J. S. Wilson. Scherrer after sixty years: A survey and some new results in the determination of crystallite size. *Journal of Applied Crystallography*, 11:102–113, 1978.

[180] W. C. Marra, P. Eisenberger, and A. Y. Cho. X-ray total-external-reflection-Bragg diffraction: A structural study of the GaAsAl interface. *Journal of Applied Physics*, 50(11):6927–6933, 1979.

[181] M. Neuschitzer, A. Moser, A. Neuhold, J. Kraxner, B. Stadlober, M. Oehzelt, I. Salzmann, R. Resel, and J. Novák. Grazing-incidence in-plane X-ray diffraction on ultra-thin organic films using standard laboratory equipment. *Journal of Applied Crystallography*, 45(2):367–370, 2012.

[182] P. R. Willmott, D. Meister, S. J. Leake, M. Lange, A. Bergamaschi, M. Böge, M. Calvi, C. Cancellieri, N. Casati, A. Cervellino, Q. Chen, C. David, U. Flechsig, F. Gozzo, B. Henrich, S. Jäggi-Spielmann, B. Jakob, I. Kalichava, P. Karvinen, J. Krempasky, A. Lüdeke, R. Lüscher, S. Maag, C. Quitmann, M. L. Reinle-Schmitt, T. Schmidt, B. Schmitt, A. Streun, I. Vartiainen, M. Vitins, X. Wang, and R. Wullschleger. The materials science beamline upgrade at the Swiss light source. *Journal of Synchrotron Radiation*, 20(5):667–682, 2013.

[183] D. M. DeLongchamp, E. K. Lin, and D. A. Fischer. Organic semiconductor structure and chemistry from near-edge X-ray absorption fine structure (NEXAFS) spectroscopy. *SPIE Proceedings*, 5940:59400A1–11, 2005.

[184] J. Stöhr and R. Jaeger. Absorption-edge resonances, core-hole screening, and orientation of chemisorbed molecules: CO, NO, and N_2 on Ni(100). *Physical Review B*, 26:4111–4131, 1982.

[185] J. Yano and V. K. Yachandra. X-ray absorption spectroscopy. *Photosynthesis Research*, 102(2-3):241–254, 2009.

[186] J. Stöhr and D. A. Outka. Determination of molecular orientations on surfaces from the angular dependence of near-edge x-ray-absorption fine-structure spectra. *Physical Review B*, 36:7891–7905, 1987.

[187] U. Hörmann. *V_{OC} from a morphology point of view: On the open circuit voltage of polycrystalline organic heterojunction solar cells*. PhD thesis, Universität Augsburg, 2014.

[188] L. Gross, F. Mohn, N. Moll, P. Liljeroth, and G. Meyer. The chemical structure of a molecule resolved by atomic force microscopy. *Science*, 325(5944):1110–1114, 2009.

[189] L. Gross, F. Mohn, N. Moll, G. Meyer, R. Ebel, W. M. Abdel-Mageed, and M. Jaspars. Organic structure determination using atomic-resolution scanning probe microscopy. *Nature Chemistry*, 2(10):821–825, 2010.

[190] G. Binnig, C. F. Quate, and C. Gerber. Atomic force microscope. *Physical Review Letters*, 56:930–933, 1986.

[191] Q. Zhong, D. Innis, K. Kjoller, and V. B. Elings. Fractured polymer/silica fiber surface studied by tapping mode atomic force microscopy. *Surface Science Letters*, 290(1-2):688–692, 1993.

[192] V. Shrotriya, G. Li, Y. Yao, T. Moriarty, K. Emery, and Y. Yang. Accurate measurement and characterization of organic solar cells. *Advanced Functional Materials*, 16(15):2016–2023, 2006.

[193] American Society for Testing and Materials. Terrestrial reference spectra for photovoltaic performance evaluation. http://rredc.nrel.gov/solar/spectra/am1.5/ downloaded on 8/24/2015.

[194] M. Gruber. *Analyse der Verluste organischer Donor/Akzeptor - Solarzellen*. PhD thesis, Universität Augsburg, 2014.

[195] R. Ahmed, A. Kadashchuk, C. Simbrunner, G. Schwabegger, M. Havlicek, E. Głowacki, N.S. Sariciftci, M.A. Baig, and H. Sitter. Photosensitivity of top gate C_{60} based OFETs: Potential applications for high efficiency organic photodetector. *Organic Electronics*, 15(1):175–181, 2014.

[196] F. Reinert and S. Hüfner. Photoemission spectroscopy-from early days to recent applications. *New Journal of Physics*, 7(1):97, 2005.

[197] S. Krause, M. B. Casu, A. Schöll, and E. Umbach. Determination of transport levels of organic semiconductors by UPS and IPS. *New Journal of Physics*, 10(8):085001, 2008.

[198] J. H. Weaver. Electronic structures of C_{60}, C_{70} and the fullerides: Photoemission and inverse photoemission studies. *Journal of Physics and Chemistry of Solids*, 53(11):1433–1447, 1992.

[199] R. Könenkamp, G. Priebe, and B. Pietzak. Carrier mobilities and influence of oxygen in C_{60} films. *Physical Review B*, 60(16):11804–11808, 1999.

[200] A. Hinderhofer, T. Hosokai, K. Yonezawa, A. Gerlach, K. Kato, K. Broch, C. Frank, J. Novak, S. Kera, N. Ueno, and F. Schreiber. Post-growth surface smoothing of thin films of diindenoperylene. *Applied Physics Letters*, 101(3):033307, 2012.

[201] S. Kowarik, A. Gerlach, S. Sellner, F. Schreiber, L. Cavalcanti, and O. Konovalov. Real-time observation of structural and orientational transitions during growth of organic thin films. *Physical Review Letters*, 96:125504, 2006.

[202] M. B. Casu, S.-A. Savu, B.-E. Schuster, I. Biswas, C. Raisch, H. Marchetto, T. Schmidt, and T. Chassé. Island shapes and aggregation steered by the geometry of the substrate lattice. *Chemical Communications*, 48:6957–6959, 2012.

[203] S. Yu, A. Opitz, S. Grob, R. Resel, M. Oehzelt, W. Brütting, I. Salzmann, and N. Koch. Performance enhancement of diindenoperylene-based organic photovoltaic cells by nanocolumn-arrays. *Organic Electronics*, 15(10):2210–2217, 2014.

[204] M. M. Hawkeye and M. J. Brett. Glancing angle deposition: Fabrication, properties, and applications of micro- and nanostructured thin films. *Journal of Vacuum Science & Technology A*, 25(5):1317–1335, 2007.

[205] J. G. Van Dijken, M. D. Fleischauer, and M. J. Brett. Solvent effects on ZnPc thin films and their role in fabrication of nanostructured organic solar cells. *Organic Electronics*, 12(12):2111–2119, 2011.

[206] F. Kouki, P. Spearman, P. Valat, G. Horowitz, and F. Garnier. Experimental determination of excitonic levels in α-oligothiophenes. *The Journal of Chemical Physics*, 113(1):385–391, 2000.

[207] H. Bedis. Effect of self-assembled monolayers on the performance of organic photovoltaic cells. *Journal of Surface Engineered Materials and Advanced Technology*, 1(2):42–50, 2011.

[208] U. Heinemeyer, R. Scholz, L. Gisslén, M. I. Alonso, J. O. Ossó, M. Garriga, A. Hinderhofer, M. Kytka, S. Kowarik, A. Gerlach, and F. Schreiber. Exciton-phonon coupling in diindenoperylene thin films. *Phys. Rev. B*, 78:085210, Aug 2008.

[209] B. P. Rand, S. Schols, D. Cheyns, H. Gommans, C. Girotto, J. Genoe, P. Heremans, and J. Poortmans. Organic solar cells with sensitized phosphorescent absorbing layers. *Organic Electronics*, 10(5):1015–1019, 2009.

[210] M. Sim, J. Shin, C. Shim, M. Kim, S. B. Jo, J.-H. Kim, and K. Cho. Dependence of exciton diffusion length on crystalline order in conjugated polymers. *The Journal of Physical Chemistry C*, 118(2):760–766, 2014.

[211] S. Schmidt. Beweglichkeitsmessungen an DIP, DBP und Fulleren Feldeffekttransistoren. Bachelor's thesis, Universität Augsburg, 2013.

[212] U. Rau, P. O. Grabitz, and J. H. Werner. Resistive limitations to spatially inhomogeneous electronic losses in solar cells. *Applied Physics Letters*, 85(24):6010–6012, 2004.

[213] J. Xue, S. Uchida, B. P. Rand, and S. R. Forrest. 4.2 % efficient organic photovoltaic cells with low series resistances. *Applied Physics Letters*, 84(16):3013–3015, 2004.

[214] J. D. Servaites, S. Yeganeh, T. J. Marks, and M. A. Ratner. Efficiency enhancement in organic photovoltaic cells: Consequences of optimizing series resistance. *Advanced Functional Materials*, 20(1):97–104, 2010.

[215] K. Itaka, M. Yamashiro, J. Yamaguchi, M. Haemori, S. Yaginuma, Y. Matsumoto, M. Kondo, and H. Koinuma. High-mobility C_{60} field-effect transistors fabricated on molecular-wetting controlled substrates. *Advanced Materials*, 18(13):1713–1716, 2006.

[216] H. Yan, T. Kagata, and H. Okuzaki. Ambipolar pentacene/C_{60}-based field-effect transistors with high hole and electron mobilities in ambient atmosphere. *Applied Physics Letters*, 94(2):023305, 2009.

[217] F. Yang, M. Shtein, and S. R. Forrest. Controlled growth of a molecular bulk heterojunction photovoltaic cell. *Nature Materials*, 4(1):37–41, 2005.

[218] P. Kovacik, H. E. Assender, and A. A.R. Watt. Morphology control in co-evaporated bulk heterojunction solar cells. *Solar Energy Materials and Solar Cells*, 117:22–28, 2013.

[219] T. Stübinger and W. Brütting. Exciton diffusion and optical interference in organic donor-acceptor photovoltaic cells. *Journal of Applied Physics*, 90(7):3632–3641, 2001.

[220] A. Hofmann. Einfluss von Morphologie und Schichtdicke auf DIP/C_{60}-Solarzellen in Experiment und Simulation. Bachelor's thesis, Universität Augsburg, 2011.

[221] A. N. Bartynski, S. Grob, T. Linderl, M. Gruber, W. Brütting, and M. E. Thompson. Organic solar cells with open circuit voltage over 1.25 V employing tetraphenyldibenzoperiflanthene as the acceptor. *To be published*, 2015.

[222] Y.-T. Fu, D. A. da Silva Filho, G. Sini, A. M. Asiri, S. G. Aziz, C. Risko, and J.-L. Brédas. Structure and disorder in squaraine–C_{60} organic solar cells: A theoretical description of molecular packing and electronic coupling at the donor–acceptor interface. *Advanced Functional Materials*, 24(24):3790–3798, 2014.

[223] Y. Yi, V. Coropceanu, and J.-L. Brédas. Exciton-dissociation and charge-recombination processes in pentacene/C_{60} solar cells: Theoretical insight into the impact of interface geometry. *Journal of the American Chemical Society*, 131(43):15777–15783, 2009.

[224] Y. Yi, V. Coropceanu, and J.-L. Brédas. A comparative theoretical study of exciton-dissociation and charge-recombination processes in oligothiophene/fullerene and oligothiophene/perylenediimide complexes for organic solar cells. *J. Mater. Chem.*, 21:1479–1486, 2011.

[225] P. Erwin and M. E. Thompson. Elucidating the interplay between dark current coupling and open circuit voltage in organic photovoltaics. *Applied Physics Letters*, 98(22):223305, 2011.

[226] G. A. H. Wetzelaer, L. J. A. Koster, and P. W. M. Blom. Validity of the Einstein relation in disordered organic semiconductors. *Phys. Rev. Lett.*, 107:066605, Aug 2011.

[227] N. C. Giebink, G. P. Wiederrecht, M. R. Wasielewski, and S. R. Forrest. Ideal diode equation for organic heterojunctions. I. Derivation and application. *Physical Review B*, 82:155305, 2010.

[228] G. Horowitz and P. Delannoy. An analytical model for organic-based thin-film transistors. *Journal of Applied Physics*, 70(1):469–475, 1991.

[229] W. Shockley and W. T. Read. Statistics of the recombinations of holes and electrons. *Physical Review*, 87(5):835–842, 1952.

[230] R. N. Hall. Electron-hole recombination in germanium. *Physical Review*, 87(2):387–387, 1952.

[231] T. Kirchartz, F. Deledalle, P. S. Tuladhar, J. R. Durrant, and J. Nelson. On the differences between dark and light ideality factor in polymer:fullerene solar cells. *The Journal of Physical Chemistry Letters*, 4(14):2371–2376, 2013.

[232] S. Grob, M. Gruber, A. N. Bartynski, U. Hörmann, T. Linderl, M. E. Thompson, and W. Brütting. Amorphous vs crystalline exciton blocking layers at the anode interface in planar and planar-mixed heterojunction organic solar cells. *Applied Physics Letters*, 104(21):213304, 2014.

[233] S. Naka, H. Okada, H. Onnagawa, and T. Tsutsui. High electron mobility in bathophenanthroline. *Applied Physics Letters*, 76(2):197–199, 2000.

[234] M. Y. Chan, C. S. Lee, S. L. Lai, M. K. Fung, F. L. Wong, H. Y. Sun, K. M. Lau, and S. T. Lee. Efficient organic photovoltaic devices using a combination of exction blocking layer and anodic buffer layer. *Journal of Applied Physics*, 100(9):094506, 2006.

[235] A. N. Bartynski, C. Trinh, A. Panda, K. Bergemann, B. E. Lassiter, J. D. Zimmerman, S. R. Forrest, and M. E. Thompson. A fullerene-based organic exciton blocking layer with high electron conductivity. *Nano Letters*, 13(7):3315–3320, 2013.

[236] K. Cnops, B. P. Rand, D. Cheyns, and P. Heremans. Enhanced photocurrent and open-circuit voltage in a 3-layer cascade organic solar cell. *Applied Physics Letters*, 101(14):143301, 2012.

[237] C. M. Proctor and T.-Q. Nguyen. Effect of leakage current and shunt resistance on the light intensity dependence of organic solar cells. *Applied Physics Letters*, 106(8):083301, 2015.

[238] S. L. M. van Mensfoort, V. Shabro, R. J. de Vries, R. A. J. Janssen, and R. Coehoorn. Hole transport in the organic small molecule material: evidence for the presence of correlated disorder. *Journal of Applied P*, 107(11):113710, 2010.

[239] C. Diez, T. C. G. Reusch, S. Seidel, and W. Brütting. Investigation of energy transfer mechanisms between two adjacent phosphorescent emission layers. *Journal of Applied Physics*, 111(11):113102, 2012.

[240] N. Koch, A. Elschner, J. Schwartz, and A. Kahn. Organic molecular films on gold versus conducting polymer: Influence of injection barrier height and morphology on current-voltage characteristics. *Applied Physics Letters*, 82(14):2281–2283, 2003.

[241] M. A. Baldo, Z. G. Soos, and S. R. Forrest. Local order in amorphous organic molecular thin films. *Chemical Physics Letters*, 347(4-6):297–303, 2001.

[242] Y. Shirota and H. Kageyama. Charge carrier transporting molecular materials and their applications in devices. *Chemical Reviews*, 107(4):953–1010, 2007.

[243] J. D. Zimmerman, B. Song, O. Griffith, and S. R. Forrest. Exciton-blocking phosphonic acid-treated anode buffer layers for organic photovoltaics. *Applied Physics Letters*, 103(24):243905, 2013.

[244] J. Xue, B.P. Rand, S. Uchida, and S.R. Forrest. A hybrid planar-mixed molecular heterojunction photovoltaic cell. *Advanced Materials*, 17(1):66–71, 2005.

[245] T. Ripolles-Sanchis, S. R. Raga, A. Guerrero, M. Welker, M. Turbiez, J. Bisquert, and G. Garcia-Belmonte. Molecular electronic coupling controls charge recombination kinetics in organic solar cells of low bandgap diketopyrrolopyrrole, carbazole,

and thiophene polymers. *The Journal of Physical Chemistry C*, 117(17):8719–8726, 2013.

[246] S. Grob, A. N. Bartynski, A. Opitz, M. Gruber, F. Graßl, E. Meister, T. Linderl, U. Hörmann, C. Lorch, E. Moons, F. Schreiber, M. E. Thompson, and W. Brütting. Solvent vapor annealing on perylene-based organic solar cells. *Journal of Materials Chemistry A*, 3:15700–15709, 2015.

[247] B. Song, C. Rolin, J. D. Zimmerman, and S. R. Forrest. Effect of mixed layer crystallinity on the performance of mixed heterojunction organic photovoltaic cells. *Advanced Materials*, 26(18):2914–2918, 2014.

[248] Z. Bao, A. J. Lovinger, and A. Dodabalapur. Organic field-effect transistors with high mobility based on copper phthalocyanine. *Applied Physics Letters*, 69(20):3066–3068, 1996.

[249] A. Mittelberger. Herstellung und Charakterisierung von Polymersolarzellen mit molekularen Akzeptoren. Bachelor's thesis, Universität Augsburg, 2012.

[250] F. Graßl. Solvent-annealing an DBP-basierten Solarzellen. Bachelor's thesis, Universität Augsburg, 2014.

[251] D. Bartesaghi and L. J. A. Koster. The effect of large compositional inhomogeneities on the performance of organic solar cells: A numerical study. *Advanced Functional Materials*, 25(13):2013–2023, 2015.

[252] D. Gebeyehu, C. J. Brabec, F. Padinger, T. Fromherz, J. C. Hummelen, D. Badt, H. Schindler, and N. S. Sariciftci. The interplay of efficiency and morphology in photovoltaic devices based on interpenetrating networks of conjugated polymers with fullerenes. *Synthetic Metals*, 118:1–9, 2001.

[253] Y. Zhao, X. Guo, Z. Xie, Y. Qu, Y. Geng, and L. Wang. Solvent vapor-induced self assembly and its influence on optoelectronic conversion of poly(3-hexylthiophene): Methanofullerene bulk heterojunction photovoltaic cells. *Journal of Applied Polymer Science*, 111(4):1799–1804, 2009.

[254] E. Verploegen, C. E. Miller, K. Schmidt, Z. Bao, and M. F. Toney. Manipulating the morphology of P3HT–PCBM bulk heterojunction blends with solvent vapor annealing. *Chemistry of Materials*, 24(20):3923–3931, 2012.

[255] A. Hinderhofer and F. Schreiber. Organic–organic heterostructures: Concepts and applications. *European Journal of Chemical Physics and Physical Chemistry*, 13(3):628–643, 2012.

[256] A. Hinderhofer, A. Gerlach, K. Broch, T. Hosokai, K. Yonezawa, K. Kato, S. Kera, N. Ueno, and F. Schreiber. Geometric and electronic structure of templated C_{60} on diindenoperylene thin films. *The Journal of Physical Chemistry C*, 117(2):1053–1058, 2013.

[257] I. McCulloch, M. Heeney, C. Bailey, K. Genevicius, I. MacDonald, M. Shkunov, D. Sparrowe, S. Tierney, R. Wagner, W. Zhang, M. L. Chabinyc, R. J. Kline, M. D. McGehee, and M. F. Toney. Liquid-crystalline semiconducting polymers with high charge-carrier mobility. *Nature Materials*, 5(4):328–333, 2006.

[258] R. A. Street, J. E. Northrup, and A. Salleo. Transport in polycrystalline polymer thin-film transistors. *Physical Review B*, 71:165202, 2005.

[259] M. B. Casu, I. Biswas, B.-E. Schuster, M. Nagel, P. Nagel, S. Schuppler, and T. Chassé. Molecular orientation in diindenoperylene thin films deposited on polycrystalline gold. *Applied Physics Letters*, 93(2):024103, 2008.

[260] W. Tress, K. Leo, and M. Riede. Influence of hole-transport layers and donor materials on open-circuit voltage and shape of I–V curves of organic solar cells. *Advanced Functional Materials*, 21(11):2140–2149, 2011.

[261] S. Duhm, G. Heimel, I. Salzmann, H. Glowatzki, R. L. Johnson, A. Vollmer, J. P. Rabe, and N. Koch. Orientation-dependent ionization energies and interface dipoles in ordered molecular assemblies. *Nature Materials*, 7(4):326–332, 2008.

[262] Y. L. Huang, W. Chen, H. Huang, D. C. Qi, S. Chen, X. Y. Gao, J. Pflaum, and A. T. S. Wee. Ultrathin films of diindenoperylene on graphite and SiO_2. *The Journal of Physical Chemistry C*, 113(21):9251–9255, 2009.

[263] P. Linsmayer. Zinkchlorodipyrrin als Akzeptormaterial in organischen Solarzellen. Bachelor's thesis, Universität Augsburg, 2014.

[264] G. Juska, K. Arlauskas, M. Viliunas, and J. Kocka. Extraction current transients: New method of study of charge transport in microcrystalline silicon. *Physical Review Letters*, 84:4946–4949, 2000.

[265] L. M. Terman. An investigation of surface states at a silicon/silicon oxide interface employing metal-oxide-silicon diodes. *Solid State Electronics*, 5(5):285–299, 1962.

List of publications

- S. Grob, A. N. Bartynski, A. Opitz, M. Gruber, F. Graßl, E. Meister, T. Linderl, U. Hörmann, C. Lorch, E. Moons, F. Schreiber, M. E. Thompson, and W. Brütting. Solvent vapor annealing on perylene-based organic solar cells. *Journal of Materials Chemistry A*, 3: 15700 - 15709, 2015.

- T. Linderl, U. Hörmann, S. Beratz, M. Gruber, S. Grob, A. Hofmann, and W. Brütting. Temperature dependent competition between different recombination channels in organic heterojunction solar cells. *Journal of Optics*, 2015, submitted.

- A. N. Bartynski, S. Grob, T. Linderl, M. Gruber, W. Brütting, and M. E. Thompson. Organic solar cells with open circuit voltage over 1.25 V employing tetraphenyldibenzoperiflanthene as the acceptor, 2015, to be submitted.

- U. Hörmann, C. Lorch, A. Hinderhofer, A. Gerlach, M. Gruber, J. Kraus, B. Sykora, S. Grob, T. Linderl, A. Wilke, A. Opitz, R. Hansson, A. S. Anselmo, Y. Ozawa, Y. Nakayama, H. Ishii, N. Koch, E. Moons, F. Schreiber, and W. Brütting. V_{OC} from a morphology point of view: the influence of molecular orientation on the open circuit voltage of organic planar heterojunction solar cells. *The Journal of Physical Chemistry C*, 118 (46): 26462 - 26470, 2014.

- S. Grob, M. Gruber, A. N. Bartynski, U. Hörmann, T. Linderl, M. E. Thompson, and W. Brütting. Amorphous vs crystalline exciton blocking layers at the anode interface in planar and planar-mixed heterojunction organic solar cells. *Applied Physics Letters*, 104 (21): 213304, 2014.

- S. Yu, A. Opitz, S. Grob, R. Resel, M. Oehzelt, W. Brütting, I. Salzmann, and N. Koch. Performance enhancement of diindenoperylene-based organic photovoltaic cells by nanocolumn-arrays. *Organic Electronics*, 15 (10): 2210 - 2217, 2014.

- U. Hörmann, J. Kraus, M. Gruber, C. Schuhmair, T. Linderl, S. Grob, S. Kapfinger, K. Klein, M. Stutzmann, H. J. Krenner, and W. Brütting. Quantification of energy losses in organic solar cells from temperature-dependent device characteristics. *Physical Review B*, 88: 235307, 2013.

Danksagung - Acknowledgement

Zu guter Letzt möchte ich mich bei allen bedanken, die auf unterschiedlichste Weise zum Gelingen dieser Arbeit beigetragen haben. Hätte ich all die Aufgaben der letzten vier Jahre alleine bewältigen müssen, wäre eine Arbeit in der vorliegenden Form definitiv nicht möglich gewesen. Daher danke ich ...

- Prof. Dr. **Wolfgang Brütting** zunächst einmal für die Möglichkeit, überhaupt eine Doktorarbeit in seiner Arbeitsgruppe aufzunehmen. Für das mir entgegengebrachte Vertrauen bedanke ich mich sehr. Danke auch für die fortwährende Unterstützung während der gesamten Dauer der Promotion. Das gilt nicht nur für Tipps und Ratschläge bei wissenschaftlichen Fragen, sondern insbesondere auch für die stets reibungslose Unterstützung bei allem Weiteren. Vor allem die lückenlose Ausstattung mit Arbeitsverträgen, sowie die Möglichkeit zwei Forschungsaufenthalte in Spanien bzw. den USA durchzuführen hat mir persönlich enorm geholfen.

- Prof. Dr. **Achim Wixforth** für die Bereitschaft das Zweitgutachten meiner Dissertation zu erstellen.

- Prof. Dr. **Bernd Stritzker** und Prof. Dr. **Manfred Albrecht** in ihrer Position als Lehrstuhlinhaber für die freundliche Aufnahme an den Lehrstuhl Experimentalphysik IV, sowie die angenehme Arbeitsatmosphäre, die sie dort geschaffen haben.

- Dr. **Mark E. Thompson** von der University of Southern California in Los Angeles und Prof. **Juan Bisquert** von der Universitat Jaume I in Castellón de la Plana für die jeweilige Möglichkeit mehrwöchige Forschungsaufenthalte in ihren Arbeitsgruppen durchführen zu können.

- der **Bayerischen Forschungsstiftung** sowie der **Deutschen Forschungsgesellschaft**, ohne deren finanzielle Förderung das Erstellen dieser Arbeit überhaupt nicht möglich gewesen wäre.

- meinen Kollegen aus der Teilarbeitsgruppe organische Photovoltaik. Durch die Einarbeitung in das Arbeitsgebiet und die ständige Unterstützung bei praktischen und theoretischen Fragestellungen, haben sie mir erst das Werkzeug in die Hände gelegt, mit dem diese Arbeit bewältigt werden konnte. Daher bedanke ich mich

besonders bei Dr. **Mark Gruber**, Dr. **Ulrich Hörmann**, Dr. **Julia Kraus**, **Theresa Linderl** und **Alexander Hofmann**.

- auch allen anderen Doktoranden der Arbeitsgruppe organische Halbleiter, insbesondere Dr. **Tobias Schmidt**, **Lars Jäger**, **Eduard Meister**, **Bert Scholz** und **Sebastian Wehrmeister** für die stets reibungslose Zusammenarbeit und Hilfe bei Fragestellungen im Labor oder im Büro.

- all unseren Kooperationspartnern, d.h. den Mitarbeitern der Arbeitsgruppen um Prof. Dr. **Frank Schreiber** (Universität Tübingen), Prof. Dr. **Jens Pflaum** (Universität Würzburg) und Prof. Dr. **Norbert Koch** (Humboldt-Universität Berlin). Insbesondere möchte ich bei denen bedanken, ohne deren Zutun manche Messergebnisse in dieser Arbeit gar nicht auftauchen würden. Hier gilt mein Dank allen voran Dr. **Andreas Opitz**, Dr. **Andreas Wilke**, **Andrew Bartynski**, **Shuwen Yu** und **Christopher Lorch**.

- **Andreas Mittelberger**, **Stefan Schmidt**, **Florian Graßl** und **Philippe Linsmayer**, welche ich während ihrer Bachelorarbeiten betreut habe und deren Ergebnisse in Teilen in dieser Arbeit präsentiert werden. Durch ihre engagierte und gewissenhafte Arbeit haben sie mir geholfen einen näheren Einblick zu spezifischen Fragestellungen zu erhalten.

- **Michael Weinl** und **Stefan Gsell** für ihre Hilfe wenn es Probleme mit dem Röntgendiffraktometer gab.

- allen weiteren Personen am Lehrstuhl Experimentalphysik IV, die durch ihre Arbeit im Hintergrund, eine vernünftige wissenschaftliche Arbeit überhaupt erst ermöglichen. Dabei gilt mein Dank der Technik-Crew um **Wolfgang Reiber**, **Birgit Knoblich**, **Olga Lik** und **Sybille Heidemeyer**, sowie dem Sekretariat um **Maria Fuso**, **Bettina Schestak**, **Christine Schäfer** und **Claudia Löflath**.

- Prof. **Ellen Moons**, **Rickard Hansson**, **Leif K. E. Ericsson**, **Paul Beyer**, **Alexei Preobrajenski** und **Alexander Generalov**, die auf unterschiedlichste Weise zu den in dieser Arbeit enthaltenen NEXAFS-Daten beigetragen haben.

Der größte Dank gilt trotz allem meiner Familie. Meinen Eltern und meinem Bruder danke ich für die uneingeschränkte Unterstützung von Anfang an, das Vertrauen und den Rückhalt. Insbesondere danke ich auch Dir Tanja für das ganz große Glück, das ich mit dir und unseren Töchtern gefunden habe.